Earthquake Cycle Deformation in New Zealand Using Spatio-Temporal Techniques

THESIS

Submitted in partial fulfilment of the requirements for the degree of

DOCTOR OF PHILOSOPHY

by

NEHA

Under the Supervision of

DR. SUMANTA PASARI

BIRLA INSTITUTE OF TECHNOLOGY AND SCIENCE, PILANI

2023

"*Divide each difficulty into as many parts as is feasible and necessary to resolve it.*"

By René Descartes

BIRLA INSTITUTE OF TECHNOLOGY & SCIENCE, PILANI

CERTIFICATE

This is to certify that the thesis titled **"Earthquake Cycle Deformation in New Zealand Using Spatio-Temporal Techniques"** submitted by **Ms. Neha**, ID No. **2018PHXF0423P** for the award of Ph.D. of the institute embodies original work done by her under my supervision.

Signature of the Supervisor
Name: **DR. SUMANTA PASARI**
Designation: **Associate Professor**

Date: **April 21, 2023**

Acknowledgments

I wish to acknowledge all those who have helped and encouraged me during my Ph.D. research. First of all, I would like to express my deepest gratitude and everlasting indebtedness to my research supervisor, **Dr. Sumanta Pasari**, Department of Mathematics, Birla Institute of Technology and Science (BITS), Pilani (Pilani Campus), for his continuous encouragement and guidance with full of patience, motivation, moral support with his care and influences, enthusiasm, and immense knowledge. I think I am fortunate not only to get an opportunity to work with him on the problem ***"Earthquake Cycle Deformation in New Zealand Using Spatio-Temporal Techniques"*** but also to learn the life lessons from him, such as consistency, communication skill, and most important time management. His cheering illustration and intriguing ideas enlightened me and always directed me to the correct path during my Ph.D. time.

Besides my Ph.D. supervisor, I would like to express my special thanks to **Prof. Kuo-En Ching**, National Cheng Kung University, Taiwan for giving me valuable suggestions and constructive ideas during the presentations. His punctuality, gentleness, and brilliant insight inspire me.

I am thankful to **Prof. Souvik Bhattacharyya**, Vice-Chancellor, **Prof. Sudhirkumar Barai**, Director (BITS Pilani, Pilani Campus), **Prof. M. B. Srinivas**, Dean, Academic-Graduate Studies & Research, and **Prof. Shamik Chakraborty**, Associate Dean (AGSRD) for giving me an opportunity to achieve a challenging position in respective field pertinent to my qualification which allowed me to use my skills to prove myself worthy. I am further thankful to them for providing me the facilities regarding research work and a healthy environment.

It is an honor for me to be a doctoral student at the Department of Mathematics, BITS Pilani. I owe my sincere gratitude to **Prof. Devendra Kumar**, HoD, Department of Mathematics and Ex-Hod, **Prof. B. K. Sharma** who provided me a golden opportunity to work in the Department of Mathematics and in finalizing this work within time. I would like to acknowledge all the faculty members and staff of the Mathematics Department for demonstrating genuine interest and enthusiasm in their teaching and relentless support.

I am also thankful to the Doctoral Advisory Committee (DAC) members **Prof. Rakhee** and **Prof. Udayan Chanda** for their valuable comments and suggestions during my Ph.D. research work.

I thank **Prof. Benjamin F. Chao**, Academia Sinica, Institute of Earth Sciences, Taipei, Taiwan, for providing research ideas and fruitful discussion on empirical orthogonal function

analysis for coseismic studies. I thank **Dr. Yogendra Sharma** (National Cheng-Kung University, Taiwan) and **Dr. Utpal Kumar** (University of California, Berkeley) for their time-to-time support and for providing the essential codes.

I cherish all the moments spent with my best friends **Dr. Ankit Kumar** and **Ms. Shilpa**. I thank them for always there for me and making my time memorable in BITS Pilani. I would like to thank my batchmates **Mr. Chandan, Ms. Riya Jain, Mr. Sajan**, and **Ms. Sarita** and my other colleagues of the Department for supporting and encouraging me during my Ph.D. tenure in direct or indirect ways. I also thank my juniors **Mr. Himanshu Verma**, **Ms. Sakshi Shukla**, **Ms. Sonu Devi**, and **Ms. Sharmila Devi** for helping me to figure out technical errors in the thesis draft. I also want to thank my family friends **Ms. Kiran Sharma, Ms. Sarita,** and **Dr. Poonam Meena** to be with me in each and every good or bad situation. A special thank goes to **Dr. Vivek Tiwari** for cheering and encouraging me.

Last but not the least, I would like to thank my family members, to my father **Mr. Umed Singh** and to my mother **Mrs. Sunita Devi**. I am deeply indebted to all the pains taken by them to make my dream come true. Thank you for giving me the confidence and courage to make the choices I have made. I also thank my uncles and aunts **Mr. Shersingh** and **Mrs. Krishna Devi**, **Mr. Balber Bhalothia** and **Mrs. Sajana Devi**, **Mr. Ramchandra Bhalotia** and **Mrs. Nirmla Devi**, **Mr. Jitendra Janu** and **Mrs. Rajani Dager**, and **Mr. Ravinder Janu** and **Mrs. Sulochana Dager**. My sincere thank to my loving brothers and sisters **Mr. Prashant Bhalothia, Mr. Manish Bahlothia, Mr. Vikas Bhalothia, Mr. Hemant Bhalothia, Mr. Himanshu Janu, Mr. Abhay Janu, Mrs. Chitra Choudhary, Mrs. Ruchika Choudhary, Ms. Ayushi Janu** and **Ms. Hiya Janu**. Their constant love and care empowered me to accomplish my thesis and also ignited me to take more challenges in my life. My special love goes to my little sister "**Laddo**" for the joy of my heart.

I thankfully acknowledge **University Grant Commission** (UGC), New Delhi for providing me financial assistance as Junior and Senior Research Fellowships during my tenure at BITS Pilani as a Ph.D. research scholar. I am thankful to **Science and Engineering Research Board** (SERB) to provide International Travel Support (ITS) scheme during this work.

Place: **BITS Pilani** — **NEHA**

Date: **April 21, 2023** — (Department of Mathematics)

Abstract

Large earthquakes have deep societal and economic impact. Over time, seismic risks to people and economic losses have dramatically increased due to the rapid pace of urbanization and growing dense city population. Improvement of earthquake hazard thus becomes the need of the hour not only for the safety of millions of inhabitants in and around the seismogenic regions but also for social policymaking, insurance, city-planning, and several other end-user applications. In light of this, characterization of the regional earthquake cycle is an inevitable task for the contemporary seismic hazard analysis of a geographic region. The present thesis addresses the problem of earthquake cycle deformation in New Zealand using spatio-temporal methods.

The static and/or dynamic nature of crustal deformation associated with an earthquake cycle includes three primary phases, namely the interseismic phase, coseismic phase, and the post-seismic phase. The interseismic deformation reveals how the Earth's crust deforms under the plate tectonic forces and it is measured through several crustal parameters, such as the velocity distribution, strain field characterization, and relevant seismic moment estimation. The coseismic deformation shows how the Earth's crust responds during an earthquake and it is realized through various indicators, such as the spatial and temporal evolution of earthquake, coseismic dislocation, and the coseismic strain field distribution. The postseismic deformation depicts how the Earth's crust readjusts to return to its initial level and it is assessed through the afterslip distribution and the exponentially decaying surface velocities. Among these three dominant phases, the concentration is often given to the interseismic phase due to its close relevance to the earthquake hazard estimation of a given region.

To analyze earthquake cycle deformation, two basic approaches, namely the theory-based technique and the data-driven method are often utilized. Though the theory-driven models provide important characteristics of the earthquake cycle deformation, their applications are quite limited due to the requirement of stringent boundary conditions, subjective knowledge of the hyperparameters, and an ideal physical model. On the other hand, the data-driven models are purely based on earthquake-relevant observational data, such as space geodetic data (e.g., GNSS measurements and InSAR observations) and historical seismicity data. Moreover, the data-driven models inherently account for several physical properties of earthquake cycle, such as multiplicity of scales in space and time, multifault interactions, complex fault geometries, and nonlinear space-time behavior of earthquake occurrences, as the data of necessity arises from such interactions. The common data-driven techniques in studying earthquake cycle include the empirical orthogonal function (EOF), seismic moment budget estimation, and the earthquake nowcasting technique. These methods exhibit a wealth of information related to the ongoing seismic cycle and consequent earthquake hazards. For instance, the spatio-temporal

EOF method is an effective utility to decompose the space-time data into individual spatial and temporal patterns for extracting the prevalent hidden signals, such as preseismic, coseismic, postseismic, common mode error, and other random noises, separately. The data-driven seismic moment estimation geodetically computes the earthquake potential associated with the regional earthquake cycle, whereas the area-based nowcasting method statistically determines the contemporary state of earthquake cycle progression in several city regions. In view of this, the present thesis aims to analyze the earthquake cycle deformation in New Zealand using the three aforementioned spatio-temporal techniques. The study area has been selected based on two reasons, namely the occurrence of the 2016 "complex multifault rupture" Kaikoura earthquake and the availability of sufficient geodetic and earthquake data.

The thesis essentially highlights the efficacy of the spatio-temporal techniques, particularly for coseismic and interseismic deformation and associated seismic hazard analysis in New Zealand. For this, Chapter 1 introduces the evolution of New Zealand and its tectonic classification, along with the historical seismicity. Chapter 2 includes the fundamental algorithm of the EOF method and its sequential extensions along with their prominent applications, especially for geohazard analysis. Chapter 3, Chapter 4, and Chapter 5 are in a sense the core of the thesis, for which the obtained results are directly relevant to the seismic hazard evaluation. Chapter 3 should be considered as a toolbox, demonstrating the versatile EOF method for investigating the coseismic deformation caused by the 2016 Kaikoura earthquake. Chapter 4 provides a segment-wise seismic energy budget that can be interpreted as a significant indicator of the maximum earthquake potential along different segments in New Zealand. Using the earthquake nowcasting technique, Chapter 5 presents a numerical value, known as the earthquake potential score (0%–100%) that can be seen as a way of earthquake cycle progression in a city region since the last major event. Finally, Chapter 6 summarizes the major contributions of the thesis work along with some future direction.

To achieve the research goals, first, a comprehensive coseismic deformation associated with the 2016 Kaikoura earthquake is examined through the EOF-based coseismic spatial and temporal modes (EOF modes) along with the coseismic strain field distribution. For this, 15 days refined time series data (straddling the event date of the Kaikoura earthquake) of 127 CGPS stations (at every 30 min epoch) comprising the earthquake-induced jumps and unmodelled residuals is incorporated. The dominant EOF modes, a pair of spatial pattern and corresponding principal time series, enable us to determine the coseismic and early postseismic deformation pattern associated with the Kaikoura event. It is observed that (i) the horizontal coseismic deformation with an amplitude of 150 mm in the east and 200 mm in the north is aligned in the NE-SW direction from the central South Island to the end shore of the North Island, whereas the vertical deformation with an amplitude of 200 mm in the up direction is observed along the offshore boundary of the North Canterbury region; (ii) the pattern of the postseismic relaxation

follows the same direction as observed in the coseismic displacement, and (iii) the coseismic horizontal strain fields (i.e., dilatation and shear strain) reveal a large-scale extensional behavior in the northern Canterbury region and compressional concentric pattern near the uppermost South Island and lower North Island, along with a radial and concentric SW-NE shear pattern. In addition, a comparison study between the EOF-based displacement vectors and the least-squares estimates indicates that the EOF method outperforms the traditional least-squares estimation, even in the presence of various prevalent signals, such as pre and postseismic signals, common mode errors, outliers, and other noises in a given dataset.

After performing the EOF-based coseismic analysis, the second task is to estimate seismic moment budget along 14 different segments in New Zealand. For this, geodetic moment rates and seismic moment rates for each segment are calculated and compared. The geodetic moment rates are calculated from the geodetic strain fields estimated through the updated velocity field of about 180 CGPS stations, whereas the seismic moment rates are computed from the historical seismicity data of $\sim$ 180 years. A comparison of these two rates reveals segment-wise total energy budget that could possibly release in future devastating earthquakes. The results show that (i) the geodetic strain field has a dominant compressional rate (0–75 nstrain/yr) rather than extensional rate (0–30 nstrain/yr) along the Alpine fault; (ii) the higher value of the maximum shear strain rates ($\sim$ 225 nstrain/yr) is aligned to the northeastern boundary of the South Island; (iii) the estimated geodetic moment rate ranges from 3.15×10^{17} Nm/yr to 9.00×10^{17} Nm/yr, whereas the seismic moment rate lies in the range of 0.10×10^{17} Nm/yr to 83.92×10^{17} Nm/yr, and (iv) finally, based on the comparison between the segment-wise moment accumulation rate and the moment release rate, the possible maximum earthquake potential of 14 segments in New Zealand varies from M_w6.7 to M_w8.0. In essence, the spatial distribution of seismic moment budget in New Zealand suggests that the segments with high seismic potential indicate the areas of interseismic strain accumulation, whereas the segments with lower earthquake potential corresponds to the areas encompassing the rupture areas of recent large events.

To statistically address the current progression of regional earthquake cycle at 15 major cities in New Zealand, an empirical area-based technique, known as earthquake nowcasting, is utilized. In this method, the natural times, the cumulative number of intermittent small magnitude events between pairs of large earthquakes, are utilized to mark the evolution of the seismic process rather than the traditional clock or calendar times. Four reference probability distribution models, namely the exponential, gamma, Weibull, and the exponentiated exponential are fitted to the observed natural time counts. The best fit Weibull distribution is then used to compute the earthquake potential score (EPS) of a circular city region. The EPS values (0%–100%) for 15 city regions in New Zealand are observed to lie in the range of 6% to 97%. Higher values of the nowcast scores (above 80%) at 13 cities, including Auckland and Wellington, indicate that most of the cities have reached to their rear end in the seismic cycle of large magnitude

events.

In summary, the present study has significantly improved our understanding of earthquake cycle deformation in New Zealand through spatio-temporal techniques, purely dictated by the observed geodetic and earthquake data characteristics. The obtained EOF-based coseismic displacement vectors, EOF-based coseismic strain field, interseismic strain pattern, seismic moment budget and associated earthquake potential, and the city-wise nowcast scores are not only useful for earthquake cycle deformation in New Zealand but also facilitate fault reconstruction, study of slow slip events, and seismic risk mapping for several end-user applications.

Contents

List of Figures

List of Tables

List of Abbreviations

CDF	Cumulative Distribution Function
CME	Common Mode Error
EDM	Elastic Dislocation Model
EOF	Empirical Orthogonal Function
EPS	Earthquake Potential Score
GeoNET	GNSS Earth Observation Network System
GNSS	Global Navigation Satellite System
GPS	Global Positioning System
InSAR	Interferometric Synthetic Aperture Radar
ITRF	International Terrestrial Reference Frame
KLE	Karhunen–Loéve Expansion
LSE	Least-Squares Estimation
MIDAS	Median Interannual Difference Adjusted for Skewness
MFS	Marlborough Fault System
MMI	Modified Mercalli Intensity
NGL	Nevada Geodetic Laboratory
NSHM	National Seismic Hazard Models
PCA	Principal Component Analysis
PCAIM	Principal Component Analysis Based Inversion Model
PDF	Probability Distribution Function
PGA	Peak Ground Acceleration
RINEX	Receiver Independent Exchange Format
SVD	Singular Value Decomposition

Dedicated To

My Nana-ji and Nani-ji,

Late Rameshwar Lal and Late Shanti Devi,

for being my guardian angels

and

My Beloved Family,

for encouraging and supporting me in this journey

Chapter 1

Introduction

"*We learn geology the morning after the earthquake.*"

by Ralph Waldo Emerson

This chapter presents a general overview and motivation of the thesis work. The chapter discusses the evolution and tectonic setting of New Zealand along with its major tectonic domains and subsequent historical seismicity. It also includes the main research objective and the scope of the present work. A chapter-wise road map of the thesis is also presented towards the end of this chapter.

Contents

1.1 Overview and motivation

Earth deformation driven by plate tectonic movements is a multi-phase process and occurs in a large spectrum of timescales ranging from seconds (dynamic/seismic deformation) to millions of years (tectonic deformation) [8, 11, 75, 109, 150]. However, the characterization of an earthquake deformation cycle is intricated due to numerous physical factors, for instance, the cyclic nature of earthquakes and long recurrence intervals of large earthquakes. According to Reid's elastic rebound model (1910) [195] and Okada and Nagata theory (1953) [168], the earthquake cycle is traditionally divided into three main phases, namely interseismic, coseismic, and postseismic phases. Each phase carries significant information of the crustal deformation caused by the earthquake cycle. A pictorial sketch of the earthquake cycle is shown in Fig. 1.1.

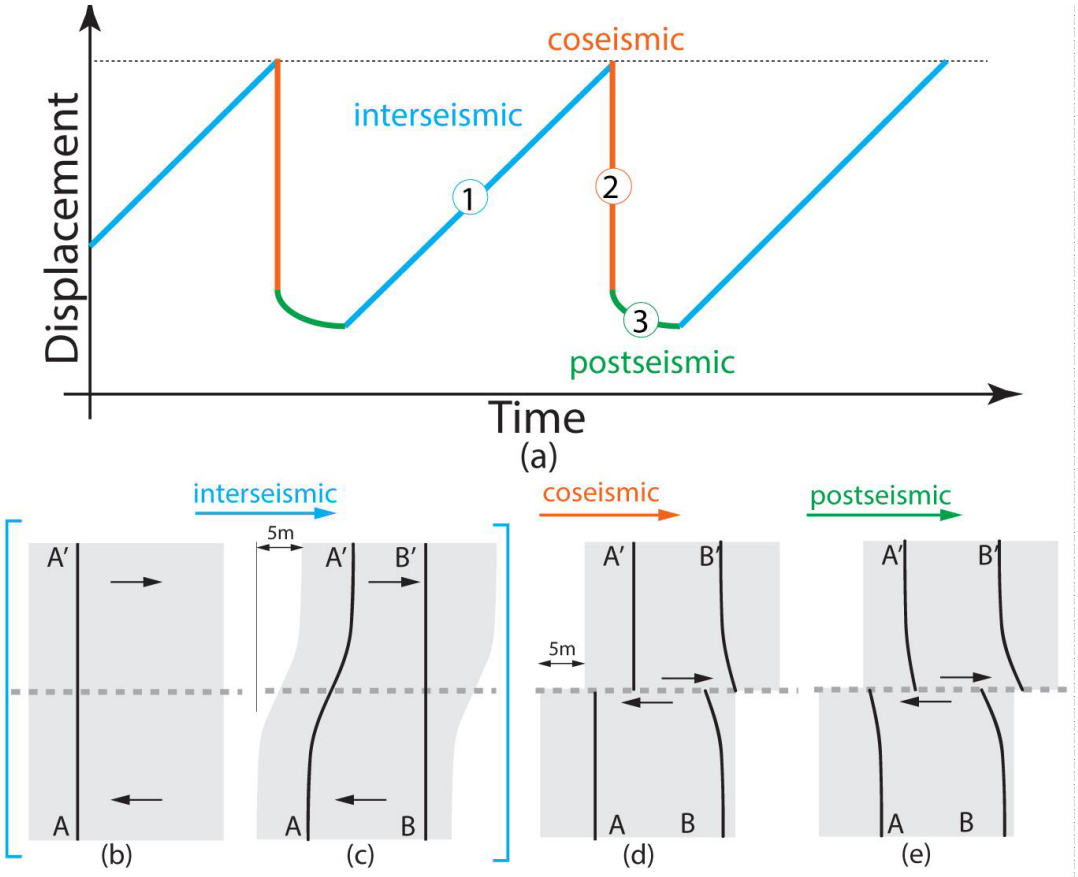

Fig. 1.1: Sketch of the deformation cycle and survey markers at three different phases of the earthquake cycle. Theoretical geodetic time series is shown in the subplot (a), whereas two survey markers (A-A'and B-B') at different phases are shown in the subplots (b-e). Further, the subplots in (b-c) show the displacement and distortion of profile A-A' in the interseismic phase, the subplot in (d) indicates the displacement and distortion of both profiles A-A' and B-B' in the coseismic phase, and the subpot in (e) shows the displacement readjustment of profiles A-A' and B-B'during the postseismic phase (Aslan (2019) [8]).

The interseismic phase (phase 1) refers to the longest time period of years to centuries. It describes the period of slow accumulation of the strain energy due to the plate tectonic motion [75]. This phase corresponds to the earthquake recurrence interval. In order to estimate the earthquake hazard potential and the physical properties (e.g., plate collison, fault geometry, and recurrence interval) of the underlying earthquake dynamics, the assessment of the interseismic accumulated strain is an inevitable step. Despite the plethora of data-driven interseismic studies using seismic observations, earthquake data, and geodetic measurements, the investigation of interseismic deformation is a complex process due to the presence of inseparable other deformation factors, such as delayed postseismic deformation and/or slow and transient slip events [8, 75, 109].

The coseismic phase (phase 2) considers the smallest time scale of milliseconds to minutes. It denotes the time period in which the earthquake event nucleates, propagates, and stops. In other words, when the accumulated strain exceeds the frictional strength of the fault, it releases in the form of earthquakes [150]. The amount (energy release) and spatial distribution of the crustal deformation caused by the event rely on several factors, such as magnitude of the event, focal depth of the event, and tectonic setting of the epicentral area. The coseismic deformation is of paramount importance in earthquake mechanics as it determines the earthquake mechanism, reveals the tectonic characteristics and fault geometry, and it delineates the resisted shear stress and the stress drop [8]. As of now, reliable estimation of the coseismic deformation is still difficult due to the presence of preseismic and postseismic signals, and low signal-to-noise ratio in the geodetic time series.

The postseismic phase (phase 3) refers to the intermediate time frame of hours to years. It defines a transient mechanical response of the lithosphere. More specifically, the stress asperities caused by the earthquake event are leveled up by the occurrence of afterslips [109]. In short, the deformation process after an earthquake returns to the background level as before the earthquake by releasing the remaining energy in terms of earthquakes. The postseismic phase is completely controlled by two factors, namely the magnitude of coseismic slip and the regional rheology [109]. Among all these three phases of crustal deformation during an earthquake cycle, the postseismic phase is the least understood phase due to the combination of three different mechanisms, namely aseismic afterslip, poroelastic rebound, and viscoelastic relaxation [109].

Therefore, a complete characterization of the earthquake cycle on a given fault system remains a challenging task. In fact, among the three phases of earthquake cycle, the concentration is often given to the interseismic phase due to its close relevance to the earthquake hazard estimation of a given region. In order to investigate the active crustal deformation caused by earthquake cycles and consequent seismic hazard assessment, several studies based on geological, seismological, paleoseismological, geodesy, and geophysical approaches have been carried out in past years [8, 15, 18, 42, 168, 184, 195, 227, 232, 270]. Though such approaches provide

better insights and valuable input parameters for seismic hazard analysis, much of the knowledge of different phases of earthquake cycle is gained based on the interpretation of the space geodetic observations (e.g., global positioning system, GPS and interferometric synthetic aperture radar, InSAR) as well as the historical seismicity data. This is due to the fact that these data sets contain relevant space-time information of the underlying tectonic system.

In general, the approaches to study earthquake dynamics are often classified into two basic types, theory-driven approaches and data-driven approaches. The theory-driven models utilize the idea of physics and conditions leading to earthquake phenomena, such as rate-and-state friction law and coulomb stress changes, and seismic wave-propagation effects, whereas the data-driven models incorporate the space-time interaction of the earthquake-relevant data, such as geodetic data and seismicity data [217]. Although the theory-driven models provide important characteristics of the earthquake threshold system, they may lead to poor results due to the complex nature of the earthquake system, such as the multiplicity of scales in space and time [219], multi-fault interactions [87], complex fault geometries [231], and nonlinear space-time behavior of earthquake occurrences [211]. To deal with such situations, data-driven models are often used to analyze inherent space-time characteristics of the earthquake system [218]. Examples of such spatio-temporal techniques include earthquake nowcasting for analyzing earthquake cycle recharge and discharge patterns [179, 218], principal component analysis (PCA) or empirical orthogonal function (EOF) for identifying the space-time evolution patterns [35, 36, 156], seismic moment budget estimation for contemporary phase of earthquake cycle [173, 227], least-squares estimation (LSE) for determining the phases of the earthquake cycle [114, 229], and Bayesian inference for earthquake forecasting [45]. These empirical methods have been widely implemented worldwide in order to understand the different phases of earthquake cycle and its relevant information of the earthquake system linking to the regional tectonic geometries.

In order to investigate earthquake cycle deformation and associated seismic hazard analysis, the spatio-temporal technique, namely EOF (interchangeable with the PCA method) is proposed by Chang and Chao (2011) [36], specifically for the coseismic deformation analysis. In this study, they have investigated the detailed view of the coseismic deformation associated with the 2011 Tohoku earthquake through the EOF-based spatial and corresponding temporal modes. They have also highlighted the strength of the self-organizing EOF method in terms of its potential to extract the inherent hidden and dominant patterns through individual spatial patterns along with time history from the coherent space-time data [92]. Further, the authors have suggested that the EOF method outperforms the traditional techniques (e.g., LSE and elastic dislocation model) by providing adequate coseismic displacement field even in the presence of other signals and noises (e.g., pre and postseismic signals, and common mode error) [35]. Based on the inevitable strength of the EOF, the EOF method and its integration with the

PCA-based inversion model (PCAIM) have been implemented in numerous studies, such as the coseismic analysis of two earthquakes (the 2002 Hualien earthquake (M_w7.1) and the 2010 Jiashian earthquake (M_w6.3)) in Taiwan [35], quantification of common mode error in Taiwan [132], coseismic slip distribution associated with the 2011 Tohoku earthquake [156], and the aseismic slow slip event triggered by the earthquakes in Guerrero, Mexico [193].

For analyzing the interseismic phase of the contemporary earthquake cycle, one of the data-oriented approaches, namely the area-based earthquake nowcasting method, was proposed by Rundle et al. (2016) [218]. This statistical method stems from the concept of stochastic "renewal" process of earthquake cycles through a "short-term fault memory". It uses the novel concept of "natural time" to track the changing state of the earthquake system over time. The natural time, unlike the clock/calendar time, refers to a measure of small event counts in between two successive large earthquake events. The earthquake nowcasting method has been applied in various tectonically active areas, such as Ankara, California, Dhaka, Jakarta, Kolkata, Kathmandu, Los Angeles, Manila, Medan, New Delhi, Oklahoma, Palu, Taipei, Tokyo, and San Francisco to quantify the current progression of the contemporary earthquake cycle of the given region in terms of earthquake potential score [179, 183, 208, 215]. Likewise, for assessing the surface deformation associated with the interseismic phase, the seismic-moment budget (earthquake potential) estimation method has been employed by comparing the accumulated geodetic moment and released seismic moment in a given geographic area. This method uses mainly two types of data, namely geodetic data and earthquake data. Using the dense network of geodetic data and historical earthquake records, the seismic moment budget estimation has been carried out in several earthquake-prone regions, such as Eastern Iran, Egypt, Greece, Indonesia, Northeast Tibet, Ordos Plateau in northern China, the Himalayan region, and the Sicily-Calabria subduction [6, 39, 152, 172, 194, 202, 224, 227].

From the above-mentioned space-time approaches, it is evident that the data-driven techniques not only extract the inherent information of the contemporary earthquake cycle purely from the data but also connect the observable pattern to the underlying regional tectonic regime, such as stress buildup, strain release, and elastic rebound associated with large destructive earthquakes. These space-time techniques offer a plethora of advantages, such as (i) easily accessible earthquake-relevant data, including GPS, InSAR, and seismicity data, (ii) ease of implementation and computationally inexpensive, with minimum a-priori or subjective information, (iii) rich in model pre-processing (e.g., data cleaning, data tranformation, and data reduction), model processing, and model post-processing in order to assess reliability, uncertainty and sensitivity analysis over space and time, (iv) suitability for recursive operations, such as dynamic strain estimation, progression in earthquake clustering and thereby, earthquake monitoring, and

(v) especially, provides a state-of-the-art toolkit in the area of prediction, estimation, and detection as commonly needed in a variety of science and engineering disciplines, such as Climate and Atmospheric, Geophysics, Biostatistics, Physiology, and Meteorology. Consequently, these methods have gained enormous attention in the geoscience community mainly to understand the crustal deformation caused by the earthquake cycle and associated seismic hazard evaluation. Moreover, these spatio-temporal techniques seek to answer some of the common questions often asked by the public, scientists, political leaders, and decision-makers for the socio-economic development of a region. For instance, (i) what is the space-time distribution of surface deformation associated with a large-size earthquake in its coseismic phase of earthquake cycle? (ii) what is the current level of seismic progression of a city in its earthquake cycle of large-size events? and (iii) what is the spatial distribution of earthquake potential in a study region within the interseismic phase of earthquake cycle?

In view of the above, the present study focuses on the area-based spatio-temporal techniques to analyze the coseismic and interseismic phases of the earthquake cycle in New Zealand. The emphasis is on the identification of the present-day earthquake hazard in New Zealand from a combination of statistical and geodetic approaches. In addition, the coseismic deformation associated with the 2016 Kaikoura earthquake (M_w7.8) is incorporated. For this purpose, geodetic measurements and historical seismicity data are used to determine the crustal velocity field, strain distribution, earthquake potential score, and the moment budget estimation in the study region. The results lead to the re-evaluation of the contemporary earthquake potential in New Zealand and its adjoining regions. However, before proceeding further, some background of the study region in terms of its evolution, tectonic classification, and historical seismicity is presented below for an easy understanding of the proposed methodology.

1.2 Evolution of New Zealand

The plate tectonic theory describes most of the dynamism of Earth's crust and features of the endogenic forces [123]. This scientific theory is fundamentally based on two hypotheses, the convection current hypothesis and the concept of seafloor spreading [80, 123]. The seafloor spreading describes the process of formation of the oceanic plate tectonics. The theory of convection current is the soul of the seafloor spreading concept, which helps to explain the system of these currents in the entire mantle portion generated by radioactive substances in the mantle. On the basis of these two key principles, the tectonic theory suggests that the Earth's lithosphere is broken into major and minor tectonic plates. These plates move, collide, slide by, converge with, or separate from each other. Consequently, the relative motion of plate boundaries determines whether they form convergent, divergent, or transform boundaries [123].

In essence, the movement and interaction of these plates include the formation, movement, collision, and destruction of plates, resulting in various geological events such as earthquakes, volcanic activity, and mountain-building along the plate boundaries [80, 123, 153].

According to the continental drift theory of the science of plate tectonics, the whole world's landmass formerly existed in one supercontinent, known as Pangaea [80, 123]. The supercontinent assembled two main landmasses, namely Laurasia and Gondwanaland (Fig. 1.2). Due to plate tectonic motion, the Pangaea first broke apart into two major continents around 200 Ma ago. Later on, about 180 Ma ago, the western Gondwanaland (Africa and South America) moved away from eastern Gondwanaland (Madagascar, India, Australia, and Antarctica) [32, 126, 154]. During the time period of 150−85 Ma ago, about 4000-km-long ribbon continent is separated from Antarctica and Australia, forming a submerged continent, known as Zealandia [32, 131, 154, 257]. The Gondwanaland origin of Zealandia is undisputed. The identification and formulation of Zealandia from Gondwanaland are explained based on various lines of geological and geophysical evidences, thereby providing a fresh context on the processes of continental rifting, thinning, and breakup [154].

Comprising of about 4.9 million km^2 area of continental crust, the continent Zealandia encompasses the main emergent landmass, namely New Zealand. Further, it includes the Campbell Plateau to the south side of New Zealand, the Challenger Plateau to the west side of New Zealand, the Chatham Rise to the east side of New Zealand, and the Lord Howe rise and Norfolk ridge to the north side of New Zealand (Fig. 1.2) [32, 126, 154, 257]. The present shape of New Zealand is the result of profound tectonic change during the Cretaceous-Cenozoic period. During that time, the apparent tectonic change was formed from subduction-related process to extension and widespread basin formation, eventually culminating in seafloor spreading and formation of the Tasman sea and the south Pacific [32]. Modern New Zealand is world-renowned study area for being a geologically active region. As a consequence of tectonic collision, subduction and transition, high mountains, frequent earthquakes, geothermally active areas, and volcanoes are evident in New Zealand and its surrounding regions. A brief characterization of the underlying tectonic setting of New Zealand is provided in the next section.

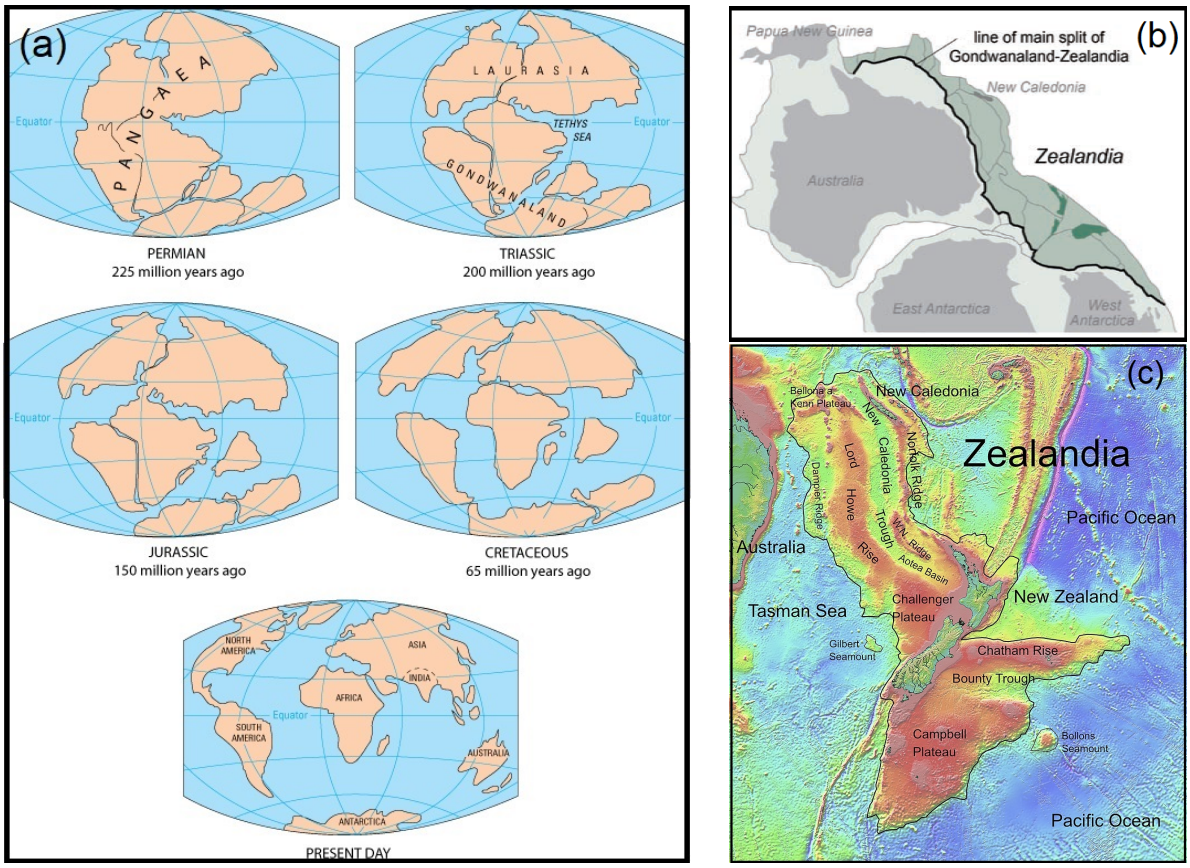

Fig. 1.2: Evolution of New Zealand: (a) break up of the supercontinent Pangaea (source: www.usgs.gov), (b) formulation of Zealandia, as a part of Gondwanaland (Campbell et al. (2012) [32]), and (c) overview of present-day Zealandia (source: https://en.wikipedia.org/wiki/Zealandia [257]).

1.3 Tectonic classification of New Zealand

Situated at the edge of the Pacific plate boundary and the Australian plate boundary, New Zealand covers 268,021 km^2 of surface landmass of the Zealandia continent (Fig. 1.3) [80]. New Zealand consists of two separate islands, namely the North Island and the South Island, connected by the Cook Strait.

From northernmost to southernmost, the plate tectonic in New Zealand is configured as below. (i) The oceanic Pacific plate is undergoing beneath the continental Australian plate with a rate of about $\sim$ 45 mm/yr in the east of the North Island along the Tonga trench, Kermadec trench, and Hikurangi margin; (ii) the continental Pacific plate is overriding upon the oceanic Australian plate with the convergence rate of $\sim$ 35 mm/yr in the west of the South Island along the Puysegur margin, and (iii) between the two opposite-dipping subduction, the continental Pacific plate and the continental Australian plate are moving parallelly from northeast-southwest direction with the rate of $\sim$ 40 mm/yr in the center along the Alpine fault, forming a continental

transpression zone (Fig. 1.3) [18, 40, 89, 231, 268]. As a result, the tectonic configuration of New Zealand has led to form various geological structures in New Zealand and its surrounding regions, such as mountains, faults, troughs, trenches, rifts, ridges, and volcanoes [126, 154]. These geological structures in New Zealand include Axial mountain ranges comprising the Southern Alps in the South Island, Tararua, Ruahine, Kaweka, Kaimanawa and Raukumara ranges in the North Island, Kermadec, Puysegur and Tonga trenches, Harve trough and Hikurangi trough, and the Taupo rift and the Taupo volcanic zone in North Island (Fig. 1.3) [18, 32, 88, 126, 140, 233, 241, 267]. Thus, these known geological features not only characterize the complex tectonic configuration in New Zealand but also showcase significant aspects of various stages of seismic activities throughout New Zealand and its adjacent regions.

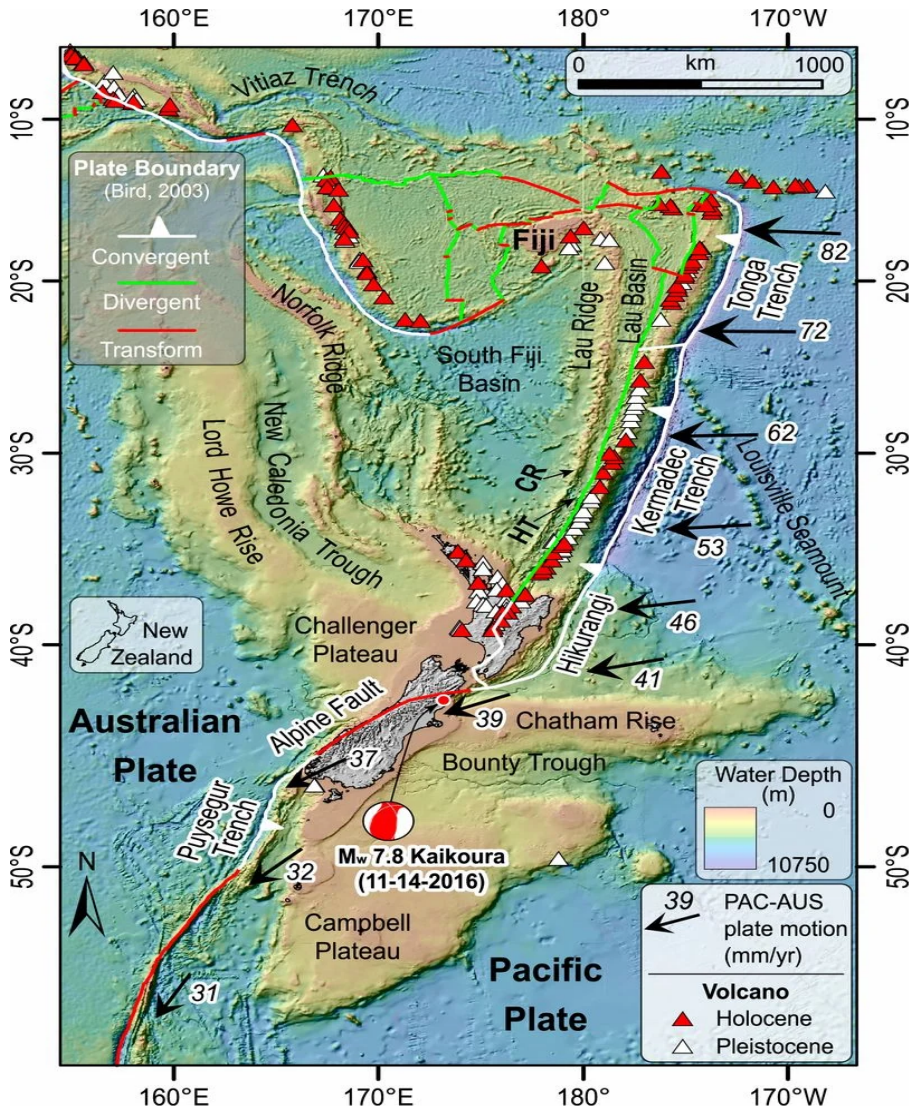

Fig. 1.3: Tectonic setting of New Zealand (Shi et al. (2019) [231]).

Based on the extent of similarity of the style and rate of deformation, and estimated seismic hazard related to tectonic blocks, the developers of the National Seismic Hazard Model (NSHM) have divided New Zealand into three main tectonic blocks [240, 241]. These three blocks are the continental-oceanic subduction block, continental-continental transpression block, and the oceanic-continental subduction block. Each of these blocks is characterized by distinct stratigraphy and metamorphic rocks, and is comprised of a variety of smaller tectonic faults system. The subdivision of these blocks into smaller tectonic domains is pictorially shown in Fig. 1.4. It may be noted that the boundaries between these smaller tectonic domains are rarely well-defined or sharp.

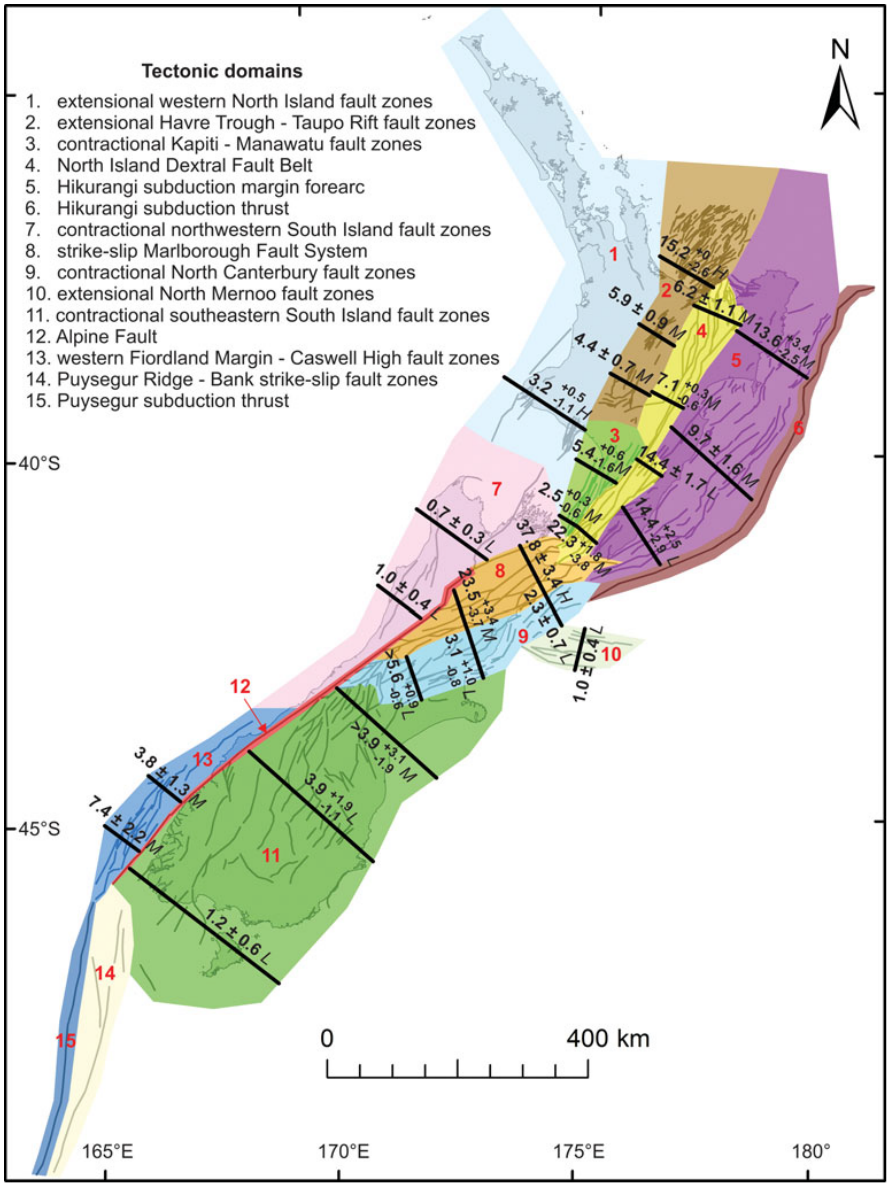

Fig. 1.4: Tectonic classification of New Zealand. Major tectonic domains in New Zealand are primarily defined by grouping fault zones with similar sense of movements (Litchfield et al. (2014) [140]).

1.3.1 The continental-oceanic subduction block

The continental-oceanic subduction block consists of the entire part of the North Island, the Hikurangi subduction forearc, and some parts of the Cook Strait (Fig. 1.4) [140]. Within this block, several smaller tectonic domains have been recognized according to similar geometries and kinematics. The group of such tectonic domains comprises the extensional fault zones of the western North Island and the Havre trough-Taupo rift, contractional fault zones of the Kapiti-Manawatu, dextral fault belt of the North Island, and the margin forearc and thrust zone of the Hikurangi subduction [240]. Each tectonic block bears a close resemblance to the underlying crust characteristics.

More specifically, the western North Island fault domain is considered to be relatively stable due to the presence of few active faults. Currently, this domain contains only two active fault zones, namely Hauraki rift with north-northwest striking faults and the Taranaki basin with north-northeast striking faults. At the east of western North Island, the extensional Havre trough-Taupo rift is located. With a transition from the Taupo rift to the southern Harve trough, this domain is characterized by the continental arc and back-arc of the Hikurangi margin [140]. The highly active Taupo volcanic arc and its associated volcanic calderas, namely Mount Ruapehu, Mount Ngauruhoe, White Island, and Okataina caldera are located in this region. All active faults within this extensional region have a northeast normal strike, relatively small and closely spaced. Centered in between the Taupo rift and the North Island axial ranges, the contractional Kapiti-Manawatu fault zone consists of a majority of reverse fault structures with the uplift movement in the eastern side of the Wanganui basin [140]. Many faults also have blind tips associated with hanging wall anticlines and footwall synclines [240].

In continuation to the above, the North Island dextral fault belt is extended from the Bay of Plenty to the Cook Strait. Along with the North Island axial ranges, this domain contains a series of dextral strike-slip faults, such as the Wairarapa fault, Alfredton fault, Waipukaka fault, and the Saunders Road fault with northeast striking [155, 240]. Some of the existing faults near the eastern margin of the Taupo rift have an oblique nature (equal components of normal and dextral slip) [155]. Due to margin-parallel plate motion, this domain is inferred to splay upwards off the Hikurangi subduction zone. The North Island dextral belt is separated from the Marlborough fault system due to slightly different directions of the active faults of both fault systems. This crustal scale hinge or kink between the two dextral slip fault systems is thought to transfer some of the slip on the Marlborough fault system northward onto the Hikurangi subduction thrust [140, 240]. The Hikurangi subduction forearc is covered by the accretionary wedge portion of the subduction zone from the west, the North Island dextral fault belt from the east, and the Havre trough from the northeast [13, 17, 240]. In this subduction forearc, majority of faults have a thrust environment along the northeast striking, whereas some

faults exhibit dextral strike-slip and normal slip patterns [140, 240]. These faults are associated with hanging walls anticlines and footwalls synclines [240]. Consequently, a partly uplift forearc and trenchward collapse are formed due to the subduction of the buoyant, oceanic, and plateau. Further, the Hikurangi subduction thrust is spread from northeastern part of the Marlborough fault system to the Kermadec trench and it is expressed by frontal thrust-faulted anticlinal ridges and a proto-thrust zone [18]. This region is a combination of three sections with different strikes, where the strike direction is considered on the basis of margin, historical seismicity, interseismic coupling distribution, and slow slip events. Overall, the plate motion of the oceanic-continental subduction zone is controlled by the subduction interface and Taupo volcanic zone.

1.3.2 The continental-continental transpression block

The continental-continental transpression block encompasses the central area of New Zealand. Tectonically, this block includes the northwestern and southeastern contractional fault zones of South Island, the contractional North Canterbury region, the strike-slip Marlborough fault system, and the Alpine fault zone (Fig. 1.4) [20, 140, 240]. The Alpine fault accommodates majority of the Pacific-Australian relative plate motion, leading to high seismic hazard in most of the South Island. Apart from the Alpine fault, each fault zone of this transitional block is highly seismic prone due to underlying complex tectonic setup, that is, transition belt from subduction to strike-slip [140].

The contractional northwestern South Island fault zone forms a collision zone on the west side of the South Island. Previous studies suggest that the normal faults of this region are currently reactivated in range-bounding reverse fault style [74, 133, 140]. This collision zone comprises some existing ruptured faults, for example, the Lyell fault, Inangahua fault, and the White Creek fault. In contrary to the contractional Northwestern South Island, the southeastern part of the South Island represents the largest segment of New Zealand containing all of the active faults of onland South Island, the southeastern section of the Alpine fault, and the southern North Canterbury faults zone [240, 241, 267]. This zone encloses reverse faults within much of the domain as well as strike-slip faults near the Alpine fault. The Wharekuri fault, Fox Peak fault, and the most recently identified Greendale fault are located in the given region [140, 231]. In addition, this collision region contains the Southern alps and the Canterbury plains.

Apart from the above-discussed two contractional zones, there is one youthful contractional zone, namely the North Canterbury fault zone in this block [140, 266, 271]. The North Canterbury fault zone lies between the southeastern Marlborough fault zone and the southern Hikurangi subduction margin, where both fault zones meet mixed fault orientations and slip types. In addition, this domain evolves by migrating the southeast boundary in the south and thereby

shows an encroachment of plate boundary deformation into the region from the north. Further, one of the predominating fault sources of the continental-continental transpression block is the strike-slip Marlborough fault zone [196, 240, 266]. The Marlborough fault system connects the Hikurangi subduction thrust to the Alpine fault. Most of the faults in this domain are characterized as dextral strike-slip fault, whereas some of the faults have measurable dip-slip motion (reverse faults). Few documented faults of this domain are the Awatere fault, Clarence fault, Cloudy fault, Hope fault, Jordan fault, Kekerengu fault, Needles fault, Poulter fault, Wairau fault, and the Vernon fault. In the South Island, the main fault source zone of the western side of the South Island continental-convergence zone is formed by the Alpine fault (760 km) [24, 140, 165, 244, 267]. The Alpine fault is treated as a connecting bridge between the Marlborough fault zone and the Puysegur subduction zone, which is bounded by the western side of the Southern Alps. On the basis of slip rate changes and along strike fault geometry, the Alpine fault shows variations in slip rates. Since there are no active faults on the west side of the Alpine fault, it indicates that the Australian plate is acting as a rigid indentor [140].

1.3.3 The oceanic-continental subduction block

Starting from the southern end of the Alpine fault, the oceanic-continental subduction block comprises two subduction margins, namely the western Fiordland margin and Caswell High fault zones and the Puysegur subduction margin (Fig. 1.4). Furthermore, the western Fiordland margin and Caswell High fault zones forms two parallel domains: (i) west-verging reverse/thrust belt on the eastern Fiordland basin and (ii) normal fault zone along the southeastern Caswell High [140]. At the southern edge of the western Fiordland margin and Caswell High fault zones, the Puysegur subduction margin is a faulted gully, which is located parallel to the Puysegur ridge fault. The structure analogous to this margin is in such a way that much of the plate motion of the Puysegur margin transfers into the subduction thrust via the Snares fault zone (situated northern end of the Puysegur ridge) [19, 140, 241, 258].

In light of the above, New Zealand offers a package of a variety of tectonic major blocks and their subdomains. Due to the juncture of complex tectonic environments, these blocks have potential to produce large to major earthquakes. Therefore, in order to better understand the kinematics of the underlying physical system, several multidisciplinary studies including geodetic investigation of crustal deformation, geological and paleoseismological findings of mapped faults, seismological observations, and geophysical techniques have been carried out in the past [20, 34, 42, 48, 84, 89, 231, 258, 267]. The present study aims to carry out crustal deformation caused by different phases of the earthquake cycle over New Zealand using the spatio-temporal data-driven techniques. For this, the first part focuses on quantifying coseismic deformation of the 2016 Kaikoura earthquake through the EOF analysis, whereas the second

part concentrates on determining the contemporary earthquake hazard potential in New Zealand through a combination of geodetic and statistical methods. Throughout this study, the above discussed segmentation strategy of New Zealand will be utilized.

1.4 Historical seismicity of New Zealand

The continuous oblique subduction of the Pacific and Australian plates causes enormous stress accumulation in New Zealand along the Alpine fault zone as well as two major subduction zones, the Hikurangi subduction interface and Puysegur subduction margin. As a consequence, the accumulated strain energy in New Zealand and its adjacent regions, located at the edge of the "Ring of Fire", has in turn produced several moderate to great earthquakes in the past [140, 244, 270]. In other words, New Zealand is involved in a continuing cycle of geological events and the level of tectonic activity remains high. These tectonic activities have not only impacted the socio-economic scale but also have an effect on the land. For example, in the 1855 Wairarapa earthquake ($M_w 8.1 - 8.2$), the coastline of Wellington Harbour was uplifted by 1.5 meters and there were alteast 10 reported deaths during the earthquake. The ground damages caused by the 1855 Wairarapa earthquake is shown in Fig. 1.5.

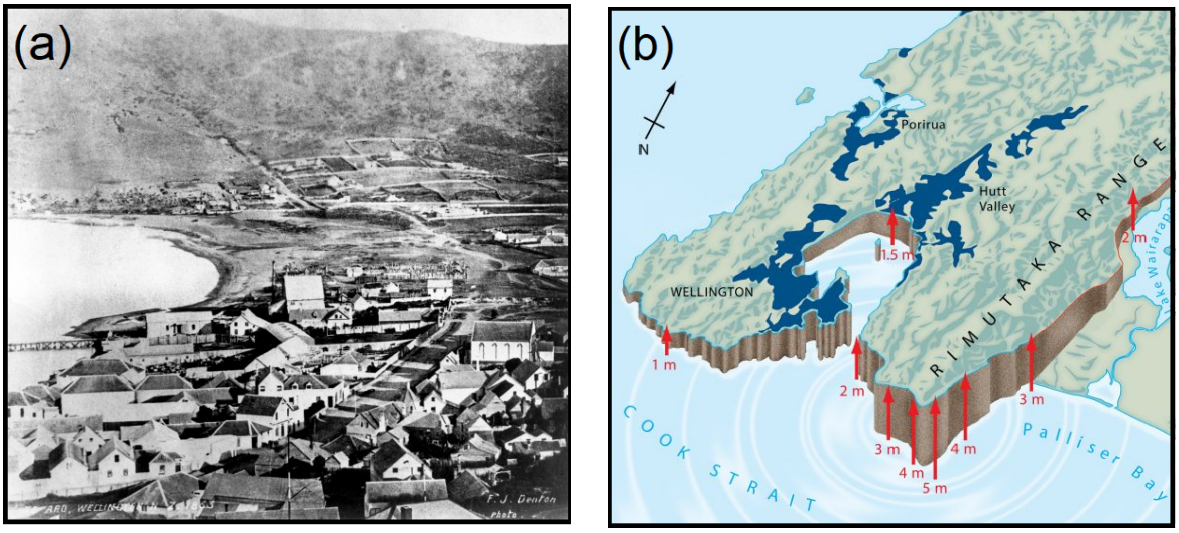

Fig. 1.5: (a) Ground damage caused by the 1855 Wairarapa earthquake and (b) vertical movement of the Wellington region (source: https://www.nzgeo.com/stories/the-day-the-earth-shifted/).

As per the report of the GNSS Earth observation network system (GeoNet; https://www.geonet.org.nz/) of New Zealand, prior to the 1930's, earthquakes are documented from oral and written records which are provided by several authors [58, 59, 239]. Afterwards,

the earthquakes in the catalog have been documented by instrumental records. The below section provides a brief description of the pre-instrumental and instrumental seismicity, in which the events are described in chronological order.

In 1968, Eiby (1968) [59] documented earthquakes that occurred in New Zealand before 1845, based on all available historical and archival material or by their felt effects and damages. He reported that a large earthquake, namely the Haowhenua (Māori for 'land swallower') earthquake, occurred around 1460 AD, causing uplift to parts of Wellington, New Zealand. In addition, 80 earthquake events along with two major earthquakes, namely the 1843 Whanganui earthquake (M_w7.5) and the 1848 Marlborough earthquake (M_w7.5) were struck in New Zealand. Severe damages were observed in the Whanganui area and Wellington region, reaching IX–X on the Modified Mercalli intensity scale (MMI). In continuation, Eiby (1968) [58] annotated a list of New Zealand earthquakes during the time period of 1460−1965. In 1855, the Wairarapa earthquake ($M_w8.2-8.3$) rocked the southern part of the North Island as slip propagated northward from the Wairarapa fault across a six kilometer wide step. The spatial distribution of the intensity of this event extended over New Zealand. The Wairarapa earthquake not only damaged Wellington, Whanganui, and Kaikoura regions but also produced tsunamis and landslides in the local region. The North Canterbury earthquake in 1888 with magnitude $M_w7.0-7.3$ was the first event where the horizontal fault displacement is observed in a range of about $1.5-2.6$ m along the Hope fault.

In the 19^{th} century, two large earthquakes, namely the 1929 Arthur's Pass earthquake (M_w7.3) and the 1929 Murchison earthquake (M_w7.3) hit the central New Zealand. The Murchison earthquake produced about 4.5 m of vertical movement and 2.5 m of lateral movement near the Buller river. During the period of 1930 to 1934, a sequence of four large to major earthquakes, namely the 1931 Napier earthquake (M_w7.6), the deadliest 1931 Hawke's Bay earthquake (M_w7.3), the 1932 Wairoa earthquake (M_w6.9), and the 1934 Pahiatua earthquake (M_w7.4) occurred in the Hawke's Bay region of New Zealand. There were 256 human deaths along with thousands of injuries and a large amount of devastation in the Hawke's Bay region. In 1942, two severe earthquakes with magnitude M_w7.2 and M_w6.8 struck the lower North Island of New Zealand. The 1968 Inangahua earthquake (M_w7.4) shook the west coast basin and range province of the northern South Island. This event had an intensity of X (extreme) in MMI scale and it was followed by numerous aftershocks and triggered landslides. At the end of this century, two earthquakes occurred in the North Island. These are the 1987 Edgecumbe earthquake (M_w6.5) in the Bay of Plenty region and the 1995 East Cape (M_w7.0) on the northern offshore of North Island.

At the beginning of the 20^{th} century, the 2003 Fiordland earthquake (M_w7.2) occurred in the remote area of the Fiordland in the South Island. This event was followed by 6,365 aftershocks

and triggered at least 200 landslides in the surrounding regions [140]. In 2004, a large earthquake with magnitude M_w7.1 hit the Puysegur trench. In 2009, the Dusky Sound earthquake (M_w7.6) struck at the northern edge of the Puysegur trench off the coast of Fiordland. These earthquakes indicate that the Puysegur trench and its adjacent areas are seismically very active. In 2010, the central South Island experienced a major event, known as Darfield earthquake (M_w7.1). The epicenter of this event was near the Darfield town and Christchurch city and the surface rupture of the previously unrecognized Greendale fault extended west-east for at least 29.5 km across alluvial plains west of Christchurch [240]. The Darfield earthquake produced a sequence of aftershocks with magnitude M_w6.2, M_w6.0, M_w5.9, and M_w5.8 in the Canterbury region, popularly known as the 2010−2011 Canterbury earthquake sequence. The strongest aftershock of the mainshock is the 2011 Christchurch earthquake (M_w6.2). It caused widespread damage across Christchurch, killing 185 people. In fact, the Canterbury earthquake sequence caused multiple instances of tectonic surface deformation ($\geq$ 3 events), surface manifestations of liquefaction ($\geq$ 11 events), lateral spreading ($\geq$ 6 events), rockfall ($\geq$ 6 events), cliff collapse ($\geq$ 3 events), and subsidence ($\geq$ 4 events) in the region [240].

Recently, the 2016 Kaikoura earthquake (M_w7.8) occurred at 15 km north-east of Culverden, North Canterbury region, South Island, where the subducting Pacific plate transitions into the dextral Alpine transform fault. It has been observed that large to major earthquake often involve rupture of multiple geometrically complex faults rather than a single planar fault. Similarly, the Kaikoura event caused rupture of at least 21 faults, propagating 150 km from south of the eastern Hope fault northeastward to Cape Campbell, including almost 34 km of offshore rupture along the northeast-trending Needles fault. This event is known as the "complex multifault rupture" earthquake [40, 87, 89, 231]. In addition, this event produced significant distributed uplift along the north-eastern part of the South Island, reaching a peak amplitude of $\sim$ 8 m, which was accompanied by large ($\geq$10 m) horizontal coseismic displacements at the ground surface along discrete active faults. The historical large earthquakes of New Zealand with their occurrence time and magnitude are pictorially shown in Fig. 1.6.

As discussed in the previous section, New Zealand and its adjoint regions are categorized into three major tectonic blocks, where the subdivision is carried out based on the underlying tectonic configuration. The geodynamical processes of these blocks cause the occurrence of tectonic events and form an axial tectonic belt along the northeast-to-southwest strike in New Zealand. From the seismicity distribution of New Zealand in Fig. 1.7, it is observed that, from north to south, the seismicity is aligned (i) along the Hikurangi subduction interface and the Taupo volcanic zone in the continental-oceanic block, (ii) along the Alpine fault zone with the Marlborough fault zone in the continental-continental transpression block, and (iii) along the Puysegur subduction margin in the oceanic-continental subduction block. Depthwise, the shallow seismicity (depth 0−40 km) is concentrated (i) along the east coast of the North Island,

(ii) along the central North Island, and (iii) along the Alpine fault with a band of seismicity at the southern tip associated with the Puysegur subduction (Fig. 1.7). The deep seismicity (depth≥40 km) is marked mainly in the North Island and upper South Island, where the Pacific plate is subducting, and in the southwest part of the South Island where the Australian plate is subducting (Fig. 1.7). Fig. 1.7 shows the distribution of seismicity in New Zealand in terms of earthquake magnitude and focal depth.

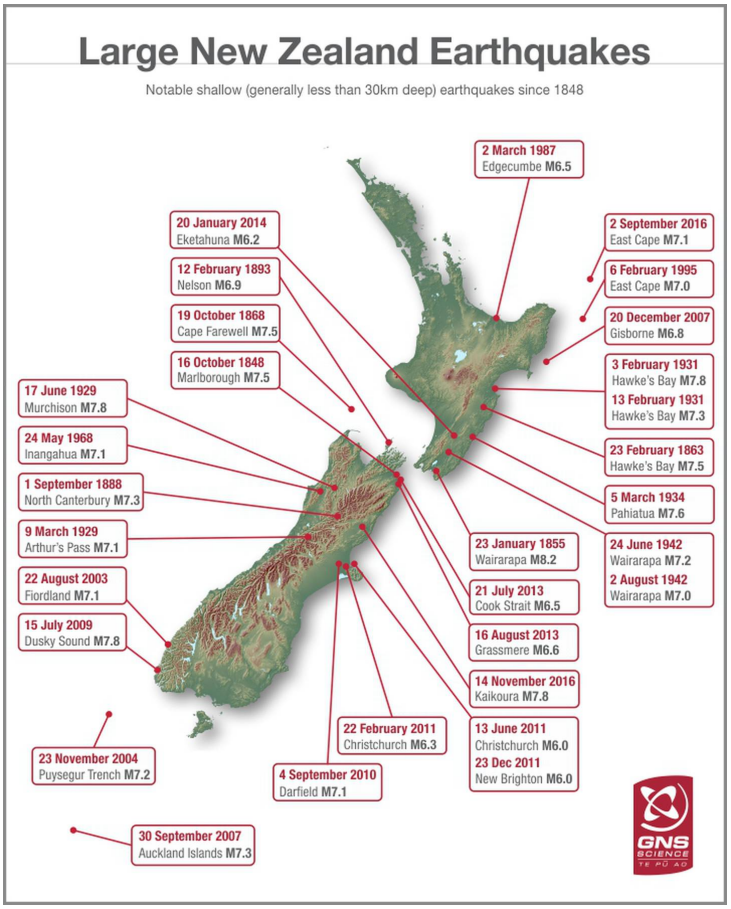

Fig. 1.6: Historical large earthquakes of New Zealand (source: http://www.gns.cri.nz).

New Zealand's tectonic diversity has resulted in numerous earthquakes, shallow and deep, onland and offshore. On an average, New Zealand experiences about one earthquake of magnitude 6.0 per year, one greater than magnitude 7.0 per decade, and one greater than magnitude 8.0 per century [1]. As a consequence, the hazard from damaging earthquakes is substantial. In order to assess the seismic hazard in New Zealand, understanding the kinematics of such large to great earthquake and their associated characteristics are the need of the hour. In past, although several efforts are made to investigate crustal deformation and associated earthquake potential in New Zealand [20, 50, 74, 88, 102, 240, 247, 267], the devastating 2016 Kaikoura earthquake has re-ignited the requirement of re-assessment of earthquake cycle deformation,

in terms of crustal velocity field, strain distribution, earthquake potential score, and seismic moment budget estimation in New Zealand. In this regard, the present study concentrates on the crustal deformation analysis caused by the contemporary earthquake cycle and associated seismic hazard in New Zealand using data-driven spatio-temporal techniques.

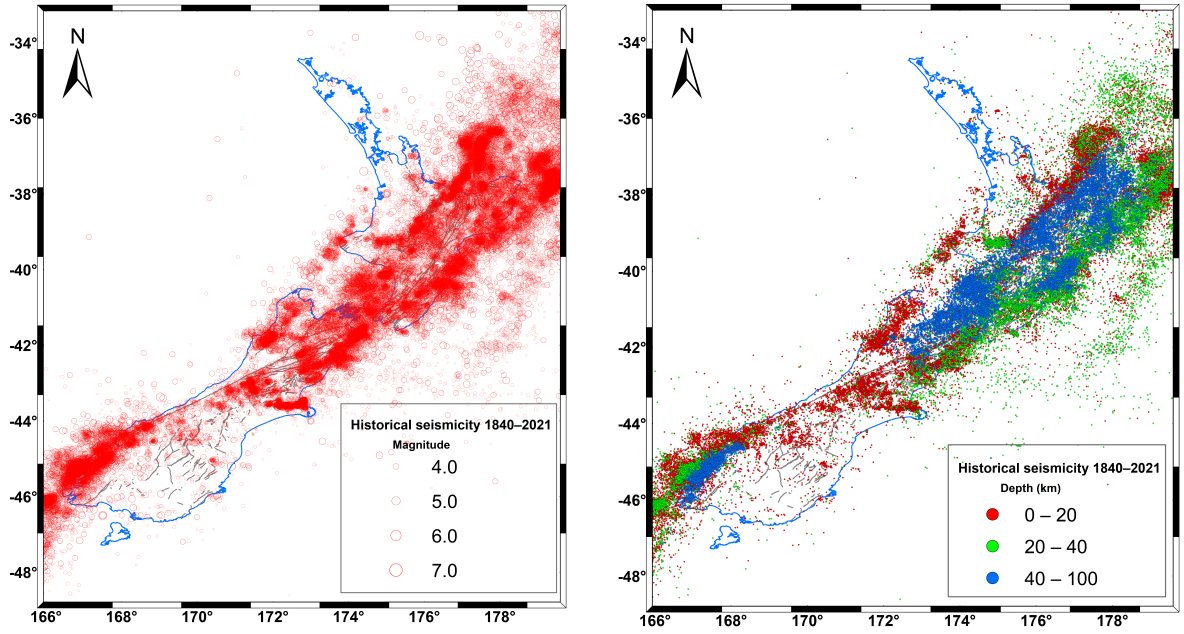

(a) (b)

Fig. 1.7: Distribution of historical seismicity in New Zealand: (a) magnitude-wise distribution and (b) depth-wise distribution.

1.5 Thesis objective

The main objective of the thesis work is to characterize earthquake cycle deformation and consequently to re-assess seismic hazards in New Zealand using the spatio-temporal techniques. To achieve this primary objective, three sub-objectives are framed as follows:

1. To identify the coseismic deformation associated with the 2016 Kaikoura earthquake of New Zealand using the data-adaptive EOF method

2. To estimate the spatial distribution of contemporary earthquake potential in New Zealand using the data-driven seismic moment budget estimation technique

3. To quantify the current progression of earthquake cycle of large events at 15 major cities of New Zealand using the area-based earthquake nowcasting approach

1.6 Scope of the thesis

The current section explains various scopes and key work elements to accomplish the above-mentioned research goal. In the first sub-objective, the coseismic analysis of the 2016 Kaikoura earthquake is conducted by carrying out the following subsequent tasks.

1. GPS data collection at all available continuous GPS (CGPS) sites in New Zealand during the Kaikoura event (15 days data straddling the Kaikoura event)
2. GPS data processing using GAMIT-GLOBK suite of post-processsing software
3. Extracting position time series of each CGPS site at every 30 min interval
4. Arranging the CGPS data set into a rigorous space-time matrix and performing the EOF analysis
5. Computing and selecting the principal EOF modes along with their interpretations
6. Deriving the coseismic strain rate distribution (dilatation and maximum shear strain maps) using the leading EOF modes as velocity gradients

The second objective that focuses on the seismic hazard analysis in New Zealand is obtained by utilizing geodetic and earthquake data in the following manner.

1. Collection of the updated velocity data and historical seismicity data
2. Characterization of the strain distribution through various strain rate patterns (dilatation, maximum shear, and rotation strain rates)
3. Calculation of geodetic moment rates from strain rates and seismic moment rates using historical seismicity data
4. Estimation of spatial distribution of earthquake potential in New Zealand by comparing geodetic and seismic moment rates

The third and last sub-objective that focuses on the earthquake nowcasting in New Zealand is obtained through natural time statistics. The subsequent tasks are as follows.

1. Description of the required parameters, such as large magnitude threshold, small magnitude threshold, large geographic area, and local city area
2. Conducting the magnitude of completeness test and tabulating natural time counts based on earthquake data (1963–2021)

3. Statistical inference of observed natural times in New Zealand and subsequent earthquake potential score (EPS) computation for 15 major cities

4. Sensitivity analysis of the nowcast scores

5. Finally, identification of high seismic hazard regions in New Zealand from a combination of geodetic and statistical approaches

1.7 Structure of the thesis

Having discussed the main objective and scope of the thesis, this section provides a brief thematic overview of the chapter-wise road map.

Chapter 1 explains the three primary phases of earthquake cycle deformation. This chapter covers the evolution of New Zealand and its tectonic classification, along with the historical seismicity. In addition, it includes the thesis objective, scope of the thesis, and a brief summary of each chapter.

Chapter 2 provides a step-wise formulation of the EOF analysis. The EOF analysis comprises three broader steps: data preparation, mathematical formulation of the EOF method, and interpretation of the derived results. Some extensions of the conventional EOF method and their applications are also explained.

Chapter 3 presents a comprehensive coseismic analysis of the 2016 Kaikoura earthquake using the EOF method. The derived EOF modes are interpreted in terms of coseismic deformation and subsequent early postseismic deformation. In addition, this chapter includes the EOF-based coseimsic strain rate distribution.

Chapter 4 provides the spatial distribution of earthquake potential along 14 different segments in New Zealand by comparing the accumulated geodetic moment (calculated from strain rates) with the associated released seismic moment (calculated from $\sim$180 years of seismicity data).

Chapter 5 presents an empirical data-driven technique, known as earthquake nowcasting, to statistically address the current state of regional earthquake hazard at 15 major populous cities in New Zealand.

Finally, **Chapter 6** summarizes the thesis work with an emphasis to the major contributions and future recommendations.

Chapter 2

Mathematical Formulation of the Empirical Orthogonal Function: A Leading Spatio-Temporal Technique

"*Reality is observer-determined – it's a spatio-temporal process, which fortunately means that things must change.*"

by Robert Lanza

This chapter focuses on the mathematical overview of a leading spatio-temporal technique, namely the empirical orthogonal function (EOF). The EOF method is interchangeable with the well-known principal component analysis (PCA). This chapter provides a detailed description of the EOF method (referred to as conventional EOF) including data preparation, mathematical formulation of the EOF method, and interpretation of the derived results, which are in the form of individual EOF modes. The current chapter also contains an abbreviated formulation of its extensions, namely the rotational EOF, simplified EOF, complex EOF, extended EOF, periodically extended EOF, cyclostationary EOF, and the Karhunen-Loeve expansion method. In addition, based on the strength and limitations of the conventional EOF and its extensions, this chapter mentions a plethora of applications of these methods in several domains. The overall content of this chapter is presented below.

Contents

Parts of this chapter have been published in the following refereed publication:
Neha and S. Pasari, "A review of empirical orthogonal function (EOF) with an emphasis on the coseismic crustal deformation analysis", *Natural Hazards*, vol. 110, pp. 29–56, 2022 (SCIE).

2.1 Introduction

The ability to visualize and interpret a large, unstructured, and high dimensional data set is a crucial component in the characterization of any nonlinear dynamic system. Such a system often exhibits spatio-temporal correlation among the data variables [35, 92]. While retaining the maximum data variability, the reduction of a large number of correlated variables into fewer number of unobserved variables is a standard approach [27, 159]. In dealing with a high dimensional data set, we often encounter the issues of (i) regional dependency of variables [92], (ii) intermittent data gaps due to missing observations, outliers, leverage values, or influential points [97, 127, 281], and (iii) non-linearity of system features [92]. As a consequence, a number of space-time based techniques, such as linear interpolation methods for gap filling [175], principal component analysis (PCA) or empirical orthogonal function (EOF) for the dimensionality reduction and pattern recognition [92, 118], least-squares estimation (LSE) for data fitting [116, 118], and clustering algorithms for the outlier detection [170] have been proposed. Among these, the EOF method has gained significant attention due to its unique capability to account for the three above-mentioned issues simultaneously. The EOF approach not only extracts the hidden and dominant patterns of the data set in a versatile way but also can decompose the coherent spatio-temporal field into individual spatial and temporal modes to better interpret the underlying process [27, 116]. Considering the strength of the EOF method, the present work concentrates on the mathematical formulation of the EOF method for any observation data, which can arise from various scientific and nonscientific domains.

Since the inception of the EOF method in the atmospheric and climate science [70, 142, 167] in late 1940s, it has been widely used in a variety of science and engineering disciplines, such as Geophysics, Biostatistics, Physiology, and Meteorology [36, 37, 198]. This EOF method, often termed as "conventional" EOF (hereafter called simply as EOF), provides a robust numerical framework to segregate different signals of a data set and also to separate out the regular fluctuations of the random noise in terms of their individual mode of variability [37]. As a consequence, the EOF technique enhances the signal-to-noise ratio of any time series data [35]. In addition, acting as a "map-series" method, the EOF can also quantify the small-scale, short-term, and long-term variations in a high dimensional data set [255]. As an essential tool in the area of prediction, estimation, and detection, the EOF analysis is collectively known as "linear estimation study" [124]. Taking full advantage of the space-time coherency of a physical system, the EOF method serves as a data-adaptive technique, purely dictated by the observational data characteristics without any a-priori or subjective information [37]. Moreover, this technique is relatively easy to implement and is computationally faster. Based on the nature of

the data (e.g., stationarity, moving, and propagating features), several extensions of the conventional EOF method have been proposed especially in the field of Climate Science to identify and estimate the unseen patterns in the data set (see the review of Hannachi et al. 2007 [92]). Some of these extensions are the rotational EOF (REOF), simplified EOF (SEOF), complex EOF (CEOF), extended EOF (EXEOF), periodically extended EOF (PXEOF), cyclostationary EOF (CSEOF), and the Karhunen-Loeve expansion (KLE) method.

Considering the all above-mentioned advantages of the EOF and its extensions, the present chapter provides a mathematical overview of these methods, which can be applicable to any observational data. The mathematical overview comprises three steps: (1) data preparation, (2) mathematical concept of the EOF method, and (3) interpretation of estimated results as individual spatial patterns along with their time series. This chapter also presents a brief mathematical description of several EOF extensions. In addition, the current chapter highlights some of the prominent applications of the EOF methods in various domains, such as ionospheric variation modeling, climate and atmospheric related studies, crustal deformation analysis, gap filling interpolation technique, and other applications of EOF along with computational packages. The following sections provide the mathematical description and prominent applications of the EOF and its extensions in detail.

2.2 Mathematical overview

In any observational study, the data set comprising either direct observations or experimental/simulated data contains important information of the underlying physical system. Such data set over space and time is often represented in a uniform or a non-uniform grid pattern. In the case of EOF analysis, the uniform spatio-temporal data set is preferable. The below section provides a mathematical formulation of the EOF method along with its extensions in a three-fold way.

2.2.1 Data preparation

In data preparation, pre-processing is an essential and fundamental step to ensure the completeness of the data prior to performing any analysis [264]. The main purpose of the pre-processing step is to encode the raw data in a useful and efficient format while retaining its original information. Relevant to the EOF implementation, the data pre-processing step is further divided into three stages: data cleaning, data transformation, and data reduction [158].

Data cleaning methods such as linear interpolation techniques, machine learning approaches, and clustering algorithms are often used to account for the missing values, inconsistent data, noise, detecting and removing outliers, and influential points [158]. Consequently, the data

transformation step is employed to convert the raw data into a specific format according to the modeling purpose. Scaling the data within a small and specific range (normalization) and data aggregation are some of the transformation methods. While working with a large amount of data, the data reduction step enables a condensed representation of the raw data with preserving the integrity of the original. Two effective methods of dimensionality reduction are PCA and Wavelet transformation [71]. In addition, it is important to verify the data stationarity requiring the mean and variance to be constant over time. After pre-processing of data, the refined or filtered data set will be used for EOF implementation as discussed below.

2.2.2 Method implementation

After pre-processing, the refined data points of each grid can be arranged into a matrix $A_{(m\times n)}$, where $A_i = [a_i(1)\ a_i(2)...\ a_i(n)]$ represents the row vector and each element a_{ij} denotes the observation for epoch $i = 1,2,...,m$ at station $j = 1,2,...,n$. In essence, the space-time field matrix can be written as:

$$A_{(m\times n)}(t,x) = \sum_{i=1}^{m}\sum_{j=1}^{n} a_{ij} \tag{2.1}$$

Using the above field matrix $A_{(m\times n)}(t,x)$, an eigenvalue problem $Ax = \lambda x$ is formulated for the EOF implementation. Though there are many numerical methods to solve this problem, either the singular value decomposition (SVD) on $A_{(m\times n)}(t,x)$ or the eigenvalue decomposition of the covariance matrix C of $A_{(m\times n)}(t,x)$ is often preferred [53, 92, 281]. Prior to decomposition, the data set represented by $A_{(m\times n)}(t,x)$ should be demeaned so as to account for the variations in the signals. In the present work, the formulation is carried out by considering the eigenvalue decomposition of the covariance matrix due to its advantage of estimating how strongly/poorly are the variables related to each other.

The covariance matrix is a symmetric matrix, defined as:

$$C = \frac{1}{N}AA^{*T} \quad \text{or} \quad \langle A_i, A_j\rangle \tag{2.2}$$

The elements of the covariance matrix are represented as:

$$s_{ij} = \frac{1}{N}\sum_{k=1}^{K} A(t_k,\ x_i)A^*(t_k,\ x_j) \tag{2.3}$$

Here, s_{ij} denotes the covariance between the data points of any pair of grid points (s_i, s_j) for $i = 1,2,...,m$, and $j = 1,2,...,n$. In the eigenvalue decomposition approach, the covariance matrix C is decomposed as $C = V\Lambda V^T$ by using the SVD method [35, 36, 53, 91, 281]. The matrix V^T comprises the orthogonal eigenvectors (EOFs) of C indicating the spatial patterns,

and the diagonal matrix Λ contains the eigenvalues λ_K $(n \geq K)$ of C. The multiplication of V and Λ (say U, where $U = V\Lambda$), as a projection of sampled data onto eigenvectors, represents the principal components (PCs) associated with the EOFs. The main characteristic of the EOF is the orthogonality property of eigenvectors and uncorrelatedness of the time expansions (PCs) [91, 92]. Moreover, the ratio (r_k) of an eigenvalue to the sum of the eigenvalues (trace Λ) provides a measure of the individual contribution (%) of each EOF mode in explaining the total variation of the data set.

$$r_k = \frac{\lambda_K}{trace\ \Lambda} \times 100\% \tag{2.4}$$

At this juncture, it is important to emphasize that the original space-time field can be retrieved with the help of the derived EOF solutions. The compact form of the retrieved data field can be expressed as:

$$A_{(m\times n)}(t,x) = \sum_{k=1}^{M} U_k(t)V_k(x) \tag{2.5}$$

Here, t and x represent the time scale and spatial position, respectively and M shows the first few optimal modes contained in the field [118]. The choice of M significant modes varies from purpose to purpose. For instance, in the study of crustal deformation through the EOF method, the first two EOF modes significantly capture the maximum variability of geodetic observations, and therefore, only these two are considered for interpretation [35, 36]. Similarly, in the EOF-based interpolation techniques, the above compact form of the retrieved data will be used iteratively [281].

2.2.3 Interpretation of the EOF modes

Having discussed the pre-processing and method implementation steps, the last step of the EOF analysis is the interpretation of the derived EOF modes. In practice, such an interpretation enables an "identification" of unobserved structures of the underlying dynamical system. The first principal mode explains most of the dominant structure of the physical system. The second and third modes express the residual variance that represents small fluctuations in the data set. Collectively, first few principal modes contribute to identifying recurrent patterns of variations in the data set. However, the EOF modes do not directly provide any indication of the causes of the variations, though their interpretation and analysis may provide a correspondence between the EOF modes and the original problem [118]. Fig. 2.1 represents a flowchart of the mathematical formulation of the conventional EOF method.

As the natural processes fundamentally exhibit non-linearity and interlinking behavior among the data variables, there are some limitations of the empirically observed EOF solutions, such as poor identification of natural variability or background fluctuations [198], separation of an

oscillatory component buried in the noisy data [92], and determination of the propagating disturbances in the data set [159]. As a result, to avoid any misleading or illusory representation of the data structures, there have been several extensions of the conventional EOF approach to emphasize the recurrent patterns in the data.

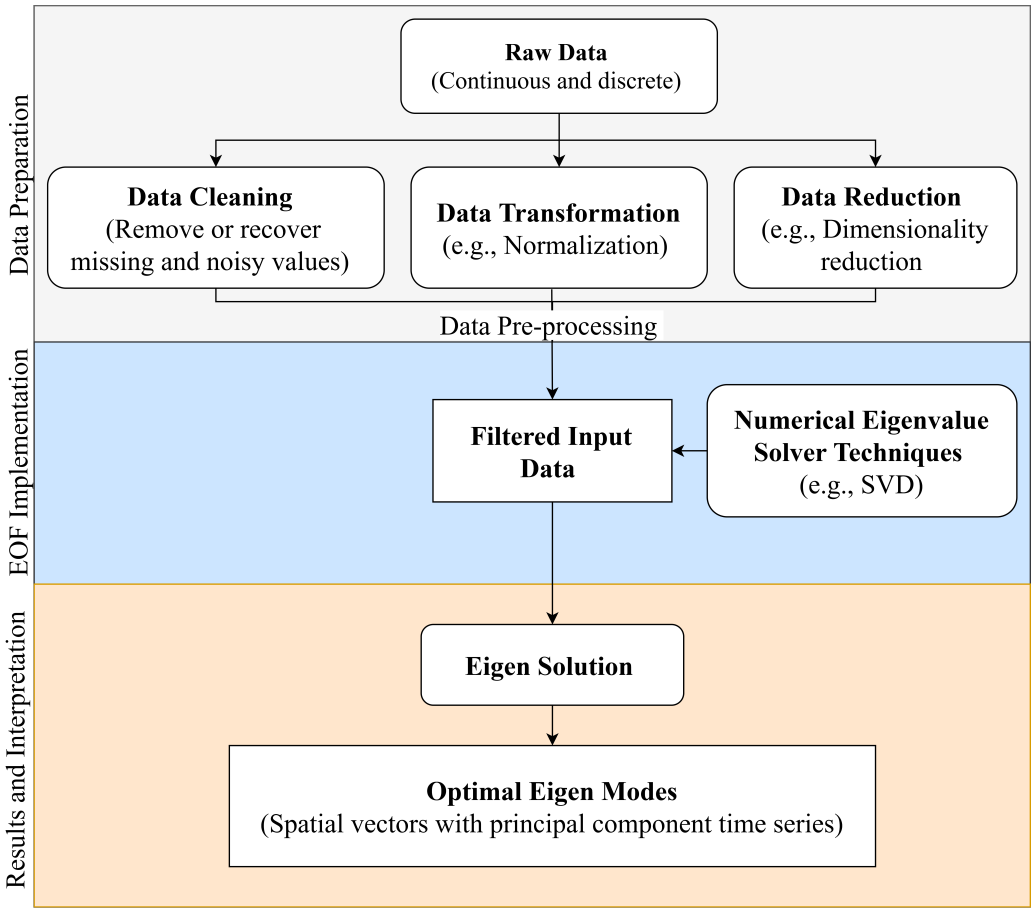

Fig. 2.1: Flowchart of the mathematical formulation of the conventional EOF method.

2.3 Several extensions of the conventional EOF method

The conventional EOF and its several extensions provide a plethora of methods to deal with a large, unstructured, and high dimensional data set. Each one of them has its own strength and limitations. An abbreviated formulation of some of these extensions is discussed below.

2.3.1 The rotational EOF (REOF) method

Apart from the conventional EOF, the rotational EOF (REOF) is another promising approach to deal with the stationary data [33, 120, 198]. In this method, a fixed number of EOF vectors are rotated using orthogonal or oblique rotation matrix in order to maximize the "simplicity"

function S_f. In case of orthogonal rotation (Kaiser-Varimax rotation), the function S_f takes the following form:

$$S_f(u_1, u_2, ..., u_r) = \sum_{k=1}^{r} f(u_k) \tag{2.6}$$

with

$$f(u_k) = \frac{1}{n}\sum_{i=1}^{n}\left(\frac{p_{ik}}{s_i}\right)^4 - \frac{1}{n^2}\left(\sum_{i=1}^{n}\left(\frac{p_{ik}}{s_i}\right)^2\right)^2 \tag{2.7}$$

Here, p_{ik} is the grid-point value of the k^{th} EOF pattern that is being rotated and s_i is the corresponding point by point standard deviation.

2.3.2 The simplified EOF (SEOF) method

As an alternative of the REOF method, to obtain the simple structure of the EOF modes while retaining the useful properties of the EOF, the simplified EOF (SEOF) technique has been proposed by Jolliffe et al. (2003) [117]. In SEOF method, the main attempt is to maximize variance of the data set while transforming the patterns to be orthogonal and simple [92]. Here, the simplicity means the loadings of the EOF patterns have either close to zero or close to one. In addition to EOF method, to achieve the simplicity, the SEOF method requires the following extra constraint to be satisfied:

$$||u_k||_1 = \sum_{j=1}^{d} |u_{kj}| = u_k^T sign(u_k) \leq \tau \tag{2.8}$$

where, $||u_k||_1$ is the $L1$ norm of the vector u_k, τ is threshold parameter, and $sign(u_k) = \big(sign(u_{k1}), sign(u_{k2}), ..., sign(u_{kp})\big)^T$ is the sign of u_k.

2.3.3 The complex EOF (CEOF) method

Based on the fact that a wave is expressible through complex numbers, there came the concept of complex EOF (CEOF) [103, 265]. The novelty of this method lies in its extension of the real data set into complex variables, of which the imaginary part is the Hilbert transformation of the real data set. The mathematical representation of the CEOF method is as follows:

$$\tilde{A}(i,j) = A(i,j) + H(A(i,j)) \tag{2.9}$$

where,

$$A(i,j) = \sum_{w} c(i,w)e^{-2\pi iwt} \quad \text{and} \quad \tilde{A}(i,j) = \sum_{w} c_H(i,w)e^{-2\pi iwt}$$

Here, $c(i,w)$ and $c_H(i,w)$ are the expansion coefficients of the $A(i,j)$, defined as:

$$c_H(i,w) = \begin{cases} ic(i,w) & \text{for } w \geq 0 \\ -ic(i,w) & \text{for } w < 0 \end{cases} \tag{2.10}$$

where, w is the natural frequency. The imaginary part (Hilbert transform) represents the phase shift by a quarter of a period.

2.3.4 The extended EOF (EXEOF) method

Taking the advantage of the time-lagged information in the covariance matrix, the extended EOF (EXEOF) method was introduced in the 1980s [77, 135, 278]. In this setup, the covariance matrix is augmented as:

$$S = \begin{bmatrix} S(0) & S(1) & . & S(l) \\ S(1) & S(0) & . & . \\ . & . & . & S(l-1) \\ S(l) & . & S(l-1) & S(0) \end{bmatrix} \tag{2.11}$$

where, $S(l)$ denotes the lag-l spatial covariance matrix, defined as:

$$S(l) = \langle A(i,j)\, A(i^{'}, j+l) \rangle \tag{2.12}$$

The resulting covariance matrix $S(l)$ takes into account both spatial and temporal covariance measures. Notice that considering the time-lagged information, elements of the new matrix $\tilde{A}(i,j)$ take the following form:

$$\tilde{A}(i,j) = [A(i,j),\, A(i,j+1), \ldots A(i,j+l)] \tag{2.13}$$

2.3.5 The periodically EOF (PXEOF) method

As a variant of the EXEOF method, the periodically extended EOF (PXEOF) [124] is based on the concept of periodic statistics of the given variable. For the PXEOF method, the covariance matrix is defined as:

$$S = \begin{bmatrix} S_{1,1} & S_{1,2} & . & S_{1,l} \\ S_{2,1} & S_{2,2} & . & S_{2,1} \\ . & . & . & . \\ S_{l,1} & S_{l,2} & . & S_{l,l} \end{bmatrix} \tag{2.14}$$

where,

$$S_{p,q} = \langle A(i, p+lj)\ \ A(i^{'}, q+lj)\rangle \quad p,q = 1,2,...,l \tag{2.15}$$

Here, j and l denote the periods. The resulting covariance matrix is basically derived by dividing data into l periodic segments and treating them as different variables; that is:

$$\tilde{A}(i,j) = [A(i,1+lj),\ A(i,2+lj),\ldots A(i,l+lj)] \tag{2.16}$$

Overall, the derived covariance matrix considers the lagged information as well as the periodicity of the observational data.

2.3.6 The cyclostationary EOF (CSEOF) method

Unlike the above-discussed EOF methods, the cyclostationary method is based on the concept of the multivariate autoregression (AR) model [125]. The CSEOF technique is characterized by two temporal scales. In essence, the compact form of CSEOF matrix for a given data can be written as:

$$A(i,j) = \sum_{k=0}^{d-1} a_k(i,j) e^{2\pi i k j/d} \tag{2.17}$$

where, d represents the nested period of a cyclostationary process and $a_k(i,j)$ is known as coefficient time series. Taking the coefficient time series, a new variable is defined as:

$$\tilde{A}(i,j) = \big(a_1(i,j), a_2(i,j), ..., a_d(i,j)\big) \tag{2.18}$$

Then, the covariance matrix associated to the new variable is solved by numerical techniques and the obtained EOFs are known as CSEOFs.

2.3.7 The Karhunen-Loeve expansion (KLE) method

While all of the aforementioned EOF methods consider the conventional covariance approach, the Karhunen-Loeve expansion (KLE) method utilizes the concept of the correlation matrix [249, 251]. In view of this, the covariance matrix (Eq. 2.2) of given data is converted to a correlation operator by dividing each element of the covariance matrix by their associated variance. The obtained correlation matrix (C_r) is defined as:

$$C_r = \begin{bmatrix} \frac{s_{11}}{\sigma_1\sigma_1} & \frac{s_{12}}{\sigma_1\sigma_2} & . & \frac{s_{1p}}{\sigma_1\sigma_p} \\ \frac{s_{21}}{\sigma_2\sigma_1} & \frac{s_{22}}{\sigma_2\sigma_2} & . & \frac{s_{2p}}{\sigma_2\sigma_p} \\ . & . & . & . \\ \frac{s_{p1}}{\sigma_p\sigma_1} & \frac{s_{p2}}{\sigma_p\sigma_2} & . & \frac{s_{pp}}{\sigma_p\sigma_p} \end{bmatrix} \tag{2.19}$$

Here, $\sigma_p = \sqrt{\frac{1}{m}\sum_{k=1}^{m}(a_{kj})^2}$ for $j = 1,2,...,n$ represents the variance of p^{th} time series and s_{ij} denotes the elements of the covariance matrix for each $i = 1,2,...,m$ and $j = 1,2,...,n$.

It has been observed that the traditional EOF and its extensions have the potential to enhance a variety of unseen patterns in a data set [92, 125, 281]. A summary of EOF methods along with the corresponding data features and estimated patterns is provided in Table 2.1.

Table 2.1: A summary of EOF methods along with the corresponding data features and estimated patterns.

S.No	Method name	Data features	Augmented matrix	Estimated patterns	References
1	Conventional EOF	Stationary (spatially correlated process)	Covariance	Time expansion with spatial pattern	Fukuoka, 1951 [70]; Lorenz 1956 [142]
2	Rotational EOF (REOF)	Stationary (spatially correlated process)	Covariance	Stable, simple structure, less sensitive, and orthogonal spatial pattern in general	Horel 1981 [103]; Richman 1986 [198]
3	Simplified EOF (SEOF)	Stationary (spatially correlated process)	Covariance	Stable, simple structure, less sensitive, and orthogonal spatial pattern in general	Jolliffe 1990 [118]; Hannachi et al. 2007 [92]
4	Complex EOF (CEOF)	Stationary (spatially correlated process)	Covariance	Identifying irregular oscillatory patterns	Wallace and Dickinson 1972 [265]; Horel 1981 [103]
5	Extended EOF (EXEOF)	Non-stationary (spatially and temporally correlated process)	Covariance	Identifying moving pattern with time-lagged information	Weare and Nasstrom 1982 [278]
6	Periodically Extended EOF (PXEOF)	Non-stationary with period (periodically space-time correlated processes)	Covariance	Identifying moving pattern with any period	Hannachi et al. 2006 [91]; Kim and Wu 1999 [125]
7	Cyclo-Stationary EOF (CSEOF)	Cyclostationary processes (periodically correlated, multiple time scales)	Covariance	Identifying moving and deforming pattern with cyclic statistics	North et al. 1984 [166]; North and Kim 1997 [124]
8	Karhunen-Loeve Expansion (KLE)	Stationary (spatially correlated process)	Correlation	Spatial patterns associated with time signatures	Tiampo et al. 2002 [251]

2.4 Applications of the conventional EOF and its extensions

This section presents some selective applications of the conventional EOF and its extensions in different domains.

2.4.1 Ionospheric variation modeling

The ionosphere plays a key role in the field of atmospheric science including telecommunications and global navigation satellite system (GNSS) signals. Regular and irregular fluctuations in the ionosphere are mainly influenced by some factors such as solar ionizing radiations, geomagnetic effects, and meteorological influences [61, 65, 138, 200]. To investigate the short-term and long-term disturbances to the ionosphere and its inherent characteristics, the total electron content (TEC) is one of the notable descriptive parameters of the ionosphere state [138, 174, 283, 284]. The ionospheric TEC modeling plays a significant and indispensable role not only to analyze the controlling factors of ionospheric TEC [138] but also in practical applications such as GNSS satellite positioning, navigation and timing [61], error correction to operational systems, determining the scintillation of radio wave, seismic-ionospheric anomalies (pre- and post-earthquake) [141, 174], and satellite altimetry [284]. The TEC ionospheric models have been established and documented by either existing empirical models, for example, the International Reference Ionosphere (IRI) model [26], the NeQUICK modeling [255] or different fundamental based TEC measuring techniques such as Faraday rotation, differential Doppler, and group delay methods [284]. Although, these empirical models have been employed for TEC analysis but they may fail if the TEC dataset exhibits geomagnetic disturbances [284] and global/regional latitudinal dependency effects particularly in equatorial and low-latitude regions [283], and abnormal pattern of the diurnal cycle in the ionosphere [38, 255, 284]. To deal with such situations, several mathematical and optimization approaches are often used to analyze high spatio-temporal resolutions of the TEC measurements leading to more accurate results [255].

Consequently, to extract the relevant information of the ionosphere state, the conventional EOF method has been employed in several studies to signify the intrinsic variations in the TEC data [38, 43, 44, 148, 255, 284]. The EOF modes are capable of assessing significant amount of variations of the TEC, such as the first few spatial patterns show the global spatial and diurnal variation of the TEC, the hemispherically asymmetric pattern, and equatorial anomaly phenomena. The associated time series corresponding to spatial patterns indicate the solar cycle variations, annual fluctuation component, weak seasonal pattern, and annual/semi-annual oscillation components [273, 283, 284]. The EOF-based model can also resolve the complexity of electrodynamic mechanisms [255]. In comparison to the conventional IRI and NeQUICK

models, the EOF model is often observed to be more reliable in terms of its quick convergence and capability to capture the long-term variations and small-scale irregularities in TEC [283, 284]. In addition, the accuracy and quality of the EOF method have also been validated through global-scale inspection, regional, and single station inspection as well as through statistical analysis [38]. Moreover, with the increasing availability of GPS satellite signals, the EOF analysis turns out to be a promising approach to identify the inherent patterns of solar-terrestrial phenomena even with a small-scale variation in the ionosphere [141]. Therefore, the EOF-based TEC model is an effective approach not only to enhance the TEC signals but also to develop a multiple ionospheric parameter model over a single GNSS station or a network of stations to enhance delay error forecasting practices across the globe [255].

2.4.2 Climate and atmospheric related studies

Climate and atmospheric system are typical examples where the high dimensional and complex phenomena meet. These systems exhibit all sorts of features, such as stationary, cyclostationary, propagating and moving patterns, and non-linearity [92, 159]. Consequently, it is a challenging task to identify the inherent patterns of physical mechanism associated with variability linking to the original dynamical system. In this regard, the sea surface temperature (SST) and sea level pressure (SLP) are two essential variables [51, 91]. The SLP or SST is a contributing factor in weather forecasting [91], in illustrating the ocean warming tendency [51], and in explaining the phases of the El-Nino phenomenon, rainfall, upwelling water, and monsoon [151]. Various parametric and non-parametric methods have been implemented to measure the regular and irregular anomalies in the SST or SLP data set [51, 151, 159]. Due to the spatio-temporal data characteristics of the SST or SLP, the EOF method has been extensively used in this domain. The estimated EOF modes serve as a tool for detecting and predicting climate changes [92, 103, 142, 265], for example, the EOF modes provide evidences of the “Tropical Atlantic Dipole” and the “Tropical Indian Ocean Dipole” in SST data, Northern Hemisphere winter variability in SLP data [52], and EI-Nino effects in SST time series [124]. Likewise, the spatial and temporal modes of the SLP enable the determination of the dipole or multipole structure of variability in the Northern Hemisphere. The EOF method essentially explains the regular and irregular patterns of the stationary data in terms of individual spatial and temporal modes to assimilate the dynamical information corresponding to the original process [118, 199].

Due to the inherent characteristics of SLP or SST data set that is often influenced by the regional domain shape, subdomain uncertainty, sampling sensitivity, and the physical interpretability (moving and deforming patterns), the true patterns in the data set may not be well captured by the conventional EOF method [22, 166, 198]. As a consequence, to account for the stationary, cyclostationary, propagating and moving patterns, and non-linearity of the SST or

SLP data, several extensions of the traditional EOF method have been employed. Some of such EOF extensions can also address the issues related to model mixing that indicates two modes are not well separated and to model splitting that shows the existence of the evolving patterns in the data set [91, 92, 124, 198]. Though the geometric constraints of the EOF and its extensions are useful for identification of the behavior of the derived system, they are not able to detect and estimate the trends from the spatio-temporal gridded data [91]. Consequently, detrend EOF that is based the covariance or correlation matrix of the data set using the correlations between time positions of the data has been implemented [92]. Therefore, the EOF and its extensions play important role in dealing with climate related data.

2.4.3 Crustal deformation analysis

Estimating how much the Earth's crust deforms during a seismic cycle (preseismic, coseismic, and postseismic period) is the key in the evolution and prediction of the obscure patterns of the complex nonlinear earthquake fault system [251]. Moreover, the regional tectonic motion of a fault system plays a crucial role in the interseismic crustal deformation and consequent seismic hazard analysis [253]. The spatio-temporal patterns of the deformation field can characterize earthquake dynamics in terms of strain distributions and fault kinematics [35, 251]. In this regard, several types of geodetic data such as satellite-based radar images and space-time GNSS observations are often utilized to model the small-scale and large-scale variations. To analyze these space-time variations, different methods including the elastic dislocation model (EDM), least-squares estimation (LSE), principal component analysis-based inversion model (PCAIM), extended network inversion filter (ENIF), and the EOF method have been employed [36, 101, 128, 226, 227]. Although these techniques are routinely used to describe a geophysical system but they provide poor results especially in coseismic surface deformation analysis due to (i) necessity of a-priori values (often subjective) of the hyperparameters in the geodetic inversion; (ii) inefficiency in analyzing complex time series data with interseismic, coseismic, and postseismic signals simultaneously, and (iii) elusive information in the presence of outliers, noise, influential values, bad leverage points, and in the case of low signal-to-noise ratio that somehow break down the method implementation [35, 128, 253].

The above-mentioned limitations can be effectively addressed by the EOF technique that is capable of separating out space and time signals to better delineate with the regional tectonic processes in the coseismic deformation analysis [35, 36, 101, 127, 253]. The estimated spatial patterns and the associated time series represent prominent coseismic signal with the evidence of the prevalent CME in the GPS data [35, 36]. The above-mentioned conventional methods fail to capture these two patterns simultaneously. The EOF is also efficient to quantify the CME and the preseismic and postseismic signals separately or within the EOF modes and provides

the more reliable results than the conventional methods. Based on the strength of the EOF method, it has been employed to extract the 3-D pattern of coseismic deformation of the 2011 Tohoku-oki earthquake (M_w9.0) in Japan [36, 156], the 2002 Hualien earthquake (M_w7.1) in east coast Taiwan, and the 2010 Jiashian earthquake (M_w6.3) in southern Taiwan [35]. In addition, the derived EOF solutions also reveal the coseismic strain field, postseismic relaxation pattern, and slip rate distribution [36, 37]. It is observed that the EOF method notably accounts for the tectonic behavior especially for the far-field observations in comparison to the traditional methods [36]. Furthermore, the empirical EOF technique can detect the prevalent influencing factor (e.g., CME) in the residual of the GPS time series. As a result, the EOF method can even determine the small-scale deformation in the tectonic setup and can separate out the deformation patterns in terms of the individual EOF modes [36, 81, 132]. The associated EOF modes may exhibit a notable correlation among the CME and the atmospheric mass loading (AML) displacement, particularly in the tropical and sub-tropical regions [132].

To analyze the crustal deformation pattern based on GPS and InSAR time series data, a combination of EOF and geodetic inversion method, known as principal component analysis-based inversion model (PCAIM), has been proposed by Kositsky and Avouac (2010) [128]. The PCAIM method has been implemented to recover the time-evolution history of the geophysical deformation sources, such as monitoring the magmatic inflation event beneath the Long Valley Caldera, California [139], coseismic and ongoing afterslip of the 2015 Illapel (Chile) earthquake (M_w8.3) [233], aseismic slow slip event triggered by the earthquakes in Guerrero, Mexico [193], and coseismic deformation of the 2016 Kaikoura earthquake (M_w7.8) in New Zealand [113].

Similar to the conventional EOF method, the eigen pattern analysis based on the Karhunen-Loeve expansion (KLE) considers the correlation of the seismic activities with space and time scales to reveal the historical seismicity of any geographic area, such as in Southern California [251]. Moreover, this method can analyze the seasonal signals in the CGPS data in terms of individual spatial and temporal modes to better constrain the tectonic source of the fault system [252]. Therefore, the eigen pattern approaches can retrieve the data-orientated information about the non-linear characteristics of the earthquake fault system.

2.4.4 Gap filling interpolation technique

The analysis of the obtained data set through observations or experiments often serves as a prerequisite in modeling and forecasting of a dynamical system. A large data set sometimes contains missing points or unreliable values at continuous or discrete places. Missing values in an incomplete data set give rise to various modeling issues, especially where evenly spaced

data is desirable. Such issues not only affect model parameter estimation and boundary conditions of numerical models but also slow down the model processing [127, 246]. They can even provide misleading results [127, 281]. Several interpolation methods, such as the optimal interpolation [197], spline interpolation [248], ordinary Kriging interpolation method [73], and the expectation-maximization method [4] have been employed to reconstruct the missing values. One of the major disadvantages of the classical methods is the necessity for prior informations about the error statistics in a data set. Such prior informations are often poorly known [3, 23]. In addition, these methods may fail due to the noise content, the gap-amount and gap-structure, slow convergence in dealing with the spatio-temporal structure of the dataset [127, 281] and hence they may prohibit its robust applications in several domains [3, 122]. In comparison to the classical methods, the non-parametric EOF technique relies on the dataset alone to provide a self-consistent data reconstruction method without the need of any prior information.

Kaplan et al. (1997) [122] first proposed the EOF method for filling gaps using the covariance matrix of a 136-year SST data set on the Atlantic Ocean [122]. They have also implemented a least-squares regression to retrieve the best estimation of the missing values. Later on, the classical EOF interpolation method, known as data interpolating empirical orthogonal functions (DINEOF), was proposed and demonstrated based on synthetic data and advanced very high-resolution radiometer (AVHRR) data set from over the Adriatic Sea [22]. Afterward, the EOF decomposition through the Lanczos method was employed to obtain the estimated missing values of the SST data over the Adriatic Sea [3]. The EOF results lead to accurate reconstructions of data gaps as well as low CPU time (30 minutes less than the traditional OI technique) while dealing with a large data matrix [281]. In contrast to the least-squares based interpolation techniques, it is observed that the iterative EOF method is superior in estimating the periodic fluctuations, especially in the vertical GPS time series with wide data gaps [281]. The EOF technique, as a gap filling tool, has got numerous applications in climate science, in-situ measurements, and geodetic studies through InSAR or GPS methods [3, 122, 281]. Since the GNSS time series is different from other geophysical records due to the presence of offsets and colored noise in the time series, conventional techniques may not adequately capture the associated data-complexity with wide range of data gaps (e.g., $5\% - 25\%$) [281]. However, even in such cases, the EOF-based interpolations are preferable to reconstruct the missing values [281]. To assess the performance of the EOF method, either the cross-validation techniques (e.g., wavelet analysis) or the comparison of the independent data set through synthetically generated data gaps are often employed [127, 281]. Therefore, unlike the interpolation techniques for which the accuracy and reliability depend on the amount of gap, data structure, or short/noisy chaotic signals, the EOF method serves as a robust, computationally efficient, and optimal gap-filling toolkit.

2.4.5 Other applications of EOF (PCA) and computational packages

Apart from the above-mentioned applications, recently, the PCA (also known as EOF) has become a part of new emphasis to develop unsupervised machine learning algorithms to identify the key space-time correlations among data features, to extract the patterns, regularities and irregularities of the data, and to reduce a high-dimensional dataset into low-dimensional with maintaining the integrity of the original data [121, 234, 251]. These unsupervised PCA-based algorithms are adopted in different applications, such as in nowcasting earthquakes that images the time-dependent earthquake cycle [217], to generate the geothermal potential maps to understand the characteristics of geothermal exploration data [234], to develop the geodetic imaging techniques (e.g., machine learning algorithms for marsh observations) [160], for developing the industrial machine vision, psychometric quality assessment, medical image processing, and traffic sign condition monitoring [121], for identifying different classes of seismic noise signals from the continuous seismic waveforms [115], to develop the pattern dynamics model and forecasting methods in seismically active regions [251], and to design a PCA-based optimization method to carry out change detection in remote sensing images [9]. From the above discussion, it appears that PCA is a potential method to examine and analyze a large and high-dimensional space-time dataset.

In addition, for the computational purpose, there are many computational toolkits (software packages and libraries) available to evaluate the EOF modes (spatial pattern and associated time series). These software packages and libraries include National Center of Atmospheric Research (NCAR) Command Language (NCAR Command Language), Scikit-learn: Machine learning in Python [189], eofs: A Library for EOF Analysis of Meteorological, Oceanographic, and Climate Data [46], EOF package in Climate Data Toolbox for MATLAB [78], and PCAtool [96]. Except a few, most of these object-oriented computational packages are open-source. Several language platforms, such as Python, scientific libraries NumPy and SciPy, and MATLAB scripts are used in these packages.

From the above discussion, the EOF analysis turns out to be the state-of-the-art toolkit in inherent pattern identification of space-time data set. A summary of application-wise EOF parameters and their interpretation is provided in Table 2.2.

Table 2.2: Application-wise EOF parameters and their interpretation.

S.No	Applications	Spatial patterns (EOFs) and associated times series (PCs), as EOF modes	References
1	Ionospheric variation modeling	• The first EOF represents global spatial and diurnal variation of the TEC and the associated first PC indicates solar cycle variations. • The second EOF reflects the hemispherically asymmetric pattern and the associated PC shows the annual fluctuation component. • The third and fourth patterns reveal the equatorial anomaly phenomena, whereas the associated third and fourth PCs reveal weak seasonal pattern and annual/semi-annual oscillation components respectively.	Zhang et al. 2011, 2012 [283, 284]; Wan et al. 2012 [273]
2	Climate and atmospheric related studies	• The EOF modes provide evidences of the "Tropical Atlantic Dipole" and the "Tropical Indian Ocean Dipole" in SST data. • The EOF modes provide the evidence of EI Nino effects in SST time series. • They show Northern Hemisphere winter variability in sea level pressure data.	Kim and North 1997 [124]; Dommenget and Latif 2002 [52]; Hannachi et al. 2006 [91]; Hannachi 2007 [92]
3	Crustal deformation analysis (especially in coseismic analysis)	• The first EOF mode captures the prominent coseismic signal along with postseismic relaxation. • The second mode provides the evidence of the prevalent common mode error (CME).	Chang and Chao, 2011, 2014 [35, 36]; Munekane 2012 [156], Dong et al. 2006 [53]

2.5 Summary

In general, non-linear dynamical systems, such as geophysical system and climate system, exhibit space-time-dependent characteristics, like stationary, propagating and moving features, cyclostationary statistics, and non-linearity. With the presence of these prevalent properties in a

large, unstructured, and high-dimensional data set originated from a dynamical system, an automatic, transparent, and regular way is essential in accurately extracting physically meaningful modes and their space-time evolutions from data.

In order to deal with space-time statistics of the observational data, in the present chapter, a data exploratory technique, namely the empirical orthogonal method (EOF) is adopted. The conceptual mathematical base of the EOF method is thoroughly explained in a three-fold way: data preparation, mathematical formulation of the EOF, and interpretations of the estimated physical modes. A short overview of some extensions of the EOF method is also provided. In addition, a wide range of applications of the EOF methods in various domains is discussed. Overall, the present study leads to the following conclusions:

1. The spatio-temporal EOF method is a state-of-the-art toolkit in the study of prediction, estimation, and detection of small-scale, short-term, and long-term variations in a data set. The EOF method can decompose the coherent space-time signals in terms of their individual modes and consequently can enhance the signal-to-noise ratio of the time series data. Moreover, the EOF method is easy to implement and is computationally faster. The limitations of the traditional EOF method can be overcome by its several extensions.

2. The EOF method has numerous applications in diverse fields, such as: (i) to assess the intrinsic variations in TEC caused by solar and magnetic activities or latitude dependence; (ii) to identify the pattern in SST for more insights to the "Tropical Atlantic Dipole" and the "Tropical Indian Ocean Dipole"; (iii) to determine the dipole or multipole structure of variability in SLP at the Northern Hemisphere; (iv) to extract the prominent patterns from the geodetic observations in the crustal deformation analysis, and (v) to recover the intermittent gaps in a data set.

As a whole, the present chapter highlights the efficiency of the EOF methods in terms of the identification of independent physical/dynamical modes and corresponding principal component time series, purely extracted from the observational data. In addition, this chapter emphasizes numerous applications of the EOF methods with their advantages and limitations.

The present chapter has discussed the mathematical concept of a spatio-temporal method, i.e., EOF, which is capable of systematically capturing dominant patterns from correlated observations. Based on the efficacy of this method in significantly extracting the inherent space-time characteristics with the presence of short-term, small-scale, and long-term variations, the EOF method is a potential technique for the coseismic deformation analysis. In the next chapter, Chapter 3, a demonstration of the EOF method is provided to identify the coseismic deformation pattern of the 2016 Kaikoura earthquake (M_w7.8) in New Zealand.

Chapter 3

Coseismic Deformation Pattern Associated with the 2016 Kaikoura Earthquake Inferred from the EOF Analysis

"*Methods and means cannot be separated from the ultimate aim.*"

by Emma Goldman

In order to understand the crustal deformation caused by the contemporary earthquake cycle and associated seismic hazard in any active region, identification of the coseismic deformation corresponding to large earthquakes is of paramount importance. In light of this, the present chapter aims to identify the crustal deformation associated with the "complex multifault rupture" earthquake, namely the Kaikoura earthquake (M_w7.8), that occurred on November 13, 2016 in New Zealand. For this, the data-driven EOF analysis is performed and the obtained EOF modes are interpreted in terms of the coseismic and early postseismic deformation patterns corresponding to the Kaikoura event. Subsequently, the leading EOF modes are used as an input for estimating the spatial distribution of the coseismic strain. In addition, a comparative study of the EOF displacement vectors and the least-squares dislocation estimates is carried out to elucidate the efficacy of the EOF technique, especially for the coseismic analysis. The content of the present chapter is provided below.

Contents

3.1 Introduction

On a global scale, large magnitude earthquakes not only retard the economic growth and successive development of the regions but also cause great destruction to the socio-economic infrastructure in several populated areas in the seismically active region. Some notable large to major earthquakes are the 2004 Sumatra earthquake (M_w9.1), 2011 Tohoku earthquake (M_w9.1), 2015 Gorkha earthquake (M_w7.8), and the 2016 Kaikoura earthquake (M_w7.8) [36, 89, 236, 275]. The study of such seismic events not only provides unprecedented opportunities to verify the existing geodetic and geophysical models but also offers reliable information about the underlying crustal mechanism on a large range of time and spatial scale. The coseismic deformation through various crustal characteristics, such as coseismic slip distribution, earthquake-induced dislocation field, coseismic stress-strain distribution, occurrence dynamics of earthquake, and the ongoing postseismic deformation process has great implication in earthquake mechanics as it determines the underneath fault geometry and associated seismic hazard in a given region [89, 113].

In order to evaluate the above mentioned earthquake-induced crust parameters, several data-driven methods, such as the least-squares estimation (LSE), elastic dislocation model (EDM), empirical orthogonal function (EOF), principal component analysis-based inversion method (PCAIM) and the extended network inversion filter (ENIF) method have been incorporated in past [35, 107, 128, 156, 232, 243]. The obtained results may further lead to inversion modeling for other coseismic parameter estimation. For example, Fu et al. (2010) [69] applied the half-space and spherical dislocation theories to calculate the coseismic displacement field caused by the 2004 Sumatra earthquake and identified the effects of Earth's curvature and radial heterogeneity on coseismic deformation; Shestakov et al. (2012) [230] used the LSE method to quantify the coseismic displacement caused by the Tohoku earthquake and thereby developed the slip model of the mainshock rupture to estimate its main parameters (e.g., rupture area, seismic moment, and moment magnitude); Zhou et al. (2012) [285] conducted coseismic deformation study of the Tohoku earthquake from three slip models (provided by USGS, UCSB, and ARIA) based on different dislocation theories; Sreejith et al. (2016) [236] inverted coseismic InSAR and GPS data to model the slip on the causative fault of the 2015 Gorkha earthquake assuming linear superposition of rectangular dislocations in an elastic half-space, and Jiang et al. (2018) [113] and Su et al. (2020) [243] examined the coseismic and early postseismic signals of the Kaikoura earthquake using the least-squares fitting algorithm. Hsu et al. (2006) [107] adopted the ENIF model to estimate the frictional afterslip following the 2005 Nias earthquake. In an another study related to the 2005 Nias earthquake, Kositsky and Avouac (2010) [128] developed an afterslip model based on the PCAIM inversion model and

ENIF model. Their results have suggested that the PCAIM method is a suitable approach for analyzing the postseismic deformation rather than the traditional ENIF model. In 2014, Chang and Chao (2014) [35] implemented the EOF method to examine the coseismic deformation caused by two large earthquakes in Taiwan, namely the 2002 Hualien earthquake (M_w7.1) and 2010 Jiashian earthquake (M_w5.7). Based on the above discussed studies, it appears that the analysis of the coseismic phase plays a pivotal role not only in estimating the coseismic crustal characteristics but also in various purposes, such as (i) to validate the fault model by geodetic data, (ii) to interpret the displacements observed by GPS, and (iii) to provide a reference for other researchers who intend to investigate coseismic deformations as well as postseismic deformations associated to the seismic event [68, 69].

Although the above-mentioned techniques (e.g., LSE, EDM, and ENIF) are routinely used to describe the earthquake cycle deformation caused by an earthquake, some of these methods provide poor results under some situations and may lead to inadequate information for further analysis. Examples of such situations are described as follows: (i) the LSE algorithm may suffer to deal with the complex time series that has interseismic, coseismic, and postseismic signals simultaneously, low signal-to-noise ratio, and the presence of outliers, noise, influential values, and bad leverage points [35, 156]; (ii) the error in the coseismic estimates derived from the EDM may stem from model input parameters (e.g., earthquake focal location and the source mechanism solution) in the EDM calculation or from the consideration of simplistic structures of elastic continuum medium [35], and (iii) the ENIF estimates may be influenced by some constraints, such as necessity of a-priori values (often subjective) of the hyperparameters in the geodetic inversion, computationally expensive, and insufficient for the analysis of complex time series that would include interseismic, coseismic, and postseismic deformation [107, 128]. The above-mentioned limitations can be effectively addressed by the non-parametric EOF method as it has the potential to deal with interrelated space-time signals to better delineate with the regional tectonic processes in the coseismic deformation analysis [35, 156].

In late 1940s, originating from the disciplines of atmospheric and climate science [70, 142, 167], the EOF method has the potential to decompose the time series in such a way that the resulting spatial and temporal patterns can be interpreted in terms of hidden and dominant characteristics of the underlying physical process. As a consequence, the EOF technique enhances the signal-to-noise ratio of any time series data. The EOF method is also applicable to quantify the small-scale, short-term, and long-term signals from the observational data [92]. Particularly, in the coseismic analysis, the EOF is an effective method to extract the hidden space-time signals, such as preseismic, coseismic, and postseismic signals including noises (e.g., CME and colored noise) from the geodetic time series at the near-field and far-field regions [35, 36]. In addition, there is no requirement of any a-priori information for the EOF calculation. Considering the EOF method as efficient and sufficient in coseismic studies, the EOF method was firstly

implemented by Chang and Chao (2011) [36] to analyze the coseismic deformation analysis associated with the Tohoku earthquake. Later on, Munekane (2012) [156] used the same method to quantify the coseismic and the subsequent postseismic afterslip of the Tohoku earthquake. In 2014, Chang and Chao (2014) [35] conducted a case study in Taiwan in order to investigate the spatial distribution of crustal deformation associated with two earthquakes. In addition, they also carried out a comparison test of the EOF method with the LSE and the EDM methods and found it superior to both methods. Taking the advantage of the plethora of characteristics of the EOF method as a self-organized and data-adaptive, non-parametric, and optimal data filtration method, the present chapter focuses on the coseismic deformation analysis associated with the 2016 Kaikoura earthquake of New Zealand.

The Kaikoura earthquake with M_w7.8 occurred on November 14, 2016 NZDT (11:02 on 13 November UTC) in the north Canterbury region of New Zealand. This event triggered large-scale crustal deformation in the whole central South Island. In order to investigate the distribution of crustal deformation caused by the Kaikoura event over New Zealand, the spatio-temporal EOF method is adopted. For this purpose, the position time series data of 127 CGPS stations over New Zealand is incorporated. Before implementation of the EOF analysis, the time series data is refined by removing the linear trend and seasonal signals. Consequently, the refined time series consists of the jump signals and the residual part. Here, the jump signals indicate the displacement vectors induced by an earthquake and the residual part is thus the sum of the spatially correlated CME and other random noises. The refined time series data is then considered for the EOF calculation. As a result, the EOF modes, a pair of spatial pattern with the corresponding principal component, are obtained and interpreted in terms of various deformation patterns associated with the Kaikoura event. The first EOF mode contains the most dominant pattern as the coseismic signal of surface deformation, whereas the second EOF mode comprises the other prevalent signals, such as preseismic signal, postseismic signal or random noises (e.g., CME) in the CGPS time series. In the present study, the first two EOF modes are considered for interpretation, whereas the third and higher modes are not shown as they account for less than 5% of the data variance. Note that for the detailed analysis of the coseismic and early postseismic deformation caused by the Kaikoura event, the EOF analysis is performed by taking three types of test periods (discussed in Section 3.5). In addition, the leading EOF modes, consisting of the earthquake-induced displacement vectors, are further utilized to estimate the spatial distribution of the horizontal coseismic strain rates. Besides the coseismic analysis, the EOF-based coseismic displacement vectors are compared in contrast to the coseismic motion estimated by the conventional LSE method. Therefore, the estimated EOF results and subsequent parameters not only shed light on the leading coseismic information from geodetic observations but also provide further insights toward a better understanding of the subsequent phases of the earthquake cycle linking to the tectonics of New Zealand. The steps

of analysis including the data processing, data preparation, and the EOF analysis along with the estimated results are discussed in the following sections. In addition, the tectonic background of New Zealand along with existing coseismic studies related to the Kaikoura earthquake is also provided below.

3.2 Tectonic map of the study area

New Zealand's active tectonics is characterized by three main features: (i) the Hikurangi trough beneath the North Island and the upper South Island, (ii) the Alpine fault beneath the central South Island, and (iii) the Puysuger trench at the southern end of the South Island (Fig. 3.1) [201, 269]. The Hikurangi subduction interface along with existing strike-slip faults throughout the North Island is mainly responsible to produce strong to large earthquakes in the North Island and its surrounding regions. In the central South Island, the Alpine fault including the Marlborough fault system accommodates the maximum amount of the crust strain and releases the stored energy in terms of earthquakes. The Marlborough fault system consists of four dominant faults, namely Awatere, Clarence, Hope, and Wairau faults as well as other splay faults, such as Hundalee, Jordan Thrust, Kekerengu, Needles, and Papatea faults [89]. At the southern end of the South Island, the Puysegur subduction zone is capable of generating major earthquakes. As a consequence, a spate of large earthquakes has rattled New Zealand in the past, mainly along the Puysegur subduction-to-Aplinefault-to-Hikurangi interface. Some of the notable large earthquakes of New Zealand are the 1931 Hawke's Bay with M_w7.8, 2009 Fiordland earthquake with M_w7.8, 2010–11 Canterbury sequence with magnitude M_w7.1–6.2, and the most recent 2016 Kaikoura earthquake with magnitude M_w7.8 [89, 140, 240].

Famed for its geological complexity, the Kaikoura earthquake occurred at the place in the north Canterbury region, where the southern section of the Hikurangi subduction margin smoothly terminates and translates into the transpressional Alpine fault (Fig. 3.1) [34]. Geodetic and seismological studies indicate that there was a "domino effect", as the earthquake rupture jumped from fault to fault, essentially 'unzipping' along a 150 km length of the northeast coast of the South Island [87]. The rupture area broadly contains major faults of two distinctive seismotectonic domains, namely the north Canterbury region and the Marlborough fault system [113, 232]. The Kaikoura event is followed by a sequence of aftershocks with a NE-SW trend from the central South Island to the lower North Island (Fig. 3.1). From the complex network of faults exhibiting a variety of slip kinematics to the evidence of large coseismic slip, this earthquake has provoked the research community not only to understand the physical mechanism of the earthquake cycle but also has raised important questions on how multi-fault rupture scenarios are defined for seismic hazard models in plate boundary zones worldwide [87].

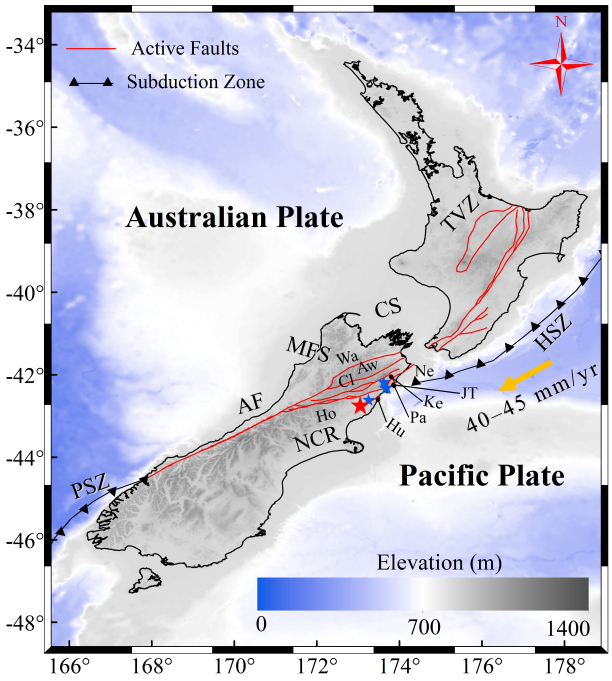

(a)

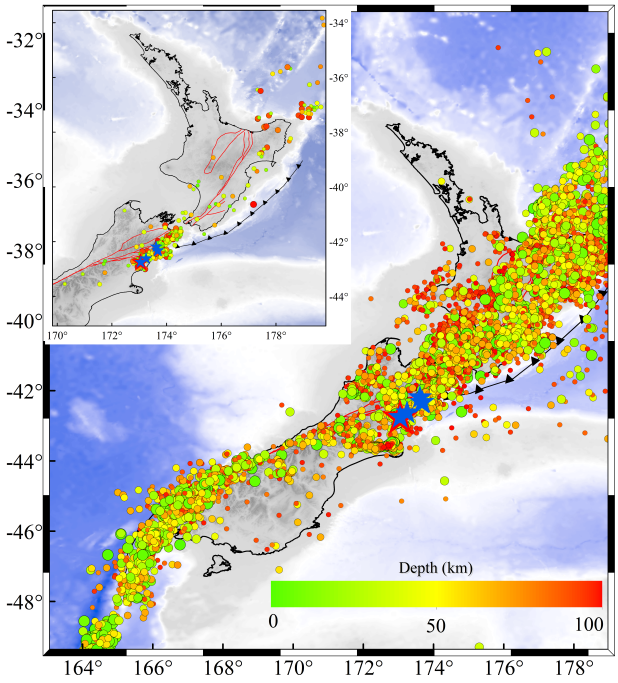

(b)

Fig. 3.1: (a) Tectonic map of New Zealand and (b) seismicity distribution in New Zealand and its surrounding regions from 1960 to 2021. The red star denotes the epicenter of the 2016 Kaikoura earthquake and blue stars indicate locations of subsequent aftershocks. The inset part in subfigure (b) shows the sequence of aftershocks ($M_w \geq 3.0$) which occurred just after the Kaikoura event. Abbreviations are as follows: AF, Alpine fault; Aw, Awatere; Cl, Clarence; CS, Cook Strait; Ho, Hope; Hu, Hundalee; JT, Jordan thrust; Ke, Kekerengu; HSZ, Hikuranngi subduction zone; MFS, Marlborough fault system; NCR, North Canterbury region; Ne, Needles; Pa, Papatea; PSZ, Puysuger subduction zone; TVZ, Taupo volcanic zone; Wa, Wairau fault.

In light of above, several coseismic studies related to the Kaikoura earthquake have been carried out by many national and international groups to unravel some of the earthquake's complexities. For instance, Hamling et al. (2017) [89] found that the earthquake rupture propagated northward about more than 170 km and there was extensive uplift along much of the coastline boundary. Hui-Hong et al. (2017) [110] investigated the coseismic stress changes of the Kaikoura earthquake and the estimated results exhibited a similar pattern to the coseismic deformation. The coseismic model of Jiang et al. (2018a) [113] suggests that the surface rupture associated with the Kaikoura event is extended up to the Hikurangi subduction interface. In addition, their results suggest that Wellington is under higher seismic hazard after the earthquake and it is a great need to pay attention to the Wellington region due to the potential of large earthquake disasters in the near future. Later on, in an another study, Jiang et al. (2018b) [114] calculated the PCAIM modes to demonstrate the spatio-temporal evolution of triggered slow slip events in New Zealand. Their estimated results suggest that the slow slips events, such as the Kapiti, north Hikurangi, and the central Hikurangi slow slip events along with Marlborough afterslip, were active during the first week after the mainshock and the associated deformation gradually decayed logarithmically with time. Clark et al. (2018) [40] examined the highly variable vertical displacements, ranging from -2.5 to 6.5 m. Shi et al. (2019) [231] observed clockwise microblock rotation south of the Hope fault, with surrounding fault ruptures. Su et al. (2020) [243] estimated the coseismic and postseismic deformation displacement caused by the Kaikoura event and found large displacement vectors mainly in the southern North Island and the northern South Island. They also identified the cumulative moment magnitude after the event during the periods $0.0-0.5$, $0.5-1.0$, and $1.0-1.5$ years, exhibiting a rapid decay of the postseismic deformation similar to the direction of coseismic deformation. Thus, the estimated characteristics associated with the Kaikoura earthquake not only provide the earthquake mechanism sources but also emphasize the importance of re-evaluating the potential of ongoing earthquake cycle and subsequent seismic hazard in New Zealand. Therefore, the present chapter demonstrates the efficacy of the spatio-temporal EOF technique in order to geodetically investigate the coseismic and early postseismic deformation associated with the Kaikoura event. Before proceeding further, a brief description of the geodetic data and its processing is provided below.

3.3 Geodetic data

In order to examine the spatial and temporal patterns of surface deformation associated with the 2016 Kaikoura earthquake, geodetic observations are considered as an input for the EOF calculation. In New Zealand, a network of continuous GPS stations is available throughout the

country to monitor geological disasters, such as earthquakes, volcanic activities, massive landslides, tsunamis, and slow-slip events. This network essentially enables to assess natural hazards in New Zealand and its surrounding regions. Particularly, these geodetic observations can be used to examine the different phases of earthquake cycle deformation and associated crustal parameters, such as crustal structure, strain distribution, and fault kinematics, and thereby, earthquake potential based on the seismic moment budget in New Zealand. A brief description of the CGPS network of New Zealand and associated geodetic observations are provided in the following sections.

3.3.1 GPS network and data acquisition

In New Zealand, the GeoNet, comprising a network of CGPS stations, provides a framework for real-time geological hazard monitoring system. The GeoNet is sponsored by the New Zealand government through its agencies Earthquake Commission (EQC), GNS Science and Land Information New Zealand (LINZ). The GeoNet consists of approximately 190 CGPS stations, which are mainly located on the east coast of the North Island above the Hikurangi subduction interface, in the Taupo volcanic zone, and in the northern South Island. It provides CGPS observations in the form of RINEX format and associated position time series. The RINEX data is available with the sampling of 30s, 1s, and high sampling rates (recorded at 1 Hz and 10 Hz sampling rates for the major geologic events), whereas the position time series data is available on a daily and hourly basis. All data are freely available in an open format to facilitate research related to precision measurement, risk analysis, and hazard assessment to benefit a range of industries and organizations.

Since the present study is focused on the coseismic deformation analysis related to the 2016 Kaikoura earthquake, 127 stations of the total 190 CGPS stations are selected based on the availability and quality of the observations. Most of these CGPS stations are situated in the central South Island and the southern North Island. The network of these selected CGPS stations is pictorially shown in Fig. 3.2. The RINEX data of these stations are collected during the time period of 15 days (November 6–20, 2016) straddling the Kaikoura event. The sampling interval of RINEX data is 30s. The selected RINEX data of 127 stations are further utilized for GPS data processing, as mentioned in the following section.

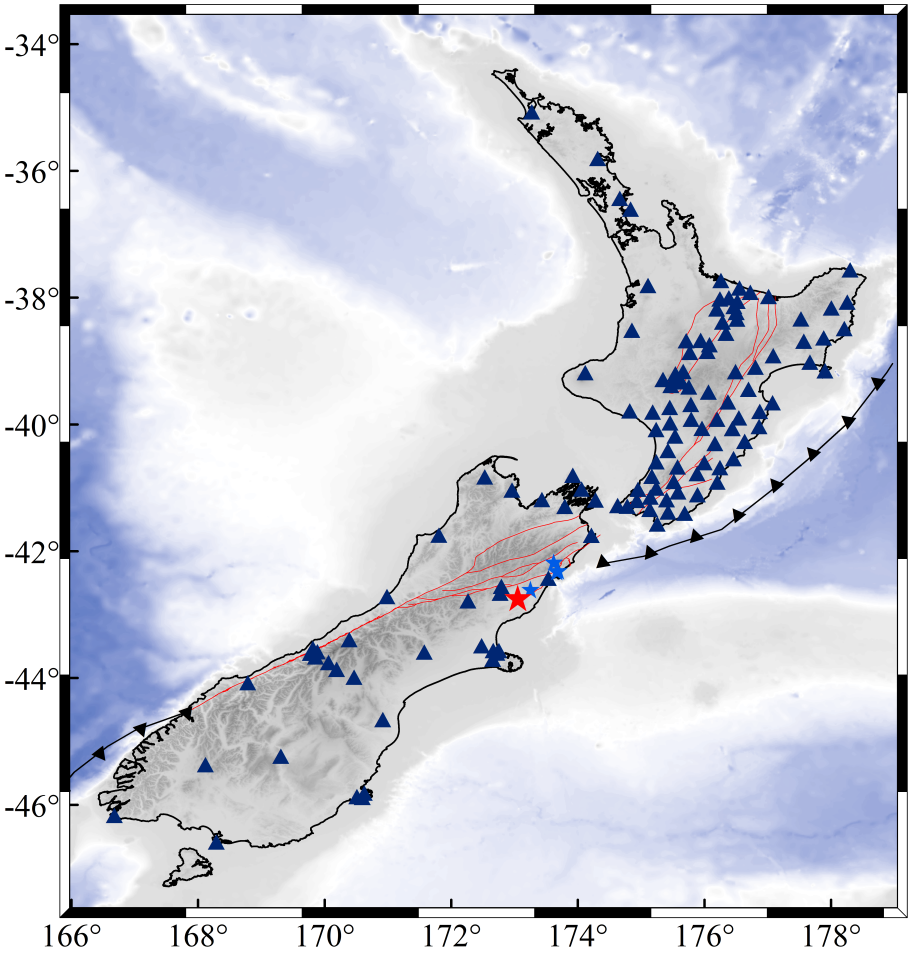

Fig. 3.2: The GPS network of selected 127 CGPS stations in New Zealand. The blue triangles denote the locations of GPS stations, whereas the red and blue stars represent the epicenters of the Kaikoura event and the following aftershocks, respectively.

3.3.2 GPS data processing

As mentioned above, the RINEX files of 127 CGPS stations are being collected during the time period of one week before and after the Kaikoura earthquake. For the detailed analysis of the surface deformation caused by the Kaikoura earthquake, the selected RINEX data is used to obtain the position vectors of a site on every 30 minutes. For high precision research work in geodesy, some standard scientific GPS post-processing software (GAMIT-GLOBK, BERNESE, and GIPSY) are mostly utilized. In the present study, the GAMIT-GLOBK suite post-processing software is used to analyze the accrued GPS data. This software, available in the LINUX environment, was developed by the Massachusetts Institute of Technology (MIT) for the estimation of three-dimensional relative positions of the ground station. The GAMIT uses GPS broadcast carrier phase and pseudorange observables (stored in RINEX file) known as GPS readings, satellite ephemeris (stored in navigation file), and satellite orbit data (stored

in orbit file). Through the least-squares estimation, it generates values of positions and other parameters such as orbits, Earth orientation, ambiguities, and atmospheric delays [95, 136]. To implement the least-squares algorithm, the simplified and linear equation form, as the observation equation, is given below:

$$d = Ax + v \tag{3.1}$$

where,

d $[n \times 1]$: vector of observations,

A $[n \times u]$: design matrix,

x $[u \times 1]$: vector of unknowns (parameter),

v $[n \times 1]$: noise or residual vector.

For further computation, let us define some additional parameters:

σ_0^2: a priori variance,

Σ : covariance matrix,

$Q_d = \frac{1}{\sigma_0^2}\Sigma$: the cofactor matrix of observations, and

$P = Q_d^{-1}$: the weight matrix.

The least-squares adjustment provides a unique solution of Equation 3.1 subject to the condition $v^T Pv$ = minimum.

This adjustment principle provides the following normal equation:

$$A^T PAx = A^T Pd \tag{3.2}$$

The solution of Equation 3.2 is

$$x = (A^T PA)^{-1} A^T Pd \ , \tag{3.3}$$

which can be simplified to

$$x = G^{-1} g \ , \tag{3.4}$$

where, $G = A^T PA$ and $g = A^T Pd$.

The cofactor matrix Q_x follows from $x = G^{-1}A^T Pd$ by the covariance propagation law as:

$$Q_x = (G^{-1}A^T P) Q_d (G^{-1}A^T P)^T \tag{3.5}$$

By substituting $Q_d = P^{-1}$, the above equation further reduces to

$$Q_x = G^{-1} = (A^T P A)^{-1} \tag{3.6}$$

The daily solutions from GAMIT provide location coordinates for each GPS station along with Earth orientation and satellite orbit corrections. Further, the estimated loosely constrained daily solutions are utilized to estimate station position and plate motion using the GLOBK [95].

Processing of the GPS data in the GAMIT-GLOBK is often performed in three stages: (i) all data are processed using GAMIT to obtain loosely constrained solutions of coordinates of a particular station together with IGS (International GNSS Service) fiducial stations, (ii) the time series of position coordinates of every station is then examined for outliers using GG-MATLAB (GAMIT-GLOBK MATLAB) tool, and finally (iii) the refined time-series data are utilized for the station velocity estimation in GLOBK [95]. For the present work, the 30 min interval GPS time series is required and therefore, only two stages of processing are performed. For the data processing, the below step-by-step process is followed:

Step 1: First, install the GAMIT-GLOBK software in a LINUX environment. Also, check a few important files:

process.defaults (edit to specify computation environment, source for internal and external data and orbit files, start time sampling interval, and instructions for archiving the results)

sestbl. (edit the *AUTCLN* postfit command to suit processing strategy)

sites.defaults (edit to specify sites to ftp from RINEX data archives, to search for RINEX files on the local system, and to exclude from automatic *station.info* updating)

station.info (edit to include all continuous stations as well as all IGS stations)

and ***lfile., leap.sec, luntab., nutabl.*** (these files need to be up to dated).

Step 2: Prepare four subdirectories in an experimental directory: brdc (contains navigation (.n) files), igs (contains sp3 or orbit files (.sp3) of satellite for all the used IGS stations), rinex (contains all the RINEX files (.o) of observations of regional as well as

IGS stations), and tables (tables folder of GAMIT).

To download the observation, navigation, and orbit-sp3 files for the chosen IGS stations, the following commands are used:

(i) **RINEX files**: *sh_get_rinex -archive <archive> -yr <year> -doy <day of year> -ndays <number of days> -sites <IGS sites>*

<archive> here the observation files of the IGS stations are stored (e.g., SOPAC, GeoNet New Zealand (geonz) and others)

<year> year of observation

<day of year> day of observation in the corresponding year

<number of days> number of consecutive days of data to retrieve

<IGS sites> List of IGS stations to be retrieved from archive (e.g., here 9 IGS stations are used: AUCK, CHTI, DUND, HOB2, MAC1, MQZG, NIUM, TIDB, WGTN)

Example *sh_get_rinex -archive geonz -yr 2016 -doy 311 -ndays 10 -sites AUCK WGTN*

(ii) **Navigation files**: *sh_get_nav -archive <archive> -yr <year> -doy <day of year> -ndays <number of days>*

Example *sh_get_nav -archive sopac -yr 2016 -doy 311 -ndays 10*

(iii) **Orbit/SP3 files** *sh_get_orbit -archive <archive> -yr <year> -doy <day of year> -ndays <number of years> -type <type of orbit file sp3/gfile> -center <IGS processing center igs/esa/sio>*

Example *sh_get_orbit -archive sopac -yr 2016 -doy 311 -ndays 10 -type gfile -center igs*

Step 3: After downloading all required files (observation, navigation, and orbit files), a global tide model FES2004 (*otlFES2004.grid*) is utilized to account for solid Earth tides and ocean loading effects. Subsequently, a series of GAMIT commands are used:

sh_gamit -d yr days/-s yr d1 d2 -expt -orbit -aprfile -yrext

-d yr days (need to use if data are processed for each specified day (e.g., 2016 311 315 316))

-s yr d1 d2 (need to use if data are processed for continuously from starting day to *n* number of days (e.g., 2020 311 320))

-sessinfo, sampling interval, number of epochs, start time (default 30 2880 0 0) (need to use if data are processed for obtaining the 30 min position time series (e.g., 30 60 2 30))

-expt (four character experiment name (e.g., BITS))

-orbit (type of orbit to be used (e.g., IGSF, SIOF, and others))

-aprfile (name of reference frame (e.g., itrf14.apr)

-yrext (to specify output directory by corresponding year and day (e.g., 2020_311))

Example *sh_gamit -orbit igsf -s 2016 311 325 -sessinfo 30 60 0 0 -expt BITS -aprfile itrf14.apr -yrext*

Step 4: GAMIT provides a sequence of daily station coordinates in terms of *h*-files of loosely constrained solutions. However, the existing outliers (e.g., unlevelled antenna error, multipath effect, snow on antenna, and others) are hard to identify from the GAMIT output files. However, the time series plots of the station coordinates allow us to identify outliers. In this regard, the GLRED program is often used. It generates a time series of three dimensional positions (North, East, and Up) using the following commands.

(i) Create two subdirectories (**glbf** and **gsoln**) in the main experimental directory.

(ii) Convert all the ASCII *h*-files into binary *h*-files (readable to GLRED and GLOBK) using **htoglb** (*htoglb [glbf_directory] [ephemeris_file] <GAMIT h-file>*). Then copy all binary *h*-files into **glbf** directory together with SOPAC global binary *h*-files from the IGS network (*sh_get_hflies*).

(iii) Create a list of binary *h*-files in the **gsoln** directory using *ls ../glbf/h*.glx >expt.gdl*. Also copy *globk_rep.cmd* and *globk_vel.cmd* files from **table** directory.

(iv) Run GLRED using

glred <crt> <prt> <log> <input_list> <globk cmd file>

Example *glred 6 globk_rep.prt globk_rep.log expt.gdl globk_rep.cmd -mb*

The last term $-mb$ creates multibase (time series) files, which are further executable in

tsveiw program of **GG-MATLAB** (GAMIT-GLOBK MATLAB) tool to remove outliers, seasonal modulations, and others, as necessary [95].

The above process generates three files such as *mb_AUCK_GPS.dat1*, *mb_AUCK_GPS.dat2*, and *mb_AUCK_GPS.dat3* for each station (e.g., for AUCK site), which contain position time series data for north, east, and up components, respectively. The time series data of several stations will be further used for EOF analysis to identify the earthquake characteristics associated with the Kaikoura event.

3.3.3 GPS time series

The final 30 min interval positions at each site, estimated in the International Terrestrial Reference Frame 2014 (ITRF14), will be the basis of the EOF analysis. As an illustration, the time series plots in the north, east, and upward direction of the CMBL station is presented in Fig. 3.3. The discontinuities or jumps that occur in the GPS position time series are possibly due to receiver stoppage, antenna error, multipath effect, seasonal variation, or earthquake offsets [98]. Here, the jump indicates the displacement caused by the Kaikoura earthquake. In addition, the seasonal variations in the GPS time series can be decomposed into the annual and semi-annual components, and major tidal signals. The modulations of seasonal variation can be the combination of surface loading related to water variations, ionospheric-tropospheric pressure, and vapor loading during the winter season [256]. Each part of time series, such as trend, seasonal signals, jumps, and residual component provides inherent information of the underlying tectonic mechanism through observations. In order to investigate the significant earthquake-induced displacements or jumps in the GPS time series, it is essential to remove the trend and seasonal signals from the given time series. Therefore, before the EOF implementation, the least-squares fitting algorithm is carried out to estimate the parameters associated with each component of the given time series. A brief description of the EOF methodology including data preparation and the EOF implementation is provided in the next section.

3.4 Methodology

The GPS position observations not only provide the present scenario of the earthquake cycle but also enable an efficient measurement of the time-dependent displacement field for understanding the geodynamic processes in active regions. In the present study, for coseismic analysis, the RINEX data of 127 CGPS sites is processed using GAMIT-GLOBK software to obtain the 30 min interval position time series. The obtained time series is prepared as input data according to the requirement of EOF calculation, as described below.

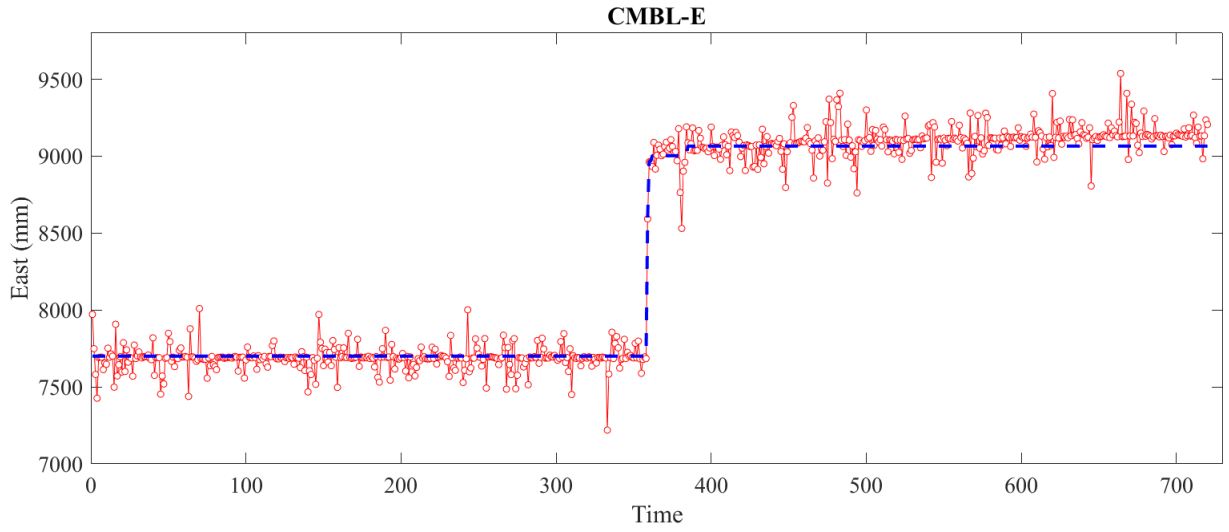

(a)

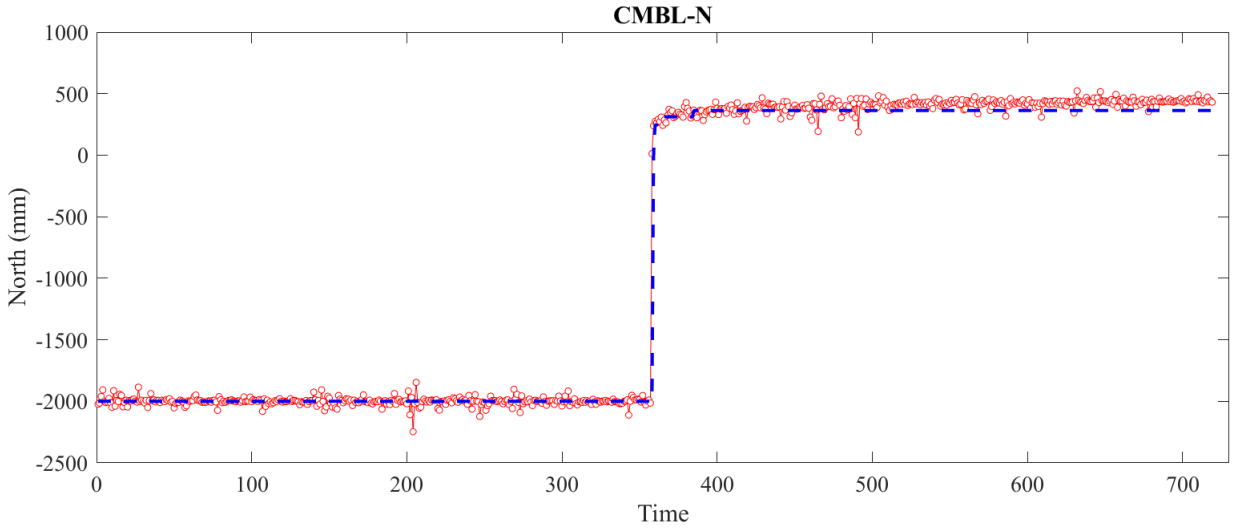

(b)

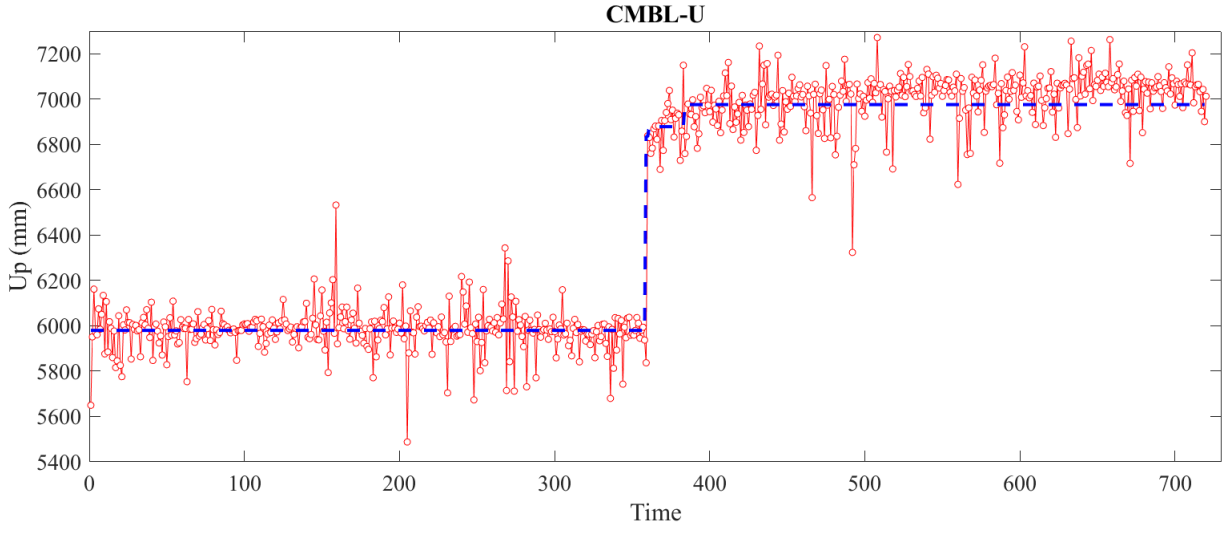

(c)

Fig. 3.3: Time series plot of CMBL station in the (a) east direction, (b) north direction, and (c) up direction.

3.4.1 Data preparation

In data preparation, refinement of the CGPS time series is an essential and fundamental step to ensure that the time series consists of important signals related to the underlying physical system. To avoid misleading results, the irrelevant signals need to be removed prior to performing any analysis. It is known that CGPS time series $x(t)$ can be decomposed as a linear combination of the deterministic components (e.g., trend, seasonal signals, and offsets) and the residuals $(\varepsilon(t))$. The mathematical expression is as follows:

$$x(t) = x_0 + v_0 t + \sum_k c_k H(t - t_0) + \sum_{k=1}^{5} \left[A_k \sin\left(\frac{2\pi t}{P_k}\right) + B_k \cos\left(\frac{2\pi t}{P_k}\right) \right] + \varepsilon(t) \tag{3.7}$$

where, $(x_0 + v_0 t)$ accounts for the temporal mean with the long-term progression of the time series (secular variation) over the observation period. The Heaviside step function (H) with amplitude c_k shows vertical offset due to an earthquake event at a particular epoch (t_0). The five periodic signals with amplitude A_k and B_k ($k = 1, 2, ..., 5$) account for two seasonal and three major tidal signals with periodicity P_k. According to the meteorological loadings, the five signals are Mf (13.6608 days), Msf (14.7653 days), Mm (27.5546 days), semi-annual (182.62 days), and annual (362.26 days) [36, 282]. The residual term represents the sum of the random noise and spatially correlated fluctuations, known as common mode error (CME). For estimating the unknown set of parameters (x_0, v_0, c_k, A_k, and B_k) associated to each data segment, the least-squares regression model is incorporated based on the concept of minimizing the variance of residuals.

Traditionally, Equation 3.7 has been widely adopted in the coseismic deformation analysis because this is very straightforward way to decompose secular tectonic motion and seasonal signals along with coseismic signals. However, the estimated results from this equation may be significantly biased in the presence of pre and postseismic signals, offsets and colored noise content, and low signal-to-noise ratio [36, 156, 232, 281]. Nevertheless, despite some limitations in the coseismic study, this equation provides some insights to the relation of spatio-temporal variations in the GPS data and estimated results may be quite useful for further analysis. In view of this, in the present work, each time series is fitted in Equation 3.7 and the associated parameters are estimated. Since the present study is related to coseismic deformation, trend and seasonal signals are subtracted from the associated time series. As a result, the refined time series consists of earthquake-induced jump signals and unmodeled residual. The refined time series will be the basis of the EOF analysis as discussed in the following section.

3.4.2 The EOF analysis

For the EOF method implementation, the refined time series of each of the three components (East, North, and Up) of the 127 CGPS sites is used. Just to recall, the implementation has three broader steps: (i) arranging the time series data into an observation matrix, (ii) decomposing the observation matrix using the numerical decomposition techniques, and (iii) selecting the appropriate EOF modes according to the purpose. These EOF modes essentially lead to interpret the inherent information about the physical process. The whole mathematical formulation of the EOF method had been described in Chapter 2.

Considering the above-mentioned steps for the EOF implementation, the position time series of each site is arranged in a space-time observation matrix $X_{(p\times n)}$, where p^{th} row denotes the position map series at n^{th} time epoch. The observation matrix is then decomposed through the singular value decomposition (SVD) method and defined as follows:

$$X_{(p\times n)} = \sum T_k(t) D_k(\lambda) S_k(x) \tag{3.8}$$

Here, $S_k(x)$ shows the spatial pattern, $T_k(t)$ represents the time history corresponding to the particular spatial pattern (combinedly known as "EOF mode"), and $D_k(\lambda)$ denotes the percentage variance that determines how much information of the original dataset is contained in the given mode. The EOF modes are consequently normalized with respect to the root mean square (RMS) value by dividing and multiplying the RMS value to the spatial and temporal patterns, respectively. This step essentially transfers the magnitude information of eigenvectors into associated time series [132]. The unit of RMS value is the same as the data, that is millimeters (mm). Usually, in the coseismic analysis, the two principal EOF modes are sufficient to capture the maximum dominant variation (coseismic, preseismic, postseismic, and CME) of the data set [35, 36]. Therefore, in the present coseismic analysis associated with the Kaikoura earthquake, the first two EOF modes are considered and subsequently interpreted in terms of physical processes.

3.5 Results

In order to analyze the coseismic deformation throughout New Zealand caused by the Kaikoura earthquake, the EOF analysis is performed on three different data segments (hereafter referred to as test period A, test period B, and test period C) of the CGPS data. The test period A contains the time series of 15 days (November 6–20, 2016) to investigate the synoptic view of surface deformation associated with the Kaikoura earthquake, whereas the test period B consist of the position data of 7 days (November 13–20, 2016) in order to analyze the distribution of early

postseismic relaxation in New Zealand. Each time series contains the position value at every 30 min epoch. In period C, the daily time series of 51 days (25 days before-and-after the Kaikoura earthquake) from October 20 to December 10, 2016 is utilized for coseismic deformation analysis in order to identify the effectiveness of the EOF technique. The extracted EOF modes from these data segments not only provide the dominant coseismic/postseismic deformation pattern but also enables to link the regional earthquake cycle with the observable pattern. It is observed that the first two modes are significantly sufficient for the present analysis. Subsequently, the selected modes are the basis of the EOF-based coseismic strain estimation. Overall, the EOF-based results include the spatial and temporal patterns related to the coseismic deformation as well as subsequent postseismic deformation and the coseismic strain field associated with the Kaikoura earthquake. In addition, a comparative study of the coseismic dislocation field derived from the EOF method and the LSE method is carried out. The results are provided in the following sub-sections.

3.5.1 EOF solutions for the test period A (November 6−20, 2016)

The results from the EOF analysis during the test period A are shown in Fig. 3.4 and Fig. 3.5 in terms of EOF mode 1 and EOF mode 2. Each EOF mode consists of three vector components as East (E), North (N), and Up (U). The EOF mode 1 accounts for 74%, 77%, and 52% of the total variance in the east, north, and up directions, respectively, whereas the EOF mode 2 captures 14%, 18%, and 27% of seismic signals correspond to East, North, and Up components, respectively. The third and higher modes are not shown as they account for less than 5% of the data variance.

As illustrated in Fig. 3.4, the EOF mode 1 corresponding to the North and Up components show dominant coseismic signals caused by the Kaikoura event. More specifically, the EOF mode 1 associated with the North component indicates the northward motion of central New Zealand, particularly along the northeastern part of the Canterbury region, with an amplitude of about 200 mm. At the same time, a slight southward motion is identified across the Marlborough fault system. For the Up component, the EOF mode 1 reveals a recognizable coastal uplift with an amplitude of 150 mm near the epicenteral area. In addition, for the far-field observations, the spatial pattern of Up component is quite noisy, probably due to higher random noises (e.g., CME) in the GPS observations. The EOF mode 1 corresponding to the East component reveals the dominant postseismic relaxation signals (Fig. 3.4). The associated temporal pattern shows the logarithmic behavior in the time series, whereas the spatial pattern indicates slow decay with the similar motion tendency of the coseismic pattern (see EOF mode 2 for the East component in Fig. 3.5).

In general, the EOF mode 2 contains deformation signals related to the postseismic relaxation or spatially correlated common mode error. However, in the present study, the EOF mode 2 corresponding to the East component shows clear coseismic dislocation signals with an amplitude of about 150 mm (Fig. 3.5). This mode reveals the recognizable eastward motion of the whole of central New Zealand and it gradually decreases towards the western boundary along the Marlborough fault system. Consequently, it indicates the relatively small coseismic displacement of the GPS sites throughout the Marlborough fault system. For the North component, the temporal pattern exhibits quasi-logarithmic behavior, indicating the postseismic relaxation in the north direction. In addition, an apparent behavior is noticed in the temporal pattern, probably due to a discernible signal associated with aftershock having a magnitude M_w6.4. In the Up component, the EOF mode does not carry any significant signal related to mainshock, aftershocks or random noises. However, this EOF mode may contain mixed signals as a combination of the CME, aseismic, and non-seismic signals in the associated time series. Overall, the EOF mode 2 conceivably contains important information linking the postseismic deformation with the underlying physical system around the epicentral area.

From the EOF mode 1 (Fig. 3.4) and EOF mode 2 (Fig. 3.5), it is clearly observed that the coseismic deformation caused by the Kaikoura earthquake has occurred along the Marlborough fault system and the North Canterbury region. The coseismic dislocation field is broadly stretched from the central South Island to the southern North Island with a northeast strike along the coastal boundary. The present EOF-based results are also consistent with several coseismic studies of the Kaikoura earthquake, such as Hamling et al. (2017) [89], Jiang et al. (2018) [114], Shi et al. (2017) [232], and Su et al. (2020) [243]. In summary, the Kaikoura earthquake has caused significant coseismic and postseismic deformation in the central New Zealand.

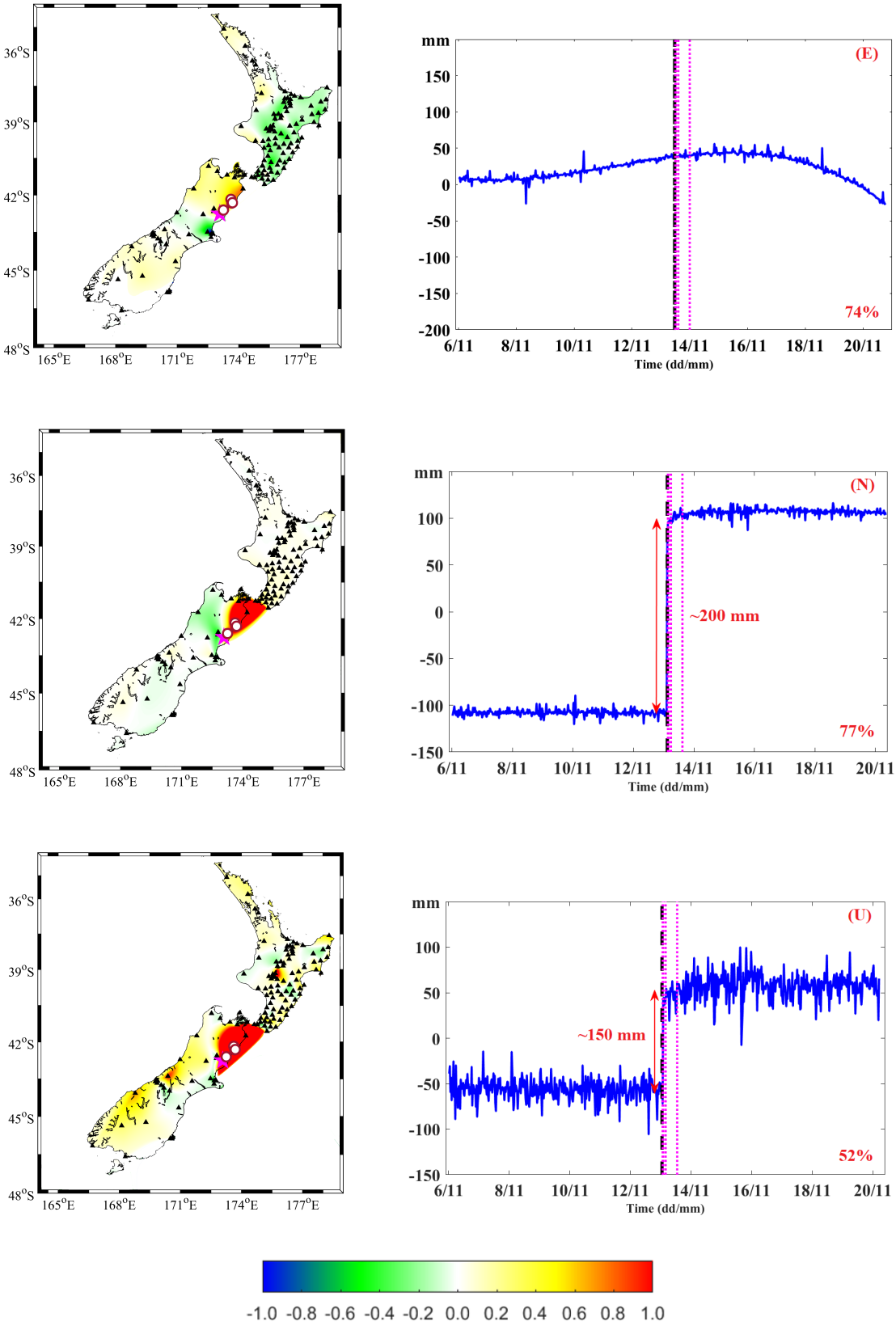

Fig. 3.4: The first EOF mode during the test period A corresponding to each of the three components (East (E), North (N), and Up (U)) is shown here. The left column shows the spatial pattern and the right column represents the associated temporal mode. The explained variations by the EOF mode 1 in the E, N, and U directions are also mentioned in the lower right corner of the right column. The pink star shows the location of the Kaikoura earthquake and the red circles filled with white color denote the epicenters of aftershocks.

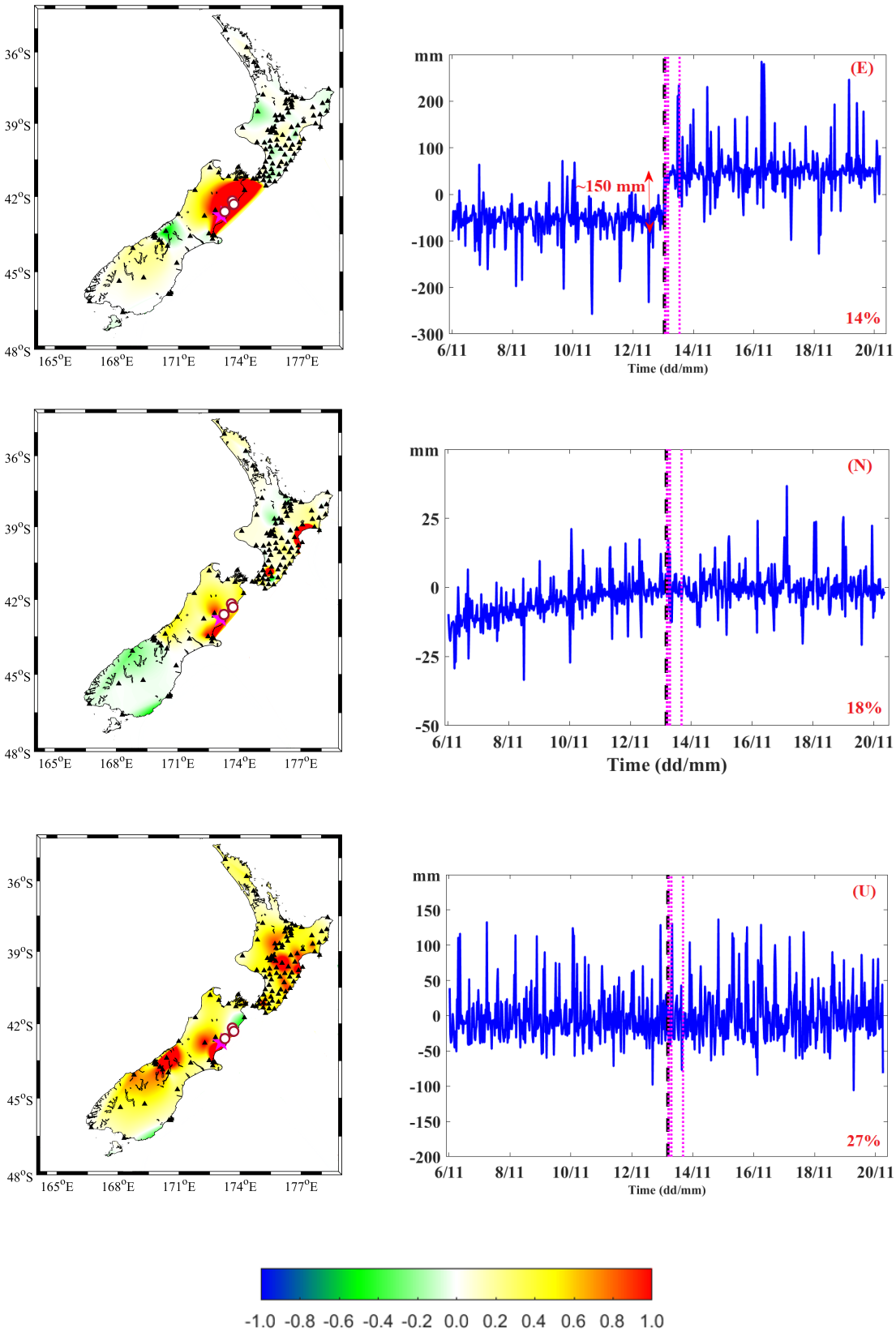

Fig. 3.5: The second EOF mode during the test period A corresponding to each of the three components (East (E), North (N), and Up (U)) is shown here. The left column shows the spatial pattern and the right column represents the associated temporal mode. The explained variations by the EOF mode 2 in the E, N, and U directions are also mentioned in the lower right corner of the right column. The pink star shows the location of the Kaikoura earthquake and the red circles filled with white color denote the epicenters of aftershocks.

3.5.2 EOF solutions for the test period B (November 13−20, 2016)

The EOF solutions derived from the test period B are shown in Fig. 3.6. The EOF mode 1 corresponding to the East, North, and the Up components explain 83%, 43%, and 45% of the total variance. For the test period B, the first EOF mode is relevant to the postseismic deformation pattern, whereas the second and higher EOF modes do not contain any specific information related to the postseismic or common mode error. Thus, the significance of the second and higher modes is negligible. In Fig. 3.6, the East component shows notable postseismic relaxation pattern in the eastward direction and the associated temporal growth follows a quasi-logarithmic function gradually reaching up to 50 mm. The North component indicates a minor postseismic relaxation signal in the northward direction, particularly near the epicentral area. Taken together, the entire north Canterbury region has experienced the east-north-east horizontal deformation that is stronger at the eastern shore, just like the coseismic behavior of the mainshock. The vertical component does not contain any mainshock and postseismic signals. Rather, it exhibits a quasi-unison fluctuation in most of the stations over New Zealand (almost the same color over the northern South Island and North Island) in a "breathing" motion according to the associated temporal pattern. Uniformity of the spatial pattern may appear due to the presence of CME in the CGPS observations, whereas the variation of color in the spatial pattern may indicate the aseismic, non-seismic events and random noise of the data. Overall, the postseismic horizontal deformation of the mainshock, although much smaller in magnitude, is similar to the coseismic deformation direction with a little more extensive towards the far-field sites.

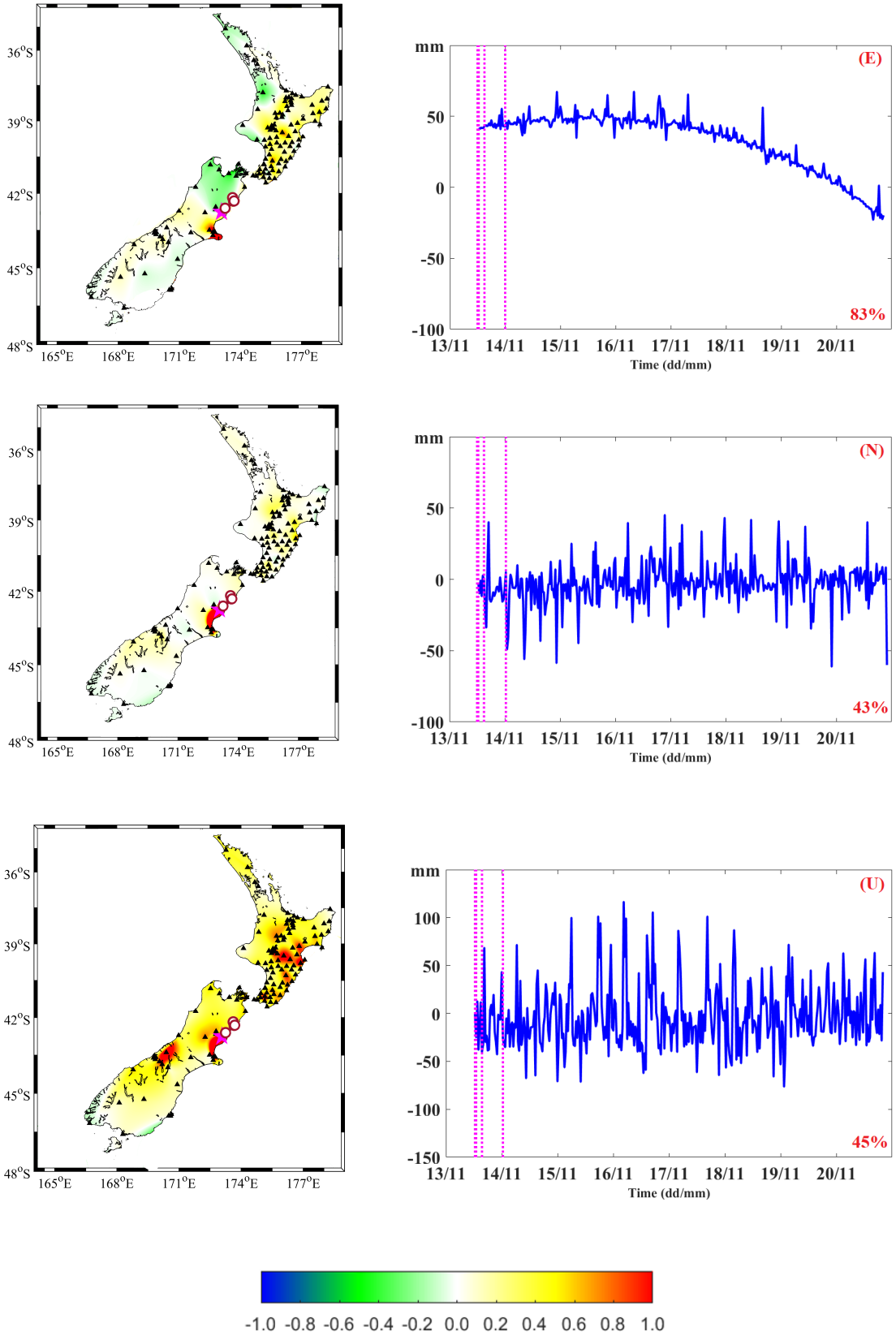

Fig. 3.6: The first EOF mode during the test period B corresponding to each of the three components (East (E), North (N), and Up (U)) is shown here. The left column shows the spatial pattern and the right column represents the associated temporal mode. The explained variations by the EOF mode 1 in the E, N, and U directions are also mentioned in the lower right corner of the right column. The pink star shows the location of the Kaikoura earthquake and the red circles filled with white color denote the epicenters of aftershocks.

3.5.3 EOF solutions for the test period C (October 20−December 10, 2016)

In order to elucidate the effective utility of the EOF method, the distribution of coseismic deformation associated with the Kaikoura earthquake is re-computed over the test period C (25 days before-and-after the Kaikoura earthquake) from October 20 to December 10, 2016. For this purpose, the daily position time series data of 94 CGPS stations is accessed by the GeoNet. After obtaining the CGPS data, the whole methodology of the EOF analysis including data preparation and the EOF implementation is repeated. The component-wise EOF modes that represent the solution field in terms of the spatial vector along with their time series are shown in Fig. 3.7. From the obtained EOF solutions, the coseismic deformation along the North, East, and Up components is approximately up to 300 mm, 200 mm, and 150 mm, respectively. The first mode captures 98–99% of the horizontal and 98% of the vertical total variance, indicating the dominance of the coseismic jump signal. For the present data set, the first EOF mode satisfactorily accounts for the maximum changeability of the coseismic signal of surface deformation, whereas the second mode represents mixed signals as the random noises and other aseismic/non-seismic signals in the GPS time series. Since the purpose of considering the data of test period C was to validate the proficiency of the EOF method in the presence of the preseismic signals, postseismic relaxation signals and the CME in the given time series, the only first principal EOF modes are utilized for interpretation. It is observed that the first EOF mode corresponding to horizontal (North and East) and vertical (Up) components has unequivocally captured the three-dimensional deformation pattern. The EOF modes corresponding to the horizontal components indicate that the central South Island motion is in the northeastward direction caused by the mainshock. In addition, the vertical component shows positive coseismic jump that suggests overall deformation in the up direction (uplift). The EOF solutions derived from the data of the test period A and the test period C suggest that coseismic deformation is quite similar in both cases. Consequently, it appears that the EOF method potentially preserves the earthquake-induced displacement information in the presence of other signals, such as preseismic signals, postseismic signals, aseismic and non-seismic events, and random noise.

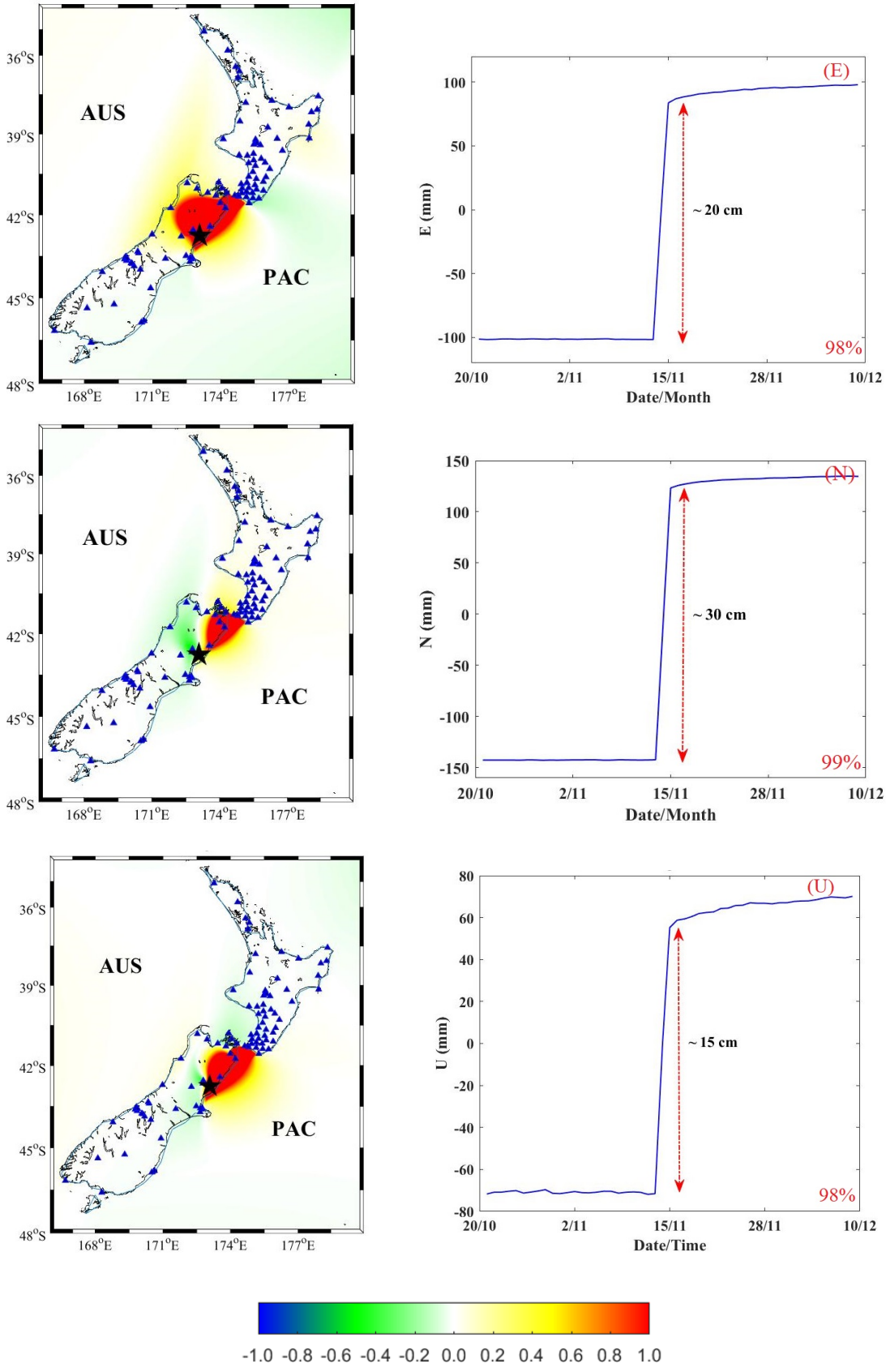

Fig. 3.7: The first EOF mode during the test period C corresponding to each of the three components (East (E), North (N), and Up (U)) is shown here. The black star shows the location of the Kaikoura earthquake.

3.5.4 Synoptic coseismic strain distribution associated with the 2016 Kaikoura earthquake

Quantifying the coseismic strain field associated with an earthquake is one of the important ways for understanding the crustal response during the earthquake. The coseismic strain field not only characterizes the earthquake rupture mechanism but also exhibits an instantaneous relationship between the seismic source and the underlying geological structure [35]. In order to get further insights into a synoptic spatio-temporal scenario of surface deformation caused by the Kaikoura earthquake, in the present analysis, the coseismic strain field estimation is carried out.

In order to estimate the coseismic strain pattern, EOF solutions will be used as an input for estimating the strain rates. The leading EOF mode, which contains the coseismic displacement signals corresponding to East and North components, is considered as an input for strain rate calculation. For the present analysis, the EOF mode 1 corresponding to the North component and the EOF mode 2 corresponding the East component during the test period A are utilized as horizontal velocity gradients. The velocity gradients are then linearly interpolated into (0.25×0.25) grid points to divide the study area into smaller sub-regions for strain rate calculation at a particular grid node. Further, these velocity gradients are incorporated in order to model the strain rate from the gridding method adopted by Shen et al. (1997) [229]. The mathematical expression of the strain rate model, as a continuous distance function, is given as:

$$w_i = exp\left[\frac{-s_i}{2D^2}\right] \tag{3.9}$$

Here, w_i denotes the weighting term; s_i represents the distance between the node i^{th} GPS stations and node points, and D represents the smoothness controlling factor in order to find the location of the fourth nearest GPS site in a grid to the estimating point. For the present estimation, the smoothness radius is considered to be about 200 km. A brief mathematical formulation of strain rate estimation is provided in Chapter 4.

After applying the strain estimation algorithm, the horizontal coseismic strain field is derived from the EOF solutions. As a result, Fig. 3.8 shows the distribution of areal dilatation rates and maximum shear strain rates over New Zealand. The areal dilatation strain rates depict the nature and direction of the surface deformation associated with the earthquake event. For example, the negative value indicates shortening (compression) and the positive value denotes lengthening (extension). In contrary, the maximum shear strain rates reveal the presence of the strike-slip faulting zone.

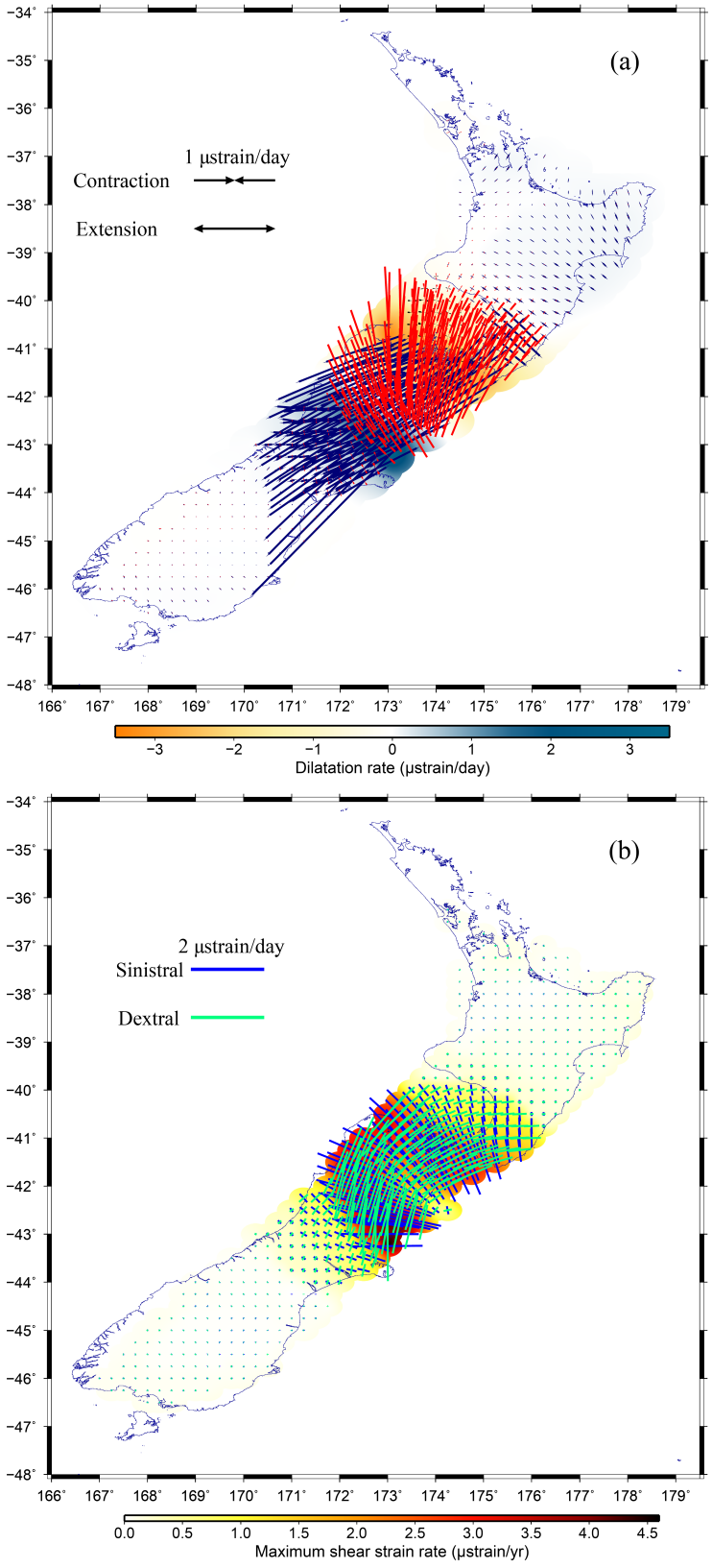

Fig. 3.8: Coseismic horizontal strain field over New Zealand: (a) principal axes of strain rates and (b) maximum shear strain rates.

In Fig. 3.8, the retrieved areal dilatation strain pattern suggests the followings: (1) the large-scale extensional pattern is observed in the northern Canterbury region near the epicentral area and it gradually decreases towards the Marlborough fault system and Alpine fault; (2) compressional pattern concentric with respect to the mainshock is noticed near the uppermost South Island and lower North Island; (3) the far-field region undergoes next-to-none deformation indicating lessly affected by the mainshock, and (4) the maximum value of extension has reached about 3.5 μstrain/day, whereas the maximum compression measure is about -3.2 μstrain/day. In a similar way, the maximum shear strain field (Fig. 3.8) indicates that (1) the deformation associated with the mainshock exhibits a radial SW-NE trending pattern; (2) a large fraction of shear strain mainly in near-field (central South Island) indicates the contribution of strike-slip faults of this region, and (3) the maximum shear rate is obtained 4.5 μstrain/day in the epicentral zone. For the validation of the EOF-based strain field, the retrieved coseismic strain patterns are compared with the horizontal coseismic stress changes studied by Hui-Hong et al. (2018) [110]. They observed the extensional normal stress with the NE strike mainly near the seismic faults and the large compressional stress at the two ends of the seismic faults. In addition, shear stress changes indicate the right-lateral slip of the south-north faults and left-lateral slip of the east-west faults. Thus, the strain pattern and stress changes caused by the Kaikoura earthquake are consistent in terms of the deformation direction. The presented coseismic strain analysis suggests that the horizontal strain deformation pattern in the north Canterbury region is lined up in such a way that dilatation rates and maximum shear strain rates are largely radial and concentric with respect to the epicenter of the Kaikoura earthquake. Moreover, a similar pattern is also observed in the EOF modes (Fig. 3.4 and Fig. 3.7) and EOF-based coseismic dislocation field (Fig. 3.9).

3.5.5 Comparison of the EOF-based and LSE-based coseismic dislocation fields associated with the Kaikoura earthquake

In general, a conventional straightforward way to estimate the coseismic "jump" dislocation is by fitting a step function to each CGPS time series independently using the LSE method. In order to validate the effectiveness of the EOF method in comparison to the traditional LSE method, the LSE algorithm is implemented to estimate the coseismic signals over the test period C (time series of 25-days before-and-after the Kaikoura earthquake). The horizontal and vertical coseismic dislocation fields derived from the EOF method and the LSE technique are pictorially presented in Fig. 3.9, whereas the estimated EOF and LSE coseismic jumps are tabulated in Appendix 6.4.

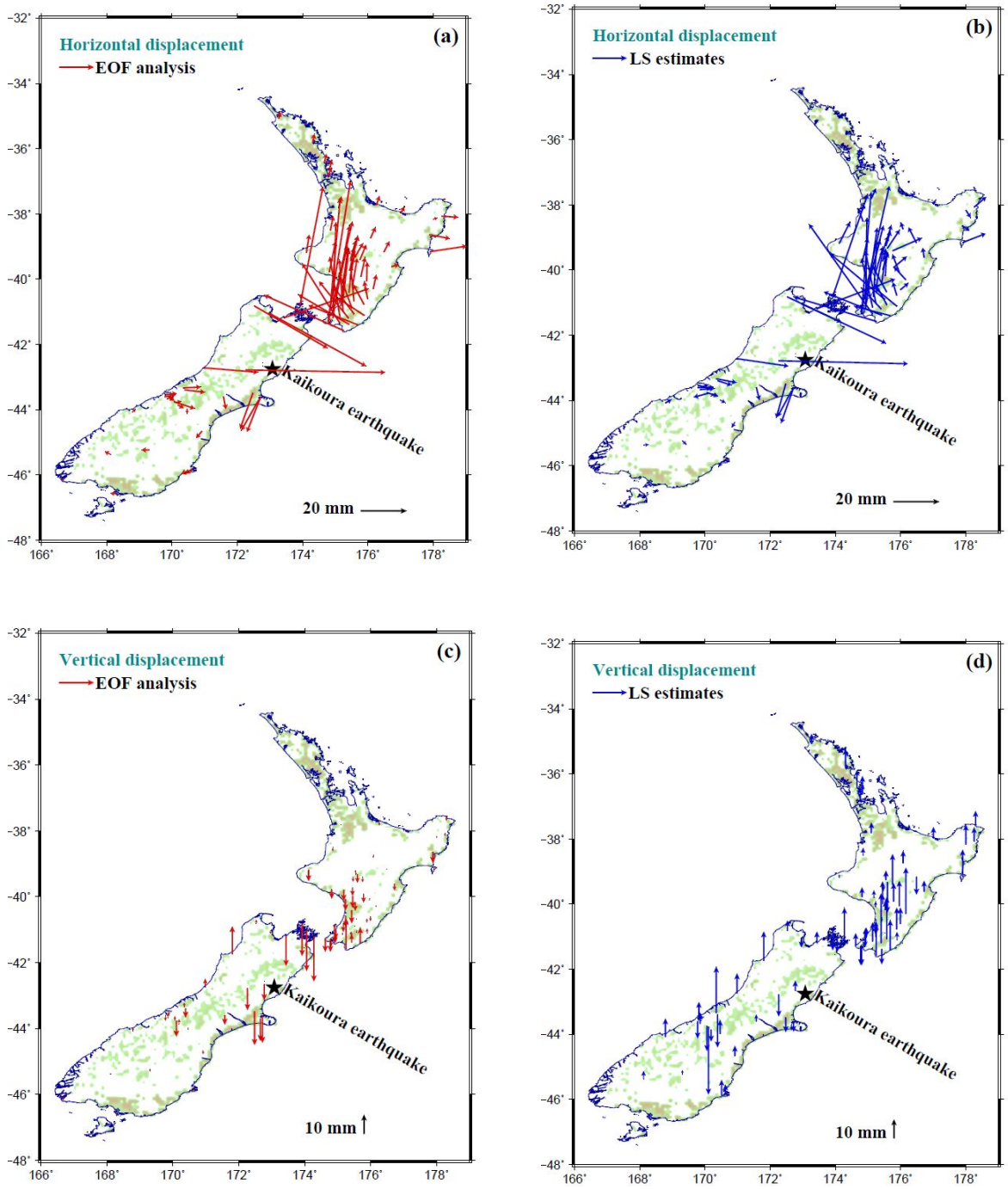

Fig. 3.9: Comparison of the coseismic dislocation field associated with the 2016 Kaikoura earthquake: (a) horizontal coseismic displacement pattern estimated through EOF, (b) horizontal coseismic displacement pattern estimated through the conventional LSE, (c) vertical coseismic displacement field derived through the EOF method, and (d) vertical coseismic displacement field derived through the LSE method. The red and blue arrows indicate the coseismic jumps through EOF and LSE, respectively. The black star indicates the epicenter of the Kaikoura earthquake.

The horizontal coseismic displacement field (Fig. 3.9) shows that the estimated horizontal patterns through both methods agree for the near field observations, whereas the LS estimates begin to "loosen" pattern (distorted pattern) and show notable discrepancies for the far-field observations (see near the southern part of the North Island in Fig. 3.9). Similarly, from the vertical coseismic displacement field (Fig. 3.9), it is observed that the EOF-derived coseismic jumps are more reliable in comparison to the conventional LSE method. The above mismatch in the coseismic vertical signals may have occurred due to the presence of common mode error and/or small fraction of signal-to-noise ratio [35, 281]. The studied EOF-derived coseismic estimates for the horizontal and vertical components are observed to closely agree with the previous findings (e.g., Hamling et al. 2017 [89]; Su et al. 2020 [243]). Thus, the EOF solutions provide an effective form of GPS observation suitable for the input data for further analysis, such as joint inversion schemes and coseismic deformation modeling.

3.6 Summary

As a distinct phase of the earthquake deformation cycle, the coseismic phase plays an important role. It not only helps to understand the earthquake mechanism but also provides valuable input for assessing the seismic hazard of a given region. Therefore, a reliable quantification of the coseismic deformation analysis is the need of the hour. The present chapter has demonstrated the effective utility of the spatio-temporal EOF method in order to investigate the coseismic deformation analysis associated with the 2016 Kaikoura earthquake. For this, three different segments of geodetic observations are used for the EOF analysis. (i) The test period A (November 6–20, 2016) is considered to quantify the elaborated view of coseismic deformation; (ii) test period B (November 13–20, 2016) is incorporated to investigate the early postseismic deformation associated to the mainshock, and (iii) the test period C (October 20–December 10, 2016) is used to validate the efficacy of the EOF method. The leading EOF modes have been used an input to model the coseismic strain field. To highlight the strength of the EOF method, a comparison test is carried out between the EOF-based displacement vectors and the LSE-based dislocation estimates. From the obtained results, several observations are noted as summarised below.

1. The derived EOF modes indicate that central South Island propagates in the east direction with amplitude of 150 mm, and in the north direction with amplitude of 200 mm. In addition, the hypocentral area (north Canturbury region) uplifts about 150 mm along the offshore boundary. Therefore, the horizontal coseismic deformation associated with the Kaikoura event is observed in the northeast direction.

2. The postseismic relaxation resembles to the coseismic pattern along with a SW-NE extension from the central South Island to the North Island.

3. There is minimal to no deformation in the far-field regions, indicating that these regions were hardly affected by the 2016 Kaikoura earthquake.

4. The emanated results derived from the EOF analysis are broadly consistent with several previous coseismic studies of the Kaikoura earthquake, such as Hamling et al. (2017) [89], Jiang et al. (2018) [113], Clark et al. (2018) [40], and Su et al. (2020) [243].

5. The horizontal coseismic strain patterns (dilatation and shear) associated with the Kaikoura earthquake reveal a large-scale extensional behavior in the northern Canterbury region and compressional concentric pattern near the uppermost South Island and lower North Island, along with a radial SW-NE shear pattern.

6. The maximum value of the lengthening (extension), shortening (compressional), and shear strain rates are 3.5 μstrain/day, $-$ 3.2 μstrain/day, and 4.5 μstrain/day, respectively.

7. The EOF-based coseismic jumps are significantly adequate in contrast to the LSE-based estimates even in the presence of the preseismic signal, postseismic signal, CME, or other noises in the given time series.

In summary, the present chapter has focused on the coseismic deformation analysis of the 2016 Kaikoura earthquake using the EOF method. It also highlights the potential of the EOF method in terms of its capability to decompose the coherent space-time data into individual modes and to extract the additional dominant information, such as postseismic relaxation or CME. Therefore, the EOF-based results not only offer the distribution of coseismic deformation caused by the earthquake but also provide significant information related to the coseismic phase of the earthquake cycle.

The present chapter has demonstrated the effective utility of the data-driven EOF method to quantify the coseismic deformation caused by the 2016 Kaikoura earthquake in New Zealand. After analyzing the coseismic phase of the earthquake deformation cycle, the successive task is to re-compute the earthquake potential associated with the contemporary earthquake cycle in New Zealand. In light of this, the next two chapters, namely Chapter 4 and Chapter 5, will focus on the quantification of the earthquake hazard caused by the regional earthquake cycle in New Zealand using geodesy-based and statistics-based spatio-temporal techniques.

Chapter 4

Spatial Distribution of Contemporary Earthquake Potential in New Zealand from Seismic Moment Budget Estimation

"*We cannot stop natural disasters but we can arm ourselves with knowledge: so many lives wouldn't have to be lost if there was enough disaster preparedness.*"

by Petra Nemcova

Among the three phases of earthquake cycle, the concentration is often given to the interseismic phase due to its close relevance to the earthquake hazard estimation of a given region. After a comprehensive coseismic deformation analysis of the 2016 Kaikoura earthquake in the previous chapter, the successive task is to re-evaluate the present-day crustal deformation caused by the contemporary earthquake cycle and re-assess seismic hazard in New Zealand and its surrounding regions. For this purpose, two state-of-the-art data-driven approaches, namely the seismic budget estimating method (Chapter 4) and the area-based earthquake nowcasting method (Chapter 5) are utilized. The present chapter, Chapter 4, deals with the seismic budget estimating method based on two key ideas, namely geodetic moment rate accumulation and seismic moment rate release, to quantify the spatial distribution of contemporary earthquake potential in New Zealand. In the following chapter, Chapter 5, a statistics-based analysis of the natural times (interevent counts of small earthquakes in the two successive large earthquakes) will be carried out to compute the current progression of the seismic cycle in terms of earthquake potential score. The emanated results from both methods may be combined and corroborated to highlight the regions of high seismic hazard in New Zealand. The overall content of this chapter (Chapter 4) is presented below.

Contents

4.1 Introduction

Knowledge of how the continental or oceanic crust accumulates and releases strain in active regions is crucial for a better understanding of the underlying physical system. The accumulated energy of hundreds of years may be released in terms of an earthquake within a few seconds. Therefore, due to the chaotic behavior of observed seismicity and associated tectonic configuration, it is important to understand the spatial distribution of contemporary seismic moment budget in a large region. In this regard, several geodetic, geological, seismological, and statistical techniques have been carried out worldwide to estimate earthquake hazard potential [19, 185, 227, 237]. Although these methods may require many assumptions and approximations, the derived results provide new insights for the present-day deformation pattern in terms of fault kinematics, maximum possible earthquake and associated location, earthquake recurrence interval, moment deficit rate, and the current state of the ongoing earthquake cycle [162, 172, 227, 241]. Particularly, in time-dependent seismic hazard analysis, the discrepancy between geodetic moment accumulation and seismic moment release over a given region is one of the key parameters to quantify the areas of high seismic potential [39, 172]. Such an approach has been widely implemented in several active regions, including China, Egypt, Europe, Greece, Himalaya, Taiwan, and Tibet [39, 108, 152, 172, 205, 224, 227]. The associated results in terms of earthquake potential maps bear important inputs for numerous end-user applications, such as revising the building codes, societal risk assessment, infrastructure planning, and seismic awareness programs. In light of the above, the present chapter aims to provide the spatial distribution of contemporary earthquake potential along 14 continuous zones over New Zealand.

New Zealand is a well-documented example, where the tectonic plate boundaries are linked through the subduction-transpressional-subduction configuration [105]. The ongoing tectonic setup in New Zealand has caused the occurrence of many strong to great earthquakes that have resulted in hundreds of thousands of casualties in the past. Some notable earthquakes in New Zealand include the giant Wairarapa earthquake (1855, M_w8.2), Hawke's Bay earthquake (1931, M_w7.3), Edgecumbe earthquake (1987, M_w6.5), Darfield and Christchurch earthquake ($2010-11$, M_w7.1, M_w6.2), and the most recent Kaikoura earthquake (2016, M_w7.8) [89, 240].

In order to analyze the earthquake process, several studies have been carried out to elucidate the notable earthquake characteristics in New Zealand by considering the tectonic deformation features, such as velocity field, strain pattern, maximum magnitude and its associated location, and earthquake recurrence interval [20, 21, 30, 50, 84, 86, 105, 162, 203, 240, 241]. For instance, Beavan et al. (2001) [20] derived the horizontal velocity field and consequently converted it into strain pattern to provide the block-wise deforming style in New Zealand. Barnes et al. (2002) [15] found that the potential moment magnitude (M_w) is up to

$7.6-8.0$ for the future event that may rupture the surface of the Hawke's Bay region in the eastern New Zealand along the Hikurangi subduction margin. Sutherland et al. (2006) [244] analyzed the pattern of seismicity and geodetic strain of the whole Alpine segment and found that it is locked above a depth of $6-12$ km. In addition, their estimated results inferred that large earthquakes ($M_w > 7.0$) on the Alpine fault will almost certainly occur in future, and it is realistic to expect one or more great earthquakes ($M_w \geq 8.0$) in this region. Nodder et al. (2007) [164] carried out earthquake source parametrization in the southern North Island. They have suggested that though the Kapiti-Manawatu fault system is capable of hosting strong to large moment magnitude earthquakes, seismic hazard of this region remains "low" probably due to the long recurrence interval ($>$ 5000 years). Wallace et al. (2007) [267] estimated tectonic motion budget across the South Island in New Zealand using geodetic data, earthquake history, and geological data. The obtained results, through the "balances" kinematic model, accounts for the deformation pattern in the South Island, that may have caused due to the tectonic motion of the Pacific plate and the Australian plate. Stirling et al. (2002) [241] developed a seismic hazard model for New Zealand, popularly known as the New Seismic Hazard Model (NSHM). The NSHM provides the information of earthquake recurrence behavior associated with its location throughout New Zealand. The model incorporates new attenuation relationship for peak ground acceleration and spectral acceleration. Robinson and Davies (2013) [204] reviewed several characteristics of the Alpine fault and found that it is close to its earthquake recurrence interval. They have suggested that the Alpine fault may host large to major earthquake in near future. Their study has mentioned that the expected magnitude of this future event is $M_w 8.0$ or greater associated with 85% probability and the potential location is in the central segment of the Alpine fault. Nicol and Dissen (2018) [163] studied the Wairau fault using 6000 years paleoearthquake data and found that it has the potential of future surface rupture. Barnes et al. (2019) [16] investigated the structure and earthquake hazard potential in the capital of New Zealand, namely Wellington city, caused by the Aotea and Evans Bay faults. Considering the 2016 Kaikoura earthquake as a harbinger for future seismic events, Hatem et al. (2019) [93] identified the patterns of earthquake occurrence in central New Zealand incorporating 2000 years of paleoearthquake records. The above-mentioned studies suggest heterogeneous earthquake potential in New Zealand, with a higher potential along the Alpine fault and around two subduction interfaces, namely the Hikurangi interface and the Puysuger interface.

In order to re-assess the seismic potential in New Zealand, the most updated geodetic observations and earthquake data are incorporated. The earthquake data provides the pattern of released energy, whereas the geodetic data reveals the distribution of accumulated energy in the study region. For the present study, $\sim$ 180 years ($1840-2021$) of earthquake data and $\sim$ 180 CGPS velocities of New Zealand are obtained. In addition, the whole seismogenic area is

segmented into 14 seismic source zones. For each zone, seismic moment rate and geodetic moment rate are calculated from earthquake data and geodetic observations, respectively. Using the geodetic and seismic moment rates of a specific zone, the moment rate ratio and moment deficit rate are derived. The moment rate ratio and moment deficit rate are collectively used to characterize present-day earthquake potential of a given zone. A step-by-step procedure of the entire methodology is provided in the following sections.

4.2 Seismotectonic background

The study region comprises the North Island and the South Island, along with some parts of the Hikurangi subduction zone and the Fiordland subduction interface. The tectonic activities in the North Island are dominated due to the Hikurangi plateau subduction interface (part of the Pacific Plate) and the Taupo volcanic zone (TVZ) [267]. In contrary, the Alpine fault with four strike-slip faults —the Awatere fault, Clarence fault, Hope fault, and the Wairau fault —as well as the Puysegur subduction zone account for the majority of the active tectonic motion in the South Island [259]. It is observed that about 75% of total tectonic motion between the Australian plate and the Pacific plate is accommodated by the Alpine fault [12, 42, 165, 245].

The transition from subduction-to-strike-slip-to-subduction is largely a consequence of strain accumulation in the North Island and the South Island [105]. The accumulated strain may be released through major ($M_w 7.0-7.9$) to great ($M_w \geq 8.0$) earthquakes [245]. For instance, due to the ongoing tectonic activity, the accumulated strain in the North Island has been released in two large sized earthquakes, namely the 1855 Wairarapa earthquake and the 1931 Hawke's Bay earthquake, whereas the South Island has experienced the $2010-2011$ Canterbury earthquake sequence and the most recent 2016 Kaikoura earthquake. Consequently, these events lead to a large amount of destruction, causing significant damages to buildings and loss of human lives. Moreover, the rapid growth of urban population and infrastructure development in New Zealand has increased the potential of catastrophic damage in future earthquakes. As a consequence, how to reasonably estimate the spatial distribution of seismic hazard in New Zealand is an important issue, especially in the high seismically active regions. Therefore, the ensemble information from the accumulated geodetic moment and released seismic moment are incorporated in this chapter to quantify zone-wise earthquake potential in New Zealand.

4.3 Data

In order to carry out a reliable quantification of earthquake hazard potential in New Zealand, two types of data have been utilized: geodetic data and earthquake data. The geodetic data

provides a measure of surface deformation and underlying fault kinematics, whereas the earthquake data provides the hypocentral information from catalog, the location of initial slip, the magnitude of the eventual earthquake, and the origin time [185].

4.3.1 Geodetic data

In the present analysis, the continuous global positioning system (CGPS) observations of New Zealand are incorporated. These CGPS stations are maintained and archived by the GNS Science (Institute of Geological and Nuclear Sciences Limited, New Zealand; http://www.gns.cri.nz.). Continuous daily GPS raw observations are routinely collected and processed by Nevada geodetic laboratory (NGL), University of Nevada, Reno (http://geodesy.unr.edu/; [28]), through GipsyX software (version 1.0). The seasonal and ocean tide loading effects have been incorporated in data processing. The final solutions of time series for each component (i.e., East, North, and Up) and formal uncertainties are provided in the International Terrestrial Reference Frame (ITRF2014) as well as in the regional reference frame, namely the Australian reference frame. The NGL also provides the velocity measures, estimated robustly using the median interannual difference adjusted for skewness (MIDAS) technique [28]. It is a median-based GPS station velocity estimator that is insensitive to outliers, seasonality, step functions (abrupt changes) arising from earthquakes or equipment changes, and statistical data variability [28]. Based on the reliable estimation of velocity data by MIDAS [29], $\sim$ 180 CGPS stations' velocity data are obtained. The velocity data was last accessed in December 2021 from the NGL. The final horizontal velocity field (in the Australian reference frame) lies in the range of $0.2-46$ mm/yr, along with the uncertainty values lying in the range of $0-3$ mm/yr. The MIDAS velocity estimates of all stations are listed in Table 4.1, whereas the spatial coverage of the CGPS stations over New Zealand is presented in Fig. 4.1. The velocity field is further utilized as an input for the strain estimation over New Zealand as described at a later section.

Table 4.1: MIDAS velocity estimates of CGPS stations in New Zealand.

Site	Longitude (°E)	Latitude (°N)	East(E) (mm/yr)	North(N) (mm/yr)	Up(U) (mm/yr)	$\sigma(E)$ (mm/yr)	$\sigma(N)$ (mm/yr)	$\sigma(U)$ (mm/yr)
AHTI	178.05	−38.41	−0.38	−18.76	0.00	0.57	0.39	0.70
AKTO	176.46	−40.54	−25.55	−11.94	−5.22	0.42	0.31	0.66
ANAU	178.29	−38.27	0.27	−19.96	−1.90	0.49	0.42	0.78
ARTA	176.14	−38.62	−0.56	−3.17	−8.19	0.49	0.51	0.91
AUCK	174.83	−36.60	−0.05	−1.10	−1.11	0.17	0.17	0.49
AUKT	174.77	−36.84	−0.65	−0.83	−1.40	0.24	0.24	0.66
AVLN	174.93	−41.20	−22.66	−6.04	−1.76	0.51	0.43	0.79

BHST	176.06	−39.49	−3.43	−7.99	−1.21	0.49	0.41	0.80
BIRF	176.25	−40.68	−26.87	−9.61	−5.67	0.33	0.33	0.61
BLUF	168.29	−46.59	−27.79	−13.67	−1.06	0.23	0.19	0.49
BM8A	172.73	−43.56	−27.72	−13.89	−7.98	2.31	2.04	2.88
BNET	170.19	−43.86	−25.22	−11.56	2.20	0.27	0.25	0.83
BTH1	175.14	−41.34	−30.06	−8.15	−4.18	0.48	0.48	1.19
CKID	177.08	−39.66	−5.95	−17.06	0.15	1.05	0.56	0.85
CLIM	175.15	−41.15	−24.17	−7.34	−2.43	0.44	0.42	0.85
CLRR	173.82	−42.15	−13.78	−18.24	−6.86	1.11	0.57	1.11
CLSK	172.75	−43.57	−33.30	−12.14	−2.12	0.88	0.76	2.47
CMBL	174.21	−41.75	−23.09	−7.47	1.55	0.49	0.38	0.85
CNCL	169.86	−43.67	−16.76	−6.21	3.06	0.21	0.19	0.58
CNST	178.21	−38.49	−4.04	−18.38	−0.83	0.97	0.37	0.63
CORM	175.75	−36.87	0.75	−0.60	−0.29	0.22	0.21	0.65
CSTP	176.20	−40.91	−28.62	−9.95	−4.67	0.32	0.29	0.75
DNVK	176.17	−40.30	−18.81	−9.03	−4.95	0.42	0.32	0.74
DUND	170.60	−45.88	−32.56	30.76	−1.58	0.20	0.21	0.50
DUNT	170.63	−45.81	−32.68	30.92	−0.95	0.23	0.24	0.55
DURV	173.92	−40.80	−9.77	−0.44	−1.81	0.39	0.28	0.63
FRTN	177.41	−38.94	−1.11	−17.76	−2.10	0.75	0.45	0.79
GISB	177.89	−38.64	−5.43	−16.15	−2.27	0.57	0.34	0.73
GLDB	172.53	−40.83	−2.46	−0.22	−1.51	0.34	0.27	0.65
GNBK	175.24	−40.08	−11.60	−4.92	−3.26	0.31	0.40	0.73
GRNG	175.46	−39.98	−10.74	−4.96	−1.57	0.30	0.42	0.65
GUNR	170.39	−43.39	−5.86	−15.47	−6.95	0.49	0.43	1.21
HAAS	168.79	−44.07	−12.79	−4.03	0.91	0.24	0.31	0.55
HAMT	175.11	−37.81	−0.88	−0.70	−0.81	0.24	0.21	0.62
HANA	177.57	−38.69	−0.08	−17.17	0.22	0.75	0.48	0.75
HANM	172.79	−42.55	−4.44	−7.65	−0.14	1.18	0.50	1.26
HAST	176.73	−39.62	−7.77	−14.18	−5.65	0.61	0.33	0.67
HIKB	178.30	−37.56	4.56	−17.68	−0.56	0.29	0.26	0.62
HOKI	170.98	−42.71	−4.21	−0.90	0.11	0.22	0.20	0.59
HOLD	175.52	−40.90	−22.98	−8.39	−4.03	0.43	0.47	1.04
HORN	170.11	−43.78	−22.43	−10.28	4.60	0.35	0.26	1.04
KAHU	176.88	−39.79	−9.50	−13.26	−0.97	0.83	0.34	0.68

KAIK	173.53	−42.43	−28.98	−11.26	1.17	0.28	0.37	0.87
KAPT	174.91	−40.86	−18.22	−4.39	−5.07	0.38	0.37	0.80
KARA	169.78	−43.61	−11.91	−3.03	0.55	0.20	0.23	0.50
KARO	175.42	−40.41	0.15	0.08	−1.21	0.24	0.32	0.78
KAWK	176.42	−39.42	−3.02	−13.78	−3.45	0.55	0.36	1.03
KERE	176.37	−39.64	−8.06	−13.21	−5.37	0.69	0.40	1.16
KOKO	177.67	−39.02	−3.09	−20.33	−1.73	0.83	0.35	0.58
KTIA	173.27	−35.07	−0.62	−0.43	−1.32	0.17	0.19	0.53
KUT1	177.07	−39.17	−1.90	−15.93	−1.62	0.70	0.43	0.85
LDRZ	169.68	−45.04	−30.44	−13.44	−1.18	0.42	0.42	1.46
LEVN	175.24	−40.59	−18.60	−5.60	−5.99	0.51	0.46	0.88
LEXA	169.31	−45.23	−29.67	−13.03	−0.94	0.29	0.22	0.65
LEYL	176.94	−39.33	−2.63	−16.64	−3.27	0.84	0.37	0.88
LKTA	172.27	−42.78	−21.96	−8.72	−1.21	0.40	0.31	0.77
LOOK	173.48	−42.01	−3.96	1.32	12.83	0.70	0.68	0.93
LYTT	172.72	−43.61	−33.28	−12.55	−1.70	0.37	0.49	0.70
MAHA	173.79	−41.29	−7.61	−0.18	−1.03	0.81	0.53	0.78
MAHI	177.91	−39.15	−5.77	−20.71	0.78	1.66	0.79	0.66
MAHO	174.85	−38.51	−1.40	−0.48	−1.74	0.27	0.25	0.65
MAKO	178.13	−38.64	−10.32	−15.62	−1.02	1.07	0.33	0.72
MANG	175.57	−40.67	−22.08	−6.46	−4.26	0.69	0.49	1.07
MAST	175.58	−41.06	−26.79	−10.83	−4.53	0.28	0.24	0.72
MATW	177.53	−38.33	1.60	−16.96	−0.10	0.34	0.25	0.68
MAVL	168.12	−45.37	−28.71	−11.53	−0.56	0.34	0.24	0.71
MCNL	176.70	−39.44	−0.29	−14.43	−2.61	0.73	0.45	0.87
METH	171.58	−43.59	−30.59	−13.22	−1.94	0.30	0.29	0.79
MKNO	176.03	−39.70	−9.11	−9.38	−3.92	0.41	0.38	1.17
MNHR	176.22	−40.47	−23.87	−10.16	−6.56	0.51	0.40	1.15
MQZG	172.65	−43.70	−33.23	−11.58	−2.54	0.20	0.24	0.61
MRBL	172.78	−42.66	−17.39	−13.48	−0.69	0.75	0.46	0.94
MTBL	175.54	−40.18	−13.68	−7.18	−5.52	0.52	0.49	1.25
MTJO	170.46	−43.99	−28.01	−12.18	−0.04	0.18	0.18	0.54
MTPR	170.35	−43.34	−11.31	−2.01	2.73	0.24	0.24	0.63
MTQN	175.24	−41.00	−22.39	−5.86	−4.58	0.56	0.46	1.07
MUL1	173.41	−42.06	44.27	12.40	34.75	6.76	2.71	4.89

NETT	170.06	−43.76	−21.06	−8.97	1.93	0.73	0.47	1.01
NLSN	173.43	−41.18	−6.52	−0.30	−3.02	0.55	0.22	0.60
NMAI	176.81	−39.10	1.14	−14.78	−0.50	0.53	0.44	0.83
NPLY	174.12	−39.18	−2.18	−0.62	−2.40	0.24	0.26	0.64
NRRD	175.76	−40.39	−19.26	−6.47	−7.80	0.63	0.60	1.01
NRSW	176.20	−40.11	−17.73	−7.67	−8.85	0.40	0.42	0.93
OHIN	175.79	−39.92	−11.68	−8.28	−4.03	0.46	0.37	1.07
OKOH	174.06	−41.02	−11.31	1.53	−0.91	0.65	0.76	0.90
OPTK	177.31	−38.05	2.93	−14.81	−2.20	0.27	0.25	0.65
OROA	176.68	−40.10	−17.09	−12.73	−1.80	0.57	0.32	0.67
OTAK	175.17	−40.82	−20.11	−4.35	−4.38	0.49	0.45	0.93
OUSD	170.51	−45.87	−32.35	30.68	−0.90	0.18	0.18	0.44
PAEK	174.95	−41.02	−20.44	−4.79	−1.12	0.44	0.38	0.85
PALI	178.08	−37.89	−33.25	−9.57	−5.64	0.26	0.33	0.82
PARI	175.25	−41.57	−6.96	−19.71	−2.92	1.19	0.60	0.65
PARW	177.88	−38.92	−33.06	−9.00	−4.55	0.24	0.27	0.63
PAWA	175.43	−41.38	−15.51	−15.77	−1.41	0.70	0.40	0.71
PGKH	176.86	−40.03	−1.36	0.13	−2.65	0.34	0.44	1.35
PGNE	174.10	−39.27	−2.21	−0.67	−3.00	0.58	0.42	1.49
PILK	169.92	−43.66	−18.16	−6.60	3.52	0.27	0.24	0.62
PKNO	175.18	−39.80	−8.26	−1.80	−1.33	0.30	0.49	0.76
PNUI	176.20	−39.92	−13.98	−10.76	−7.64	0.63	0.38	1.30
PORA	176.64	−40.27	−18.68	−13.61	−3.19	0.48	0.34	0.66
PRTU	177.70	−38.81	−0.44	−17.94	0.75	1.26	0.46	0.78
PTOI	176.00	−40.60	−25.01	−9.10	−5.71	0.39	0.37	0.93
PUKE	178.26	−38.07	5.55	−18.78	0.33	0.30	0.21	0.60
PYGR	166.68	−46.17	−24.35	−12.10	0.48	0.38	0.39	0.70
QUAR	169.82	−43.53	−8.33	−2.00	0.86	0.21	0.22	0.83
RAHI	177.09	−38.92	1.47	−15.90	−0.79	0.64	0.39	0.96
RAKW	176.62	−39.75	−13.32	−12.53	−9.06	0.65	0.42	1.01
RAUM	177.68	−37.97	2.59	−16.35	0.07	0.32	0.31	0.73
RAWI	177.42	−38.50	1.93	−16.84	−0.47	0.41	0.38	0.79
RCHD	173.31	−41.48	−2.14	−2.18	1.08	1.02	0.83	2.35
RDLV	175.40	−41.19	−30.53	−9.64	−6.74	0.36	0.36	1.01
REDD	169.92	−43.70	−17.68	−5.90	4.92	1.22	0.90	2.69

RGAR	176.34	−38.56	0.40	−6.50	−3.20	0.26	0.26	0.68
RGAW	176.90	−38.00	3.74	−12.23	−0.77	0.28	0.29	0.73
RGHD	176.37	−38.09	1.72	−5.53	−2.57	0.40	0.35	1.26
RGHL	176.35	−38.25	−0.17	−5.94	−14.91	0.35	0.33	0.96
RGHR	176.29	−38.39	−0.59	−4.29	−12.44	0.38	0.33	0.73
RGKA	176.24	−38.02	0.85	−3.30	−1.39	0.26	0.24	0.78
RGKW	176.77	−38.05	−0.46	−11.02	−2.25	0.36	0.31	0.79
RGLI	176.39	−38.00	0.99	−5.06	−2.24	0.24	0.25	0.74
RGMK	176.47	−38.14	0.90	−10.43	−17.17	0.26	0.28	0.81
RGMT	176.72	−37.92	1.53	−5.29	2.89	0.26	0.34	0.83
RGON	176.23	−38.26	5.63	−6.02	−14.72	0.35	0.28	0.86
RGOP	176.56	−37.85	−0.11	−2.92	2.14	0.29	0.24	0.67
RGRE	176.52	−38.06	0.39	−6.10	−3.44	0.32	0.32	0.74
RGRR	176.51	−38.34	−0.14	−6.53	−4.54	0.26	0.26	0.77
RGTA	176.51	−38.23	−2.43	−5.98	−14.67	0.37	0.37	0.92
RGUT	176.19	−38.18	3.83	−4.96	−5.81	0.32	0.23	0.85
RGWV	176.21	−38.35	1.02	−4.62	−15.58	0.34	0.28	0.71
RIPA	176.49	−39.17	0.95	−12.33	−0.79	0.36	0.29	0.73
SCTY	166.95	−45.27	−22.51	−5.21	0.68	1.25	1.67	2.71
SEDD	174.14	−41.66	−5.50	4.39	7.10	1.16	0.96	1.48
SNST	177.35	−38.78	2.04	−17.37	−1.60	0.63	0.34	0.88
TAKP	175.96	−40.06	−15.76	−8.79	−6.52	0.35	0.34	1.00
TAUP	176.08	−38.74	3.20	−5.84	2.03	0.35	0.39	0.69
TAUW	178.01	−38.16	0.89	−18.78	2.64	0.35	0.33	0.76
TEMA	175.89	−41.11	−29.06	−10.64	−4.18	0.27	0.33	0.70
TENN	172.79	−42.22	6.38	−5.00	−7.80	0.91	0.49	1.13
TGHO	176.00	−38.81	−0.43	−6.59	0.12	0.48	0.50	1.29
TGHR	175.71	−38.68	−1.25	−2.38	−0.71	0.27	0.27	0.71
TGOH	176.05	−38.85	1.52	−6.67	−0.35	0.30	0.33	0.79
TGRA	175.77	−38.86	−1.83	−3.61	−0.78	0.30	0.25	0.64
TGRI	175.86	−38.98	−0.76	−4.47	−2.62	0.35	0.37	0.84
TGTK	175.81	−38.61	−0.59	−2.38	−0.39	0.29	0.28	0.72
TGW2	175.94	−38.67	1.53	−1.07	−3.55	0.32	0.42	0.66
THAP	175.79	−39.68	−4.19	−6.12	0.61	0.86	0.29	0.82
TINT	175.89	−40.78	−25.58	−9.23	−6.01	0.29	0.37	0.69

TKAR	177.81	−38.44	−0.06	−18.83	−0.90	0.43	0.40	0.91
TKHL	172.96	−41.03	−2.21	−0.98	−1.69	0.65	0.41	0.99
TORY	174.28	−41.19	−11.91	−0.23	−0.24	0.56	0.56	0.92
TRAV	175.69	−41.40	−33.34	−9.73	−4.88	0.20	0.21	0.59
TRNG	176.26	−37.73	0.55	−1.41	−0.34	0.27	0.25	0.68
TRWH	174.63	−41.28	−19.25	−0.33	0.43	0.56	0.69	1.04
TURI	176.38	−40.26	−19.71	−10.43	−3.45	0.40	0.36	0.84
V47B	172.66	−43.57	−39.39	−16.46	1.78	1.02	1.22	4.76
VGET	175.71	−39.14	−1.62	−2.00	−2.34	0.56	0.52	1.16
VGFW	175.55	−39.26	−0.54	−2.72	−0.74	0.34	0.33	0.71
VGKR	175.64	−39.09	1.03	−3.88	−2.94	0.36	0.28	0.65
VGMO	175.75	−39.41	−1.18	−5.35	−0.74	0.44	0.25	0.69
VGMT	175.47	−39.39	−2.80	−1.75	−0.86	0.28	0.30	0.64
VGNG	175.60	−39.18	0.41	−1.77	−2.56	0.48	0.50	0.89
VGOB	175.54	−39.20	−0.20	−2.64	−2.26	0.29	0.31	0.63
VGOT	175.67	−39.16	−0.57	−2.93	−3.78	0.41	0.36	0.80
VGPK	175.35	−39.29	−1.62	−2.15	−0.98	0.27	0.33	0.62
VGT8	175.68	−39.10	−7.24	−11.12	−14.28	2.23	0.99	2.07
VGTM	175.70	−39.12	−1.07	−2.43	−4.10	0.51	0.53	1.17
VGTR	175.55	−39.30	−1.00	−2.83	−1.89	0.41	0.38	0.88
VGTS	175.61	−39.28	−0.61	−3.53	−1.76	0.50	0.38	0.92
VGWH	175.59	−39.28	−0.64	−3.24	−1.84	0.50	0.37	0.99
VGWN	175.60	−39.33	−1.19	−2.95	−1.48	0.43	0.39	0.77
VGWT	175.59	−39.12	0.95	−2.29	−2.35	0.46	0.42	0.88
WAHU	177.23	−39.08	0.00	−17.36	−1.65	0.75	0.59	0.85
WAIM	170.92	−44.66	−30.96	−12.43	−1.14	0.21	0.19	0.50
WAKA	169.89	−43.58	−13.92	−3.19	0.97	0.23	0.43	0.66
WANG	174.82	−39.79	−6.42	−1.28	−0.96	0.26	0.35	0.60
WARK	174.66	−36.43	−0.18	−0.69	−0.66	0.22	0.25	0.67
WEST	171.81	−41.75	−3.12	−0.82	−1.53	0.28	0.25	0.51
WGTN	174.81	−41.32	−24.31	−7.27	−1.78	0.31	0.24	0.57
WGTT	174.78	−41.29	−22.60	−6.22	−1.59	0.38	0.33	0.71
WHKT	177.01	−37.98	3.89	−12.62	−1.34	0.33	0.33	0.82
WHNG	174.32	−35.80	0.09	−0.44	−1.60	0.19	0.18	0.56
WHVR	175.45	−39.73	−7.13	−2.74	−0.72	0.47	0.51	0.88

WMAT	178.41	−37.83	5.74	−19.97	0.67	0.42	0.34	0.85
WPAW	176.54	−39.90	−15.31	−11.87	−6.63	0.52	0.33	0.85
WPUK	176.44	−40.06	−16.24	−10.37	−4.73	0.47	0.40	0.89
WRPA	175.58	−41.06	−27.35	−7.86	−2.93	0.41	0.50	1.28
YALD	172.48	−43.49	−32.50	−12.57	−3.64	0.29	0.36	0.82

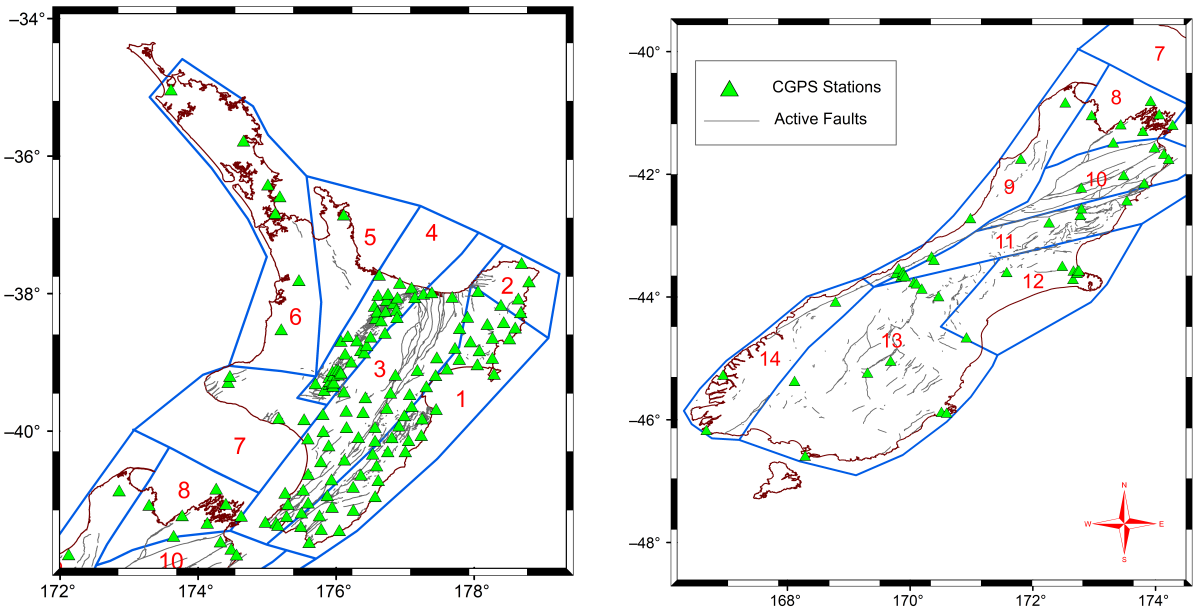

Fig. 4.1: Spatial coverage of CGPS stations in the North Island and the South Island. The grey lines represent active faults in the study region, whereas the green triangles represent the locations of CGPS stations.

4.3.2 Earthquake data

The historical earthquake data of New Zealand is obtained from the ground-based Earth observing network (GeoNet; https://www.geonet.org.nz/). The GeoNet is maintained by the group of Earthquake Commission (EQC), GNS Science, and the Land Information of New Zealand (LINZ). The GeoNet provides earthquake database that has been determined by instrumental records since the 1930's; prior to 1930's, the earthquake catalog has been compiled by several authors (e.g., [54–56, 58]). It is believed that the catalog is complete for seismic deformation analysis [129]. From the GeoNet catalog, it is observed that the whole New Zealand has magnitude completeness for the magnitude 3.5 or above, whereas some regions of New Zealand have magnitude completeness up to 2.5 or smaller [241]. After deciding the earthquake catalog length (time span of $1840-2021$), minimum magnitude of earthquakes ($M_w \geq 4.0$) and seismic depth (25 km), the resultant earthquake catalog contains 11319 events ($4.0 \leq M_w \leq 8.2$)

(Fig 4.2). This catalog comprises 73 events of magnitude $M_w \geq 6$ and 13 events of magnitude $M_w \geq 7$. The Wairarapa earthquake (M_w8.2) in 1855 and the Kaikoura earthquake (M_w7.8) in 2016 are the largest event and the most recent earthquake of New Zealand, respectively.

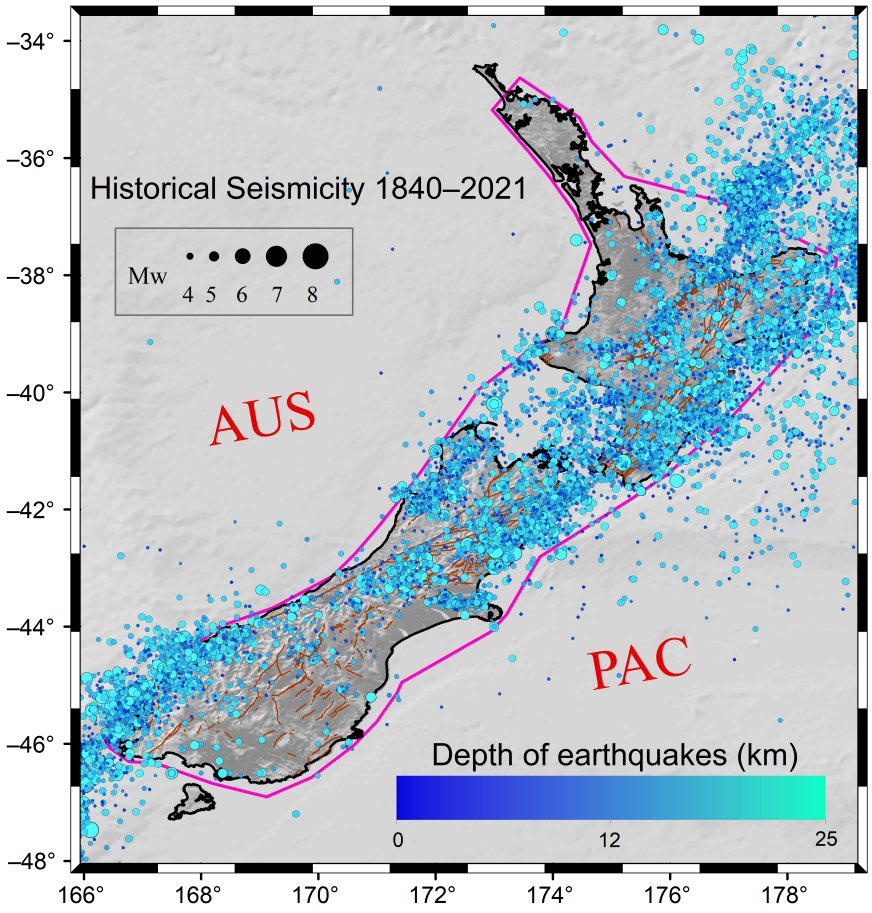

Fig. 4.2: Distribution of historical seismicity (1840 – 2021) in New Zealand; the size of circle represents the magnitudes of earthquakes, whereas the color of circle indicates the focal depths of earthquakes. The magenta polygon represents the study area.

4.4 Methodology

Taking the advantage of the high-resolution geodetic observations and the historical seismicity data of New Zealand, the geodetic moment rate and the seismic moment rate are computed. It may be noted that the geodetic moment rate is calculated through the strain field estimates, as derived from the velocity data [130]. After computation, both moment rates are compared to determine the spatial distribution of contemporary earthquake hazard potential in New Zealand. A step-by-step procedure for the earthquake hazard evaluation is provided in the below sections. The major steps of the methodology include strain field estimation, segmentation of New

Zealand, computation of geodetic and seismic moment rates, and earthquake budget estimation for each zone. In addition, the relationship of geodetic deformation with seismic signals is addressed. A sensitivity testing to various parameters is also carried out.

4.4.1 Strain rate modeling

In order to monitor the geometric changes in terms of deformation pattern and amplitude caused by the ongoing process between the plate boundaries, the crustal strain field is often determined [39, 227, 229]. The strain field is obtained by solving the velocity gradient tensor. Based on the theory of elasticity states, it can be said that the infinitesimally small fraction change of size/position (known as the displacement field) in the ductile body can be expressed as a sum of three factors: translation [T], dilatation [D], and rotation [R] [76]. These factors are approximated by the three-dimensional velocity gradient tensor. Using the Taylor series expansion, the displacement tensor (x) can be expended as:

$$u_i(x+dx) = u_i(x) + \frac{\partial u_i}{\partial x_k} |_x \, dx \qquad i = 1,2,3 \tag{4.1}$$

where, $u_i(x)$ shows the translation (T) and $d_{ik} = (\partial u_i/\partial x_k) = e_{ik}$ represents the second order approximation, known as deformation tensor. By expanding the tensor into three-dimensional components, the symmetric part (i.e., $e_{ik} = e_{ki}$) of the second order tensor shows the dilatation (D) and the antisymmetric part (i.e., $e_{ik} = -e_{ki}$) denotes the rotation (R). Applying the concept of tensor theory, Equation 4.1 can be written as follows:

$$\begin{aligned} u_i(x+dx) &= u_i(x) + \frac{d_{ik}+d_{ki}}{2}dx_k + \frac{d_{ik}-d_{ki}}{2}dx_k \qquad i = 1,2,3 \\ &= u_i^{[T]}(x) + du_i^{[D]}(x) + du_i^{[R]}(x) \end{aligned} \tag{4.2}$$

Using Equation 4.2, strain tensors in two-dimension are formulated as

$$\dot{e}_{ij} = \frac{\dot{e}_{ii}+\dot{e}_{jj}}{2} \pm \sqrt{\frac{1}{4}(\dot{e}_{ii}+\dot{e}_{jj})^2 + \dot{e}_{ij}^2} \tag{4.3}$$

$$\theta = \frac{1}{2}\tan^{-1}\left(\frac{2\dot{e}_{ij}}{\dot{e}_{ii}-\dot{e}_{jj}}\right) \tag{4.4}$$

$$\dot{e} = \sqrt{(\dot{e}_{ii}^2 + \dot{e}_{jj}^2 + \dot{e}_{ij}^2)} \tag{4.5}$$

In Equations 4.3, 4.4, and 4.5, i and j denote the east component and the north component, respectively; $\dot{e}_{ii}$ and $\dot{e}_{jj}$ represent the major and minor principal strain rates, which are computed as $\dot{e}_{ii} = \frac{\partial v_i}{\partial x_i}$, $\dot{e}_{jj} = \frac{\partial v_j}{\partial x_j}$, and $\dot{e}_{ij} = \frac{1}{2}\left(\frac{\partial v_i}{\partial x_i} + \frac{\partial v_j}{\partial x_j}\right)$; here, v_i and v_j are velocity components

of a particular point in the east and the north direction, respectively. In Equation 4.3, the positive part denotes the dilatation strain rate and the negative part shows the longitudinal strain rate (maximum shear strain rate). In Equation 4.4, θ denotes the direction of the principal strain rate. Equation 4.5 indicates the second invariant strain rate ($\dot{e}$).

The geodetic strain rate field can be estimated using several techniques, such as segmentation-based approaches (e.g., Delaunay triangulation method) [149], inversion-based techniques (e.g., seismic tomography-based method) [235], and gridding or interpolation techniques (e.g., least-squares collocation method) [119]. It may be noted that the derived strain field may be significantly different on the basis of the implemented approach, even if the velocity input data is the same [173].

In the present analysis, the strain field is computed from the gridding method. For this, the study area is divided into a small uniform grid with a grid node $(0.25^\circ \times 0.25^\circ)$. As in distance-weighted approaches, the velocity gradient tensors are utilized to model the strain rates, considering the continuous function [229], as

$$W = exp\left[\frac{-d^2}{2D^2}\right] \tag{4.6}$$

Here, W denotes the weighting term and d indicates the distance between GPS station locations and node points. The parameter D, as a distance-decaying constant, is used to smooth the derived crustal strain rate. The choice of smoothing parameter (D) is considered on the basis of capturing the full range of regional strain anomalies or the spatial coverage and resolution of the geodetic data [229]. In some cases, such as in heterogeneous area, the estimated strain rates exhibit maximum variations. Note that to avoid the oversmoothing and biased estimation of strain patterns in the high-to-low strain regions, the value of smoothing parameter (D) is assumed to be 200 km.

By applying the above-mentioned methodology of strain estimation, the 2-D strain rate patterns provide a synoptic view of ongoing crustal deformation and underlying geodynamical processes, such as regional strain build-up rate. As a result, the horizontal symmetric strain tensors in which major and minor axes correspond to the maximum and minimum principal strain, depict the changeability in area and the direction of deformation. For instance, the principal axes of strain rates display the deformation pattern in terms of extension (positive) or compression (negative) associated with thrusting or normal faulting. The symmetric strain tensor shows the maximum shear strain rates that reveal the characteristics of strike-slip faulting. The distribution of dilatation rates, maximum shear strain rates, and rotational rates are pictorially presented in the below sections (Fig. 4.3, Fig. 4.4, and Fig. 4.5). Note that the derived strain fields are invariant in any reference frame because of non-dependency on the coordinate system [227].

4.4.1.1 Dilatation strain rate

The areal dilatation rate highlights the first-order dichotomy and it is represented by the sum of eigenvalues of the strain gradient tensor. The positive and negative values of the dilatation rates reveal the deformation pattern linking to the regional tectonic settings. The positive values denote extensional behavior within the Earth's crust, whereas the negative values represent the compressional pattern of the Earth's lithosphere. A pictorial representation of the areal dilatation rates is provided in Fig. 4.3.

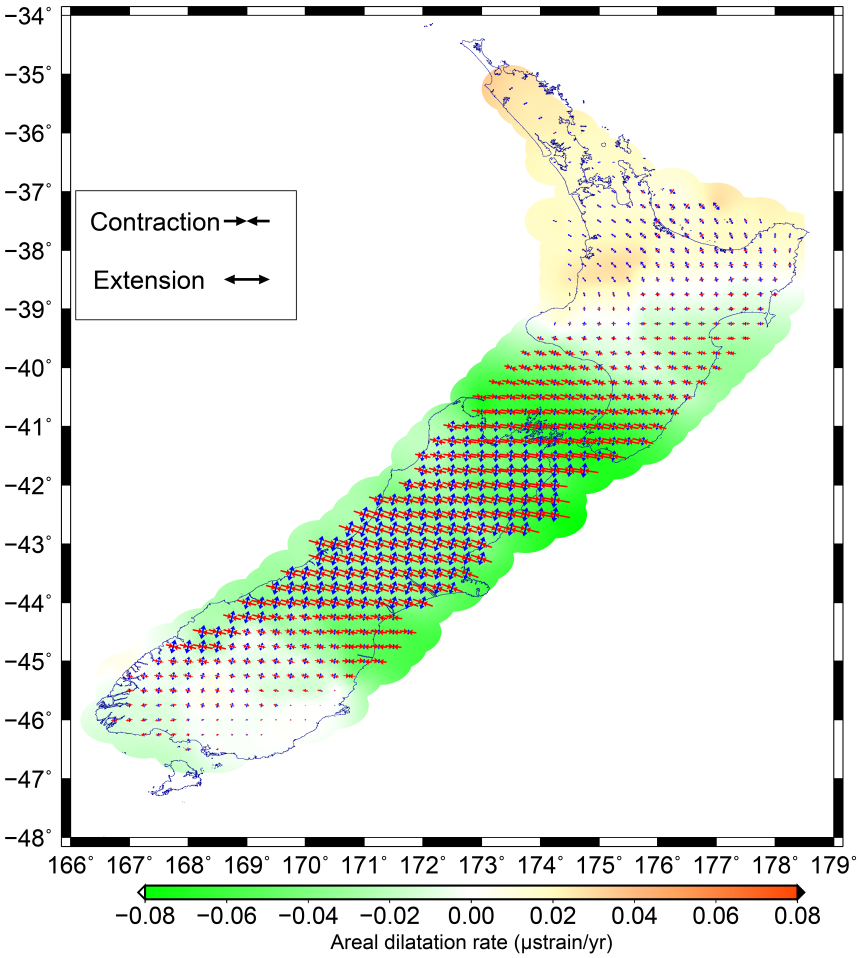

Fig. 4.3: Principal axes of strain rates in New Zealand, derived from the CGPS velocity data.

From Fig. 4.3, following points are noted: (1) a band of contractional strain rates in the South Island is noticed along the Alpine fault from the Puysegur subduction to the Hikurangi subduction interface; (2) the large compressional pattern in the central South Island depicts the existence of a series of dextral faults near the Marlborough fault system; (3) the southeastern part of the South Island has negligible strain signals that clearly indicate a relatively stable area; (4) in the North Island, a compressional belt is noticed along the Hikurangi-Kermadec-Tonga

subduction zone; (5) the shortening rates stem from a small amount of subduction slip beneath Marlborough and/or from contractional strain partitioned to the southeast of the continental transpression zone; (6) the dominating extensional pattern is observed in the northwestern part of the North Island, probably due to the existing normal faulting pattern and due to the presence of the Taupo volcanic zone, and (7) the range of lengthening is about $\sim 0-30$ nstrain/yr, whereas the range of shortening is about $\sim 0-75$ nstrain/yr. The estimated strain pattern is observed to closely agree with the previous finding of Haines et al. (2020) [84], in which the strain field is derived by the physics-based approach.
Overall, the retrieved dilatation strain pattern suggests that the compressional deformation style is more dominant than the extensional pattern. The results also demonstrate that most of the tectonic activities are controlled by the thrust/reverse environment over New Zealand. It is observed that the intensity of crustal strain rates (i.e., dilatation, shear, and rotational) is relatively low in most of the southeastern part of the South Island and northwestern part of the North Island due to relatively stable tectonic configuration. Thus, it is concluded that the estimated strain rate fields in the present study seem to concur well with the structural-geological pattern.

4.4.1.2 Maximum shear strain rate

A linear combination of symmetric velocity tensor is utilized to compute the maximum shear strain rate. The measure of maximum shear strain rate reveals deformation correlated to localized shear strain [227], whereas the pattern of shear strain rate provides significant information about the existing strike-slip faulting zone [76].

The maximum shear strain deformation pattern, presented in Fig. 4.4, shows predominant strike-slip movement in New Zealand. The results suggest a large fraction of shear strain rates in the central South Island because of the well-known strike-slip environment (Marlborough fault system) [134]. The strain rates in most of the northern South Island clearly indicate a dextral deformation that is mainly accommodated by the Awatere, Clarence, Hope, and the Wairau faults [84, 140]. The transpressional belt broadly stretches from the Puysegur subduction thrust to the Hikurangi subduction thrust (at depth) along the Alpine fault. The shear strain rates in the lower North Island indicate the presence of principal strike-slip fault trace of the Wellington fault, Wairarapa fault, Mohaka fault, and the Ruahine fault [162]. In addition, small signals of shear deformation rate are also identified in the lower region of the South Island, whereas the upper region of the North Island indicates no strike-slip faulting in these regions. The large estimated value of the maximum shear strain rate is about ~ 225 nstrain/yr near the northeastern boundary of the South Island.

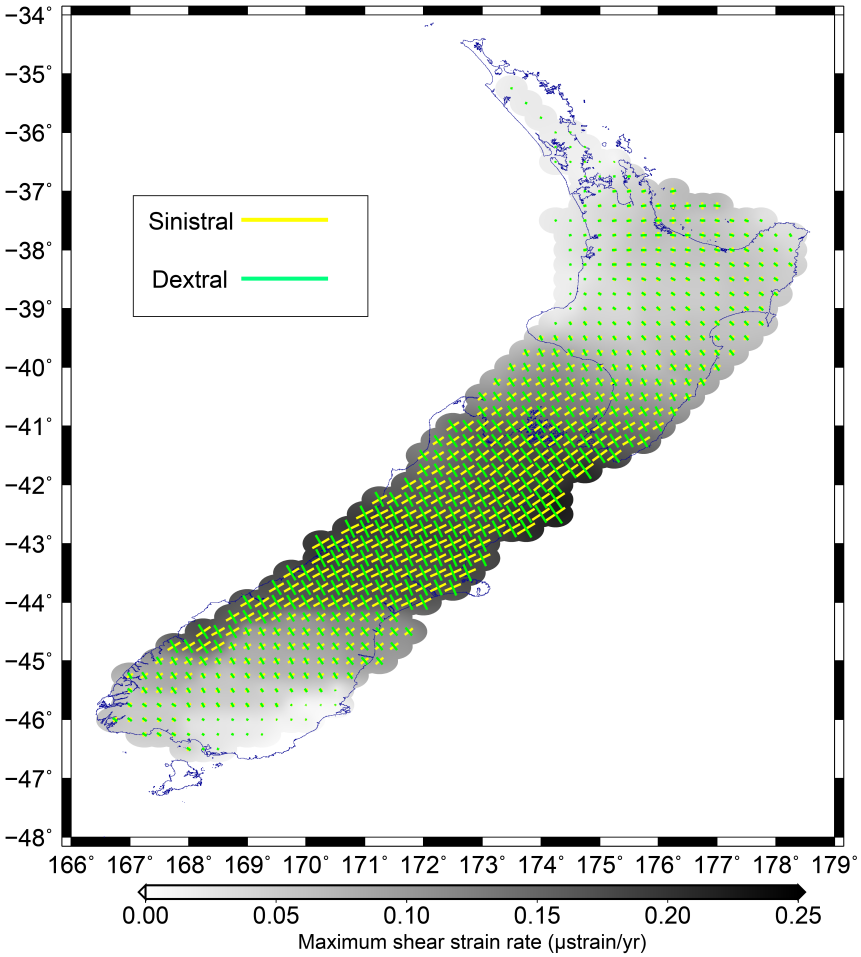

Fig. 4.4: Maximum shear strain rate axes in New Zealand, estimated from the CGPS velocity data.

4.4.1.3 Rotation rate

The antisymmetric part of partial derivatives of the displacement tensor denotes the rotational rates. There are three postulates related to the cause of rotational strain. These are: (i) non-uniform distribution of gravitational potential energy, (ii) heat flux variation of lithosphere, and (iii) plate boundary interactions and the associated configuration [60, 94]. Among these three, the third hypothesis of plate boundary interaction is dominating due to the tectonic environment in New Zealand as a result of relative motion of the Pacific plate and the Australian plate along the Alpine fault [30, 162, 268].

The rotational deformation pattern is shown in Fig. 4.5. By inspecting the deformation pattern, it is noticed that the rotational rates are relatively high in two domains, namely the Marlborough fault system and the North Island. A large fraction of clockwise rotation is captured within the Marlborough fault region and it gradually decreases towards the western boundary. Similarly, the estimated rotational pattern of the North Island indicates not only the extension

of the Taupo volcanic zone but also clockwise rotation of the Hikurangi forearc away from the Taupo volcanic zone. The results have a good agreement with the previous studies [30, 50, 140, 162]. In addition, a similar pattern was also observed in the velocity field.

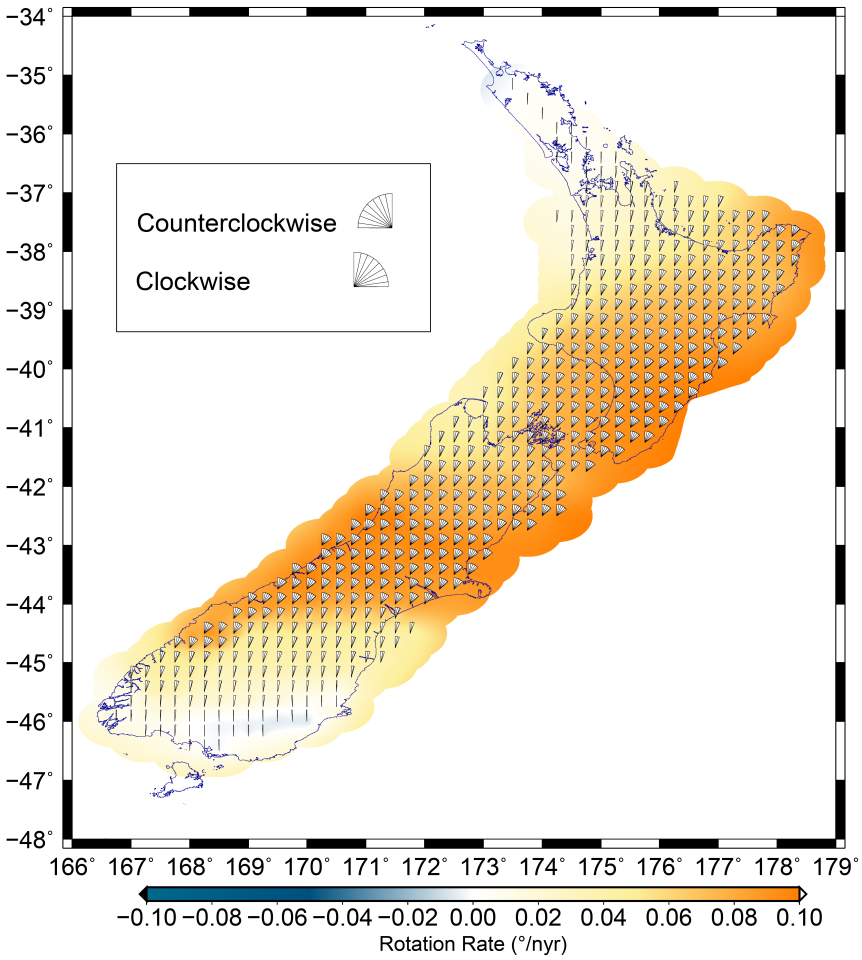

Fig. 4.5: Rotation strain rate pattern in New Zealand, calculated from the CGPS velocity data.

In conclusion, determining the consistent pattern of the strain rate field in New Zealand is an important aspect to characterize the deformation style caused by the underlying fault kinematics, such as normal faulting, reverse/thrust faulting, and strike-slip environment. The results provide a synoptic view of principal lengthening and shortening, vertical axis rotations, and two-dimensional volume strain, having a significant linkage to the regional tectonic configuration of New Zealand. The retrieved strain rates are further converted into geodetic moment rate for contemporary earthquake hazard evaluation in the following sections.

4.4.2 Comparison of geodetic deformation signals and seismic deformation signals

In order to identify relationship between GPS-derived signals and seismic signals, crustal strain patterns and focal solutions are inspected togetherly. It is known that the focal solutions describe the current tectonic stress configuration during the time of fault rupture, whereas the GPS-derived strain signals characterize the interseismic energy build-up style [6]. In light of this, the focal solutions are obtained from the global centroid moment tensor (GCMT; https://www.globalcmt.org/) since 1976. Fig. 4.6 provides a comparison between geodetic deformation signals and seismic deformation signals in New Zealand.

From Fig. 4.6, it is observed that the focal solutions in New Zealand generally agree with the crustal strain pattern. For instance, domain 1 comprising the central South Island exhibits a dominant strike-slip faulting along the Alpine fault; domain 2 consisting of the Taupo volcanic zone shows the extension mechanism; domain 3 depicts the compressional configuration along with the Hikurangi interface, and domain 4 encompassing the Puysegur subduction zone shows the reverse as well as strike-slip faulting pattern. Overall, a comparative analysis of GPS-derived signals and seismic signals offers adequate information to study the seismic moment budget in New Zealand.

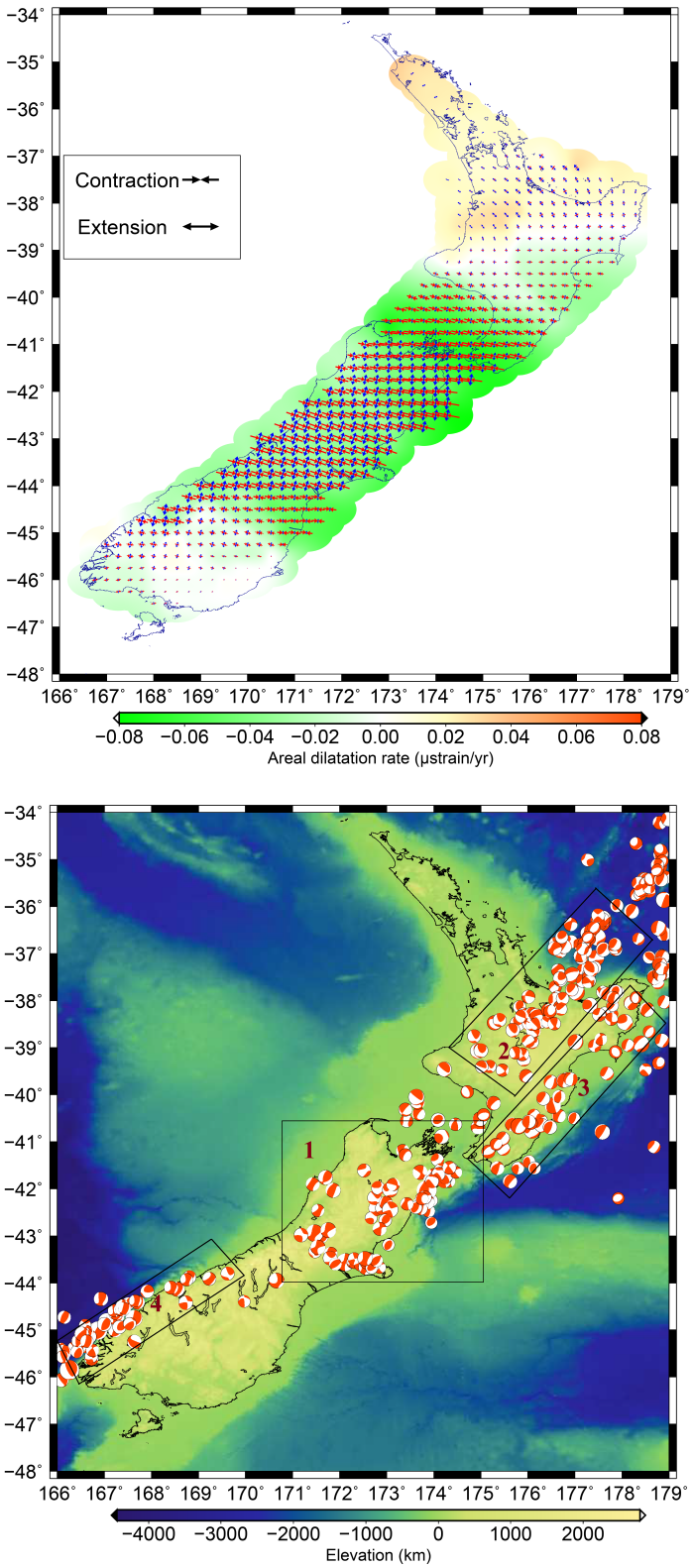

Fig. 4.6: The upper panel shows the distribution of geodetic strain rates, whereas the lower panel represents focal solutions (since 1976) in New Zealand. Note that the geodetic strain rate pattern is re-drawn from Fig. 4.3. For the figure in the lower panel, each domain (domain 1 to domain 4) represents different tectonic setting in the study region.

4.4.3 Seismogenic source segmentation for the present analysis

In order to examine the earthquake hazard potential in New Zealand based on geodetic energy accumulation and seismic energy release, the whole study region has been divided into smaller segments. In previous such type of studies, the study region was subdivided into seismic zones based on several norms. For instance, Bilham et al. (2001) [25] divided the Himalayan arc into 10 regions, with lengths approximately corresponding to those of great Himalayan ruptures (220 km); Hsu et al. (2009) [106] studied such zones in Taiwan, where at least 10 earthquakes and sufficient GPS data points are located; Chousianitis et al. (2015) [39] adopted the seismic partition of Greece, stemmed from the Seismic Hazard Harmonization (SHARE) project in Europe on the basis of latest tectonic, geological, and seismological considerations, and Sharma et al. (2020) [227] split the Himalayan region into 24 seismic zones in such a way that each zone has the sufficient coverage of geodetic data as well as the earthquake data, and fault rupture is contained in a single zone. As suggested in the above studies, the following points seem to be pivotal for segmentation.

1. Each zone should bear a close resemblance to the deformation style caused by the tectonic activities.

2. Each zone should have sufficient coverage of geodetic data and earthquake data.

3. Fault rupture caused by a large earthquake should lie in a single zone.

For a systematic analysis of New Zealand, the study region is primarily divided into three broader tectonic blocks from north to south based on the plate characteristics and movement style. These three tectonic blocks are: (i) the continental-oceanic subduction block, (ii) continental-continental transpression block, and (iii) the oceanic-continental subduction block. However, for better insights of the spatial distribution of earthquake potential, it is necessary to subdivide these three broader blocks into further smaller zones. In this regard, there exists a standard zonation scheme of New Zealand suggested by the NSHM developers [241]. In the NSHM model, the categorization was made based on a similar sense of tectonic movements, similar geometries and kinematics of active faults, and the historic seismicity [241]. In that model, the study region was divided into 14 crustal seismic zones [241]. By inspecting the spatial distribution of earthquakes and geodetic observations, fault ruptures (wherever exists), maximum magnitudes, and distribution of faulting style of these 14 seismic zones, it can be observed that each zone fulfils the above three essential criteria of segmentation. Therefore, the present study directly adopts the above segmentation, as displayed in Fig. 4.7.

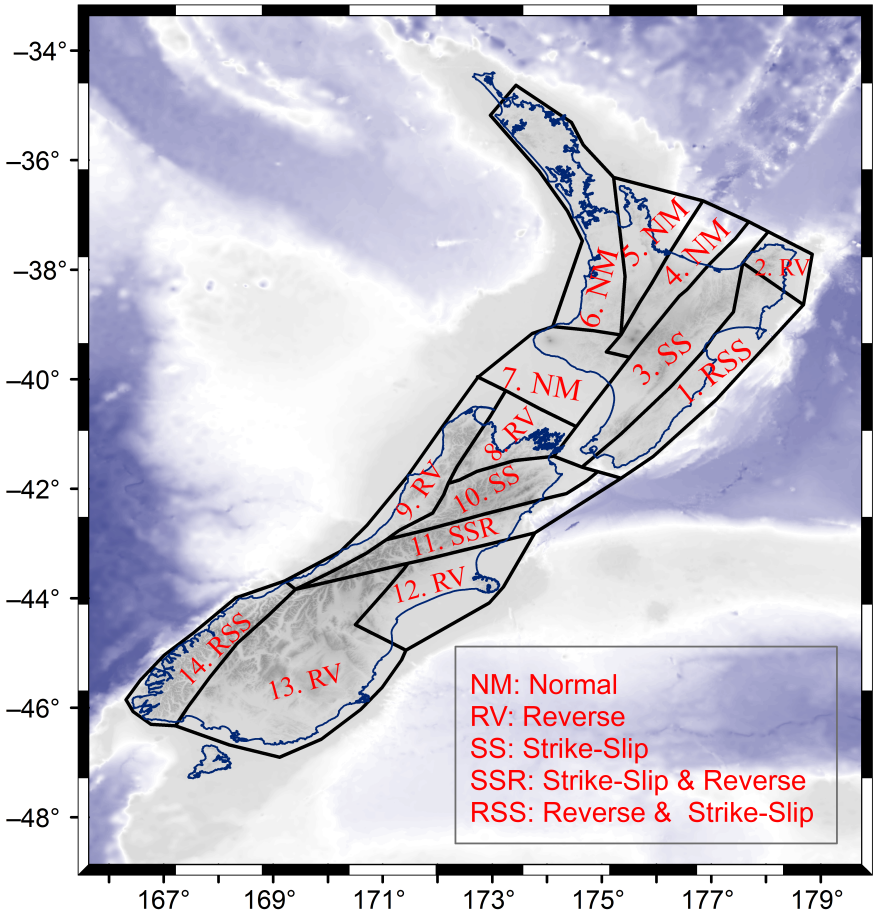

Fig. 4.7: Seismotectonic zones in New Zealand (Stirling et al. (2002) [241]). Abbreviations are as follows: NM, Normal; RV, Reverse; SS, Strike-Slip; SSR, Strike-Slip & Reverse; RSS, Reverse & Strike-Slip.

The 14 smaller zones essentially belong to the three broader blocks. The first block contains seven zones (Zone-1 to Zone-7); the second block consists of six zones (Zone-8 to Zone-13), and the third block encloses only one zone (Zone-14). Each zone exhibits a particular type of slipping pattern. For instance, Zone-1 and Zone-14 have a dominant reverse faulting with strike-slip pattern; Zone-2, Zone-8, Zone-9, Zone-12 and Zone-13 have a reverse environment; Zone-3 and Zone-10 have strike-slip configuration; Zone-4, Zone-5, Zone-6, and Zone-7 have normal faulting style, whereas Zone-11 has a dominant strike-slip with reverse faulting. Therefore, the entire study region reveals a complex tectonic set up. Moreover, the observed seismicity in New Zealand over these 14 zones is not homogeneous. For example, the 1931 Hawke's Bay earthquake (M_w7.3) occurred in Zone-1, 1843 Whanganui earthquake (M_w7.6) in Zone-2, 1855 Wairarapa earthquake (M_w8.2) in Zone-3, 2013 Cook Strait sequence (M_w6.6) in Zone-10, 2016 Kaikoura earthquake (M_w7.8) in Zone-11, 2010 – 11 Canterbury earthquake

sequence (M_w7.2, 6.2) in Zone-12, and the 2009, Dusky Sound earthquake (M_w7.8) occurred in Zone-14. Therefore, due to the variation in seismic energy release, it is important to re-estimate contemporary seismic moment budget over New Zealand.

4.4.4 Computation of geodetic moment rate

As mentioned in Section 4.4.1, the retrieved strain rates will be used as an input for estimating the geodetic moment rate. Acknowledging the nonuniqueness and uncertainty involved in converting surface strain to a scalar geodetic moment rate, several equations, such as Anderson (1979) [5], Ward (1994, 1998) [276, 277], and Savage and Simpson (1997) [223] have been employed in previous studies. These studies have suggested that the estimated results are closely similar. In the present analysis, the method provided by Savage and Simpson (1997) [223] is utilized for calculating the geodetic moment rate for each seismic source zone. The adopted equation is as follows:

$$\dot{M}_o^g = 2\mu H_c A_c Max(|\dot{e_1}|, |\dot{e_2}|, |\dot{e_1} + \dot{e_2}|) \tag{4.7}$$

Here, $\dot{M}_o^g$ denotes the tectonic moment rate; $|\dot{e_1}|$ and $|\dot{e_2}|$ are absolute values of the major and minor principal strain tensors within each zone; μ is the rigidity constant for the elastic layer with value 3×10^{10} N/m^2; A_c is the area of seismic zone, and H_c denotes the potentially seismogenic thickness of the study region.

In determining the geodetic moment rate, the seismogenic thickness of the study region is an important parameter. In order to figure out the appropriate seismogenic thickness, several authors have provided basic guidelines on the basis of tectonic configuration and depth-wise distribution of events. For instance, Pancha et al. (2006) [173] utilized the depth distribution of microearthquakes to choose the most appropriate seismic thickness; Pan et al. (2020) [172] considered average seismogenic layer thickness, which contains approximately 95% of the total events in depth distribution of earthquakes, and Sharma et al. (2020) [227] identified the seismic depth on the basis of focal depth distribution along the main fault system in the Himalayan region. Therefore, guided by the above studies, the seismogenic depth in New Zealand is considered to be 20 km, based on the following observations: (1) about 95% of the total microearthquakes ($M_w \leq 2.0$) have occurred at depth less than 20 km; (2) most of the existing faults ($\sim$ 90% of the faults considered in NSHM) in New Zealand have depth within $0-20$ km, and (3) 75% earthquakes of the total events ($4.0 \leq M_w \leq 8.2$) have a focal depth of $0-20$ km. Therefore, the consideration of seismogenic depth as 20 km seems to be appropriate for the present analysis. Nevertheless, for the sensitivity analysis presented at a later section, the seismogenic depth is considered to be 15 km, 20 km, and 25 km.

4.4.5 Computation of seismic moment rate

Similar to the seismogenic thickness in geodetic moment rate calculation, the earthquake database for each zone is prepared based on the maximum focal depth of 20 km. The total seismic moment release in each zone is thereby computed. For this, the magnitude-moment relationship formula is applied to convert the moment magnitude (M_w) into the seismic moment (M_o^s) for each event in a given zone. The formula is as follows:

$$logM_o^s = 1.5M_w + 9.1 \tag{4.8}$$

For the present analysis, all events with $M_w \geq 4.0$ during the time period of $1840-2021$ are considered. Using Equation 4.8, the total seismic moment of a particular zone is computed. The seismic moment rate for each zone is then calculated from the ratio of total seismic moment to the catalog length of the respective zone (T) as $\dot{M}_o^s = \frac{\sum M_o^s}{T}$.

4.4.6 Computation of seismic-geodetic moment rate ratio and associated earthquake potential

In this section, the derived geodetic and seismic moment rates are incorporated to identify the spatial distribution of earthquake potential in terms of seismic-geodetic moment rate ratio and associated moment deficit rate. The moment rate ratio is expressed as the ratio of geodetic moment rate to the seismic moment rate. The expression is as follows:

$$\text{Seismic-geodetic moment rate ratio} = \frac{\dot{M}_o^g}{\dot{M}_o^s} = 1(>1, <1) \tag{4.9}$$

In Equation 4.9, the seismic-geodetic moment rate ratio has three possible cases: either 1, greater than 1, or less than 1. The measure of moment rate ratio reveals the strain accumulation and release rate of a particular zone. For instance, if the moment rate ratio is 1, it indicates that the large amount of accumulated energy has been released by earthquakes and thereby it is normalized by the background seismicity; if the ratio is greater than 1, it implies that either the associated region has the sufficient amount of accumulated energy and may host one or more earthquakes in near future, or it has a significant proportion of aseismic deformation; and, if the ratio is less than 1, it points out that the whole part of seismic energy is released and stress accumulation is underway [227].

The difference between geodetic moment rate and seismic moment rate corresponds to the moment deficit rate of a zone. The positive value of moment deficit rate for a zone indicates that the associated region has a possibility to host one or more earthquake events, whereas the

negative value for a zone suggests no seismic potential within a zone. Therefore, the moment deficit rate provides an equivalent earthquake potential in a zone and it will be released by one or more earthquakes within the zone. A simple flowchart of the data-driven seismic moment budget estimation technique is illustrated in Fig. 4.8.

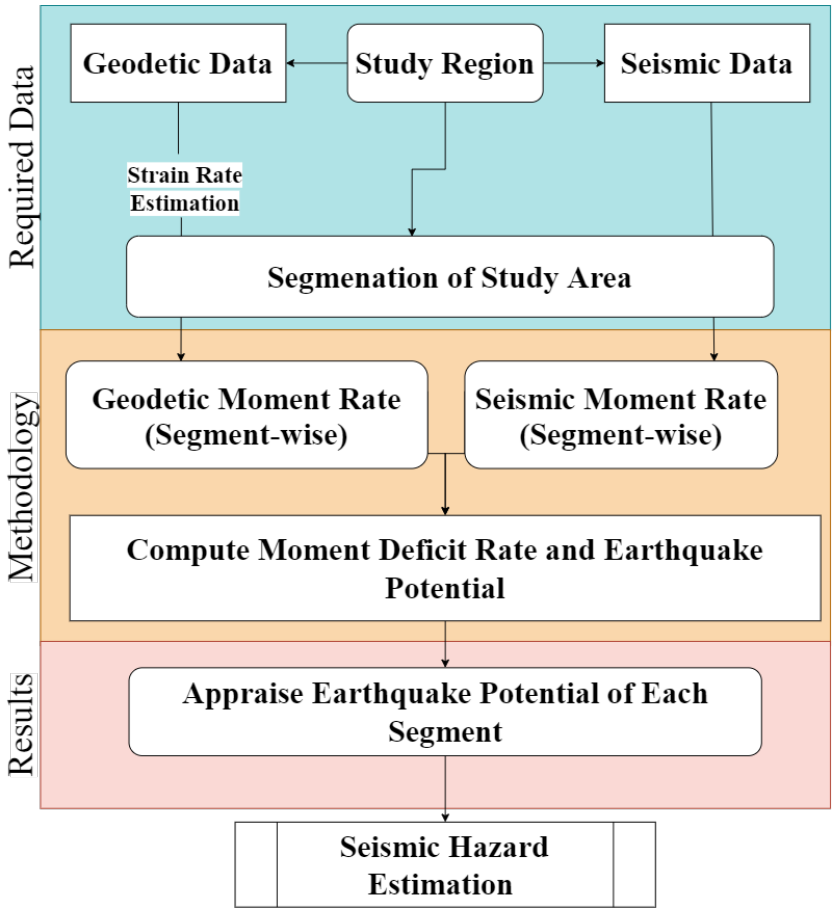

Fig. 4.8: Flowchart of the data-driven seismic moment budget estimation technique for seismic hazard estimation.

4.5 Results and discussion

It is known that geodetic measurements can detect both seismic and aseismic moment accumulation, whereas earthquake-based moment release only counterbalances the seismic component of moment accumulation. The seismic moment budget, the resultant of the difference between geodetic and seismic moment rates, can thus highlight the seismic deformation, aseismic deformation style, or a combination of both factors. It thereby reveals regions of potential seismic hazard [39]. A detailed analysis of the spatial distribution of seismic moment budget is provided in the below section.

4.5.1 Seismic-geodetic moment rate ratio in New Zealand

A comparative analysis of moment rate estimates in terms of seismic-geodetic moment rate ratio and current earthquake potential is provided in Table 4.2 and Fig. 4.9. From Table 4.2, it is observed that the estimated moment rates of Zone-11 and Zone-14 are below unity, indicating that the accumulated crustal energy has been released through earthquakes. The emanated result of each zone in Zone-11 and Zone-14 has a good agreement with the historical seismicity. On the other hand, in Zone-5, Zone-6, Zone-7, and Zone-13, the moment rate ratio is significantly high (ratio $\geq$ 50), indicating high strain accumulation rate in comparison to the strain release rate. The high ratio of these zones essentially indicates higher energy accumulation, probably due to the low occurrence rate of large earthquakes, larger earthquake recurrence interval, low strain field, aseismic crustal deformation style, or a combination of these factors. In addition, the intermediate moment rate ratio, ranging between 2 to 12, is observed in the remaining seismic zones (Zone-1, Zone-2, Zone-3, Zone-4, Zone-8, Zone-9, Zone-10, and Zone-12).

Table 4.2: Summary of geodetic moment rate, seismic moment rate, moment rate ratio, seismic moment budget and associated earthquake potential of 14 continuous zones corresponding to a seismogenic depth of 20 km and an earthquake catalog length of $\sim$ 180 years (1840 – 2021); the dash (–) denotes the absence of present seismic potential.

Zone	$\dot{M}_0^g$ (10^{17} Nm/yr)	$\dot{M}_0^s$ (10^{17} Nm/yr)	$\dot{M}_0^g/\dot{M}_0^s$	M_0^b (10^{20} Nm)	Current earthquake potential (M_w)
1	54.52 ± 0.44	31.00	1.76	2.77	7.6
2	3.15 ± 0.15	1.57	2.00	0.16	6.7
3	61.53 ± 0.49	17.91	3.44	7.76	7.9
4	11.67 ± 0.15	2.18	5.36	1.20	7.3
5	10.27 ± 0.09	0.13	81.36	0.77	7.2
6	20.40 ± 0.19	0.10	212.28	1.93	7.5
7	32.07 ± 0.22	0.36	88.22	2.54	7.5
8	22.23 ± 0.18	1.94	11.47	1.75	7.4
9	34.28 ± 0.71	16.94	2.02	2.65	7.5
10	32.44 ± 0.29	11.66	2.78	3.59	7.6
11	40.16 ± 0.45	56.96	0.71	-2.35	–
12	40.95 ± 0.83	6.34	6.46	5.26	7.7
13	90.02 ± 1.26	0.41	217.13	12.99	8.0
14	27.37 ± 0.78	83.92	0.33	-4.47	–

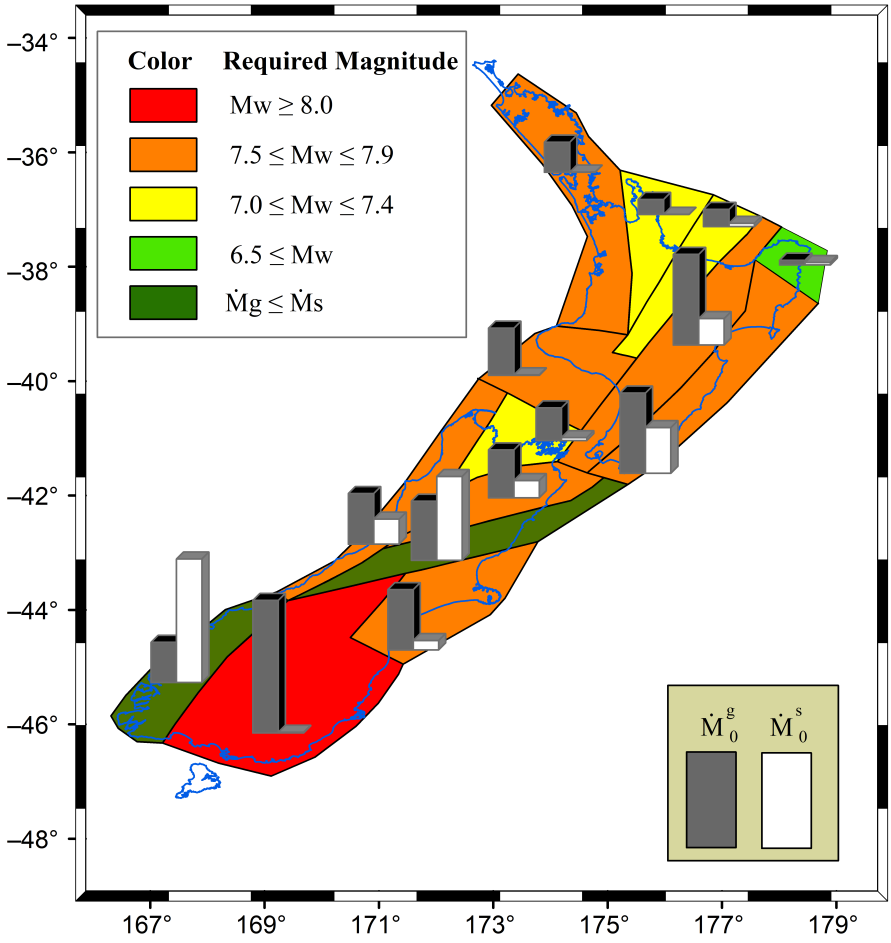

Fig. 4.9: Spatial distribution of earthquake potential in New Zealand. The color bar of each zone indicates the current measure of seismic potential magnitude. The bar chart filled with gray and white corresponding to each zone illustrates the accumulated moment rate and release moment rate.

Considering the hypothesis that the complete moment deficit rate in a zone will be released by one or more earthquakes within the zone, the maximum size of possible earthquake is determined to eliminate the mismatch between the geodetic and the seismic moment rates [39, 172, 206, 227]. The moment deficit rate of each zone is summarized in Table 4.2 and is pictorially shown in Fig. 4.9. The range of current earthquake potential in New Zealand lies between M_w6.7 to M_w8.0. Most of the seismogenic zones have the potential for near-future earthquakes with a magnitude of more than M_w7.0. The emanated result of each zone shows a close resemblance to peak ground acceleration (PGA) values, which reveal similar pattern of earthquake hazard in New Zealand [240, 241].

Just to recall, the study region was initially divided into three broader seismotectonic blocks from north to south, namely the continental-oceanic subduction block, continental-continental transpression block, and the oceanic-continental subduction block. The obtained results of each zone belonging to the above-mentioned blocks are discussed in the following sections.

4.5.2 Earthquake potential in the continental-oceanic subduction block (Zone-1 to Zone-7)

The continental-oceanic subduction block comprises first seven seismic zones of the total 14 zones, covering the entire North Island. Most of the seismic potential in this region is accommodated due to the presence of the Hikurangi interface and the Taupo volcanic zone, which are situated in the eastern North Island and in the central North Island, respectively. The estimated earthquake potential corresponding to this region varies from M_w6.7 to M_w7.9 (Table 4.2 and Fig. 4.9). In particular, Zone-1 has the potential to host a major earthquake (M_w7.6) due to high geodetic strain accumulation rate and seismic release rate; Zone-2 has sufficient amount of moment deficit rate to produce a strong earthquake (M_w6.7), and Zone-3, that covers the rupture area of the giant 1855 Wairarapa earthquake (M_w8.2), has the largest seismic potential (M_w7.9) in this region. One of the main reasons of high seismic potential in Zone-3 is the existence of the well-known active and fast-slipping Wairarapa fault. This estimated result of Zone-3 is supported by the study of Manighetti et al. (2020) [147] in which they have suggested that the Wairarapa fault had repeatedly produced giant earthquakes and is capable of hosting a strong forthcoming event. In addition, Zone-4 is prone to break with a possible magnitude of M_w7.3, whereas Zone-5, Zone-6, and Zone-7 currently hold the energy equivalent to one or more major earthquakes $M_w \geq 7.0$. Overall, there is a possibility of one or more large earthquakes in the North Island.

4.5.3 Earthquake potential in the continental-continental transpression block (Zone-8 to Zone-13)

The continental-continental transpressional block encompasses six seismic zones, namely Zone-8 to Zone-13. Apart from Zone-11, all zones have sufficient accumulated energy that might get released in one or more major earthquakes ($M_w \geq 7.0$). In Zone-11, the accumulated energy over the last 100 years is released in the 2016 Kaikoura earthquake (M_w7.8). Therefore, the associated moment deficit rate is negative, indicating no seismic signals in this zone. The remaining zones belong to the Alpine fault system, where most of the seismicity is driven by the relative plate motion of the Pacific plate and the Australian plate along the Alpine fault and its adjacent fault network. As a consequence, these zones have potential to generate next forthcoming earthquakes. The possible maximum magnitudes of the prospective events in Zone-8, Zone-9, Zone-10, and Zone-12 are about M_w7.4, M_w7.5, M_w7.6, and M_w7.7, respectively, whereas Zone-13 has the highest seismic potential (M_w8.0). From the estimated results, it is observed that the seismic hazard in this block is relatively high in comparison to the remaining two blocks. The obtained results are also supported by the study of Sutherland et al. (2007)

[244], Robinson et al. (2013) [204], Denys et al. (2016) [48], Nicol and Diseen (2018) [163], and Griffin et al. (2021) [79]. More specifically, Sutherland et al. (2007) [244] have suggested that the large earthquakes ($M_w > 7.0$) on the Alpine fault will almost certainly occur in future. Robinson et al. (2013) [204] found that the Alpine fault is close to the average inferred recurrence interval ($\sim$ 300 years) and it will host a great earthquake ($M_w \geq 8.0$) in near future with 85% probability. They have also suggested that the most likely location of the forthcoming event is around the Mount Cook region on the central segment of the fault. Both findings agree to the present earthquake potential of Zone-9. A close agreement of the potential in Zone-10 is observed to the study of Nicol and Diseen (2018) [163]. They have noticed that the dextral strike-slip Wairau fault, one of the most active faults of the Marlborough fault system, has no evidence of surface rupture since the last 2000 years and is capable of generating large earthquakes of $M_w \geq 7.5$. Note that co-rupture of the Wairau fault and the Alpine fault during great earthquakes is rare. Therefore, different zones (Zone-9 and Zone-10) may be affected by forthcoming rupture associated to a particular fault. Furthermore, due to the largest geodetic moment rate (9.0×10^{18} Nm/yr) and very low seismic moment rate (0.4×10^{17} Nm/yr) in Zone-13, this zone has the highest current earthquake potential in New Zealand. The mismatch of geodetic moment rate and seismic moment rate of this zone is high probably due to the underlying fault network, in which some of the faults may be in an active phase, whereas the others may be quiescent [48, 79, 238]. Overall, it is concluded that the central South Island is a highly active region in New Zealand.

4.5.4 Earthquake potential in the oceanic-continental subduction block (Zone-14)

The oceanic-continental subduction block contains only one zone, Zone-14. The estimated seismic moment budget corresponding to Zone-14 suggests that the entire region has no potential to trigger immediate future seismic events. This is due to the fact that the seismic moment of Zone-14 is dominated due to occurrence of the 2007 George Sound earthquake (M_w6.8) and the 2009 Dusky Sound earthquake (M_w7.8). Consequently, the released seismic energy (8.32×10^{18} Nm/yr) is three times higher than the accumulated energy (2.73×10^{18} Nm/yr). Therefore, the above estimation suggests that Zone-14 is in the interseismic period of the next earthquake cycle.

4.6 Sensitivity Analysis

In order to determine whether the estimated earthquake potential for each zone is consistent or not, a sensitivity analysis of contributing parameters is often essential. The contributing

factors in the present analysis are: (a) the seismogenic thickness, (b) the catalog length of the historical seismicity, and (c) the lower limit and upper limit of the geodetic moment rate. Therefore, to perform sensitivity testing, the following parameter settings are considered: (1) with a fixed earthquake catalog length ($\sim$ 180 years), the earthquake potential is evaluated by varying the seismogenic thickness $H_c = 15$ km, 20 km, 25 km; (2) with a fixed seismogenic thickness (20 km), the seismic potential is determined by differing the earthquake catalog length $T = 50$ years, 100 years, $\sim$ 180 years, and (3) with a fixed seismogenic thickness (20 km) and earthquake catalog length ($\sim$ 180 years), the seismic moment budget is calculated using the lower limit $((\dot{M}_0^g)_{min})$ and upper limit $((\dot{M}_0^g)_{max})$ of the geodetic moment rate. For each of the above-mentioned cases, the earthquake potential corresponding to 14 seismic zones is re-computed. The resultant earthquake potential for each zone is represented below in Table 4.3 to Table 4.11.

4.6.1 Impact of seismogenic depth on earthquake potential

Using different seismogenic depths, such as 15 km, 20 km, and 25 km, the earthquake potential corresponding to each zone is re-calculated. The results are summarized in Table 4.3 to Table 4.5. The re-calculated results lead to the following observations: (a) except for a few regions, such as Zone-2 and Zone-11, the obtained earthquake potential is generally consistent; (b) the range of the earthquake potential has changed from $M_w6.7 - M_w8.0$ to $M_w6.5 - M_w8.1$, and (c) Zone-2 reveals a considerable variation in seismic potential ($M_w6.5$ to $M_w7.1$), probably due to high geodetic moment rate as a result of large (i.e., 25 km) seismogenic thickness, and (d) at the depth of 15 km, Zone-11 exhibits a potential of future large earthquake ($M_w7.5$), due to the non-consideration of the 2016 Kaikoura earthquake that has occurred at a depth of 16 km. The above results show that the variation in the seismogenic depth has quite insignificant impact on the associated earthquake potential.

Table 4.3: Seismic moment budget and associated earthquake potential corresponding to a seismogenic depth of 15 km and an earthquake catalog length of $\sim$ 180 years; the dash (–) denotes the absence of present seismic potential.

Zone	$\dot{M}_0^g$ (10^{17} Nm/yr)	$\dot{M}_0^s$ (10^{17} Nm/yr)	$\dot{M}_0^g/\dot{M}_0^s$	M_0^b (10^{20} Nm)	Earthquake potential (M_w)
1	40.89±0.33	14.03	2.91	3.17	7.6
2	2.36±0.11	1.56	1.51	0.08	6.5
3	46.15±0.36	17.90	2.58	5.03	7.7
4	8.75±0.11	1.54	5.69	0.91	7.2
5	7.70±0.07	0.12	61.64	0.58	7.1
6	15.30±0.14	0.10	160.09	1.44	7.4
7	24.06±0.16	0.34	71.29	1.90	7.5
8	16.67±0.13	1.94	8.61	1.27	7.3
9	25.71±0.53	9.30	2.77	2.51	7.5
10	24.33±0.22	11.17	2.18	2.28	7.5
11	30.12±0.34	11.83	2.55	2.56	7.5
12	30.71±0.62	5.99	5.12	3.76	7.6
13	67.51±0.95	0.41	162.98	9.73	7.9
14	20.53±0.59	83.59	0.25	−4.98	–

Table 4.4: Seismic moment budget and associated earthquake potential corresponding to a seismogenic depth of 25 km and an earthquake catalog length of $\sim$ 180 years; the dash (–) denotes the absence of present seismic potential.

Zone	$\dot{M}_0^g$ (10^{17} Nm/yr)	$\dot{M}_0^s$ (10^{17} Nm/yr)	$\dot{M}_0^g/\dot{M}_0^s$	M_0^b (10^{20} Nm)	Earthquake potential (M_w)
1	68.15±0.55	34.27	1.99	5.93	7.8
2	3.94±0.18	1.00	3.94	0.51	7.1
3	76.92±0.61	18.35	4.19	10.60	8.0
4	14.59±0.19	2.20	6.63	1.56	7.4
5	12.84±0.11	0.09	137.58	2.00	7.5
6	25.50±0.24	0.07	356.09	4.25	7.7
7	40.09±0.27	0.32	124.08	7.08	7.8
8	27.79±0.22	1.15	24.16	4.61	7.7
9	42.85±0.89	15.61	2.74	4.77	7.7
10	40.55±0.36	11.80	3.43	4.97	7.7
11	50.21±0.56	57.01	0.88	−0.95	–
12	51.19±1.03	5.48	9.35	8.09	7.9
13	112.52±1.58	0.36	311.56	18.95	8.1
14	34.21±0.98	85.05	0.40	−4.02	–

Table 4.5: A comprehensive summary of earthquake potential (M_w) at varying seismogenic depths (15 km to 25 km); the dash (–) denotes the absence of present seismic potential.

Zone	Seismogenic depth (H_c)			Range (M_w)
	15 km	20 km	25 km	
1	7.6	7.6	7.8	7.6–7.8
2	6.5	6.7	7.1	6.5–7.1
3	7.7	7.9	8.0	7.7–8.0
4	7.2	7.3	7.4	7.2–7.4
5	7.1	7.2	7.5	7.1–7.5
6	7.4	7.5	7.7	7.4–7.7
7	7.5	7.5	7.8	7.5–7.8
8	7.3	7.4	7.7	7.3–7.7
9	7.5	7.5	7.7	7.5–7.7
10	7.5	7.6	7.7	7.5–7.7
11	7.5	–	–	7.5
12	7.6	7.7	7.9	7.6–7.9
13	7.9	8.0	8.1	7.9–8.1
14	–	–	–	–

4.6.2 Impact of catalog length on earthquake potential

In this section, the earthquake potential of each zone is estimated based on three different time spans of the earthquake catalog, such as 50 years, 100 years, and $\sim$ 180 years. The results are listed in Table 4.6 to Table 4.8. Based on the obtained results, following observations

are made: (a) though the overall range of earthquake potential remains same, there is a zone-wise earthquake potential variation (Table 4.8) and (b) except Zone-1, the earthquake potential decreases when the catalong length is reduced from $\sim$ 180 years to 100 years and to 50 years; in Zone-1, the respective earthquake potential turns out to be M_w7.6, M_w7.4 and M_w7.6, due to the seismic release in the 1931 Hawke's Bay earthquake (M_w7.3), 1934 Pahiatau earthquake (M_w7.2), and the 1942 Wairarapa earthquake (M_w7.2) corresponding to catalog length of 100 years ($1921-2021$). Overall, it is suggested that the catalog length has a very less effect on the resulting contemporary seismic potential.

Table 4.6: Seismic moment budget and associated earthquake potential corresponding to a seismogenic depth of 20 km and an earthquake catalog length of 50 years ($1971-2021$); the dash (–) denotes the absence of present seismic potential.

Zone	$\dot{M}_0^g$ (10^{17} Nm/yr)	$\dot{M}_0^s$ (10^{17} Nm/yr)	$\dot{M}_0^g/\dot{M}_0^s$	M_0^b (10^{20} Nm)	Earthquake potential (M_w)
1	54.52±0.44	0.44	124.83	2.70	7.6
2	3.15±0.15	0.14	22.04	0.13	6.7
3	61.53±0.49	0.11	544.58	3.07	7.6
4	11.67±0.15	4.10	2.85	0.37	7.0
5	10.27±0.09	0.09	109.42	0.31	6.9
6	20.40±0.19	0.01	1879.06	0.67	7.2
7	32.07±0.22	0.26	125.38	1.59	7.4
8	22.23±0.18	0.01	1740.63	0.91	7.2
9	34.28±0.71	0.61	56.21	1.68	7.4
10	32.44±0.29	6.94	4.68	1.28	7.3
11	40.16±0.45	135.25	0.30	−4.75	–
12	40.95±0.83	18.24	2.24	1.14	7.3
13	90.02±1.26	0.64	139.69	4.47	7.7
14	27.37±0.78	131.70	0.21	−5.22	–

Table 4.7: Seismic moment budget and associated earthquake potential corresponding to a seismogenic depth of 20 km and an earthquake catalog length of 100 years (1921 – 2021); the dash (–) denotes the absence of present seismic potential.

Zone	$\dot{M}_0^g$ (10^{17} Nm/yr)	$\dot{M}_0^s$ (10^{17} Nm/yr)	$\dot{M}_0^g/\dot{M}_0^s$	M_0^b (10^{20} Nm)	Earthquake potential (M_w)
1	54.52±0.44	33.96	1.61	1.85	7.4
2	3.15±0.15	0.18	17.61	0.22	6.8
3	61.53±0.49	0.28	219.81	5.64	7.8
4	11.67±0.15	2.64	4.42	0.89	7.2
5	10.27±0.09	0.13	81.36	0.77	7.2
6	20.40±0.19	0.06	345.60	1.61	7.4
7	32.07±0.22	0.36	88.22	2.54	7.5
8	22.23±0.18	1.94	11.47	1.75	7.4
9	34.28±0.71	19.53	1.75	1.36	7.4
10	32.44±0.29	4.59	7.07	2.23	7.5
11	40.16±0.45	80.04	0.50	−3.67	–
12	40.95±0.83	9.73	4.21	3.09	7.6
13	90.02±1.26	0.44	203.27	8.33	7.9
14	27.37±0.78	83.92	0.33	−4.47	–

Table 4.8: Summarization of earthquake potential (M_w) variation for each seismic source zone corresponding to earthquake catalog length of 50 years, 100 years and $\sim$ 180 years; the dash (–) denotes the absence of present seismic potential.

Zone	Earthquake catalog length			Range (M_w)
	50 years	100 years	$\sim$ 180 years	
1	7.6	7.4	7.6	7.4–7.6
2	6.7	6.8	6.7	6.7–6.8
3	7.6	7.8	7.9	7.6–7.9
4	7.0	7.2	7.3	7.0–7.3
5	6.9	7.2	7.2	6.9–7.2
6	7.2	7.4	7.5	7.2–7.5
7	7.4	7.5	7.5	7.4–7.5
8	7.2	7.4	7.4	7.2–7.4
9	7.4	7.4	7.5	7.4–7.5
10	7.3	7.5	7.6	7.3–7.6
11	–	–	–	–
12	7.3	7.6	7.7	7.3–7.7
13	7.7	7.9	8	7.7–8.0
14	–	–	–	–

4.6.3 Impact of the lower limit and upper limit of geodetic moment rate on earthquake potential

To account for the uncertainty in the estimated geodetic moment rate, the lower and upper bounds are chosen to study its impact on earthquake potential. The maximum possible earthquake size for each zone is listed below in Table 4.9 to Table 4.11. From the results, it is observed that the current earthquake potential remains consistent across all zones.

Table 4.9: Seismic moment budget and associated earthquake potential using the lower bound of the geodetic moment rate (with a seismogenic depth of 20 km and an earthquake catalog length of $\sim$ 180 years); the dash (–) denotes the absence of present seismic potential.

Zone	$\dot{M}_0^g$ (10^{17} Nm/yr)	$(\dot{M}_0^g)_{min}$ (10^{17} Nm/yr)	$\dot{M}_0^s$ (10^{17} Nm/yr)	$\frac{(\dot{M}_0^g)_{min}}{\dot{M}_0^s}$	M_0^b (10^{20} Nm)	Earthquake potential (M_w)
1	54.52±0.44	54.08	31.00	1.74	2.72	7.6
2	3.15±0.15	3.00	1.57	1.91	0.15	6.7
3	61.53±0.49	61.05	17.91	3.41	7.68	7.9
4	11.67±0.15	11.52	2.18	5.29	1.18	7.3
5	10.27±0.09	10.18	0.13	80.65	0.76	7.2
6	20.40±0.19	20.21	0.10	210.30	1.91	7.5
7	32.07±0.22	31.85	0.36	87.62	2.52	7.5
8	22.23±0.18	22.05	1.94	11.38	1.73	7.4
9	34.28±0.71	33.57	16.94	1.98	2.54	7.5
10	32.44±0.29	32.15	11.66	2.76	3.54	7.6
11	40.16±0.45	39.72	56.96	0.70	−2.41	–
12	40.95±0.83	40.13	6.34	6.33	5.14	7.7
13	90.02±1.26	88.75	0.41	214.08	12.81	8.0
14	27.37±0.78	26.59	83.92	0.32	−4.53	–

Table 4.10: Seismic moment budget and associated earthquake potential using the upper bound of the geodetic moment rate (with a seismogenic depth of 20 km and an earthquake catalog length of $\sim$ 180 years); the dash (–) denotes the absence of present seismic potential.

Zone	$\dot{M}_0^g$ (10^{17} Nm/yr)	$(\dot{M}_0^g)_{min}$ (10^{17} Nm/yr)	$\dot{M}_0^s$ (10^{17} Nm/yr)	$\frac{(\dot{M}_0^g)_{min}}{\dot{M}_0^s}$	M_0^b (10^{20} Nm)	Earthquake potential (M_w)
1	54.52±0.44	54.96	31.00	1.77	2.83	7.6
2	3.15±0.15	3.30	1.57	2.10	0.18	6.8
3	61.53±0.49	62.02	17.91	3.46	7.85	7.9
4	11.67±0.15	11.82	2.18	5.43	1.22	7.3
5	10.27±0.09	10.36	0.13	82.08	0.78	7.2
6	20.40±0.19	20.59	0.10	214.26	1.95	7.5
7	32.07±0.22	32.29	0.36	88.83	2.55	7.5
8	22.23±0.18	22.41	1.94	11.57	1.76	7.4
9	34.28±0.71	34.99	16.94	2.06	2.76	7.6
10	32.44±0.29	32.73	11.66	2.81	3.64	7.6
11	40.16±0.45	40.61	56.96	0.71	−2.29	–
12	40.95±0.83	41.78	6.34	6.59	5.39	7.8
13	90.02±1.26	91.28	0.41	220.17	13.18	8.0
14	27.37±0.78	28.15	83.92	0.34	−4.41	–

Table 4.11: Summarization of earthquake potential variation for each seismic source zone, using the lower and upper bounds of geodetic moment rate, corresponding to a seismogenic depth of 20 km and an earthquake catalog length of $\sim$ 180 years; the dash (–) denotes the absence of present seismic potential.

Zone	Uncertainty of geodetic moment rate			Range (M_w)
	$(\dot{M}_0^g)_{min}$	$\dot{M}_0^g$	$(\dot{M}_0^g)_{max}$	
1	7.6	7.6	7.6	7.6
2	6.7	6.7	6.8	6.7–6.8
3	7.9	7.9	7.9	7.9
4	7.3	7.3	7.3	7.3
5	7.2	7.2	7.2	7.2
6	7.5	7.5	7.5	7.5
7	7.5	7.5	7.5	7.5
8	7.4	7.4	7.4	7.4
9	7.5	7.5	7.6	7.5–7.6
10	7.6	7.6	7.6	7.6
11	–	–	–	–
12	7.7	7.7	7.8	7.7-7.8
13	8.0	8.0	8.0	8.0
14	–	–	–	–

Therefore, it is concluded that the obtained earthquake potential measures are largely consistent to the variations in seismogenic depth, catalog period time, and the uncertainty in the geodetic moment rate.

4.7 Earthquake potential prior to the 2016 Kaikoura earthquake: a step towards method validation

Just to recall, the above-mentioned earthquake potential analysis was carried out by utilizing about 180 CGPS velocity data and the earthquake data during the time period of 1840 – 2021. The velocity data was acquired from Nevada Geodetic Laboratory (NGL), University of Nevada, Reno [28]), whereas the earthquake data was taken from the Ground-Based Earth Observing Network (GeoNet, https://www.geonet.org.nz/). Both data sets provide the synoptic view of the contemporary seismic moment budget distribution throughout the entire New Zealand. By knowing the present-day earthquake potential distribution in New Zealand, it is interesting to know "what was the scenario of contemporary earthquake potential in New Zealand prior to the Kaikoura earthquake?" To answer this, the whole methodology is repeated to compute the then earthquake potential before the Kaikoura earthquake.

For this analysis, (1) $\sim$ 900 stations velocity data with the time span of 1995 – 2013, provided by Beavan et al. (2016) [21], is incorporated to estimate the strain field and associated geodetic moment rate; (2) the historic earthquake data, for the time period of 1840 – 2015 is used to determine the seismic moment rate, and (3) using the above-mentioned data, the entire procedure is applied to compute the pre-Kaikoura earthquake potential of 14 seismic zones (same as the previous analysis). Before proceeding, it is important to clarify the inclusion of $\sim$ 900 stations in pre-Kaikoura earthquake potential. The main advantages of taking $\sim$ 900 stations velocity data are: (1) the velocity data does not include the effect of Kaikoura event (coseismic and postseismic effects) and (2) the velocity field has dense spatial coverage of geodetic observations over New Zealand. Therefore, instead of taking $\sim$ 180 CGPS velocity data, the dense geodetic data ($\sim$ 900 stations) are preferable for the quantification of earthquake potential for each zone prior to the 2016 Kaikoura earthquake.

After applying the whole methodology, the obtained results including geodetic moment rate, seismic moment rate, seismic-geodetic moment rate ratio, the seismic moment budget and associated earthquake potential corresponding to each zone are compiled in Table 4.12. In addition, Table 4.13 provides zone-wise earthquake potential before and after the Kaikoura earthquake. Except for a few zones (Zone-2, Zone-9, and Zone-11), the distribution of seismic potential prior to the Kaikoura event is almost similar to the present-day earthquake potential distribution in New Zealand. Since the Kaikoura earthquake had occurred in Zone-11, the accumulated energy in Zone-11 has been released in this event. Thus, at present time, it has no seismic potential to trigger immediate future events (Table 4.2). On the otherhand, before the Kaikoura event, this region holds energy equivalent to a major event (M_w7.7) (Table 4.12). In addition, a minor noticeable variation in earthquake potential has been observed in Zone-2

(M_w7.7 to M_w6.7) and Zone-9 (M_w7.8 to M_w7.5), probably due to high geodetic moment rates in these regions. Although the velocity pattern for both velocity data ($\sim$ 180 stations and $\sim$ 900 stations) are similar, a significant difference is observed in the estimated geodetic strain rates from the dense spatial coverage of CGPS observations. The difference in geodetic strain rates leads to high geodetic moment rates, for example, the geodetic moment rate associated to Zone-2 varies from 3.15×10^{17} Nm/yr to 6.01×10^{17}Nm/yr.

Table 4.12: Seismic moment budget and associated earthquake potential using $\sim$ 900 stations' velocity data (with a seismogenic depth of 20 km and an earthquake catalog length of $\sim$ 180 years); the dash (–) denotes the absence of present seismic potential.

Zone	$\dot{M}_0^g$ (10^{17} Nm/yr)	$\dot{M}_0^s$ (10^{17} Nm/yr)	$\dot{M}_0^g/\dot{M}_0^s$	M_0^b (10^{20} Nm)	Earthquake potential (M_w)
1	70.09±0.44	32.65	2.14	4.19	7.7
2	6.01±0.15	1.62	3.71	0.44	7.0
3	80.61±0.49	18.53	4.35	10.67	8.0
4	15.92±0.15	2.27	7.01	1.63	7.4
5	15.36±0.09	0.13	121.65	1.15	7.3
6	21.49±0.19	0.10	223.63	2.03	7.5
7	48.39±0.22	0.38	127.18	3.55	7.6
8	29.06±0.18	1.94	14.99	2.33	7.5
9	56.93±0.71	17.63	3.22	5.77	7.8
10	40.90±0.29	11.30	3.62	4.94	7.7
11*	47.39±0.45	10.75	4.41	4.91	7.7
12	46.11±0.83	6.56	7.02	5.77	7.8
13	132.08±1.26	0.43	307.01	18.29	8.1
14	47.58±0.78	90.68	0.52	−3.14	–

* Kaikoura event occurred in this zone.

Table 4.13: Summarization of earthquake potential (M_w) variation for each seismic source zone before and after the Kaikoura earthquake; the dash (–) denotes the absence of present seismic potential.

Zone	Distribution of earthquake potential	
	Before Kaikoura	After Kaikoura
1	7.7	7.6
2	7.0	6.7
3	8.0	7.9
4	7.4	7.3
5	7.3	7.2
6	7.5	7.5
7	7.6	7.5
8	7.5	7.4
9	7.8	7.5
10	7.7	7.6
11*	7.7	–
12	7.8	7.7
13	8.1	8.0
14	–	–

From the obtained results of pre-Kaikoura earthquake, it appears that the adopted methodology offers a valid approach for the time-dependent seismic hazard analysis in terms of earthquake potential distribution in New Zealand.

4.8 Summary

This chapter has concentrated on two key ideas, geodetic moment accumulation and seismic moment release for the contemporary seismic hazard assessment in New Zealand. While there is no simple translation of crustal strain rates into the seismic hazard, the moment rate derived from earthquake or geodetic observation has an impactful bearing on the earthquake hazard evaluation. Therefore, the earthquake records are used to derive the seismic moment release rate, whereas geodetic observations are utilized to derive the geodetic moment accumulation rate. The discrepancies in the geodetic and seismic moment rates are thereby investigated in terms of moment deficit rate. These moment deficit rates provide a reliable information of spatial distribution of seismic moment budget in different seismogenic zones.

For the quantification of contemporary earthquake hazard potential over New Zealand, $\sim$ 180 years of earthquake data and a network of $\sim$ 180 CGPS data are incorporated to quantify the seismic moment rate and geodetic moment rate, respectively. In addition, the study region has been divided into 14 seismic zones based on the tectonic configurations, distribution of historic seismicity, earthquake focal solutions, and their related style of faulting [241]. The seismic-geodetic moment rate ratio, moment deficit rate, and earthquake potential for each seismic zone have been computed and analyzed. Based on the obtained results, the following remarks are made.

1. Strain distributions (dilatation, shear, and rotational) in New Zealand reveal a dominating compression deformation style rather than the extensional pattern, especially in the central South Island along the Alpine fault. In addition, small signals of strain tensors are observed in the southeastern South Island and the northwestern North Island.

2. By utilizing the strain estimates and earthquake data, the obtained moment deficit varies from 0.16×10^{20} to 12.99×10^{20}, which corresponds to the possible maximum magnitude of earthquake $M_w 6.7 - M_w 8.0$ over New Zealand.

3. The continental-oceanic subduction block (Zone-1 to Zone-7) has a possibility of one or more large earthquakes in the North Island, probably due to the Hikurangi subduction interface, the Taupo volcanic zone, and the Wairarapa fault.

4. The continental-continental transpressional block (Zone-8 to Zone-13) is deemed to have high seismic potential and it is capable of hosting the next major earthquake in the central South Island, due to the Alpine fault and its associated Marlborough fault system. In addition, Zone-13 has the highest earthquake potential ($M_w 8.0$), whereas Zone-11 has no seismic potential.

5. The oceanic-continental subduction block (Zone-14) has no potential to trigger immediate future seismic event. It is probably in the interseismic period of the next earthquake cycle.

6. The obtained earthquake potential measures are largely consistent to the variation in seismological depth, earthquake catalog length, and the lower and upper bounds of the geodetic moment rate.

7. The case study of the pre-Kaikoura earthquake potential attempts to provide a possible validation of the adopted methodology through the earthquake potential of each zone before and after the 2016 Kaikoura earthquake.

As a summary, the present chapter demonstrates the distribution of earthquake potential over the entire New Zealand region. The findings not only provide invaluable inputs for time-dependent seismic hazard analysis but also produce important information to the academia, industry, and public on the present-day dynamical state of earthquake potential in New Zealand.

The present chapter has discussed the spatial distribution of contemporary earthquake potential in New Zealand by comparing the geodetic and seismic moment rates. The next chapter, Chapter 5, will present an empirical data-driven technique, known as earthquake nowcasting, to statistically address the current progression of the regional earthquake cycle of major populous city regions in New Zealand.

Chapter 5

Spatial Distribution of Earthquake Cycle Progression in New Zealand Using Earthquake Nowcasting Method

"*The most reliable way to forecast the **future** is to try to understand the present.*"

by John Naisbitt

Similar to the notion of the previous chapter that has geodetically addressed the spatial distribution of earthquake potential in New Zealand, the present chapter has employed an area-based statistical earthquake nowcasting method to quantify the current state of the earthquake cycle in 15 major cities of New Zealand. Essentially, this chapter addresses one of the common questions asked by the academia, industry, and public: "what is the spatial distribution of present crustal deformation cycle and how far along is a city in the earthquake cycle of large-sized events?". To be precise, this chapter examines the current level of seismic progression of a city in its earthquake cycle of large events. The nowcasting approach utilizes the concept of natural times, a quantitative measure of interevent small earthquake counts between two consecutive large events, to provide the current progression of contemporary earthquake cycle of a specified region in terms of earthquake potential score (EPS). As a result, the present chapter provides a nowcast value corresponding to 15 major cities in New Zealand. These EPS values may offer an implicit physical interpretation of regional earthquake dynamics characterized by the cycles of recharge (stress buildup) and discharge (stress release) associated with large events. Therefore, a combination of statistically computed earthquake potential scores (Chapter 5) may be complemented and corroborated with the geodetically observed spatial distribution of earthquake potential (Chapter 4) in order to analyze the current phase of the contemporary earthquake deformation cycle in New Zealand. The content of the present chapter is provided below.

Contents

Parts of this chapter have been published in the following refereed publication:

S. Pasari and **Neha**, "Nowcasting based earthquake hazard estimation at major cities in New Zealand", *Pure and Applied Geophysics*, vol. 179, pp. 1597–1612, 2022 (SCI).

5.1 Introduction

New Zealand and its adjacent regions have experienced many large earthquakes, typically in a well-defined NE-SW belt stretching from Fiordland to East Cape and the Bay of Plenty [14, 47, 102, 241]. Due to the complex tectonic setup of New Zealand, the entire portion of this region observes a very high seismicity exhibiting a number of large to great earthquakes. Consequently, New Zealand regularly suffers from loss of lives along with large amount of socio-economic devastation. For instance, a massive Wairarapa earthquake in 1855 occurred in New Zealand, causing high destruction in Wellington (level 10 in MMI scale), and severe devastation in Whanganui and Kaikoura regions; the 2011 Christchurch earthquake (M_w6.2), an aftershock of the 2010 Canterbury event, damaged the Christchurch and Lyttelton regions and killed 185 people from this region; and, the most recent 2016 Kaikoura earthquake (M_w7.8) caused tremendous damages in terms of landslides and tsunami in the central South Island [86, 161, 267]. Yet, often times, many destructive earthquakes occur in unexpected, assumed-to-be tectonically smooth places, where neither records of previous large earthquakes exist in writing, nor any geological faults have been mapped so far [180, 216]. Such large size earthquakes not only retard the economic growth and successive development of the regions but also cause great destruction to the socio-economic infrastructure in New Zealand. In the wake of long-lasting socio-economic impact from massive earthquakes, developing a robust and reliable metric to determine the "current" level of seismic hazard of a city has become an inevitable task for the safety of millions of people.

As earthquakes have a multiplicity of scales in space and time, such as coherent space–time structures by means of their internal dynamics and the clustering pattern in the earthquake dynamical system, they are typically driven and dissipative. Several other characteristics of earthquakes, for instance, empirical scaling relationship, as illustrated by the Gutenberg-Richter frequency-magnitude power law and Omori's law of aftershock decay [228], spatio-temporal migration and switching mechanism of fault systems [89, 225], streak and hierarchical fault plane geometry [169, 171], macroscopic behavior (e.g., ergodicity and Boltzmann distributions in energy) of far-from-equilibrium earthquake dynamics [213, 214], and the time-series of an ordered pair of earthquake events (e.g., large and small) in a nonlinear, self-organizing, strongly dissipative threshold system [218, 262, 263] exhibit a wealth of information related to the underlying earthquake fault network and consequent hazard analysis.

In order to determine the seismic hazard and current phase of the contemporary earthquake deformation cycle of a region, several techniques, such as geodetic methods and statistical methods, have been employed in past studies. In this thesis, using geodetic observations and

historical seismicity data, Chapter 3 has determined the coseismic phase of the 2016, Kaikoura earthquake by investigating the spatio-temporal surface deformation pattern and Chapter 4 has quantified the strain accumulation and spatial distribution of earthquake potential in New Zealand, whereas the present chapter employs an area-based earthquake nowcasting method that incorporates the idea of earthquake cycle (renewal process) and natural times (the cumulative counts of small events between large earthquakes) to examine the spatial variation in the "current" state of earthquake hazard in terms of earthquake cycle progression at 15 city regions in New Zealand.

Although high-resolution geodetic and geophysical measurements of crustal deformation provide precise information to the tectonic stress regime and earthquake fault kinematics in a defined area, their observational timescales are certainly inadequate to characterize a complete seismic-cycle behaviour [209, 218]. Even in seismological observations, due to the shorter time-span of earthquake catalog, the concept of "seismic-cycle" that traditionally refers to the large repeating earthquakes in a specific fault segment, is slowly being revised to account for the recurrent events in a larger fault system comprising a variety of geological faults [177, 218]. In such situations, statistical view of surrogate-model based seismicity analysis has proved to be more effective in understanding earthquake dynamics and associated earthquake hazard. Likewise, driven by the physical plausibility, the assumption of Poissonian distributed seismicity and associated time-independent seismic hazard evaluations [e.g., 67] have been relaxed in several recent implementations of the time-dependent seismic hazard estimations, including clustering based hazard assessment [e.g., 254], aftershock probabilistic seismic hazard estimation [e.g., 280], sequence-based probabilistic seismic hazard analysis [e.g., 63, 112], and many others [31, 225]. As a consequence, there has been a considerable amount of interest to develop innovative ways to empirically assess earthquake hazard for a strategic disaster mitigation planning. One of the major questions that have certainly garnered attention to the public, policymakers, and earthquake professionals is "what is the spatial distribution of current earthquake hazard and how far along is a city in the earthquake cycle of large sized events?" In order to statistically address this question, the present chapter utilizes the "earthquake nowcasting" method to the evaluation of the current state of seismic hazard at different cities in New Zealand.

Originating from the domains of economics and climate science, the nowcasting method has recently been explored in seismology and disaster science, where the dataset of interest exhibits a typical frequency–size power-law distribution [179, 181, 185, 190, 208, 210, 218]. The nowcasting method is based on two key concepts; one is the stochastic nature of large earthquakes (earthquake cycle) and second is the seismicity statistics of interspersed small event counts (natural times) in a defined fault system [263]. Natural time analysis considers

all seismic events including foreshocks, aftershocks and triggered events to derive the ensemble seismicity statistics in the study area. As the entire study region is presumed to follow a unified driven threshold system, the natural time analysis turns out to be space–time-invariant [143–145, 218]. Since its first formulation in 2016, the seismic nowcasting approach has been used in several countries including the United States, India, Indonesia, Bangladesh, and Pakistan to estimate the contemporary state of regional earthquake hazard [178, 179, 181, 185–188, 215, 218, 227], analysis of induced seismicity [144], spatiotemporal clustering in global seismicity [145], and risk exposure from great global earthquakes or megatsunamis [208, 215]. Several recent studies have shed light on the possible connection of nowcasting with earthquake forecasting and plate tectonics using, for example, natural time Weibull projection, slider-block toy model, space–time clustering behavior of bursts of small earthquakes and time-dependent earthquake cycle analysis through machine learning [100, 190, 208]. A comprehensive review of nowcasting, forecasting and earthquake prediction is provided by Rundle et al. (2021) [217].

Influenced by the thoughtfulness and robustness of the nowcasting approach, the present chapter focuses on statistically addressing the problem related to the evaluation of the current state of seismic hazard at 15 major cities in New Zealand. The nowcasting analysis consists of three broad steps: preparing data (natural times), deriving seismicity statistics of natural times, and computing earthquake potential score (nowcast scores) for a given city in the study region. In this regard, the earthquake data is collected for the time period of $1963-2021$. Using the collected earthquake data, the natural times are tabulated. The sequence of observed natural times thereby leads to develop several probability distribution models. After developing the natural time statistics, the best-fit cumulative distribution of natural times is further used to quantify the spatial distribution of time-dependent earthquake potential score (EPS) over New Zealand. These EPS scores essentially serve as a yardstick to statistically assess the current progression of a city in its seismic cycle of large earthquakes. The spatial distribution of earthquake hazard through natural times, analogous to conventional seismic hazard maps, provides useful information to the decision-makers, engineers, scientists, and citizens to improve preparedness and mitigation strategies in the active regions of New Zealand. A step-by-step procedure of the earthquake nowcasting technique is provided in the following sections.

5.2 The genesis and state-of-the-art of the nowcasting method

A driven, nonlinear, self-organizing earthquake fault system strongly correlates in space and time and typically displays a multiplicity of spatial and temporal scales. In order to analyze the earthquake fault systems, the statistical mechanics of earthquakes is essential to understand. In view of this, Rundle et al. (1996, 1997) [213, 214] proposed the “traveling density wave”

(TDW) model to characterize the physical processes of driven nonlinear threshold systems. They observed that the earthquake threshold systems exhibit Boltzmann energy distribution, which essentially suggests that it is reasonable to consider ergodicity in seismogenesis processes. Later on, in continuation of the previous work, Rundle et al. (1997) [211] studied several modern statistical mechanical concepts of earthquakes and earthquake fault-systems as a kind of "phase-transition" in order to understand the interrelation between scaling laws (G-R frequency-magnitude and Omori's law of aftershock decay) and earthquake dynamics. These studies have suggested that the macroscopic behavior (e.g., ergodicity, Gibbs Boltzmann distributions) of some far-from-equilibrium systems (e.g., earthquakes) is obtainable in terms of equilibrium statistical mechanics and thereby, these properties can be analyzed using the method of statistical mechanics [57]. In addition, origin of the physics of scaling, critical phenomena, and nucleation behavior in earthquake system appear to lie in the ergodic properties of the earthquake threshold system [207]. Moreover, based on the fundamental of physics of earthquakes, several statistical physics-based approaches, such as sand-pile models, forest-fire models, and slider-block models have been developed and consequently demonstrated to forecast earthquakes in a different viewpoint than the conventional probabilistic earthquake hazard assessment techniques [57, 219]. For the development of possible forecasting methods for earthquakes or for showing that such methods are not possible, Ferguson et al. (1999) [62] and Tiampo et al. (2003, 2007) [249, 250] identified the equilibrium property of ergodicity in an earthquake fault system. At a later stage, this ergodic nature of earthquake was used in the foundation of earthquake forecasting and subsequent earthquake nowcasting method.

While the development of several properties related to statistical mechanics of earthquakes or ergodicity in earthquake fault networks is still in progress, the "natural time" concept, proposed by Varotsos et al. (2001) [261], is a path-breaking idea. This concept utilizes an interevent count of the small earthquakes between two large earthquake events in place of conventional clock/calendar time. Natural time analysis enables the study of the dynamical phase evolution of a complex earthquake system and identifies when the system enters into a critical state [222]. For instance, Varotsos et al. (2011) [263] carried out the natural time analysis for modeling the seismic electric signals, earthquakes, and other complex systems; Rundle et al. (2012) [212] incorporated the natural times to develop a forecast probability method, namely the natural time Weibull method (NTW), in which the conditional probabilities of occurrence of avalanche event sizes are computed as projecting the current activity forward in time. Thereafter, Holliday et al. (2016) [100] improved the NTW method by considering a finite correlation length and by employing the correlation function for near mean-field systems having long-range interactions and elastic interactions. The key idea of the NTW model is to understand how the probability of a forthcoming large earthquake in a region is affected by the progress of the earthquake cycle of that region. This chapter deals with the area-based earthquake nowcasting

approach in New Zealand.

The nowcasting refers to the quantification of present seismic level of the earthquake cycle and provides the current state of a regional fault system. The earthquake nowcasting was firstly implemented by Rundle et al. (2016) [218] in the California-Nevada region. The crux of the nowcasting method is that it initially develops seismicity statistics of natural times over a larger region, and then applies the same seismicity statistics for several smaller regions embedded in the larger region. In essence, the nowcasting analysis uses ergodicity nature in its implementation. Thus, using the seismicity statistics of natural times, the earthquake potential score (EPS) is computed as the cumulative probability distribution for the current count for small earthquakes in the region. Physically, the EPS corresponds to an estimate of the level of progress through the earthquake cycle in the defined region at the current time. Such a concept can rapidly and efficiently estimate the "current" dynamic state of a regional fault system and consequent earthquake hazards. Also, these are useful for disaster preparation and allied tasks.

Over time, the nowcasting method has gained more attention and has been widely implemented to determine the current state of the fault system and its current level of progress through the earthquake cycle in different regions over the world. For instance, Luginbuhl et al. (2018) [143] applied the nowcasting method to better understand induced seismicity at the Geysers geothermal area, California, and in Oklahoma; in another study, Luginbuhl et al. (2018) [145] adopted the nowcasting idea to examine the temporal clustering of large global earthquakes with respect to natural time, as opposed to regular clock time; Pasari (2018) [179] applied this method to quantify the earthquake potential score of the two most seismically exposed megacities, Dhaka and Kolkata; Rundle and Donnellan (2020) [208] utilized the natural time idea to characterize earthquake processes by cycles of recharge and discharge though some noticeable patterns in the seismicity clustering of aftershock sequences and seismic swarms in Southern California; in 2020 and 2021, Pasari et al. [178, 185–187] also carried out natural time analysis for quantification of the synoptic view of earthquake potential in the whole Himalayan region, Sumatra, Java Island, and Sulawesi Island; and, Perez-Oregon et al. (2020) [190] are utilized a combination of the slider block model of Olami-Feder-Christensen and log-normal distribution fitted model for transforming the nowcasting models into forecasting models. In addition, the nowcasting method has implications in the study of volcano eruptive sequence, megatsunami, and most recently in the prediction of the extreme events of air pollution in megacities [64, 208, 260].

In the recent development of the seismic nowcasting method, several machine learning approaches (supervised and unsupervised) are used for the purpose of anticipating future earthquake activity and relating that activity to the underlying physics. For instance, Rundle et al. (2021) [210] used principal component analysis to compute the nowcasting time series that resembles the hypothesized regional stress accumulation and release process characterizing the

current state of the earthquake cycle; Fox et al. (2022) [66] introduced new approaches based on deep learning using three distinct models based on recurrent neural networks and transformers for the earthquake nowcasting, and Rundle et al. (2022) [220] carried out optimizing earthquake nowcasting with machine learning in order to reveal the hidden variables relates to a mechanism of seismic quiescence arising from the physics of strain-hardening of the crust prior to major events. In essence, the advancement of earthquake nowcasting enables researchers to expose the unseen features, that are otherwise seemingly chaotic earthquake seismicity, related to a seismic mechanism of the crust prior to major events [220] as well as to establish the correlation with regional tectonic stress to earthquake statistics [210]. Therefore, earthquake nowcasting is a promising approach for better characterizing the present and future state of earthquake cycle in a given region. In the present study, the earthquake nowcasting method is implemented in New Zealand and the results are presented in terms of earthquake potential score (EPS) at 15 major population centers in New Zealand.

5.3 Preliminaries

In order to develop the seismicity statistics on natural times, the earthquake nowcasting method utilizes the probability distribution models. Recall that, natural time is a quantitative measure of small event counts between two large successive events. Natural times are random in nature and are distributed independently and identically. Assuming natural times as a random variable and its inherent characteristics having exponential scaling according to G-R frequency-magnitude law (see Equation 5.22), several probability distribution models, such as exponential family and its closely related distributions have been used in previous studies [177, 179, 180, 217, 218]. Therefore, the present study considers four candidate probability distributions, namely exponential, gamma, Weibull, and exponentiated exponential distributions to derive the natural time statistics in New Zealand. A brief description of these four probability distributions is provided below.

5.3.1 Distribution models

In this section, a brief explanation on the genesis of the above-mentioned four studied distributions, their model properties and interrelationships among themselves are provided.

5.3.1.1 Exponential distribution

Since earthquake events are traditionally assumed to occur according to the Poissonian principle, the exponential distribution is often used as a basis in earthquake modeling. This distribution has wide application in a variety of domains, such as reliability engineering, survival

analysis, chemical engineering, hydrology, psychology and finance [177, 180]. In the earthquake nowcasting method, it is considered to be the benchmark distribution for developing natural time statistics [180].

Let T be a random variable. If T follows an exponential distribution, then the density function is expressed as:

$$F(t,\alpha) = \frac{1}{\alpha} exp\left[-\frac{t}{\alpha}\right]; \qquad t > 0,\ \alpha > 0 \tag{5.1}$$

Here, α is the scale parameter that assumes positive value, known as decay rate.

5.3.1.2 Gamma distribution

Gamma distribution, as a generalization of the exponential distribution, belongs to the family of the two-parameter continuous probability distributions. This distribution is often applied to model the time between independent events (e.g., stochastic process) that occur at a constant average rate [115]. It is a versatile distribution and provides useful inherent characteristics of many physical situations, such as rainfall estimation, seismic recurrence analysis, and econometrics. In addition, the gamma distribution is used as a conjugate prior distribution for many scale parameters in Bayesian statistics, such as the parameter in an exponential distribution or a normal distribution with a known mean [115].

If a random variable T follows gamma distribution, then the density function is given as:

$$F(t,\alpha) = \frac{1}{\Gamma(\beta)} \frac{t^{\beta-1}}{\alpha^{\beta}} exp\left[-\frac{t}{\alpha}\right]; \quad t > 0,\ \alpha > 0,\ \beta > 0 \tag{5.2}$$

Here, $\Gamma(.)$ denotes the gamma function, whereas α and β are the scale and shape parameters, respectively.

5.3.1.3 Weibull distribution

Like the gamma distribution, the Weibull distribution has stemmed from the exponential distribution. The Weibull distribution is characterized by a continuous random variable whose probability distribution is controlled by two parameters: $\alpha-$scale parameter and $\beta-$shape parameter [279]. There is a close relationship between the Weibull distribution and other probability distributions by taking the different choices of scale and shape parameters. For example, it turns out to be exponential and Rayleigh distributions for $\beta = 1$ and $\beta = 2$, respectively. In addition, it has the ability to provide a reasonable prediction even with extremely small sample size. Therefore, the Weibull distribution has been the most popular and versatile probability distribution in the field of reliability and survival analysis. Besides, it has been widely used in

numerous fields such as engineering psychology, seismology, hydrology, business, economics, and ecology [157].

The density function of the two-parameter Weibull random variable T is given as:

$$F(t,\alpha) = \frac{\beta}{\alpha} t^{\beta-1} exp\left[-\left(\frac{t}{\alpha}\right)^{\beta}\right]; \quad t>0,\ \alpha>0,\ \beta>0 \tag{5.3}$$

Here, α and β denote the scale and shape parameters, respectively.

5.3.1.4 Exponentiated exponential distribution

The exponentiated exponential distribution, like the gamma and Weibull distributions, is an extension of classical exponential distribution [82]. In this model, an exponential distribution is taken as the base distribution. Due to similar physical properties as gamma and Weibull distributions, the exponentiated exponential distribution has widespread applications in the field of medical, earthquake modeling, and biological research [83, 182].

The density function of the exponentiated exponential random variable T is defined as:

$$F(t,\alpha) = \alpha\beta\left(1-e^{-\alpha t}\right)^{\beta-1} e^{-\alpha t}; \quad t>0,\ \alpha>0,\ \beta>0 \tag{5.4}$$

Here, α and β are the inverse-scale parameter and shape parameter, respectively. The shape parameter β plays the most important role in exponentiated exponential model description. It is easy to note that if $\beta = 1$, exponentiated exponential distribution coincides with its base distribution which is exponential distribution.

After a brief description of the probability models and their associated properties, the statistical inference in terms of parameter estimation, uncertainty analysis, and model validation has been discussed below.

5.3.2 Parameter estimation

In order to develop the seismicity statistics in the earthquake nowcasting, the successive step is to estimate the parameters of four studied distribution models. To choose an appropriate estimator, several statistical methods, such as the method of moments (MoM), linear estimation methods, and the maximum likelihood estimation (MLE) have been employed in practice. Among these methods, the suitable estimator is often selected based on its performance in terms of favourable properties, such as unbiasedness, consistency, and efficiency [99, 157]. In the present study, the MLE method is considered for estimating the parameters associated to the underlying distribution due to its consistency, compactness, and rigorous asymptotic normality properties. The MLE method not only estimates the model parameters but also provides an

uncertainty measure for the estimated parameters. A step-by-step implementation of the MLE method for all of the studied distributions is discussed here.

Maximum likelihood estimation

For any probability distribution model, the MLE method can be implemented in a two-fold way. (i) Define the likelihood function as a function of model parameters θ and (ii) solve the associated likelihood equations to obtain the corresponding parameter estimates [115]. In general, the likelihood function is defined as:

$$L(\theta|t) = \prod_{i=1}^{n} f(t_i;\theta) \tag{5.5}$$

It may be noted that θ could be a single parameter or a vector of parameters like $\theta = (\theta_1, \theta_2, ..., \theta_p)$, for some integer p. The estimated value of parameter is denoted as $\hat{\theta}$. The likelihood function (log-likelihood function) and associated likelihood equations for all distributions are provided below.

- **Exponential distribution**

  The log-likelihood function for exponential distribution is given as:

$$\ln L(\theta|t) = \ln L(\alpha;t_1,t_2,...,t_n) = -n\ln\alpha - \sum_{i=1}^{n}\frac{t_i}{\alpha} \tag{5.6}$$

  The corresponding estimate from the log-likelihood equation is obtained as:

$$\frac{\partial}{\partial\alpha}\ln L(\alpha;t_1,t_2,...,t_n) = 0 \implies \hat{\alpha} = \frac{1}{n}\sum_{i=1}^{n} t_i \tag{5.7}$$

- **Gamma distribution**

  The log-likelihood function of gamma distribution is given as:

$$\ln L(\theta|t) = \ln L(\alpha,\beta;t_1,t_2,...,t_n) = -n\beta\ln\alpha - n\ln\Gamma(\beta) - \sum_{i=1}^{n}\frac{t_i}{\alpha} + (\beta-1)\sum_{i=1}^{n}\ln t_i \tag{5.8}$$

  The likelihood equations are

$$\frac{\partial}{\partial\alpha}\ln L(\alpha,\beta;t_1,t_2,...,t_n) = 0 \implies \alpha\beta = \frac{1}{n}\sum_{i=1}^{n} t_i \tag{5.9}$$

$$\frac{\partial}{\partial\beta}\ln L(\alpha,\beta;t_1,t_2,...,t_n) = 0 \implies \ln\alpha + \frac{\Gamma'(\beta)}{\Gamma(\beta)} = \frac{1}{n}\sum_{i=1}^{n}\ln t_i \tag{5.10}$$

The explicit solution of the above likelihood equations is extracted by using the numerical approaches, such as bracketing method, Newton Raphson method, and fixed point iteration [180].

- **Weibull distribution**
  The log-likelihood function for Weibull distribution is given as:

$$\ln L(\theta|t) = \ln L(\alpha,\beta;t_1,t_2,...,t_n) = n\ln\beta - n\beta\ln\alpha + (\beta-1)\sum_{i=1}^{n}\ln(t_i) - \sum_{i=1}^{n}\left(\frac{t_i}{\alpha}\right)^{\beta} \quad (5.11)$$

  The associated log-likelihood equations are

$$\frac{\partial}{\partial\alpha}\ln L(\alpha,\beta;t_1,t_2,...,t_n) = \alpha^{\beta} - \frac{1}{n}\sum_{i=1}^{n}t_i^{\beta} = 0 \quad (5.12)$$

$$\frac{\partial}{\partial\beta}\ln L(\alpha,\beta;t_1,t_2,...,t_n) = \frac{n}{\beta} + \sum_{i=1}^{n}\left[1-\left(\frac{t_i}{\alpha}\right)^{\beta}\right]\ln\left(\frac{t_i}{\alpha}\right) = 0 \quad (5.13)$$

  Explicit solution of the above likelihood equations cannot be obtained. Hence, single variable non-linear approach is used to estimate $\hat{\beta}$. Subsequently, the scale parameter $\hat{\alpha}$ can be estimated.

- **Exponentiated exponential distribution**
  The log-likelihood function of the exponentiated exponential distribution is defined as:

$$\ln L(\theta|t) = \ln L(\alpha,\beta;t_1,t_2,...,t_n) = n\ln\beta + n\ln\alpha - \alpha\sum_{i=1}^{n}t_i + (\beta-1)\sum_{i=1}^{n}\ln(1-e^{-at_i}) \quad (5.14)$$

  The associated log-likelihood equations are

$$\frac{\partial}{\partial\alpha}\ln L(\alpha,\beta;t_1,t_2,...,t_n) = \frac{n}{\alpha} + (\beta-1)\sum_{i=1}^{n}\left(\frac{t_i e^{-\alpha t_i}}{1-e^{-\alpha t_i}}\right) - \sum_{i=1}^{n}t_i = 0 \quad (5.15)$$

$$\frac{\partial}{\partial\beta}\ln L(\alpha,\beta;t_1,t_2,...,t_n) = \frac{n}{\beta} + \sum_{i=1}^{n}\ln(1-e^{-\alpha t_i}) = 0 \quad (5.16)$$

  The above likelihood equations can be solved by various numerical techniques as mentioned above.

Having estimated the model parameters, it is imperative to assess the quality of the estimated parameters. In this regard, an uncertainty analysis of estimated parameters is carried out in the following section.

5.3.3 Uncertainty measures

In order to assess the quality of the estimated parameters, it is essential to carry out uncertainty analysis in the estimation process. In this regard, statistical estimation methods have been employed to assess different uncertainty measures, such as standard error and confidence bounds for each of the estimated parameters [99]. The confidence bounds (interval) of the estimated parameters play a key role in decision making. However, most of the time, the exact distributions of the estimated model parameters are not available. In such cases, the law of large samples is often used as a proxy to asymptotically estimate the variance-covariance matrix and confidence bounds of the estimated parameters [115]. In this present work, the asymptotic variance-covariance matrix of estimated parameters is obtained in terms of a matrix, called the Fisher information matrix (FIM) and the associated confidence interval is calculated using the Cramer-Rao lower bound theorem.

5.3.3.1 Fisher information matrix

The Fisher information enables a way of measuring the amount of information that an observable random variable (let, T) carries about an unknown parameter (let, θ) upon which the probability of T depends. In another way, the FIM provides an amount of uncertainty (in terms of asymptotic variance) of the estimated parameters. Therefore, the FIM associated with any distribution is important both from the theoretical as well as application point of view.

To illustrate, let T be a single variable with n parameters $\theta = (\theta_1, \theta_2, ..., \theta_n)$. If T follows a probability distribution with its density function $f(T;\theta)$, then the FIM is defined as:

$$I_{n\times n}(\theta) = E\left[\left[\frac{\partial}{\partial\theta_i}\ln f(T;\theta)\right]_{n\times 1} \times \left[\frac{\partial}{\partial\theta_i}\ln f(T;\theta)\right]^{T}_{1\times n}\right]; \qquad i = 1,2,...,n \tag{5.17}$$

Here, $\frac{\partial}{\partial\theta_i}$ denotes the partial derivative with respect to θ_i; $i = 1,2,...,n$, and E denotes the expectation operator. Using Equation 5.17, the Fisher information matrix of four studied probability distributions is computed and provided in Table 5.1. Note that the Fisher information matrix will be further used to compute the confidence interval of the estimated parameters.

Table 5.1: Fisher information matrix (FIM) of four studied probability distributions.

Distribution	FIM $I(\theta)$
Exponential	$\frac{1}{\alpha^2}$
Gamma[a]	$\begin{bmatrix} \frac{\beta}{\alpha^2} & \frac{1}{\alpha} \\ \frac{1}{\alpha} & \psi'(\beta) \end{bmatrix}$
Weibull[a]	$\begin{bmatrix} \frac{\beta^2}{\alpha^2} & -\frac{1}{\alpha}(1+\psi(1)) \\ -\frac{1}{\alpha}(1+\psi(1)) & \frac{1}{\beta^2}(\psi'(1)+\psi^2(2)) \end{bmatrix}$
Exponentiated exponential[a]	$\begin{bmatrix} a_{11} & a_{12} \\ a_{21} & a_{22} \end{bmatrix}$
	$a_{11} = \frac{1}{\alpha^2}\left[1+\frac{\beta(\beta-1)}{\beta-2}(\psi'(1)-\psi'(\beta-1))+(\psi(\beta-1)-\psi(1))^2\right]$
	$-\frac{\beta}{\alpha^2}\left[\psi'(1)-\psi(\beta)+(\psi(\beta)-\psi(1))^2\right];\beta\neq 2$
	$a_{12}=a_{21}=\frac{1}{\alpha}\left[\frac{\beta}{\beta-1}(\psi(\beta)-\psi(1))-(\psi(\beta+1)-\psi(1))\right];\beta\neq 1$
	$a_{22}=\frac{1}{\beta^2}$

[a] $\psi(t)$ and $\psi(t)'$ denote the digamma function and it's first derivate.

5.3.3.2 Cramer-Rao lower bound theorem

The Cramer-Rao bound refers to the lower bound on the variance of n unbiased estimators of a deterministic (fixed, though unknown) parameter. For example, let $\hat{\theta}$ be the MLE estimate of θ, then the $(1-\delta)\%$ two-sided confidence interval of the parameter is obtained from the asymptotic normality of the MLE estimated parameters, as:

$$\hat{\theta} - z_{\delta/2}\sqrt{Var(\hat{\theta})} < \theta_1 < \hat{\theta} + z_{\delta/2}\sqrt{Var(\hat{\theta})} \tag{5.18}$$

Here, $Var(\hat{\theta})$ represents the variance of the estimated parameter $\hat{\theta}$ and it is obtained from the diagonal entries of Fisher information matrix and $z_{\delta/2}$ is the critical value corresponding to a significance level of δ on the standard normal distribution (obtained from standard normal distribution table). Further, it is important to note that the MLE is a UMVE (Uniform Minimum

Variance Estimator) and it attains Cramer-Rao lower bound when the sample size tends to infinity. This implies that neither any other estimator can be more efficient than the MLE, nor the variance of the estimated parameters obtained from any other estimators can be lesser than that of obtained in MLE [99, 115, 157].

After estimating the model parameters and their confidence bounds, it is essential to choose the best fit model that represents the given data more meaningfully. For this, several model selection criteria have been adopted to appraise the comparative fitness of the studied distributions. A brief detail of such model selection criteria is provided in the following section.

5.3.4 Model selection

To choose the best-fit probability model among four studied distributions, two goodness-of-fit tests are incorporated in the present study. These methods are the Akaike information criteria (AIC) and the Kolmogorov-Smirnov (K-S) minimum distance criterion. Both methods provide a measure of model performance based on the discrepancy between observed values and the expected values under the model. As a result, the best-fit parametric model is obtained and will be further used to compute the EPS score through the associated cumulative distribution function. An overview of each method is provided below.

5.3.4.1 Akaike information criterion

The Akaike information criterion is an operational way to measure the tradeoff between the fitting accuracy and the complexity of the model due to more number of parameters [2]. The AIC provides a relative goodness-of-fit of a statistical model. The AIC value of the model is defined as:

$$\mathrm{AIC} = 2k - 2\ln L \tag{5.19}$$

Here, k denotes the number of parameters in the model and $\ln L$ is the log-likelihood value as obtained in MLE. The first term is known as the penalty and the second term is known as the goodness-of-fit term. Increasing complexity of the candidate model in terms of more number of parameters leads to an increase in the penalty term. As a result, the model with the minimum AIC value is chosen as the most economic model for representing a data set.

5.3.4.2 Kolmogorov-Smirnov minimum distance criterion

The Kolmogorov-Smirnov (K-S) minimum distance criterion prioritizes the competing models based on their "closeness" to the empirical distribution function of the sample data $(t_1, t_2, \ldots, t_n)$. The empirical distribution function H_n, for n i.i.d. random variables T_1,T_2,...,T_n, is calculated

as:

$$H_n(t) = \frac{1}{n}\sum_{i=1}^{n} I_{T_i \leq t} \tag{5.20}$$

Here, $I_{T_i \leq t}$ is the indicator function that equals to 1 if $T_i \leq t$ and otherwise it equals to 0. This makes $H_n(t)$ a step function.

To illustrate, let F and G be two competitive models. Then, the corresponding K-S distances are calculated as:

$$\begin{aligned} D_1 &= \sup_{-\infty<t<\infty} |H_n(t) - F(t)| \\ D_2 &= \sup_{-\infty<t<\infty} |H_n(t) - G(t)| \end{aligned} \tag{5.21}$$

In the above expression, $\sup_t$ denotes the supremum of the set of distances. As a result, the model with a minimum distance measure is chosen as the best-fit model. For instance, if $D_1 < D_2$, model F is chosen, otherwise model G is chosen. The K-S test is highly recommended for comparison and validation of distributions arising from different families due to its dual advantages: non-parametric nature and possibility to appraise overall fitting analysis from the K-S plot. Therefore, the K-S test is one of the efficient methods to choose the best-fit distribution [115, 157].

In summary, in order to develop the natural time statistics in the earthquake nowcasting method, it includes probability model assumption, parameter estimation, uncertainty measure of these estimated parameters, and model selection, as discussed above. The resultant best-fit model will be used to compute the earthquake potential score of the target regions.

In the present study, the natural time statistics is formulated for the quantification of the current progression of earthquake cycle of major cities in New Zealand. For this purpose, the entire New Zealand and its surrounding regions are considered as the study area.

5.4 Study area

New Zealand is one of the documented examples of a plate boundary where the plate configurations change from subduction to strike-slip by a 1000-km long stretch of dextral oblique slip faults, collectively known as the Axial tectonic belt (Fig. 5.1) [14, 102, 191, 241, 267]. New Zealand consists of two major continents, namely the North Island and the South Island, straddling between two tectonic plates–the Pacific plate to the east and the Australian plate to the west. The north-eastern part of the North Island displays the collision zone in which the Pacific plate is subducting under the Australian plate at a rate of $40-60$ mm/year along the Hikurangi subduction zone, whereas the northern part of the South Island shows a dominant strike-slip movement on the Marlborough fault zone along the Alpine fault, at a decreasing rate up to $\sim 35-37$mm/year at the south-western tip of the Island, and it finally returns to the subduction

zone at the Puysegur Trench offshore Fiordland (Fig. 5.1) [14, 21, 24, 184, 231]. Because of the complex geodynamical process of New Zealand, the tectonic setup can be described as follows. The active tectonics dominate at the Hikurangi trough and the back-arc of the Taupo Volcanic Zone in the North Island, on the Marlborough fault system comprising four strike-slip faults, namely the Hope, Clarence, Awatere, and Wairau faults in the central South Island, and at the Alpine fault that connects the Marlborough fault system into the Fiordland region (Fig. 5.1) [111, 259, 272]. Therefore, all of the relative motion is accommodated by the faults of the Axial tectonic belt and Hikurangi subduction zone along with the Taupo Volcanic Zone [272].

The active faults of New Zealand have produced frequent large earthquakes in the historical period. Some notable earthquakes are the 1855 Wairarapa earthquake ($M_w 8.1-8.2$), 1929 Buller earthquake ($M_w 7.6$), 1931 Hawke's Bay earthquake ($M_w 7.8$), 1968 Inangahua earthquake ($M_w 7.2$), 1987 Edgecumbe earthquake ($M_w 6.5$), 1993 Fiordland earthquake ($M_w 7.0$), $2010-2011$ Canterbury earthquakes ($M_w 7.1-6.2$), 2013 Cook Strait earthquake sequence ($M_w 6.6$) and the 2016 Kaikoura earthquake ($M_w 7.8$) [18, 49, 88, 89, 192, 232, 274]. Most of these earthquakes in the study region (164°E–183°E, 32°S–51°S) occur at a shallow to intermediate depth [85]. A pictorial illustration of the seismotectonic setup of the study region is provided in Fig. 5.1.

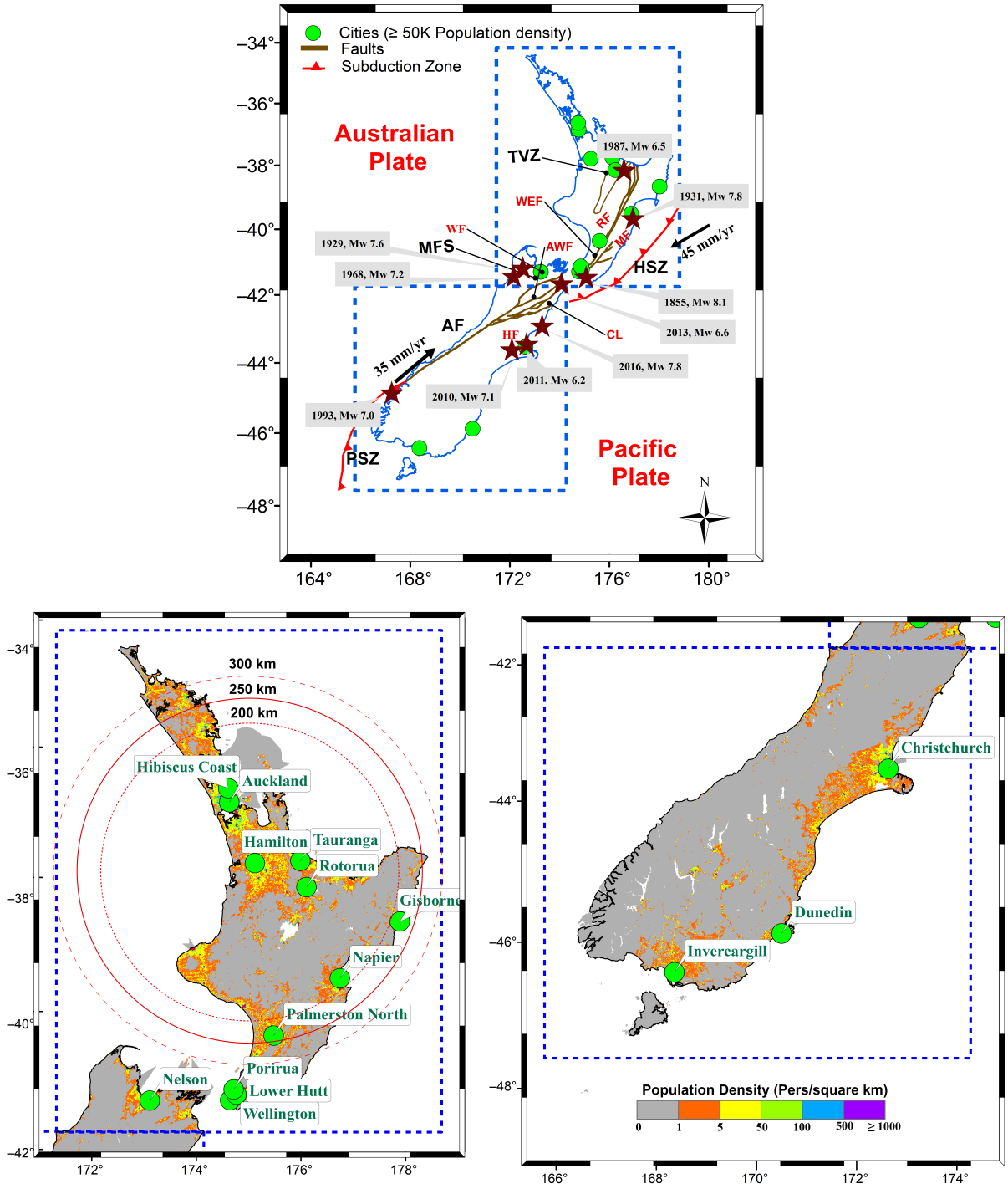

Fig. 5.1: (a) Tectonic setup of New Zealand along with some geologically active faults; some historic earthquakes are represented by dark red stars, (b) population density map and major populated cities of North Island; red circles centered at Hamilton and radii of 200, 250, and 300 km demonstrate "small" local regions that have been considered to compute nowcast values, and (c) major populated cities of South Island. Abbreviations are as follows: HSZ, Hikurangi subduction zone; MFS, Marlborough fault system; PSZ, Puysegur subduction zone; AF, Alpine fault; TVZ, Taupo volcanic zone; HF, Hope fault; WF, Wairau fault; CL, Clarence fault; AWF, Awatere fault; WEF, Wellington fault; RF, Ruahine fault; M, Mohaka fault.

5.5 Earthquake data

To develop nowcasting technique, the earthquake data for the present analysis comprises $M \geq 4.0$ events during the time period of $1963-2021$. The instrumental seismicity data are acquired from two global earthquake sources, namely ANSS (Advanced National Seismic System) and ISC (International Seismological Center), to prepare this dataset. Within a focal depth of 100 km, there are 8532 events ($4.0 \leq M \leq 7.8$), including 91 cycles of large earthquakes ($M \geq 6.0$). The earthquake data is pictorially shown in Fig. 5.2. Considering magnitude 4.0 as the threshold of small earthquake events (also, the magnitude completeness threshold) and magnitude 6.0 as the large earthquake, the natural time counts are computed. Subsequently, these counts will be used to develop the natural time statistics. Recall that nowcasting analysis via natural time statistics does not require declustering of dependent events, such as foreshocks and aftershocks [218].

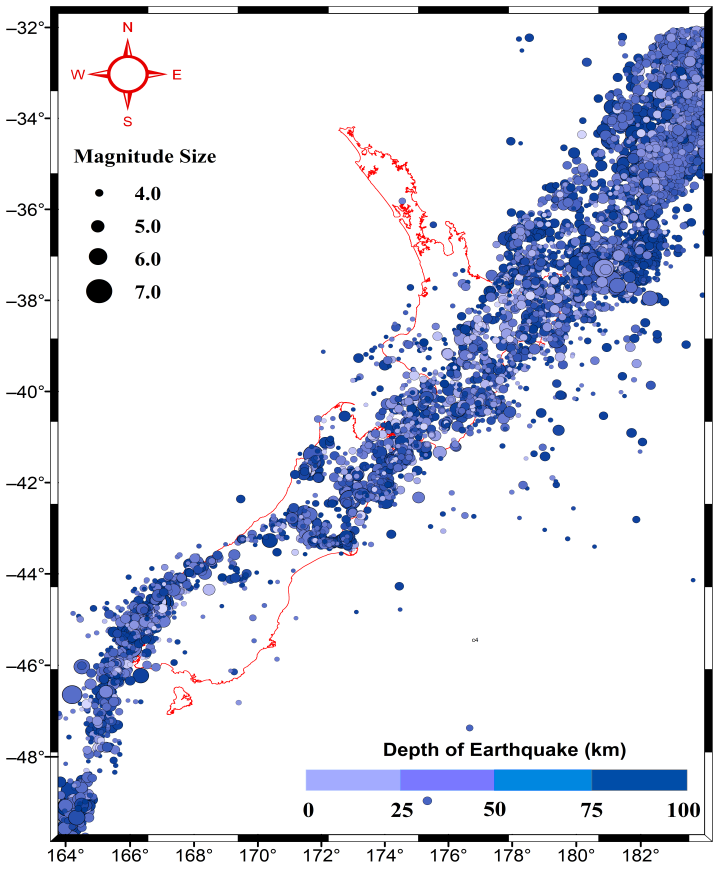

Fig. 5.2: Seismicity map of the study region. The colored circles represent the earthquake events during the time period $1963-2021$. The seismicity of New Zealand is aligned to the NE-SW direction along the Axial tectonic belt.

5.6 Method and results

To derive the ensemble statistics of natural times, it is essential to define a large geographic area, small local area, threshold magnitude of large event (M_λ) and the threshold magnitude of small event (M_σ) to determine the EPS for the region. While the "large" geographic area usually comprises the entire study region, a smaller circular city area embedded in the larger region demarcates the "local" area. Similarly, the "large" earthquake threshold is determined based on the extent of possible damage or destruction to the study area, whereas the threshold magnitude of "small" events is often determined from the data completeness level. To illustrate, let N_σ be the cumulative number of small earthquakes having magnitudes greater than M_σ and N_λ be the number of earthquakes having magnitudes greater than M_λ. Using the G-R power law for cumulative count of earthquakes having magnitudes greater than M_σ and M_λ, the relation is defined as, $N_\sigma = 10^{(a-bM_\sigma)}$ and $N_\lambda = 10^{(a-bM_\lambda)}$ respectively, for some constants a and b. Thus, the mean intermittent count of the small events N, that occur between two subsequent large earthquakes, can be computed by setting, $N_\lambda = 1$, as

$$N = \frac{N_\sigma - N_\lambda}{N_\lambda} = 10^{b(M_\lambda - M_\sigma)} \tag{5.22}$$

From Equation 5.22, it can be observed that the average statistics measure of natural times is independent of background seismicity rate (a), which may be dominated by aftershocks, triggering events, or earthquake swarms, and it scales exponentially with the difference of magnitudes M_σ and M_λ. As a consequence, the natural time statistics are generally homogenous in space, provided that the $b-$value is close to a constant. Fig. 5.3 provides a pictorial summary of the catalog in terms of the classical Gutenberg-Richter frequency-magnitude plot and magnitude-time graph. It is observed that the magnitude completeness threshold based on the least-squares linear regression equation turns out to be around 4.0 and the completeness threshold is largely homogeneous over time.

Having discussed the ensemble statistics of the natural times above, the next section describes a step-wise mathematical formulation of the earthquake nowcasting method. This method comprises three major steps in succession: tabulation of natural times (interevent counts between large events), performing statistical inference, and computation of earthquake potential score (nowcast scores). In the present analysis, the "area-source" nowcasting method is performed to compute the earthquake potential score of 15 major cities of New Zealand. The implementation of this method and its corresponding results are also discussed in the following sections.

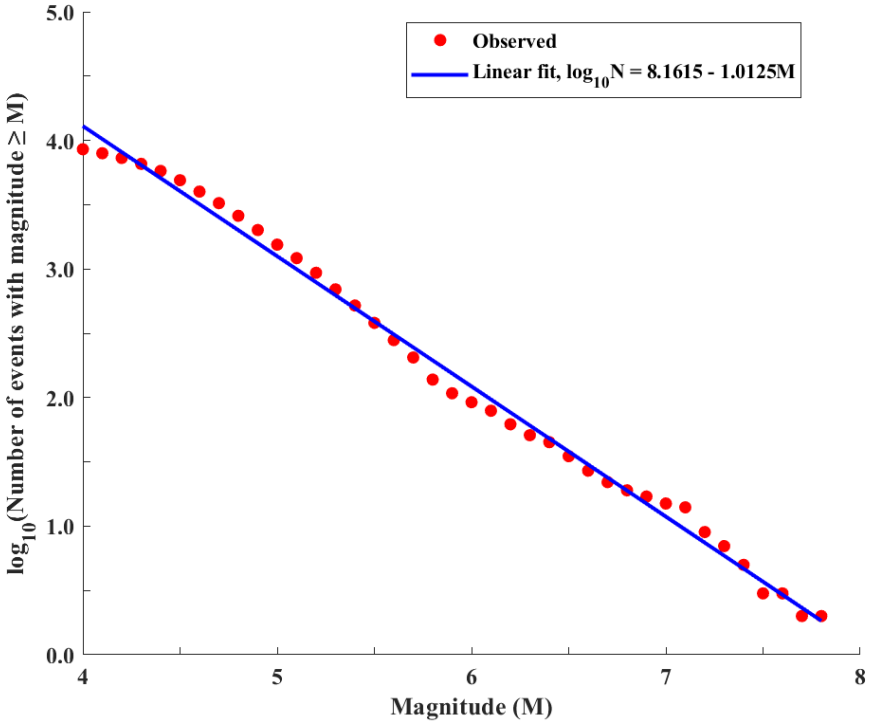

(a)

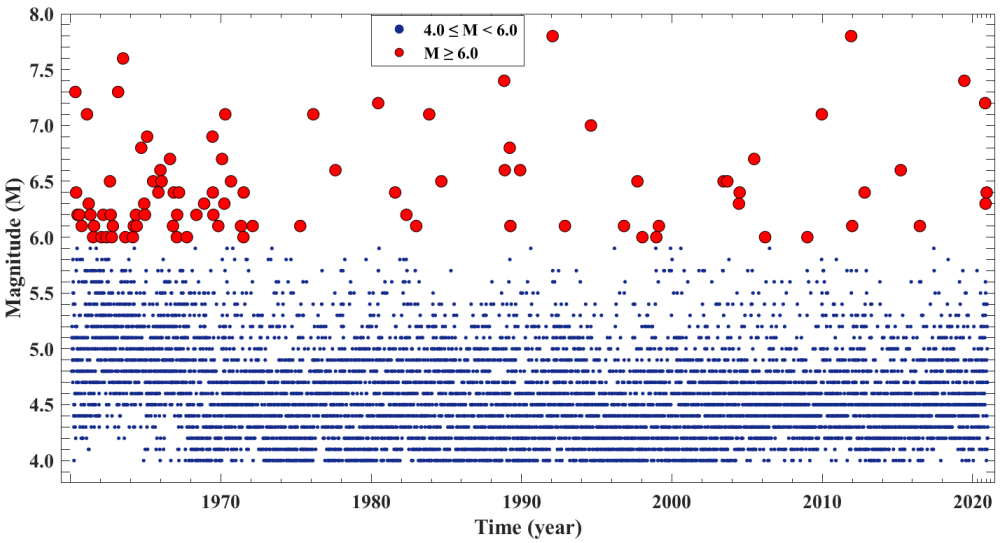

(b)

Fig. 5.3: (a) Ordinary least-squares fitting to the frequency-magnitude distribution and (b) magnitude versus time plot for the present earthquake catalog in the study region.

5.6.1 The earthquake nowcasting analysis: mathematical formulation

As mentioned before, in order to compute the nowcast value associated to the target region, the earthquake nowcasting method is implemented in three steps.

The first step is to tabulate natural times, the cumulative counts of "small" earthquakes between successive "large" events, in order to derive ensemble seismicity statistics of natural times (say, X) for the entire geographic region (A). This step necessitates defining two threshold magnitudes M_σ and M_λ corresponding to "small" and "large" earthquakes, respectively. For the present study, the threshold magnitude of the small and large events are chosen as $M_\sigma = 4.0$ and $M_\lambda = 6.0$, respectively. Considering these threshold magnitudes, the studied earthquake catalog ($1963-2021$) provides a sample data of 91 natural times, say $x_1, x_2, ..., x_{91}$ for analysis.

In the second step of the procedure, the statistical distribution models are developed to the observed natural time counts. To do so, four probability distribution models, namely exponential, gamma, Weibull, and exponentiated exponential distributions are incorporated based on the previous nowcasting-related studies [183, 218]. With the inferred natural time statistics of the "large" region based on selected reference probability distributions, the method applies the same seismicity statistics to all 15 target city regions (say, $A_1, A_2, A_3, ..., A_{15}$) that lie within the geographical boundary of A (see Fig. 5.1). It may be noted that the space–time invariance of natural time statistics follows from the theoretical ergodic dynamics in earthquake mechanics, in which the seismicity statistics of smaller areas and associated larger area over longer time periods is assumed to be identical [100, 218, 250].

In the final step, the earthquake potential score (EPS) for each local region (say, A_1) is computed through the value of the cumulative distribution function (CDF) of X evaluated at the current count of small-magnitude events (say, $n(t)$) since the occurrence of the last major event in the local region: $\mathrm{EPS}(n(t)) \equiv F_X(n(t)) \equiv P(X \leq n(t))$. Therefore, earthquake nowcasting is a stochastic renewal process, in which the EPS determines the current progression of regional earthquake cycles at the time of evaluation t. The EPS values corresponding to several target city regions in New Zealand thus enable a meaningful ranking of target city regions on the basis of their seismic risk exposure at present time. A simple flowchart of the earthquake nowcasting approach is illustrated in Fig. 5.4.

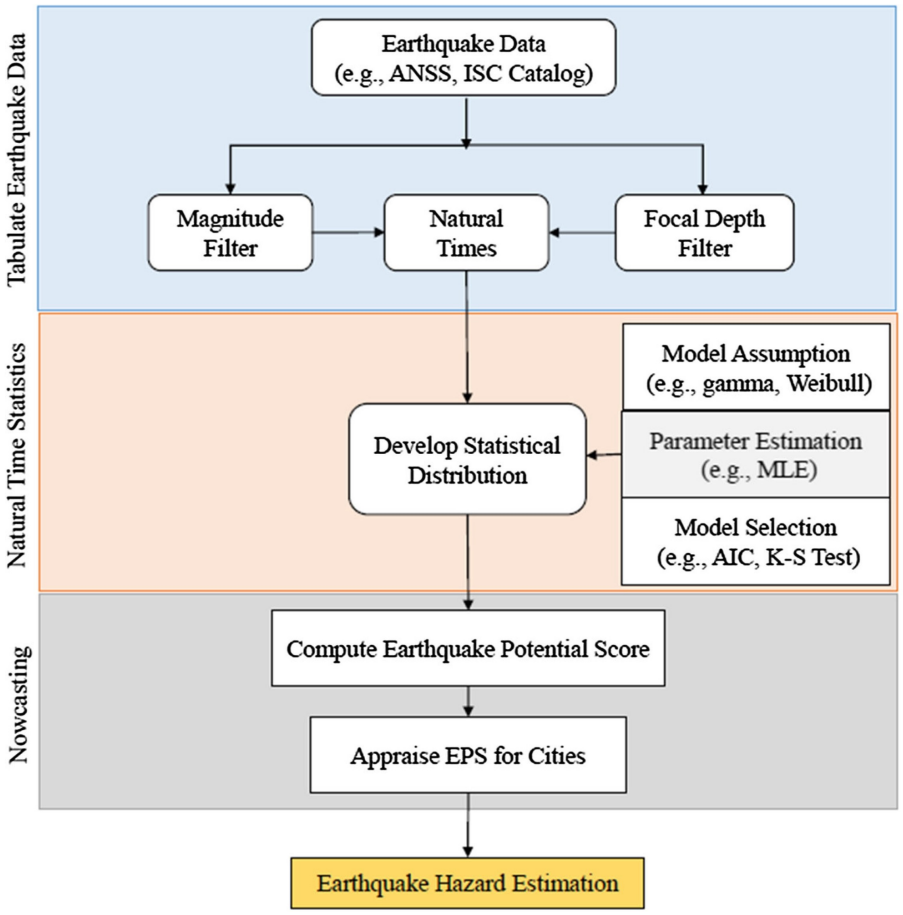

Fig. 5.4: Flowchart of the nowcasting approach for earthquake hazard estimation (Pasari (2019) [179]).

With the above set-up, the nowcasting method derives the ensemble natural time statistics of New Zealand by fitting a number of potential reference distributions to the tabulated natural time data corresponding to 91 seismic cycles. The derived natural time statistics and associated results for New Zealand are given below.

5.6.2 Descriptive measures of natural time statistics

The measures of descriptive statistics often guide us to choose appropriate reference probability distributions for statistical inference [180]. In the present analysis, the observed 91 natural time counts in New Zealand vary from 1 to 601, with sample mean, median, standard deviation and coefficient of variation of 92.2, 45.0, 126.6 and 1.4, respectively. With a positive skewness of about 2.3, the dataset exhibits asymmetry, indicating a right-tailed probability distribution of natural times. The kurtosis, a measure of "tailedness" of the underlying distribution, turns out to be 5.2 for the present dataset, suggesting a leptokurtic (positive excess of kurtosis) fatter-tailed distribution (e.g., exponential) for the associated random variable. Both skewness and kurtosis play an important role in characterizing the shape of the probability distribution. In addition,

the histogram and box-plot are displayed in Fig. 5.5 to graphically depict observed natural time counts. The histogram shows the frequency of the dataset and provides preliminary information of the density shape, whereas the box-plot summarizes the dataset based on their quartiles, collectively known as five-number summary: the minimum, the maximum, the sample median, and the first and third quartiles (Q_1 and Q_3).

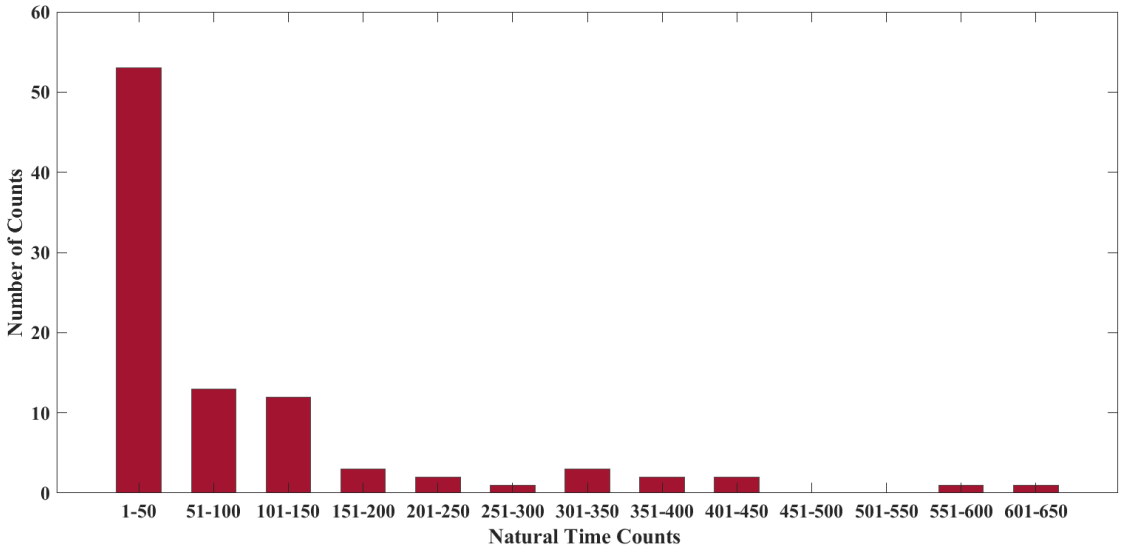

(a)

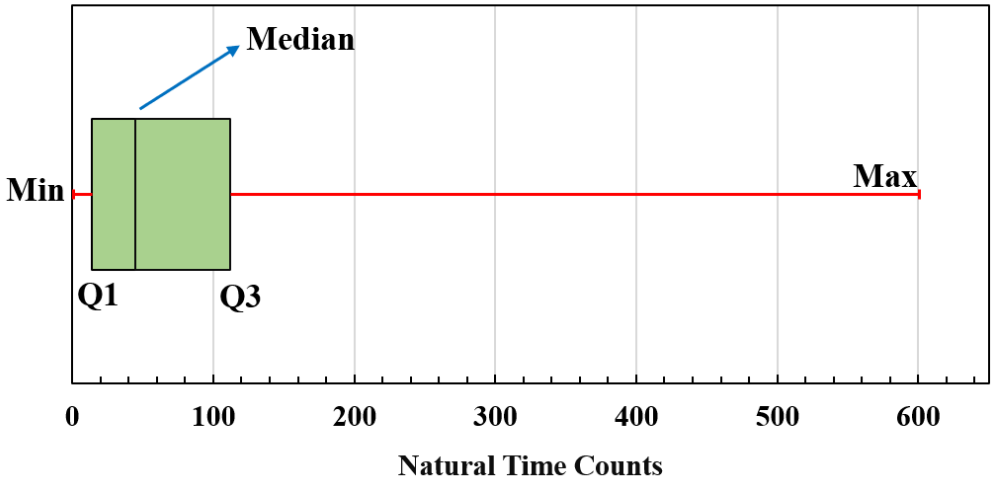

(b)

Fig. 5.5: (a) Histogram of observed natural time counts and (b) box-plot of natural time counts.

5.6.3 Statistical inference

Based on the shape of the histogram and the theoretical property that natural time counts scale exponentially with the difference in large magnitude M_λ and small magnitude M_σ [179, 218], both the time-independent exponential model and associated time-dependent variants, namely exponentiated exponential, gamma and Weibull models, are considered to perform natural time analysis. Just to mention the readers that the characteristics of the earthquake, such as the Poissonian assumption of earthquake events, pattern of earthquake occurrence, early failure (infant mortality) and intrinsic failure (random failure) of earthquake fault system, lead to develop the statistical model using these above-mentioned probability distributions. Each distribution has its own advantages and limitations. These distribution models are profound in analyzing stochastic properties of earthquake interevent times, elapsed times, natural times (nowcasting) and residual times (time remaining to a future earthquake) [180, 182, 183]. Therefore, these parametric models have been widely implemented in statistical seismology.

Since only scale and shape parameters are the influencing factors in the parametric models, hence reliable estimation of model parameters thus becomes very crucial to illustrate the model characteristics. In light of this, the present study incorporates a statistical method, namely maximum likelihood approach (MLE) to estimate the model parameters, which provides consist, compact, and rigorous asymptotic normality results [177, 180, 181]. In addition, to evaluate the asymptotic variance in estimated parameters corresponding to the probability distribution, the Fisher information matrix (FIM) and Cramer-Rao lower bound are applied. The suitability of the candidate models is assessed from two goodness-of-fit criteria, namely the Akaike information criterion (AIC) and the Kolmogorov-Smirnov (K-S) test. Subsequently, the best-fit probability model will be used to compute the EPS score of the specified city region.

As mentioned above, four candidate probability models are used to demonstrate the earthquake nowcasting method by developing natural time statistics in New Zealand. The derived results including estimated parameter values, their asymptotic standard deviations, and 90% confidence limits, and goodness-of-fit measures corresponding to four studied distributions are summarized in Tables 5.2 and 5.3. Both goodness-of-fit tests suggest that Weibull distribution provides the best representation for the observed natural times in New Zealand. The K-S graph of the studied distributions is presented in Fig. 5.6.

Table 5.2: Density function of reference distributions, estimated parameter values and goodness-of-fit measures.

Distribution	Density function ($t > 0$)	Statistical Inference		
		MLE	AIC	K-S
Exponential	$\frac{1}{\alpha} exp\left[-\frac{t}{\alpha}\right]$	$\hat{\alpha} = 92.2517$	1007.4648	0.1668
Gamma	$\frac{1}{\Gamma(\beta)} \frac{t^{\beta-1}}{\alpha^{\beta}} exp\left[-\frac{t}{\alpha}\right]$	$\hat{\alpha}$=161.5194, $\hat{\beta}$=0.5712	1002.1601	0.0942
Weibull (Best-fit)	$\frac{\beta}{\alpha} t^{\beta-1} exp\left[-\left(\frac{t}{\alpha}\right)^{\beta}\right]$	$\hat{\alpha}$=77.8695, $\hat{\beta}$=0.7680	996.8513	0.0626
Exponentiated Exponential	$\alpha\beta\left(1-exp\left[-\alpha t\right]\right)^{\beta-1} \times exp\left[-\alpha t\right]$	$\hat{\alpha}$=119.7594, $\hat{\beta}$=0.6859	1000.5018	0.0932

Table 5.3: Uncertainty analysis of estimated parameters in terms of asymptotic standard deviations and confidence intervals.

Model	Parameter values		Asymptotic standard deviation[1]		Confidence interval[2] (90%)	
					Lower	Upper
Exponential	$\hat{\alpha}$	92.2517	$\sigma_{\hat{\alpha}}$	9.6706	76.3436	108.1598
Gamma	$\hat{\alpha}$	161.5194	$\sigma_{\hat{\alpha}}$	29.9080	112.3207	210.7181
	$\hat{\beta}$	0.5712	$\sigma_{\hat{\beta}}$	0.0707	0.4549	0.6875
Weibull	$\hat{\alpha}$	77.8695	$\sigma_{\hat{\alpha}}$	11.1915	59.4595	96.2795
	$\hat{\beta}$	0.7680	$\sigma_{\hat{\beta}}$	0.0624	0.6654	0.8706

[1] As the value of the trigamma function $\psi'(\beta - 1)$ is undetermined for $\hat{\beta} < 1$ (see Pasari and Dikshit, 2015 [180]), the uncertainty analysis for the model parameters of the exponentiated exponential model is not carried out.

[2] The step-by-step procedure to carry out model parameter uncertainty using the Fisher information matrix and the Cramer-Rao lower bound theorem can be found in Pasari and Dikshit (2015) [180].

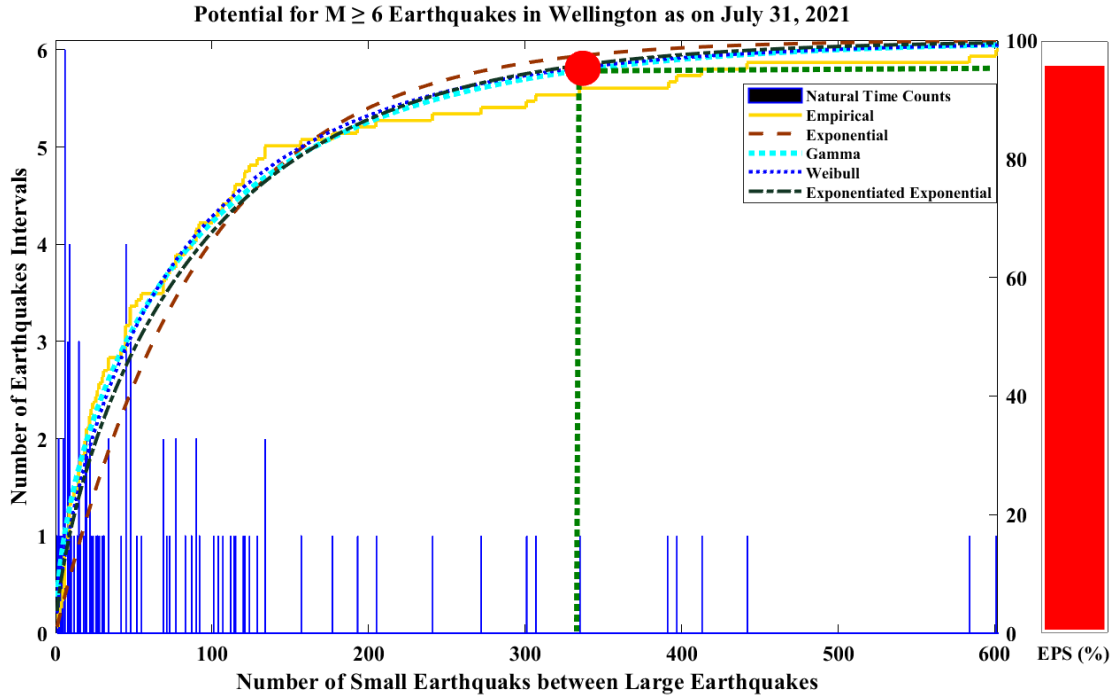

Fig. 5.6: K-S graph of the studied distributions and demonstration of EPS calculation as a "thermometer" reading. The blue bars show the histograms of the cumulative number of small events ($4.0 \leq M \leq 6.0$) between large-magnitude events ($M \geq 6.0$). The empirical distribution function derived from the histogram values is denoted by the yellow step function, whereas the best-fit Weibull distribution is shown by the dashed blue curve. The present natural time counts as on July 31, 2021, since the last large earthquake in Wellington region are shown by the red solid circle. The EPS, current progression of the ongoing earthquake cycle in Wellington, is represented by the thermometer-type red bar.

5.6.4 Earthquake potential scores

As mentioned before, the nowcasting method produces "earthquake potential score (EPS)", a numerical value (between 0 and 1) that can serve as a yardstick to determine the current level of earthquake hazard at 15 large cities in New Zealand. A circle of radius 250 km around the respective city center defines the local city region ($A_i, i = 1,2,3,...,15$). For each city region, the present event count of small earthquakes (since the last large earthquake) $n_i(t), i = 1,2,3,...,15$ at the time of evaluation t, is noted and the nowcast score is calculated based on the derived Weibull statistics; $\text{EPS}_i \equiv F_X(n_i(t)) \equiv P(X \leq n_i(t)),\ \forall i = 1,2,3,...,15$. Table 5.4 lists the EPS values along with the information of city-center coordinate, date of latest major event and the present cumulative count of small earthquakes for each target region. As on July 31, 2021, the EPS scores corresponding to $M \geq 6.0$ events reveal the following ranking of cities in decreasing order: Palmerston North (97%), Auckland (96%), Lower Hutt (95%), Porirua (95%), Wellington (95%), Nelson (94%), Hibiscus Coast (93%), Christchurch (92%), Invercargill (91%), Napier (87%), Rotorua (84%), Tauranga (82%), Dunedin (81%), Hamilton

(77%) and Gisborne (6%). Physically, the result of EPS score indicates, for instance, that the capital city Wellington has produced about 95% of the regional earthquake cycle of magnitude 6.0 or higher magnitude earthquakes (see Fig. 5.6).

Table 5.4: Earthquake potential scores (as on July 31, 2021) at 15 population centers of New Zealand corresponding to $M \geq 6.0$, $M_\sigma = 4.0$ and $R = 250$ km.

City[1]	City center		Number of large event	Date of last large event	Magnitude of last large event	Current small event count	EPS(%), with (90%) CI
	Lat (°N)	Long (°E)					
AUK	36.8509	174.7645	07	12/15/1994	6.3	341	96 (95 – 96)
WLG	41.2924	174.7787	13	11/14/2016	6.4	333	95 (95 – 96)
HAM	37.7826	175.2528	12	01/20/2014	6.3	131	77 (73 – 82)
TRG	37.7476	176.1220	18	09/01/2016	7.1	156	82 (78 – 85)
LWH	41.2127	174.8997	12	11/14/2016	6.4	335	95 (95 – 96)
NAP	39.5109	176.8764	15	01/20/2014	6.3	200	87 (85 – 89)
GSB	38.6641	178.0228	22	04/05/2021	6.4	02	06 (03 – 10)
PMS	40.3545	175.6097	11	11/13/2016	6.1	386	97 (96 – 97)
PRU	41.1381	174.8472	12	11/14/2016	6.4	335	95 (95 – 96)
ROT	38.1446	176.2378	18	09/01/2016	7.1	175	84 (81 – 87)
HBC	36.6017	174.6966	05	12/15/1994	6.3	286	93 (92 – 94)
NLS	41.2985	173.2444	16	11/14/2016	6.4	308	94 (94 – 95)
CST	43.5320	172.6306	16	11/14/2016	6.4	268	92 (91 – 93)
DND	45.8795	170.5006	02	09/03/2010	7.0	148	81 (77 – 84)
ICG	46.4179	168.3615	13	08/05/2009	6.1	238	91 (89 – 92)

Overall, it is noted that, the EPS scores for most of the cities in New Zealand lie in the range of 77% and 97%, except one city (Gisborne). The high EPS scores indicate that these

[1]The abbreviations are as follows: AUK (Auckland), WLG (Wellington), HAM (Hamilton), TRG (Tauranga), LWH (Lower Hutt), NAP (Napier), GSB (Gisborne), PMS (Palmerston North), PRU (Porirua), ROT (Rotorua), HBC (Hibiscus Coast), NLS (Nelson), CST(Christchurch), DND (Dunedin), and ICG (Invercargill).

cities have reached to their rear end in the seismic cycle of large earthquakes. In the following section, some other characteristics of the underlying earthquake system including $b-$value homogeneity in space and time, sensitivity analysis of the EPS scores by varying the value of required parameters (small-event magnitude, large-event magnitude, and city region), and the relevance of EPS score to earthquake hazard in New Zealand are discussed.

5.7 Discussion

Although major earthquakes in large seismically active regions are observed to occur in approximately repetitive cycles, direct observation of tectonic stress accumulation and release at a region of interest is not yet available [218, 225]. As a result, research in this area often uses empirical data-driven approaches, such as earthquake nowcasting, to help estimate the current state of earthquake hazard at major population centers. Here, an area-based earthquake nowcasting method is applied to compute nowcast scores at 15 population centers in New Zealand. In principle, the method follows a stochastic renewal process, representing a "short-term" memory of the regional fault system in which the system has no leftover stress for the next cycle, unlike the idea of earthquake "supercycles" in tectonics [185, 218, 221]. By definition of the renewable process, history before the last large earthquake is all forgotten, though it can characterize the progress of the developing earthquake cycle through the current number of small event counts $n(t)$ at the time of evaluation t [187]. The nowcasting technique uses the novel idea of "natural time" that comprises discrete event counts of small earthquakes between two successive large earthquakes in a specified region [144, 218]. The "natural time" concept therefore replaces clock time (days passed) as a way of tracking time between large-magnitude events [218, 263]. One of the main advantages of using natural time analysis is that declustering is not necessary. Based on simulated natural time counts, Luginbuhl et al. (2018) [143] showed that even without declustering, the natural time counts exhibit complete randomness. Hence, aftershock cluster removal is not necessary. Using natural time analysis, the data-driven nowcasting method outputs EPS values as a proxy measure of the current state of earthquake hazard in a network of geological faults to facilitate city planning, social policymaking and thus disaster preparation. The prerequisite of space–time homogeneity of $b-$values in the study region, consistency in EPS values against some variations in the threshold magnitude, catalog time period and city region, and the relevance of EPS values to the seismic risk exposure in New Zealand are discussed below. Some physical interpretation of the data-driven area-based nowcasting technique is also provided in below section.

5.7.1 Space-time homogeneity in $b-$values

As mentioned before, the seismic nowcasting method considers that ensemble natural time seismicity statistics of a large region are the same as the seismicity statistics of several local regions within the large area [215, 218]. To utilize this space–time invariance property of natural time statistics through ergodicity in earthquake physics, the method theoretically requires that $b-$values are homogeneous over space and time in the study region. To verify, ordinary least-squares fitting of a straight line to the frequency-magnitude distribution is performed for different space–time combination of the studied earthquake catalog (Table 5.5). In the present study, five different segments of catalog length (time span) are considered and their corresponding $b-$values are estimated. The main purpose of variations in catalog length is to observe the presence of any significant bias in the instrumental data, for example, whether small earthquakes are correctly recorded or whether the magnitude completeness threshold is slightly higher in the early instrumental period. Results show that $b-$value estimates are stable against the variations in time period. Likewise, in spatial variation, to understand whether the frequency-magnitude statistics do not vary significantly over different local city areas, $b-$values in 15 circular city regions are obtained. From Table 5.5, it is noted that $b-$value estimates are generally stable against the spatial variations. Therefore, the frequency-magnitude statistics are largely stable over space and time variations, providing a justification for the theoretical assumption of earthquake nowcasting in the study area.

Table 5.5: Estimated $b-$values for different time and space consideration in the study area.

	Catalog span	Total number of events	Estimated $b-$value	Coefficient of determination (R^2) in G-R frequency-magnitude linear regression model (using the principle of least-squares estimation)
Several	1963 – 2021	8532	1.0125	0.9942
$b-$value	1970 – 2021	8338	1.0163	0.9942
estimates	1980 – 2021	8090	1.0132	0.9939
in time	1990 – 2021	7557	1.0215	0.9916
	1970 – 2000	1965	1.0043	0.9842
	1980 – 2010	4562	1.0082	0.9915
Several	Auckland	464	0.9957	0.9912
$b-$value	Wellington	1464	0.9598	0.9773
estimates	Hamilton	1027	1.1077	0.9813

in space	Tauranga	1375	0.9857	0.9943
	Lower Hutt	1437	0.9931	0.9588
	Napier	1494	1.0789	0.9924
	Gisborne	2017	1.0122	0.9932
	Palmerston North	1487	1.1060	0.9901
	Porirua	1441	0.9933	0.9588
	Rotorua	1484	0.9994	0.9940
	Hibiscus Coast	391	0.9666	0.9931
	Nelson	1606	0.9398	0.9875
	Christchurch	1303	0.9047	0.9880
	Dunedin	282	0.9505	0.9660
	Invercargill	836	0.8239	0.9899

5.7.2 Sensitivity of the EPS values

To examine the overall consistency of the natural time induced nowcast scores, the sensitivity analysis is essential. As the area-based nowcasting method and associated EPS values are computed based on selected magnitude thresholds ($M_\sigma = 4.0$ and $M_\lambda = 6.0$) and defined geographical regions (A and $A_i, i = 1,2,3,...,15$), the sensitivity testing is performed to examine whether the nowcast scores are largely stable against the changes of magnitude thresholds and local city areas. For this, the following settings are considered: (1) with magnitude thresholds $M_\sigma = 4.0$ and $M_\lambda = 6.0$, find the effect of city area variations $R = 250,\ 300,\ 350$ km on the EPS value; (2) with fixed city area $R = 250$ km and large threshold magnitude $M_\lambda = 6.0$, determine the effect of small-magnitude threshold variations $M_\sigma = 4.0,\ 4.5$ on the EPS score; (3) with fixed city area $R = 250$ km and small-magnitude threshold $M_\sigma = 4.0$, determine the effect of large-magnitude threshold variations $M_\lambda = 6.0,\ 6.5$ on the EPS score, and (4) impact of other variations in earthquake catalog, such as the focal depth (from 100 to 150 km) or the time-span of the catalog (say, $1980-2021$). For each of the above cases, the EPS values are re-computed and are pictorially summarized in Fig. 5.7. Several observations are made from the sensitivity

testing: (1) a steady increase in the city radius often yields a steady increase in EPS scores, though there are a few cases where the inclusion of the most recent large event in the enlarged city area leads to decreased EPS values; (2) a higher value of M_σ ($M_\sigma = 4.5$) yields a consistent decrease in EPS scores; (3) an increase in the large-magnitude threshold M_σ ($M_\lambda = 6.5$) lowers the EPS scores by about 10–15%, except in a few cases, and (4) the computed EPS values are largely consistent with the changes in earthquake catalog due to a change in (i) focal depth, say from 100 to 150 km, providing 9069 events comprising 93 cycles of large events, and (ii) catalog time period, say from $1963-2021$ to $1980-2021$, providing 8090 events comprising 74 cycles of large events. Therefore, the EPS values are largely consistent with the variations in threshold magnitude, catalog time period and city area in the seismically active New Zealand and adjacent regions.

It can be observed from Fig. 5.7 that some cities, such as Dunedin and Napier, exhibit larger variations in EPS values. For Dunedin, as the city region lies in the junction of two tectonic systems, it may appear that this variation comes from the complex seismotectonic setting of the region. However, it is a reminder for readers that in the empirical nowcasting method, the entire large seismogenic region (e.g., New Zealand) is considered as "one driven threshold system" rather than dealing with targeted regional tectonic blocks or regional fault systems [215, 218]. Therefore, the larger variation in EPS values at a city region cannot be directly attributed to the seismotectonic setting of a region; rather, the variation in EPS values comes from the possible inclusion of any recent large event in the extended city region. For example, in Wellington, as the city radius increases from 200, 250, to 300 km, the natural time counts (see Table 5.4) gradually increase from 302 (92%), 333 (94%), to 342 (95%). However, in Napier, as the city radius increases from 200, 250, to 300 km, the natural time counts increase from 145 (80%) to 200 (87%), but then suddenly falls to 3 (8%). The sudden drop in EPS for a radius of 300 km is due to the inclusion of the recent large event on April 05, 2021. In particular, for Dunedin, it may be noted that in the PSHA model of New Zealand [240], the developers first considered two different blocks around Dunedin for computing peak ground acceleration (PGA) values. However, based on the similarity of seismic processes and slip patterns of both blocks, the developers later grouped both blocks into a single domain to carry out PGA computation around Dunedin [240].

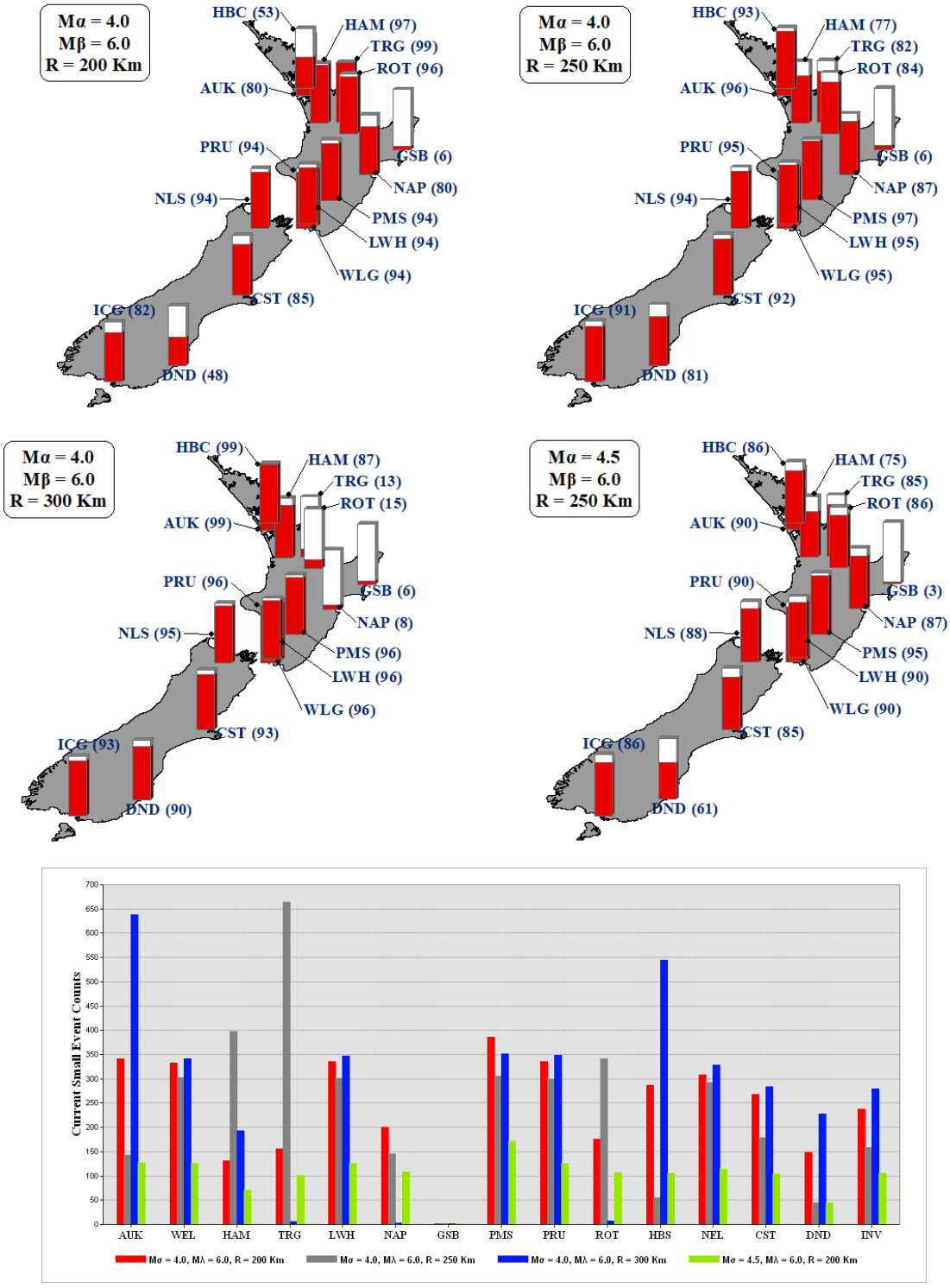

Fig. 5.7: Earthquake potential scores for $M \geq 6.0$ events at 15 population centers in New Zealand are shown by solid bars in the upper panel, whereas the current natural time counts are represented by the stacked bar-chart in the lower panel; AUK (Auckland), WLG (Wellington), HAM (Hamilton), TRG (Tauranga), LWH (Lower Hutt), NAP (Napier), GSB (Gisborne), PMS (Palmerston North), PRU (Porirua), ROT (Rotorua), HBC (Hibiscus Coast), NLS (Nelson), CST(Christchurch), DND (Dunedin), and ICG (Invercargill). Notice that due to proximity of a few locations, the bars for their nowcast scores are overlapping.

From Fig. 5.7 and Table 5.4, it also observed that some cities have very high EPS scores. Can these high EPS values (either due to longer earthquake interval or due to high seismicity in the local region) indicate the occurrence of a much larger earthquake magnitude in the local region? To answer this question, it may be noted that just like any fault-based approaches which require definition of the target faults for modeling, the area-based nowcasting method requires the definition of "large" magnitude events for method implementation. This means that if the considered large event is $M_\lambda = 6.0$, then only cycles of magnitude 6.0 events (rather than the cycles of larger magnitude events, say M 8.0) are considered. However, due to the randomness of the process, a few "early failures" (infant mortality) or "late failures" are inevitable, though they would not hamper the "general trend" (average behavior) of the considered earthquake cycles. Thus, the high EPS values due to longer elapsed time or the natural time statistics of background seismicity cannot be considered as an indicator of impending larger-magnitude (larger than the considered threshold) earthquakes.

5.7.3 Relevance of EPS to earthquake hazards in New Zealand

Except for the situation where the underlying natural time seismicity statistics is a stationary Poisson process (e.g., Pasari et al. 2021, Pasari, 2022 [176, 187]), the current level of seismic progression has direct relevance to the seismic hazard (risk). In a progressive earthquake cycle, the current state of seismic hazard (instantaneous risk) can be estimated through conditional probability of a large earthquake in the near future (in the natural time domain) on the basis of the current state EPS$(n(t))$. In this case, an extremely short-term risk, P_{next}^{large}, is defined as the probability by assuming that the next earthquake in the local region is actually a large event. Moreover, the risk of large events in the entire cycle can be estimated through the probability distribution of the waiting time τ until the next large earthquake in the local region. At this point, it may be emphasized that the EPS defined through CDF or survival function describes the distribution of the "waiting time between successive large earthquakes", whereas the risk assessment concerns "the waiting time until the next large earthquake" based on the current status EPS$(n(t))$.

The EPS values of 15 major cities with different magnitude and radius settings are shown in Fig. 5.7. From these nowcast scores, it can be observed that the current level of earthquake hazard pattern is relatively higher along the north-east-trending zone. The higher values of EPS in these cities also correspond to the greatest concentrations of active faults and high seismicity in these areas, particularly at the Fiordland zone in south-western South Island, along Alpine and Hope fault in central South Island, and along the faults of the Axial tectonic belt and Taupo Volcanic Zone. The present progress of the earthquake cycle may be combined with the outcomes of the New Zealand National Seismic Hazard Model (NSHM) that incorporates the

probabilistic framework based on seismic models and ground motions for several engineering consequences [72, 240, 241]. The PGA values (see Stirling et al. 2002, 2012 [240, 241]) and the empirical nowcast scores generally reveal similar patterns of earthquake hazard in New Zealand. Specifically, the cities of Wellington, Dunedin and Christchurch have high seismic hazard in both the NSHM and EPS estimates, though for Auckland the EPS shows higher current hazard in comparison to the NSHM estimate, and for Gisborne, the NSHM estimate is much higher than the EPS score due to the occurrence of a recent large-magnitude earthquake in April 2021. Horspool et al. (2021) [104] calculated the risk coefficient of several cities in New Zealand and found that those of Napier, Dunedin, Nelson, Wellington, Invercargill, and Palmerston North are higher. From the present nowcasting analysis, these cities also have higher EPS values. In addition, the spatial distribution of current earthquake hazard agrees with the Berryman and Smith model (1986) [24] that evaluates PGA from a modified Mercalli intensity map (for details, see Stirling et al. 2002 [241]). These results, in a combination or standalone mode, contain valuable information about earthquake hazard status to facilitate a variety of end-user applications in New Zealand.

5.7.4 Possible physical interpretation of the data-driven nowcasting method

It is well known that earthquakes in seismically active regions exhibit strong space–time correlation, clustering behavior, and hierarchical property [225]. Therefore, data-driven methods are often preferred to study the nature of a nonlinear and selforganizing earthquake threshold system that displays a frequency-size power-law distribution, such as Gutenberg-Richter law and Omori's aftershock decay [214, 219]. Some previous studies (e.g., [212, 214, 219, 249, 250]) on slider block models and earthquake simulations have shown that earthquake systems may be considered "ergodic", meaning that the driven mean field threshold system can be treated as an "equilibriumlike system" with statistically stationary dynamics over long time intervals. This essentially implies that the natural time statistics are independent of the size of the geographical region [215, 218]. Thus, in nowcasting, first derive background seismicity statistics from a large region (say, all of New Zealand) is derived and then apply the same statistics to the smaller target city regions (say, 15 city regions) to derive their EPS values. Therefore, physically, the area-based nowcasting technique, through indirect natural time analysis, enables earthquake processes by cycles of recharge and discharge based on some notable seismicity patterns of "large" and "small" events. Recent works by Professor John B. Rundle and his group ([208, 210]) highlight further discussion in this direction through machine learning methods of some noticeable patterns in the seismicity clustering of aftershock sequences and seismic swarms.

Therefore, as a future work, one may develop further connections between data-driven nowcasting and theory-driven physical models in New Zealand. The concept of earthquake nowcasting may also be used for reliable earthquake forecasting. For example, Perez-Oregon et al. (2020) [190] proposed a simple prediction model based on the generalization of nowcasting as a prerequisite for forecasting. They used the concept of waiting (natural) time of stronger earthquakes, real seismicity, and the Olami-Feder-Christensen earthquake model, along with the assumptions of probability distributions.

5.7.5 Regions of high seismic hazard from the combination of EPS and seismic moment budget

A comprehensive analysis of seismic hazard potential from geodetic method (Chapter 4) and statistical method (Chapter 5) provides a synoptic view of the underlying physical system in terms of energy release and accumulation. The geodetic approach determines the spatial distribution of seismic moment budget over New Zealand, whereas the proposed area-based statistical method (earthquake nowcasting) refers to the current status of the earthquake cycle in several target localities in New Zealand. Therefore, a combination of geodetically observed spatial distribution of earthquake potential (Chapter 4) may be complemented and corroborated with the statistically computed earthquake potential scores (Chapter 5) to highlight the regions of high seismic hazard. The combined result reveals that the regions of high seismic hazard in New Zealand are aligned along the Hikurangi subduction zone and central South Island traversing the Alpine fault. In essence, the emanated results provide more insights to the spatio-temporal resolution of the current phase of the contemporary earthquake deformation cycle in New Zealand.

5.8 Summary

Extraction of information from a catalog of historical data points is vital for any engineering application. A sophisticated model fitting is probably the most common approach to undertake this. In the present chapter, the earthquake nowcasting analysis is implemented to delineate the seismic hazard assessment in New Zealand. The area-based nowcasting technique is grounded on two main concepts: the classical elastic rebound theory of earthquakes and the ergodicity in seismogenic processes. As a consequence, this method incorporated the natural time statistics for the seismically active region. Natural time is a numeric value of cumulative small events between two successive large events that act as measure of stress-strain accumulation between large earthquakes in a specific region. There are at least three advantages of this approach. First, the method inherently accounts for the possible contribution from dependent events as natural

time count is unaffected when aftershocks dominate, when background seismicity dominates, and when both contribute. Second, statistics of natural times remains unaltered with the changes of background seismicity rate as long as $b-$value remains constant. Third, the nowcast score, as a measure of the current progression of earthquake cycle, often enables a systematic ranking of cities based on their current exposure to the seismic risk in a rapid, efficient and reproducible way.

In order to prioritize major populous cities based on their nowcast score in New Zealand, the natural time counts are tabulated using the earthquake data during the time span of $1964-2021$. After tabulating discrete natural times, the natural time statistics is developed in mainly three steps: (i) the parametric model assumption step in which four candidate distribution models have been utilized, (ii) parameter estimation step, and (iii) the model selection step. Using the best-fit cumulative probability distribution, the nowcast scores (EPS) at 15 populous cities of New Zealand evaluated. The EPS incorporates ensemble seismicity statistics in a discrete natural time domain to estimate the current level of seismic cycle progress in a $0-100\%$ scale of extremity. Based on the estimated results, the present study leads to the following conclusions:

1. Seismicity in New Zealand reveals natural time Weibull statistics.

2. The EPS corresponding to $M \geq 6.0$ events at 15 major cities in New Zealand ranges between 6% and 97% with the following ranking in decreasing order: Palmerston North (97%), Auckland (96%), Lower Hutt (95%), Porirua (95%), Wellington (95%), Nelson (94%), Hibiscus Coast (93%), Christchurch (92%), Invercargill (91%), Napier (87%), Rotorua (84%), Tauranga (82%), Dunedin (81%), Hamilton (77%) and Gisborne (6%).

3. The study provides spatial distribution of earthquake cycle progression at the present time in New Zealand and thereby characterizes the current state of earthquake hazard for social policymaking, insurance, city planning and allied applications.

This present chapter has discussed contemporary state of regional earthquake hazard at 15 major population centers in New Zealand by implementing the earthquake nowcasting method and presents the results in terms of earthquake potential score (EPS).

Therefore, in order to examine the interseismic phase deformation caused by the contemporary earthquake cycle in New Zealand, two data-driven approaches have been implemented. The former data-adaptive approach, namely the seismic budget estimation method, has focused on the spatial distribution of the contemporary earthquake potential using the geodetic accumulation and seismic release rates (in Chapter 4), whereas the latter area-based method, namely the earthquake nowcasting method, has aimed to provide a synoptic statistical view of the current progression of the earthquake cycle of a given region in terms of earthquake potential score (in

Chapter 5). The estimated results not only enable researchers to understand the earthquake cycle deformation but also are useful for seismic hazard analysis in New Zealand and its adjacent regions.

Chapter 6

Conclusions and FutureWork

"*We want a story that starts out with an earthquake and works its way up to a climax.*"
by Samuel Goldwyn

The thesis has addressed earthquake cycle deformation and consequent seismic hazard re-assessment in New Zealand using spatio-temporal techniques. For this, Chapter 1 has provided an overview and rationale of the thesis, along with the thesis objective and scope of the thesis. Chapter 2 has laid the foundation of a data-driven space-time approach, namely the EOF method. Chapter 3 has identified the coseismic deformation pattern of the 2016 Kaikoura earthquake. Chapter 4 has dealt with an estimation of the spatial distribution of earthquake potential along 14 different tectonic zones in New Zealand. Chapter 5 has quantified the present state of the contemporary earthquake cycle at 15 major cities in New Zealand, and finally, the present chapter (Chapter 6) summarizes research outcomes of the thesis and it highlights some relevant future scopes. The overall content of this chapter is provided below.

Contents

6.1 Research objectives and their conclusions

In Chapter 1, the main objective of the thesis was framed as the earthquake cycle deformation analysis in New Zealand using data-driven spatio-temporal techniques. To accomplish this objective, three sub-objectives (for the sake of simplicity, called "objectives" hereafter) were framed. A brief summary of each objective and associated concluding remark is provided in the following sub-sections.

6.1.1 Research objective 1: To identify the coseismic deformation associated with the 2016 Kaikoura earthquake of New Zealand using the data-adaptive EOF method

In Chapter 3, the first research objective is accomplished by performing the EOF analysis on the 2016 Kaikoura earthquake in New Zealand, whereas a brief mathematical description of the spatio-temporal EOF method and its several extensions along with their prominent application in the different domains, such as ionospheric variation modeling, climate and atmospheric related studies, crustal deformation analysis, gap filling interpolation technique, and other applications of the EOF (PCA) along with the associated computational packages are discussed in Chapter 2. In Chapter 3, a sequence of tasks, such as CGPS data collection, data processing, EOF implementation, and interpretation of the EOF modes are carried out for the coseismic analysis. For this, 15 days RINEX data (straddling the Kaikoura event) of 127 CGPS stations were accessed by the GeoNet. The collected RINEX data was processed using the GAMIT-GLOBK software and the position time series of each station at every 30 min epoch was obtained. Further, the extracted component-wise (East, North, and Up) time series of each station was utilized for the EOF analysis. Before implementation of the EOF method, the CGPS data is refined by decomposing the time series into a linear combination of four components, namely trend, seasonality, earthquake-induced jump, and residual part. The refined time series, consisting of earthquake-induced jump signals and residual parts, was then considered for the EOF analysis. The dominant EOF modes, a pair of spatial pattern and corresponding principal time series, allowed us to determine the coseismic and early postseismic deformation pattern associated with the Kaikoura event. From EOF modes, it was observed that the horizontal coseismic deformation is aligned in the NE-SW direction from the central South Island to the end shore of the North Island, whereas the vertical deformation is observed along the offshore boundary of the North Canterbury region. The pattern of the postseismic relaxation follows the same direction as observed in the coseismic displacement. In addition, the EOF-based coseismic strain pattern revealed the regional tectonic environment linking to the associated observable patterns.

A comparison study between the EOF and LSE estimates was also performed. It indicated that the EOF method is superior to the traditional LSE method for the coseismic analysis due to its potential to adequately capture the coseismic vectors, even in the presence of various prevalent signals, such as pre and post seismic signals, common mode error, outliers, and other noises in the given data. As a conclusion, the present study on the identification of coseismic deformation of the 2016 Kaikoura earthquake in New Zealand using the versatile data-adaptive EOF method has successfully accomplished the research objective 1.

6.1.2 Research objective 2: To estimate the spatial distribution of contemporary earthquake potential in New Zealand using the data-driven seismic moment budget estimation technique

An understanding of the contemporary earthquake cycle deformation and subsequent seismic hazard is essential for better preparedness of future earthquakes in the seismically active and highly populated areas of New Zealand. In light of this, the earthquake potential in New Zealand is examined through two different space-time data-driven approaches, as explained in Chapter 4 and Chapter 5, respectively. To implement the first approach, namely the seismic moment budget estimation, a number of successive tasks, such as the collection of updated velocity field, acquisition of the historical seismicity data, and the segmentation of the study area were carried out to achieve the research objective 2. For this, (i) the updated velocity field of New Zealand, comprising the velocity vectors of 180 CGPS stations, was accessed in December 2021 from the NGL; (ii) the historical earthquake catalog of New Zealand was obtained from the GeoNet during the time period of 1840–2021, and (iii) the study area was divided into 14 seismogenic zones based on different seismo-tectonic characteristics. The velocity field was used as an input for the geodetic strain estimation over New Zealand. Further, the geodetic strain rates were translated into geodetic moment rates and compared with seismic moment rates derived from 180 years of seismicity data in each zone. The geodetic moment rates represent seismic energy accumulation, whereas the seismic moment rates indicate energy release. The comparison of these two provides a total energy budget that could possibly release in future devastating earthquakes. The spatial distribution of seismic moment budget in New Zealand suggests that the zones with high seismic potential indicate the areas of interseismic strain accumulation, whereas the zones with lower earthquake potential correspond to the areas encompassing the rupture areas of recent large events. Therefore, from the above discussions, it is concluded that the research objective 2 is successfully accomplished through the present study of assessing the contemporary earthquake cycle deformation and associated seismic hazard in 14 seismogenic zones of New Zealand.

6.1.3 Research objective 3: To quantify the current progression of earthquake cycle of large events at 15 major cities of New Zealand using the area-based earthquake nowcasting approach

After estimating the contemporary earthquake potential from geodetic strain accumulation and seismic moment release, the second state-of-the-art approach, namely the statistical area-based earthquake nowcasting method, is utilized in Chapter 5. The earthquake nowcasting analysis was performed in a three-fold way: preparing data (natural times) for the study region, deriving seismicity statistics of natural times, and computing earthquake potential score (nowcast scores) for 15 major city regions of New Zealand. For this, the earthquake catalog (1963–2021) of New Zealand was considered to tabulate the natural times, that is, the number of intermittent "small" magnitude events between the pairs of "large" earthquakes. Four reference probability distribution models, namely exponential, gamma, Weibull, and exponentiated exponential distributions were considered to develop the natural time statistics. The statistical inference on natural times including parameter estimation using the MLE method, uncertainty analysis using the FIM and Cramer-Rao lower bound theorem, and model selection using the AIC and K-S test was carried out. The CDF of the best fit Weibull distribution was used to compute the nowcast scores corresponding to 15 major cities of New Zealand. The EPS scores, like "thermometer" readings, describe the "current" level of seismic progression of a city in its earthquake cycle of large events. The estimated EPS scores above 90% at several cities (e.g., Auckland and Wellington) indicate that these cities have reached their rear end in the seismic cycle of large earthquakes. In addition, a sensitivity analysis of the nowcasting scores confirmed that the obtained results are largely consistent. Therefore, the research objective 3 is successfully accomplished through the present study of implementing the area-based earthquake nowcasting approach to quantify the current progression of earthquake cycle at 15 major cities of New Zealand.

6.2 Major findings of the study

The major findings of the present study are highlighted below.

1. The EOF-based horizontal coseismic deformation of the 2016 Kaikoura event is aligned in the east direction with an amplitude of 150 mm and in the north direction with an amplitude of 200 mm, whereas the vertical deformation is observed in the upward direction with an amplitude of 150 mm.

2. The early postseismic relaxation of the 2016 Kaikoura earthquake reveals a similar deformation pattern as observed in its coseismic deformation.

3. The horizontal coseismic strain patterns (dilatation and shear) associated with the Kaikoura earthquake reveal a large-scale extensional pattern in the northern Canterbury region and compressional concentric pattern near the uppermost South Island and lower North Island, along with a radial SW-NE shear pattern.

4. There is minimal to no deformation in the far-field regions, indicating that these regions were hardly affected by the 2016 Kaikoura earthquake.

5. The EOF-based coseismic displacement vectors for the Kaikoura event are more precise (magnitude) in comparison to the least-squares based displacement estimates, particularly in the vertical observations.

6. The geodetic dilatation strain rates, estimated from the updated velocity field of New Zealand, indicate that compressional rates (0–75 nstrain/yr) are more dominant than extensional rates (0–30 nstrain/yr) along the Alpine fault. The higher value of the maximum shear strain rates ($\sim$ 225 nstrain/yr) is observed near the northeastern boundary of the South Island.

7. The estimated geodetic moment rate ranges from 3.15×10^{17} Nm/yr to 9.00×10^{17} Nm/yr, whereas the seismic moment rate ranges from 0.10×10^{17} Nm/yr to 83.92×10^{17} Nm/yr. Based on the comparison between moment accumulation rate and moment release rate, the possible maximum earthquake potential of 14 seismic zones in New Zealand ranges from M_w6.7 to M_w8.0.

8. The EPS corresponding to $M \geq 6.0$ events at 15 major cities in New Zealand ranges between 6% and 97% with the following ranking in decreasing order: Palmerston North (97%), Auckland (96%), Lower Hutt (95%), Porirua (95%), Wellington (95%), Nelson (94%), Hibiscus Coast (93%), Christchurch (92%), Invercargill (91%), Napier (87%), Rotorua (84%), Tauranga (82%), Dunedin (81%), Hamilton (77%), and Gisborne (6%).

6.3 Contributions through this research

The present research has the following contributions towards the understanding of the contemporary earthquake cycle deformation in New Zealand using the spatio-temporal techniques.

1. The present work emphasizes the EOF analysis for determining the coseismic crustal deformation associated with the 2016 Kaikoura earthquake (M_w7.8) in New Zealand.

2. The EOF-based coseismic displacement field brings out the coseismic strain field in terms of the regions of compression, extension, and strike-slip motion corresponding to the Kaikoura event.

3. The data-driven seismic moment budget estimation method provides the spatial distribution of crustal deformation caused by the contemporary earthquake cycle over New Zealand through the moment deficit between geodetic moment rates and seismic moment rates. Consequently, the emanated results highlight the seismic zones of higher earthquake potential in New Zealand.

4. The area-based earthquake nowcasting approach measures the current level of seismic progression of a city in its contemporary earthquake cycle of large-size events, in terms of earthquake potential score. The EPS score associated to 15 major cities of New Zealand serves as a yardstick for a ranking of these cities based on their current seismic exposure.

5. Finally, the crustal velocity field, strain distribution, earthquake potential score, and seismic moment budget enable researchers to understand the contemporary earthquake cycle deformation and thereby, contribute to the seismic hazard analysis in New Zealand for social policymaking, insurance, city-planning, and several other end-user applications.

6.4 Future scope of the present research work

A number of future researches that can be developed and/or integrated from the present investigation are mentioned below.

1. **Modeling of coseismic deformation through EOF**: The adequate and robust measure of the coseismic displacement vectors, as determined through the EOF analysis, may further be used to quantify and model various crust parameters, such as coseismic slip distribution, coseismic stress-strain field, occurrence dynamics of earthquake, and the ongoing postseismic deformation process to understand the characteristics of the ongoing earthquake cycle. The outcomes may lead to invaluable inputs to seismic hazard models [35, 41, 128, 139, 156].

2. **Spatio-temporal filtering of geodetic time series through EOF**: The spatio-temporal filtration of the prevalent deformation signals, such as common mode error and other small, short-term and long-term variations in the given time series, occurring due to reference frame realization, mismodeling of the satellite (including orbits, clocks, or antenna phase center corrections), unmodeling of large-scale atmospheric and hydrologic effects, and systematic errors (caused by algorithms, software, and data processing strategies) is essential to monitor surface deformation patterns from global to regional to local scales. As data-adaptive EOF efficiently captures and filters the space-time-related signals from the given time series, the results may improve the precision of coordinate time series for regional GPS networks [35, 37, 53, 81, 132, 146].

3. **Spatio-temporal gap filling in incomplete geodetic time series (GPS/InSAR) through EOF**: Since the majority of data sets in the geosciences are obtained from observations, measurements, experiments, and numerical simulations, the missing value problem is a potential issue. Such issue not only affects model parameter estimation and boundary conditions of numerical models but also slows down the model processing encounters. In these situations, the EOF method may be utilized as a gap-filling toolkit to retrieve missing values or gaps, even in case of time series with limited size and spatio-temporally correlated gaps [3, 4, 97, 127, 281].

4. **Detecting slow slip events using the principal component analysis-based inversion method (PCAIM)**: Understanding the physics of slow slip events (SSE) (also known as "silent events") along subduction zone interfaces and how they differ from normal, high-frequency earthquakes is one of the most pressing current challenges [7]. The PCA-based inversion method (PCAIM) allows geophysicists to examine a complex slip history associated with the SSE in space and time. Consequently, the results may be useful to understand the spontaneous occurrence, the characteristics, and the scaling relationship of SSEs and earthquakes, emerging from geometrical complexities [41, 114, 128, 137, 193].

5. **An automated EOF-based web application**: To expedite the process of computing and analyzing the spatial and temporal modes, a simple automated web application may be developed using Python, HTML, CSS, and Javascript [46, 78].

6. **Integration of GPS and InSAR data for the high-resolution crustal deformation**: The GPS observations are often used to measure the three-dimensional deformation signals at discrete locations, whereas the InSAR observations are used to measure the areal deformation signals in the line-of-sight direction of the satellite. Therefore, these techniques are complementary to each other and integrating these two observation methods will provide more insights to the spatio-temporal resolution of the crustal deformation, caused by the earthquake cycle of seismically active region [10, 90].

7. **Physical interpretation of the nowcasting approach**: The empirical nowcasting analysis is built on the "short-term fault memory" based renewable or seismic cycle model, in which it is assumed that all accumulated strain will release in a single event. This means that there would not be any "leftover" stress amount, unlike the developing concept of "earthquake supercycles" in great earthquake that exhibit "long-term fault memory" [217]. Apart from identifying the high risk seismic cities, a nowcast map (similar

to seismic zonation map) may generate for the use of engineers and city planners. Besides, a web-based nowcast app can develop for an automatic, transparent, and regular monitoring of earthquake hazards in the study region [215].

8. **Theoretical advancement in statistical seismology**: The area-based earthquake nowcasting study contributes to the theoretical advancements in seismology in terms of Shannon information, Bayesian estimation, earthquake physics based concepts and possible improvement in seismic hazard assessment as well as regional earthquake likelihood models (RELM) in the suite of pattern information and ensemble methods [217].

9. **Natural times with machine learning for addressing diverse spatio-temporal scales of tectonic and earthquake processes**: Using an array of natural-time counts and associated space-time information, earthquake magnitude, clustered events including bursts, swarms and aftershocks, and global fault map, data-intensive machine learning models are appropriate to extract useful information from observations in terms of "hidden-variables". The estimated results may utilize to serve various purposes, such as (i) identifying the role of strain hardening in the earthquake cycle, (ii) visualizing the current state of the earthquake cycle from correlation in small earthquake patterns, (iii) forecasting of large destructive earthquakes, (iv) characterizing the complex dynamics of the earthquake system in terms of regional crustal structure, stress accumulation and stress release, and (v) improving seismic hazard (risk) estimation for several end-user applications [208–211, 215, 220].

10. **Improved seismic hazard map and scenario (hypothetical) earthquake studies**: Considering various factors, such as the pattern of short term crustal deformations, strain distributions, long term slip estimations, and recurrence interval of large magnitude earthquakes, the existing seismic hazard map of the study region may be revised. In addition, the present findings may be useful to develop scenario or hypothetical earthquake models for a prior understanding of the probable earthquake damages in a seismically active region [21, 240, 267].

11. **Seismic risk mapping**: As the present thesis has provided valuable inputs for the seismic hazard analysis in New Zealand and its surrounding regions, the seismic risk mapping based on the consideration of vulnerability and other aspects may be carried out as a future work [240, 242].

Appendix A
Supplementary information for Chapter 3

Coseismic displacements derived from the EOF and the LSE methods.

			EOF-derived coseismic displacements			LSE-derived coseismic displacements		
Station Name	**Longitude (°E)**	**Latitude (°N)**	**East (mm)**	**North (mm)**	**Vertical (mm)**	**East (mm)**	**North (mm)**	**Vertical (mm)**
AUCK	174.834	−36.603	1.14	4.70	1.12	0.99	1.25	13.50
AUKT	174.770	−36.844	2.22	4.76	0.00	1.30	4.23	10.55
AVLN	174.933	−41.196	1.67	53.81	−3.30	0.72	51.29	11.61
BLUF	168.292	−46.585	−3.08	0.41	−1.31	−3.22	−1.06	3.97
BNET	170.190	−43.862	3.17	−1.76	2.49	2.07	1.27	−8.90
BTHL	175.137	−41.340	−20.99	33.25	−0.24	−35.58	50.24	−55.19
CHTI	183.383	−43.735	−6.38	2.64	0.42	−3.82	2.46	10.27
CLIM	175.145	−41.145	−5.69	33.34	1.04	−6.13	27.40	14.44
CLSK	172.753	−43.566	−10.57	−20.47	−19.73	−10.92	−17.75	−4.33
CMBL*	174.214	−41.749	1377.46	2362.86	1028.66	1369.67	2364.01	987.18
CNCL	169.856	−43.666	3.37	1.00	2.37	7.87	0.55	8.25
DNVK	176.167	−40.299	1.68	7.76	0.67	−6.60	7.18	35.51
DUNT	170.629	−45.814	−3.90	−2.62	−1.41	−1.31	−0.94	6.79
DURV	173.922	−40.802	12.80	66.48	−17.13	19.59	57.34	−15.34
GISB	177.886	−38.635	11.36	−2.18	−5.84	4.20	−2.96	2.10
GLDB	172.530	−40.827	40.87	−23.58	2.26	30.17	−14.10	7.89
GNBK	175.238	−40.080	3.27	18.39	−5.75	4.15	14.63	4.07
GRNG	175.459	−39.976	2.54	14.40	−6.23	3.00	9.22	6.51
GUNR	170.389	−43.392	11.27	−1.36	−4.69	7.88	−2.49	−25.13
HAAS	168.786	−44.073	1.82	1.71	1.83	3.42	2.02	14.03
HAMT	175.109	−37.807	1.64	6.40	−0.16	2.51	5.69	8.00
HANM*	172.793	−42.553	661.84	−174.51	−61.85	677.00	−179.59	−59.45
HAST	176.727	−39.617	4.12	1.24	−3.25	−0.76	5.39	8.25
HIKB	178.303	−37.561	1.56	0.36	−2.27	−0.89	1.78	10.53
HOKI	170.984	−42.713	30.16	−2.49	3.99	28.70	−4.18	14.69
HOLD	175.515	−40.897	−7.32	20.14	−19.95	−30.88	25.88	50.47
HORN	170.106	−43.777	3.26	0.45	−8.16	−8.12	−2.22	−51.85
KAIK*	173.534	−42.425	839.55	270.87	662.75	845.72	291.41	731.13
KAPT	174.910	−40.861	11.28	48.14	−9.43	10.28	40.60	−11.58
KARA	169.775	−43.608	6.12	1.27	−2.68	8.93	0.31	−13.09
KORO	175.424	−40.409	1.98	19.85	−6.94	2.11	15.53	−3.25
KTIA	173.273	−35.069	0.83	3.53	0.14	−1.86	0.51	7.72
LEVN	175.241	−40.589	3.15	27.35	−5.81	3.96	21.69	−8.68
LEXA	169.308	−45.231	−4.24	−0.14	−1.25	2.01	−1.99	3.32
LKTA	172.266	−42.783	77.93	−1.40	−11.39	72.36	−1.66	−16.67
LYTT	172.722	−43.606	−7.75	−19.65	−14.34	−6.98	−19.76	−7.83
MAHA*	173.794	−41.291	44.75	171.67	−25.80	35.72	171.31	−17.00
MAHI	177.907	−39.153	20.43	3.07	1.37	12.87	5.01	20.68
MAHO	174.854	−38.513	1.58	8.06	−1.80	−2.64	7.30	5.85
MANG	175.575	−40.669	−1.77	19.57	−2.32	−8.15	14.79	−37.61
MAVL	168.118	−45.367	−3.10	1.47	−0.09	2.66	0.29	5.96
METH	171.575	−43.591	1.38	−6.96	−5.00	1.75	−7.01	5.12
MQZG	172.655	−43.703	−9.66	−16.99	−11.64	−7.73	−14.39	−4.55
MRBL*	172.775	−42.662	248.33	−105.21	−8.09	251.99	−109.03	7.78
MTBL	175.536	−40.181	2.52	15.00	−4.18	0.79	14.08	6.87
MTJO	170.465	−43.986	0.00	−2.26	−1.03	2.91	−1.47	10.55
MTPR	170.351	−43.336	9.68	0.55	1.93	11.19	−2.11	35.28

Coseismic displacements derived from the EOF and the LSE methods.

			EOF-derived coseismic displacements			LSE-derived coseismic displacements		
Station Name	**Longitude (°E)**	**Latitude (°N)**	**East (mm)**	**North (mm)**	**Vertical (mm)**	**East (mm)**	**North (mm)**	**Vertical (mm)**
MTQN	175.241	−41.002	−2.07	29.22	−0.31	−5.80	28.88	12.06
NETT	170.061	−43.756	11.55	−3.85	2.31	6.18	−2.00	−18.87
NLSN	173.434	−41.184	47.38	16.36	−15.97	43.87	16.57	8.47
NPLY	174.118	−39.183	1.56	9.95	−5.86	6.04	11.92	2.28
OHIN	175.791	−39.918	2.31	10.66	−4.41	7.31	6.13	14.18
OKOH*	174.060	−41.019	24.55	124.69	−21.37	20.13	118.19	−11.27
OTAK	175.170	−40.817	4.03	33.00	−4.27	1.90	31.29	1.75
OUSD	170.511	−45.870	−4.08	−1.76	−0.98	−1.55	−2.90	11.66
PAEK	174.952	−41.022	8.98	48.59	−4.31	6.15	42.24	7.39
PALI	175.255	−41.569	−44.47	19.82	15.73	−46.35	13.69	23.83
PARW	175.427	−41.382	−28.37	16.68	4.28	−32.44	13.08	−11.50
PKNO	175.182	−39.805	3.50	15.24	−5.44	3.45	13.30	5.61
PTOI	175.999	−40.601	−1.95	9.64	−2.13	4.48	3.73	12.43
PUKE	178.257	−38.071	9.13	−0.58	−1.62	6.74	5.70	10.78
PYGR	166.681	−46.166	−1.70	0.68	1.86	1.37	1.17	2.89
QUAR	169.816	−43.532	6.08	0.55	0.04	6.99	−2.27	13.17
RDLV	175.404	−41.187	−16.38	20.44	2.41	−10.99	11.80	37.91
RIPA	176.493	−39.166	3.13	5.90	0.48	−4.45	8.67	−13.55
TAKP	175.963	−40.062	0.31	10.57	−0.96	−3.82	9.84	19.55
TAUP	176.081	−38.743	2.72	6.02	−1.25	−1.37	3.72	9.65
TAUW	178.006	−38.162	2.26	0.72	−0.91	2.70	−4.17	14.92
TEMA	175.890	−41.107	−15.14	9.88	2.49	−12.45	10.25	6.31
TINT	175.886	−40.776	−5.97	11.17	2.04	−2.17	7.31	16.69
TKHL	172.960	−41.034	54.52	−29.86	−1.62	47.46	−22.20	−7.53
TORY*	174.280	−41.192	49.69	174.97	−23.80	46.52	163.25	27.01
TRAV	175.688	−41.398	−27.39	10.87	8.11	−20.22	5.26	22.73
TRNG	176.261	−37.729	1.67	4.96	−1.71	3.33	1.02	4.20
TRWH*	174.628	−41.278	27.94	108.63	−6.76	19.93	100.72	9.53
V47B	172.663	−43.567	−8.75	−19.72	−20.04	−7.29	−19.92	−7.04
VGFW	175.553	−39.255	2.60	10.70	−1.36	2.55	8.23	7.17
VGMO	175.754	−39.407	3.52	8.45	−2.46	16.40	7.15	23.61
VGMT	175.470	−39.385	2.93	10.28	−2.64	2.76	7.75	−5.61
VGOB	175.542	−39.200	2.78	9.50	−1.21	3.22	10.45	2.71
VGWN	175.598	−39.327	4.63	7.91	−4.15	6.77	10.17	−23.21
WAIM	170.920	−44.656	−3.25	−3.82	−1.96	−1.62	−2.85	7.64
WAKA	169.885	−43.584	3.39	−2.53	1.66	4.04	1.37	3.55
WANG	174.821	−39.787	3.50	17.13	−4.79	3.24	13.93	7.45
WARK	174.663	−36.434	1.24	5.09	1.11	1.64	2.34	13.97
WEST*	171.806	−41.745	100.59	−36.66	14.85	101.05	−40.21	22.64
WGTN	174.806	−41.323	6.32	69.42	−2.92	5.33	67.97	−13.87
WGTT	174.782	−41.290	12.54	78.61	−6.55	16.04	70.80	−14.53
WHKT	177.014	−37.982	1.91	3.75	−0.58	1.15	2.41	8.80
WHNG	174.315	−35.804	0.93	4.68	1.15	2.41	1.09	14.31
WHVR	175.452	−39.730	2.31	12.66	−4.10	1.78	7.04	10.81
WITH*	173.984	−41.561	260.30	866.78	84.32	250.34	864.24	74.88
WRPA	175.583	−41.063	−11.66	15.36	0.90	−6.21	11.64	32.09
YALD	172.481	−43.491	−7.09	−19.80	−17.47	−5.31	−19.07	−11.14

Note: ⋆For these sites, the values are not shown in Fig. 3.9 due to their unusually high coseismic jumps.

Bibliography

[1] R. D. Adams, "Developments in studies of earthquake risk", *Bulletin of the New Zealand Society for Earthquake Engineering*, vol. 8, no. 1, pp. 1–11, 1975.

[2] H. Akaike, "A new look at the statistical model identification", *IEEE Transactions on Automatic Control*, vol. 19, no. 6, pp. 716–723, 1974.

[3] A. Alvera-Azcárate, A. Barth, J. M. Beckers, and R. H. Weisberg, "Multivariate reconstruction of missing data in sea surface temperature, chlorophyll, and wind satellite fields", *Journal of Geophysical Research: Oceans*, vol. 112, no. C3, 2007.

[4] A. Alvera-Azcárate, A. Barth, M. Rixen, and J. M. Beckers, "Reconstruction of incomplete oceanographic data sets using empirical orthogonal functions: Application to the Adriatic sea surface temperature", *Ocean Modelling*, vol. 9, no. 4, pp. 325–346, 2005.

[5] J. G. Anderson, "Estimating the seismicity from geological structure for seismic-risk studies", *Bulletin of the Seismological Society of America*, vol. 69, no. 1, pp. 135–158, 1979.

[6] C. Angelica, A. Bonforte, G. Distefano, E. Serpelloni, and S. Gresta, "Seismic potential in Italy from integration and comparison of seismic and geodetic strain rates", *Tectonophysics*, vol. 608, pp. 996–1006, 2013.

[7] K. Arora, A. Cazenave, E. R. Engdahl, R. Kind, A. Manglik, S. Roy, K. Sain, and S. Uyeda, *Encyclopedia of Solid Earth Geophysics*. Springer Science & Business Media, 2011.

[8] G. Aslan, "Monitoring of Surface Deformation in Northwest Turkey from High-Resolution InSAR: Focus on Tectonic Aseismic Slip and Subsidence", PhD thesis, Istanbul Teknik Üniversitesi, 2019.

[9] Ü. Atasever, M. Kesikoğlu, and C. Özkan, "A new artificial intelligence optimization method for PCA based unsupervised change detection of remote sensing image data", *Neural Network World*, vol. 26, no. 2, 2016.

[10] S. Atzori, C. Tolomei, A. Antonioli, J. P. Merryman Boncori, S. Bannister, E. Trasatti, P. Pasquali, and S. Salvi, "The 2010–2011 Canterbury, New Zealand, seismic sequence: Multiple source analysis from InSAR data and modeling", *Journal of Geophysical Research: Solid Earth*, vol. 117, no. B8, 2012.

[11] J. P. Avouac, "From geodetic imaging of seismic and aseismic fault slip to dynamic modeling of the seismic cycle", *Annual Review of Earth and Planetary Sciences*, vol. 43, pp. 233–271, 2015.

[12] P. M. Barnes, "Active folding of Pleistocene unconformities on the edge of the Australian-Pacific plate boundary zone, offshore North Canterbury, New Zealand", *Tectonics*, vol. 15, no. 3, pp. 623–640, 1996.

[13] P. M. Barnes, G. Lamarche, J. Bialas, S. Henrys, I. Pecher, G. L. Netzeband, J. Greinert, J. J. Mountjoy, K. Pedley, and G. Crutchley, "Tectonic and geological framework for gas hydrates and cold seeps on the Hikurangi subduction margin, New Zealand", *Marine Geology*, vol. 272, no. 4, pp. 26–48, 2010.

[14] P. M. Barnes, B. M. de Lépinay, J. Y. Collot, J. Delteil, and J. C. Audru, "Strain partitioning in the transition area between oblique subduction and continental collision, Hikurangi margin, New Zealand", *Tectonics*, vol. 17, no. 4, pp. 534–557, 1998.

[15] P. M. Barnes, A. Nicol, and T. Harrison, "Late cenozoic evolution and earthquake potential of an active listric thrust complex above the Hikurangi subduction zone, New Zealand", *Geological Society of America Bulletin*, vol. 114, no. 11, pp. 1379–1405, 2002.

[16] P. M. Barnes, S. D. Nodder, S. Woelz, and A. R. Orpin, "The structure and seismic potential of the Aotea and Evans Bay faults, Wellington, New Zealand", *New Zealand Journal of Geology and Geophysics*, vol. 62, no. 1, pp. 46–71, 2019.

[17] P. M. Barnes and N. Pondard, "Derivation of direct on-fault submarine paleoearthquake records from high-resolution seismic reflection profiles: Wairau fault, New Zealand", *Geochemistry, Geophysics, Geosystems*, vol. 11, no. 11, 2010.

[18] S. Beanland, K. R. Berryman, and G. H. Blick, "Geological investigations of the 1987 Edgecumbe earthquake, New Zealand", *New Zealand Journal of Geology and Geophysics*, vol. 32, no. 1, pp. 73–91, 1989.

[19] J. Beavan, P. Denys, M. Denham, B. Hager, T. Herring, and P. Molnar, "Distribution of present-day vertical deformation across the Southern Alps, New Zealand, from 10 years of GPS data", *Geophysical Research Letters*, vol. 37, no. 16, 2010.

[20] J. Beavan and J. Haines, "Contemporary horizontal velocity and strain rate fields of the Pacific-Australian plate boundary zone through New Zealand", *Journal of Geophysical Research: Solid Earth*, vol. 106, no. B1, pp. 741–770, 2001.

[21] J. Beavan, L. M. Wallace, N. Palmer, P. Denys, S. Ellis, N. Fournier, S. Hreinsdottir, C. Pearson, and M. Denham, "New Zealand GPS velocity field: 1995–2013", *New Zealand Journal of Geology and Geophysics*, vol. 59, no. 1, pp. 5–14, 2016.

[22] J. M. Beckers and M. Rixen, "EOF calculations and data filling from incomplete oceanographic datasets", *Journal of Atmospheric and Oceanic Technology*, vol. 20, no. 12, pp. 1839–1856, 2003.

[23] A. F. Bennett, *Inverse Methods in Physical Oceanography*. Cambridge University Press, 1992.

[24] K. Berryman and S. Beanland, "Ongoing deformation of New Zealand: rates of tectonic movement from geological evidence", *Transactions of the Institution of Professional Engineers New Zealand: General Section*, vol. 15, no. 1, pp. 25–35, 1988.

[25] R. Bilham, V. K. Gaur, and P. Molnar, "Himalayan seismic hazard", *Science*, vol. 293, no. 5534, pp. 1442–1444, 2001.

[26] D. Bilitza, "International reference ionosphere 2000", *Radio Science*, vol. 36, no. 2, pp. 261–275, 2001.

[27] H. Björnsson and S. Venegas, "A manual for EOF and SVD analyses of climatic data", *CCGCR Report*, vol. 97, no. 1, pp. 112–134, 1997.

[28] G. Blewitt, W. C. Hammond, and C. Kreemer, "Harnessing the GPS data explosion for interdisciplinary science", *EOS Transactions*, vol. 99, no. 10.1029, pp. 485–499, 2018.

[29] G. Blewitt, C. Kreemer, W. C. Hammond, and J. Gazeaux, "MIDAS robust trend estimator for accurate GPS station velocities without step detection", *Journal of Geophysical Research: Solid Earth*, vol. 121, no. 3, pp. 2054–2068, 2016.

[30] S. Bourne, T. Arnadottir, J. Beavan, D. Darby, P. England, B. Parsons, R. Walcott, and P. Wood, "Crustal deformation of the Marlborough fault zone in the South Island of New Zealand: Geodetic constraints over the interval 1982–1994", *Journal of Geophysical Research: Solid Earth*, vol. 103, no. B12, pp. 30 147–30 165, 1998.

[31] O. S. Boyd, "Including foreshocks and aftershocks in time-independent probabilistic seismic-hazard analyses", *Bulletin of the Seismological Society of America*, vol. 102, no. 3, pp. 909–917, 2012.

[32] H. Campbell, A. Malahoff, G. Browne, I. Graham, and R. Sutherland, "New Zealand geology", *Episodes Journal of International Geoscience*, vol. 35, no. 1, pp. 57–71, 2012.

[33] J. B. Carroll, "An analytical solution for approximating simple structure in factor analysis", *Psychometrika*, vol. 18, no. 1, pp. 23–38, 1953.

[34] S. Cesca, Y. Zhang, V. Mouslopoulou, R. Wang, J. Saul, M. Savage, S. Heimann, S. Kufner, O. Oncken, and T. Dahm, "Complex rupture process of the M_w7.8, 2016, Kaikoura earthquake, New Zealand, and its aftershock sequence", *Earth and Planetary Science Letters*, vol. 478, pp. 110–120, 2017.

[35] E. T. Chang and B. F. Chao, "Analysis of coseismic deformation using EOF method on dense, continuous gps data in Taiwan", *Tectonophysics*, vol. 637, no. 3, pp. 106–115, 2014.

[36] E. T. Chang and B. F. Chao, "Co-seismic surface deformation of the 2011 off the Pacific coast of Tohoku Earthquake: Spatio-temporal EOF analysis of GPS data", *Earth, Planets and Space*, vol. 63, no. 7, pp. 649–654, 2011.

[37] B. F. Chao and J. Liau, "Gravity changes due to large earthquakes detected in GRACE satellite data via empirical orthogonal function analysis", *Journal of Geophysical Research: Solid Earth*, vol. 124, no. 3, pp. 3024–3035, 2019.

[38] Z. Chen, S. R. Zhang, A. J. Coster, and G. Fang, "EOF analysis and modeling of GPS TEC climatology over North America", *Journal of Geophysical Research: Space Physics*, vol. 120, no. 4, pp. 3118–3129, 2015.

[39] K. Chousianitis, A. Ganas, and C. P. Evangelidis, "Strain and rotation rate patterns of mainland Greece from continuous GPS data and comparison between seismic and geodetic moment release", *Journal of Geophysical Research: Solid Earth*, vol. 120, no. 5, pp. 3909–3931, 2015.

[40] K. Clark, E. Nissen, J. Howarth, I. J. Hamling, J. Mountjoy, W. Ries, K. Jones, S. Goldstien, U. Cochran, P. Villamor, and S. Hreinsdottir, "Highly variable coastal deformation in the 2016, M_w7.8, Kaikoura earthquake reflects rupture complexity along a transpressional plate boundary", *Earth and Planetary Science Letters*, vol. 474, pp. 334–344, 2017.

[41] N. Cotte, H. Perfettini, B. Rousset, V. Kostoglodov, C. Lasserre, A. Walpersdorf, and E. Cabral, "Slow slip events and degree of coupling along the Mexican subduction zone in Guerrero and Oaxaca areas: Role of the slab geometry and its lateral variations, spatio-temporal evolution, slip budget, determined from cGPS time series inversion using PCAIM code", in *AGU Fall Meeting Abstracts*, vol. 2014, 2014, S53C–4517.

[42] H. Cowan, A. Nicol, and P. Tonkin, "A comparison of historical and paleoseismicity in a newly formed fault zone and a mature fault zone, North Canterbury, New Zealand", *Journal of Geophysical Research: Solid Earth*, vol. 101, no. B3, pp. 6021–6036, 1996.

[43] J. K. Dabbakuti and D. V. Ratnam, "Characterization of ionospheric variability in TEC using EOF and wavelets over low-latitude GNSS stations", *Advances in Space Research*, vol. 57, no. 12, pp. 2427–2443, 2016.

[44] J. K. Dabbakuti and D. V. Ratnam, "Modeling and analysis of GPS-TEC low latitude climatology during the 24^{th} solar cycle using empirical orthogonal functions", *Advances in Space Research*, vol. 60, no. 8, pp. 1751–1764, 2017.

[45] A. Darzi, B. Halldorsson, B. Hrafnkelsson, and K. S. Vogfjörð, "Short-term Bayesian ETAS spatiotemporal forecasting of the Ölfus 2008 earthquake sequence in Iceland", *Tectonophysics*, vol. 839, pp. 229 522–229 530, 2022.

[46] A. Dawson, "Eofs: A library for EOF analysis of meteorological, oceanographic, and climate data", *Journal of Open Research Software*, vol. 4, no. 1, 2016.

[47] C. DeMets, R. G. Gordon, D. F. Argus, and S. Stein, "Effect of recent revisions to the geomagnetic reversal time scale on estimates of current plate motions", *Geophysical Research Letters*, vol. 21, no. 20, pp. 2191–2194, 1994.

[48] P. Denys, C. Pearson, R. Norris, and M. Denham, "A geodetic study of Otago: results of the central Otago deformation network 2004–2014", *New Zealand Journal of Geology and Geophysics*, vol. 59, no. 1, pp. 147–156, 2016.

[49] A. Diederichs, E. Nissen, L. Lajoie, R. Langridge, S. Malireddi, K. Clark, I. J. Hamling, and A. Tagliasacchi, "Unusual kinematics of the Papatea fault (2016 Kaikōura earthquake) suggest anelastic rupture", *Science Advances*, vol. 5, no. 10, eaax5703, 2019.

[50] L. Dimitrova, L. M. Wallace, A. J. Haines, and C. A. Williams, "High-resolution view of active tectonic deformation along the Hikurangi subduction margin and the Taupo Volcanic Zone, New Zealand", *New Zealand Journal of Geology and Geophysics*, vol. 59, no. 1, pp. 43–57, 2016.

[51] A. J. Dittus, D. J. Karoly, M. G. Donat, S. C. Lewis, and L. V. Alexander, "Understanding the role of sea surface temperature-forcing for variability in global temperature and precipitation extremes", *Weather and Climate Extremes*, vol. 21, pp. 1–9, 2018.

[52] D. Dommenget and M. Latif, "A cautionary note on the interpretation of eofs", *Journal of Climate*, vol. 15, no. 2, pp. 216–225, 2002.

[53] D. Dong, P. Fang, Y. Bock, F. Webb, L. Prawirodirdjo, S. Kedar, and P. Jamason, "Spatiotemporal filtering using principal component analysis and Karhunen-Loeve expansion approaches for regional GPS network analysis", *Journal of Geophysical Research: Solid Earth*, vol. 111, no. B03405, 2006.

[54] G. L. Downes, "Atlas of Isoseismal Maps of New Zealand Earthquakes", *Oceanographic Literature Review*, vol. 10, no. 43, pp. 1019–1030, 1996.

[55] G. L. Downes, *Atlas of Isoseismal Maps of New Zealand Earthquakes 1843-2003*. GNS Science, 2014.

[56] D. Dowrick and E. Smith, "Surface wave magnitudes of some New Zealand earthquakes 1901–1988", *Bulletin of the New Zealand Society for Earthquake Engineering*, vol. 23, no. 3, pp. 198–210, 1990.

[57] D. A. Egolf, "Equilibrium regained: From nonequilibrium chaos to statistical mechanics", *Science*, vol. 287, no. 5450, pp. 101–104, 2000.

[58] G. A. Eiby, "An annotated list of New Zealand earthquakes, 1460–1965", *New Zealand Journal of Geology and Geophysics*, vol. 11, no. 3, pp. 630–647, 1968.

[59] G. A. Eiby, "A descriptive catalogue of New Zealand earthquakes: Part i—shocks felt before the end of 1845", *New Zealand Journal of Geology and Geophysics*, vol. 11, no. 1, pp. 16–40, 1968.

[60] C. Faccenna, O. Bellier, J. Martinod, C. Piromallo, and V. Regard, "Slab detachment beneath eastern Anatolia: A possible cause for the formation of the North Anatolian fault", *Earth and Planetary Science Letters*, vol. 242, no. 2, pp. 85–97, 2006.

[61] J. Feng, Z. Wang, W. Jiang, Z. Zhao, and B. Zhang, "A new regional total electron content empirical model in northeast China", *Advances in Space Research*, vol. 58, no. 7, pp. 1155–1167, 2016.

[62] C. Ferguson, W. Klein, and J. B. Rundle, "Spinodals, scaling and erogodicity in a model of an earthquake fault with long-range stress transfer", *Physical Review E*, vol. 60, pp. 1359–1373, 1999.

[63] E. Field, G. Biasi, P. Bird, T. Dawson, K. Felzer, D. Jackson, K. M. Johnson, T. Jordan, C. Madden, A. J. Michael, and K. Milner, "Long-term time-dependent probabilities for the third uniform California earthquake rupture forecast (UCERF3)", *Bulletin of the Seismological Society of America*, vol. 105, no. 2A, pp. 511–543, 2015.

[64] R. A. Fildes, D. L. Turcotte, and J. B. Rundle, "Natural time analysis of quasi-periodic caldera collapse events during the 2018 Kīlauea volcano eruptive sequence", in *AGU Fall Meeting Abstracts*, vol. 2019, NH21C–0983, 2019.

[65] J. M. Forbes, S. Bruinsma, and F. G. Lemoine, "Solar rotation effects on the thermospheres of Mars and Earth", *Science*, vol. 312, no. 5778, pp. 1366–1368, 2006.

[66] G. C. Fox, J. B. Rundle, A. Donnellan, and B. Feng, "Earthquake nowcasting with deep learning", *GeoHazards*, vol. 3, no. 2, pp. 199–226, 2022.

[67] A. D. Frankel, M. D. Petersen, C. S. Mueller, K. M. Haller, R. L. Wheeler, E. Leyendecker, R. L. Wesson, S. C. Harmsen, C. H. Cramer, D. M. Perkins, and K. S. Rukstales, "Documentation for the 2002 update of the national seismic hazard maps", *US Geological Survey Open-File Report*, vol. 2, no. 420, pp. 33–52, 2002.

[68] G. Fu and W. Sun, "Global co-seismic displacements caused by the 2004 Sumatra-Andaman earthquake (M_w9.1)", *Earth, Planets and Space*, vol. 58, no. 2, pp. 149–152, 2006.

[69] G. Fu, W. Sun, Y. Fukuda, S. Gao, and T. Hasegawa, "Effects of Earth's curvature and radial heterogeneity in dislocation studies: Case studies of the 2008 Wenchuan earthquake and the 2004 Sumatra earthquake", *Earthquake Science*, vol. 23, no. 4, pp. 301–308, 2010.

[70] A. Fukuoka, "The central meteorological observatory, a study on 10-day forecast (a synthetic report)", *Geophysical Magazine*, vol. 22, no. 3, pp. 177–208, 1951.

[71] S. García, S. Ramírez-Gallego, J. Luengo, J. M. Benítez, and F. Herrera, "Big data preprocessing: Methods and prospects", *Big Data Analytics*, vol. 1, no. 1, pp. 1–22, 2016.

[72] M. C. Gerstenberger, W. Marzocchi, T. Allen, M. Pagani, J. Adams, L. Danciu, E. H. Field, H. Fujiwara, N. Luco, K. F. Ma, and C. Meletti, "Probabilistic seismic hazard analysis at regional and national scales: State of the art and future challenges", *Reviews of Geophysics*, vol. 58, no. 2, e2019RG000653, 2020.

[73] Y. Ghiasi and V. Nafisi, "Strain estimation using ordinary Kriging interpolation", *Survey Review*, vol. 48, no. 350, pp. 361–366, 2016.

[74] F. Ghisetti and R. Sibson, "Compressional reactivation of E–W inherited normal faults in the area of the 2010–2011 Canterbury earthquake sequence", *New Zealand Journal of Geology and Geophysics*, vol. 55, no. 3, pp. 177–184, 2012.

[75] D. Golriz, Y. Bock, and X. Xu, "Defining the coseismic phase of the crustal deformation cycle with seismogeodesy", *Journal of Geophysical Research: Solid Earth*, vol. 126, no. 10, e2021JB022002, 2021.

[76] M. A. Goudarzi, M. Cocard, and R. Santerre, "Geostrain: An open source software for calculating crustal strain rates", *Computers & Geosciences*, vol. 82, pp. 1–12, 2015.

[77] N. E. Graham, J. Michaelsen, and T. P. Barnett, "An investigation of the El Niño-Southern Oscillation cycle with statistical models: 1. Predictor field characteristics", *Journal of Geophysical Research: Oceans*, vol. 92, no. C13, pp. 14 251–14 270, 1987.

[78] C. A. Greene, K. Thirumalai, K. A. Kearney, J. M. Delgado, W. Schwanghart, N. S. Wolfenbarger, K. M. Thyng, D. E. Gwyther, A. S. Gardner, and D. D. Blankenship, "The climate data toolbox for MATLAB", *Geochemistry, Geophysics, Geosystems*, vol. 20, no. 7, pp. 3774–3781, 2019.

[79] J. D. Griffin, M. W. Stirling, D. J. Barrell, E. J. Van Den Berg, E. K. Todd, R. Nicolls, and N. Wang, "Paleoseismology of the Hyde Fault, Otago, New Zealand", *New Zealand Journal of Geology and Geophysics*, pp. 1–25, 2021.

[80] J. Grotzinger, T. H. Jordan, and F. Press, *Understanding Earth*. Macmillan, 2010.

[81] M. Gruszczynski, A. Klos, and J. Bogusz, "Orthogonal transformation in extracting of common mode errors from continuous GPS networks", *Acta Geodynamica et Geomaterialia*, vol. 13, no. 3, pp. 291–298, 2016.

[82] R. D. Gupta and D. Kundu, "Theory & methods: Generalized exponential distributions", *Australian & New Zealand Journal of Statistics*, vol. 41, no. 2, pp. 173–188, 1999.

[83] R. D. Gupta and D. Kundu, "Generalized exponential distribution: Existing results and some recent developments", *Journal of Statistical Planning and Inference*, vol. 137, no. 11, pp. 3537–3547, 2007.

[84] A. J. Haines and L. M. Wallace, "New Zealand-wide geodetic strain rates using a physics-based approach", *Geophysical Research Letters*, vol. 47, no. 1, e2019GL084606, 2020.

[85] R. M. Hamilton and F. F. Evison, "Earthquakes at intermediate depths in south-west New Zealand", *New Zealand Journal of Geology and Geophysics*, vol. 10, no. 6, pp. 1319–1329, 1967.

[86] I. J. Hamling and S. Hreinsdóttir, "Reactivated afterslip induced by a large regional earthquake, Fiordland, New Zealand", *Geophysical Research Letters*, vol. 43, no. 6, pp. 2526–2533, 2016.

[87] I. J. Hamling, "A review of the 2016 Kaikōura earthquake: Insights from the first 3 years", *Journal of the Royal Society of New Zealand*, vol. 50, no. 2, pp. 226–244, 2020.

[88] I. J. Hamling, E D'Anastasio, L. Wallace, S. Ellis, M. Motagh, S. Samsonov, N. Palmer, and S. Hreinsdóttir, "Crustal deformation and stress transfer during a propagating earthquake sequence: The 2013 Cook Strait sequence, central New Zealand", *Journal of Geophysical Research: Solid Earth*, vol. 119, no. 7, pp. 6080–6092, 2014.

[89] I. J. Hamling, S. Hreinsdóttir, K. Clark, J. Elliott, C. Liang, E. Fielding, N. Litchfield, P. Villamor, L. M. Wallace, T. J. Wright, and E. Danastasio, "Complex multifault rupture during the 2016 M_w7.8 Kaikōura earthquake, New Zealand", *Science*, vol. 356, no. 6334, eaam7194, 2017.

[90] I. J. Hamling, T. J. Wright, S. Hreinsdóttir, and L. M. Wallace, "A snapshot of New Zealand's dynamic deformation field from Envisat InSAR and GNSS observations between 2003 and 2011", *Geophysical Research Letters*, vol. 49, no. 2, 2022.

[91] A. Hannachi, I. T. Jolliffe, D. B. Stephenson, and N. Trendafilov, "In search of simple structures in climate: Simplifying EOFs", *International Journal of Climatology*, vol. 26, no. 1, pp. 7–28, 2006.

[92] A. Hannachi, I. T. Jolliffe, and D. B. Stephenson, "Empirical orthogonal functions and related techniques in atmospheric science: A review", *International Journal of Climatology*, vol. 27, no. 9, pp. 1119–1152, 2007.

[93] A. E. Hatem, J. F. Dolan, R. W. Zinke, R. J. Van Dissen, C. M. McGuire, and E. J. Rhodes, "A 2000 yr paleoearthquake record along the Conway segment of the Hope fault: Implications for patterns of earthquake occurrence in northern South Island and southern North Island, New Zealand", *Bulletin of the Seismological Society of America*, vol. 109, no. 6, pp. 2216–2239, 2019.

[94] D. Hatzfeld, J. Martinod, G. Bastet, and P. Gautier, "An analog experiment for the Aegean to describe the contribution of gravitational potential energy", *Journal of Geophysical Research: Solid Earth*, vol. 102, no. B1, pp. 649–659, 1997.

[95] T. A. Herring, R. W. King, and S. C. McCluskey, *"Introduction to GAMIT/GLOBK, Release 10.4. Massachusetts Institute of Technology, Cambridge"*, 2015.

[96] D. J. Higham and N. J. Higham, *MATLAB Guide*. SIAM, 2016.

[97] A. Hippert-Ferrer, Y. Yan, and P. Bolon, "Gap-filling based on iterative EOF analysis of temporal covariance: Application to InSAR displacement time series", in *IGARSS 2019-2019 IEEE International Geoscience and Remote Sensing Symposium*, IEEE, 2019, pp. 262–265.

[98] B. Hofmann-Wellenhof, H. Lichtenegger, and J. Collins, *Global Positioning System: Theory and Practice*. Springer Science & Business Media, 2012.

[99] R. Hogg, J. McKean, and A. Craig, *Introduction to Mathematical Statistics*. Pearson Education, 2005.

[100] J. R. Holliday, W. R. Graves, J. B. Rundle, and D. L. Turcotte, "Computing earthquake probabilities on global scales", *Pure and Applied Geophysics*, vol. 173, no. 3, pp. 739–748, 2016.

[101] J. R. Holliday, J. B. Rundle, K. F. Tiampo, and D. L. Turcotte, "Using earthquake intensities to forecast earthquake occurrence times", *Nonlinear Processes in Geophysics*, vol. 13, no. 5, pp. 585–593, 2006.

[102] W. E. Holt and A. Haines, "The kinematics of northern South Island, New Zealand, determined from geologic strain rates", *Journal of Geophysical Research: Solid Earth*, vol. 100, no. B9, pp. 17 991–18 010, 1995.

[103] J. D. Horel, "A rotated principal component analysis of the interannual variability of the Northern Hemisphere 500 mb height field", *Monthly Weather Review*, vol. 109, no. 10, pp. 2080–2092, 1981.

[104] N. Horspool, K. Elwood, and M. Gerstenberger, "Risk-targeted hazard spectra for seismic design in New Zealand", in *Proceedings of the 2021 New Zealand Society for Earthquake Engineering Annual Technical Conference*, 2018.

[105] S. Hreinsdóttir, "Postseismic deformation following the 2016 Kaikoura earthquake (18/754)", 2021.

[106] Y. Hsu, S. Yu, M. Simons, L. Kuo, and H. Chen, "Crustal deformation in the Taiwan plate boundary zone revealed by GPS observations, seismicity, and earthquake focal mechanisms", in *AGU Fall Meeting Abstracts*, vol. 2008, T52B–07, 2008.

[107] Y. J. Hsu, M. Simons, J. P. Avouac, J. Galetzka, K. Sieh, M. Chlieh, D. Natawidjaja, L. Prawirodirdjo, and Y. Bock, "Frictional afterslip following the 2005 Nias-Simeulue earthquake, Sumatra", *Science*, vol. 312, no. 5782, pp. 1921–1926, 2006.

[108] Y. Hsu, S. Yu, M. Simons, L. Kuo, and H. Chen, "Interseismic crustal deformation in the Taiwan plate boundary zone revealed by GPS observations, seismicity, and earthquake focal mechanisms", *Tectonophysics*, vol. 479, no. 2, pp. 4–18, 2009.

[109] M. H. Huang, *Crustal Deformation During Co-and Postseismic Phases of the Earthquake Cycle Inferred from Geodetic and Seismic Data*. University of California, Berkeley, 2014.

[110] C. Hui-Hong, Z. Bei, Z. Huai, and S. Yao-Lin, "Calculation of the co-seismic deformation and stress changes of the Kaikoura M_w7. 8 earthquake, Nov 13, 2016", *Chinese Journal of Geophysics*, vol. 60, no. 5, pp. 520–531, 2017.

[111] A. Hull and K. Berryman, "Holocene tectonism in the region of the Alpine fault at Lake McKerrow, Fiordland, New Zealand", *Recent Crustal Movements of the Pacific Region*, vol. 24, pp. 317–331, 1986.

[112] I. Iervolino, M. Giorgio, and E. Chioccarelli, "Closed-form aftershock reliability of damage-cumulating elastic-perfectly-plastic systems", *Earthquake Engineering & Structural Dynamics*, vol. 43, no. 4, pp. 613–625, 2014.

[113] Z. Jiang, D. Huang, L. Yuan, A. Hassan, L. Zhang, and Z. Yang, "Coseismic and postseismic deformation associated with the 2016 M_w7.8 Kaikoura earthquake, New Zealand: fault movement investigation and seismic hazard analysis", *Earth, Planets and Space*, vol. 70, no. 1, pp. 1–14, 2018.

[114] Z. Jiang, L. Yuan, D. Huang, L. Zhang, A. Hassan, and Z. Yang, "Spatial-temporal evolution of slow slip movements triggered by the 2016 M_w7.8 Kaikoura earthquake, New Zealand", *Tectonophysics*, vol. 744, pp. 72–81, 2018.

[115] N. L. Johnson, S. Kotz, and N. Balakrishnan, *Continuous Univariate Distributions*. John Wiley & Sons, 1995.

[116] I. T. Jolliffe, *Principal Component Analysis*. Springer, 1986.

[117] I. T. Jolliffe, N. T. Trendafilov, and M. Uddin, "A modified principal component technique based on the LASSO", *Journal of Computational and Graphical Statistics*, vol. 12, no. 3, pp. 531–547, 2003.

[118] I. T. Jolliffe, "Principal component analysis: A beginner's guide—i. introduction and application", *Weather*, vol. 45, no. 10, pp. 375–382, 1990.

[119] H. Kahle, M. Cocard, Y. Peter, A. Geiger, R. Reilinger, A. Barka, and G. Veis, "GPS-derived strain rate field within the boundary zones of the Eurasian, African, and Arabian plates", *Journal of Geophysical Research: Solid Earth*, vol. 105, no. B10, pp. 23 353–23 370, 2000.

[120] H. F. Kaiser, "Computer program for varimax rotation in factor analysis", *Educational and Psychological Measurement*, vol. 19, no. 3, pp. 413–420, 1959.

[121] H. Kälviäinen, "From pattern recognition methods to machine vision applications", in *Advances in Independent Component Analysis and Learning Machines*, Elsevier, pp. 223–247, 2015.

[122] A. Kaplan, Y. Kushnir, M. A. Cane, and M. B. Blumenthal, "Reduced space optimal analysis for historical data sets: 136 years of Atlantic sea surface temperatures", *Journal of Geophysical Research: Oceans*, vol. 102, no. C13, pp. 27 835–27 860, 1997.

[123] E. A. Keller, *Introduction to Environmental Geology*. Prentice-Hall, Inc., 2007.

[124] K. Y. Kim and G. R. North, "Eofs of harmonizable cyclostationary processes", *Journal of the Atmospheric Sciences*, vol. 54, no. 19, pp. 2416–2427, 1997.

[125] K. Y. Kim and Q. Wu, "A comparison study of EOF techniques: Analysis of nonstationary data with periodic statistics", *Journal of Climate*, vol. 12, no. 1, pp. 185–199, 1999.

[126] J. Kingma, "The tectonic history of New Zealand", *New Zealand Journal of Geology and Geophysics*, vol. 2, no. 1, pp. 1–55, 1959.

[127] D. Kondrashov and M. Ghil, "Spatio-temporal filling of missing points in geophysical data sets", *Nonlinear Processes in Geophysics*, vol. 13, no. 2, pp. 151–159, 2006.

[128] A. Kositsky and J. P. Avouac, "Inverting geodetic time series with a principal component analysis-based inversion method", *Journal of Geophysical Research: Solid Earth*, vol. 115, no. B3, 2010.

[129] V. G. Kossobokov and A. K. Nekrasova, "Aftershock sequences of the recent major earthquakes in New Zealand", *Pure and Applied Geophysics*, vol. 176, no. 1, pp. 1–23, 2019.

[130] C. Kreemer, J. Haines, W. E. Holt, G. Blewitt, and D. Lavallee, "On the determination of a global strain rate model", *Earth, Planets and Space*, vol. 52, no. 10, pp. 765–770, 2000.

[131] J. Kula, A. Tulloch, T. L. Spell, and M. L. Wells, "Two-stage rifting of Zealandia-Australia-Antarctica: evidence from 40Ar/39Ar thermochronometry of the Sisters shear zone, Stewart Island, New Zealand", *Geology*, vol. 35, no. 5, pp. 411–414, 2007.

[132] U. Kumar, B. F. Chao, and E. T. Chang, "What causes the common-mode error in array GPS displacement fields: Case study for Taiwan in relation to atmospheric mass loading", *Earth and Space Science*, vol. 7, no. 11, e2020EA001159, 2020.

[133] M. Laird, "The Paparoa tectonic zone", *New Zealand Journal of Geology and Geophysics*, vol. 11, no. 2, pp. 435–454, 1968.

[134] R. Langridge, W. Ries, N. Litchfield, P. Villamor, R. Van Dissen, D. Barrell, M. Rattenbury, D. Heron, S. Haubrock, and D. Townsend, "The New Zealand active faults database", *New Zealand Journal of Geology and Geophysics*, vol. 59, no. 1, pp. 86–96, 2016.

[135] K. M. Lau and P. H. Chan, "Aspects of the 40–50 day oscillation during the northern summer as inferred from outgoing longwave radiation", *Monthly Weather Review*, vol. 114, no. 7, pp. 1354–1367, 1986.

[136] F. Leberl, *"Observations and Least Squares"*. Elsevier, 1978.

[137] M. Li, L. Yan, Z. Jiang, and G. Xiao, "Insights into spatio-temporal slow slip events offshore the Boso Peninsula in central Japan during 2011–2019 using GPS data", *Geodesy and Geodynamics*, 2022.

[138] S. Li, J. Peng, W. Xu, and K. Qin, "Time series modeling and analysis of trends of daily averaged ionospheric total electron content", *Advances in Space Research*, vol. 52, no. 5, pp. 801–809, 2013.

[139] Y. N. Lin, A. P. Kositsky, and J. P. Avouac, "PCAIM joint inversion of InSAR and ground-based geodetic time series: Application to monitoring magmatic inflation beneath the Long Valley Caldera", *Geophysical Research Letters*, vol. 37, p. L23301, 2010.

[140] N. Litchfield, R. Van Dissen, R. Sutherland, P. M. Barnes, S. Cox, R. Norris, R. Beavan, R. Langridge, P. Villamor, K Berryman, and M. Stirling, "A model of active faulting in New Zealand", *New Zealand Journal of Geology and Geophysics*, vol. 57, no. 1, pp. 32–56, 2014.

[141] J. Y. Liu, Y. J. Chuo, S. J. Shan, Y. B. Tsai, Y. I. Chen, S. A. Pulinets, and S. B. Yu, "Pre-earthquake ionospheric anomalies registered by continuous GPS TEC measurements", in *Annales Geophysicae*, Copernicus GmbH, vol. 22, pp. 1585–1593, 2004.

[142] E. N. Lorenz, *Empirical Orthogonal Functions and Statistical Weather Prediction*. Massachusetts Institute of Technology, Department of Meteorology Cambridge, 1956.

[143] M. Luginbuhl, J. B. Rundle, A. Hawkins, and D. L. Turcotte, "Nowcasting earthquakes: a comparison of induced earthquakes in Oklahoma and at the Geysers, California", *Pure and Applied Geophysics*, vol. 175, no. 1, pp. 49–65, 2018.

[144] M. Luginbuhl, J. B. Rundle, and D. L. Turcotte, "Natural time and nowcasting induced seismicity at the Groningen gas field in the Netherlands", *Geophysical Journal International*, vol. 215, no. 2, pp. 753–759, 2018.

[145] M. Luginbuhl, J. B. Rundle, and D. L. Turcotte, "Natural time and nowcasting earthquakes: Are large global earthquakes temporally clustered?", in *Earthquakes and Multihazards Around the Pacific Rim, Vol. II*, Springer, pp. 137–146, 2019.

[146] X. Ma, B. Liu, W. Dai, C. Kuang, and X. Xing, "Potential contributors to common mode error in array GPS displacement fields in Taiwan island", *Remote Sensing*, vol. 13, no. 21, pp. 4221–4229, 2021.

[147] I. Manighetti, C. Perrin, Y. Gaudemer, S. Dominguez, N. Stewart, J. Malavieille, and S. Garambois, "Repeated giant earthquakes on the Wairarapa fault, New Zealand, revealed by Lidar-based paleoseismology", *Scientific Reports*, vol. 10, no. 1, pp. 1–11, 2020.

[148] T. Mao, W. X. Wan, and L. B. Liu, "An EOF based empirical model of TEC over Wuhan", *Chinese Journal of Geophysics*, vol. 48, no. 4, pp. 827–834, 2005.

[149] F. Masson, J. Chéry, D. Hatzfeld, J. Martinod, P. Vernant, F. Tavakoli, and M. Ghafory-Ashtiani, "Seismic versus aseismic deformation in Iran inferred from earthquakes and geodetic data", *Geophysical Journal International*, vol. 160, no. 1, pp. 217–226, 2005.

[150] B. J. Meade, "The signature of an unbalanced earthquake cycle in Himalayan topography?", *Geology*, vol. 38, no. 11, pp. 987–990, 2010.

[151] C. J. Merchant, P. J. Minnett, H. Beggs, G. K. Corlett, C. Gentemann, A. R. Harris, J. Hoyer, and E. Maturi, "Global sea surface temperature", in *Taking the Temperature of the Earth*, Elsevier, pp. 5–55, 2019.

[152] T. A. Middleton, B. Parsons, and R. T. Walker, "Comparison of seismic and geodetic strain rates at the margins of the Ordos Plateau, northern China", *Geophysical Journal International*, vol. 212, no. 2, pp. 988–1009, 2018.

[153] P. Molnar, "The structure of mountain ranges", *Scientific American*, vol. 255, no. 1, pp. 70–79, 1986.

[154] N. Mortimer, H. J. Campbell, A. J. Tulloch, P. R. King, V. M. Stagpoole, R. A. Wood, M. S. Rattenbury, R. Sutherland, C. J. Adams, J. Collot, and M. Seton, "Zealandia: Earth's hidden continent", *GSA Today*, vol. 27, no. 3, pp. 27–35, 2017.

[155] V. Mouslopoulou, A. Nicol, T. Little, and J. Walsh, "Displacement transfer between intersecting regional strike-slip and extensional fault systems", *Journal of Structural Geology*, vol. 29, no. 1, pp. 100–116, 2007.

[156] H. Munekane, "Coseismic and early postseismic slips associated with the 2011 off the Pacific coast of Tohoku Earthquake sequence: EOF analysis of GPS kinematic time series", *Earth, Planets and Space*, vol. 64, no. 12, pp. 1077–1091, 2012.

[157] D. P. Murthy, M. Xie, and R. Jiang, *Weibull Models*. John Wiley & Sons, 2004.

[158] C. Nantasenamat, C. Isarankura-Na-Ayudhya, T. Naenna, and V. Prachayasittikul, "A practical overview of quantitative structure-activity relationship", *Experimental and Clinical Sciences*, vol. 8, pp. 74–88, 2009.

[159] A. Navarra and V. Simoncini, *A Guide to Empirical Orthogonal Functions for Climate Data Analysis*. Springer Science & Business Media, 2010.

[160] C. Nguyen, "Development of Geodetic Imaging Techniques and Machine Learning for Marsh Observation", PhD thesis, Texas A&M University-Corpus Christi, 2019.

[161] A. Nicol, R. Van Dissen, M. W. Stirling, and M. Gerstenberger, "Completeness of the paleoseismic active-fault record in New Zealand", *Seismological Research Letters*, vol. 87, no. 6, pp. 1299–1310, 2016.

[162] A. Nicol and J. Beavan, "Shortening of an overriding plate and its implications for slip on a subduction thrust, central Hikurangi Margin, New Zealand", *Tectonics*, vol. 22, no. 6, 2003.

[163] A. Nicol and R. V. Dissen, "A 6000-year record of surface-rupturing paleoearthquakes on the Wairau Fault, New Zealand", *New Zealand Journal of Geology and Geophysics*, vol. 61, no. 3, pp. 341–358, 2018.

[164] S. D. Nodder, G. Lamarche, J. Proust, and M. Stirling, "Characterizing earthquake recurrence parameters for offshore faults in the low-strain, compressional Kapiti-Manawatu Fault System, New Zealand", *Journal of Geophysical Research: Solid Earth*, vol. 112, no. B12, 2007.

[165] R. J. Norris and A. F. Cooper, "Late Quaternary slip rates and slip partitioning on the Alpine Fault, New Zealand", *Journal of Structural Geology*, vol. 23, no. 3, pp. 507–520, 2001.

[166] G. R. North, "Empirical orthogonal functions and normal modes", *Journal of Atmospheric Sciences*, vol. 41, no. 5, pp. 879–887, 1984.

[167] A. M. Obukhov, "Statistically homogeneous fields on a sphere", *Uspekhi Matematicheskikh Nauk*, vol. 2, no. 2, pp. 196–198, 1947.

[168] A. Okada and T. Nagata, "Land deformation of the neighbourhood of Muroto Point after the Nankaido great earthquake in 1946", *Bulletin of the Earthquake Research Institute*, vol. 31, pp. 169–177, 1953.

[169] T. Okuda and S. Ide, "Streak and hierarchical structures of the Tohoku–Hokkaido subduction zone plate boundary", *Earth, Planets and Space*, vol. 70, no. 1, pp. 1–17, 2018.

[170] M. Orellana and P. Cedillo, "Outlier detection with data mining techniques and statistical methods", in *2019 International Conference on Information Systems and Computer Science (INCISCOS)*, IEEE, pp. 51–56, 2019.

[171] G. Ouillon and D. Sornette, "Unbiased multifractal analysis: Application to fault patterns", *Geophysical Research Letters*, vol. 23, no. 23, pp. 3409–3412, 1996.

[172] Z. Pan, Z. Yun, and Z. Shao, "Contemporary crustal deformation of Northeast Tibet from geodetic investigations and a comparison between the seismic and geodetic moment release rates", *Physics of the Earth and Planetary Interiors*, vol. 304, p. 106 489, 2020.

[173] A. Pancha, J. G. Anderson, and C. Kreemer, "Comparison of seismic and geodetic scalar moment rates across the basin and range province", *Bulletin of the Seismological Society of America*, vol. 96, no. 1, pp. 11–32, 2006.

[174] S. K. Panda, S. S. Gedam, and S. Jin, "Ionospheric TEC variations at low latitude Indian region", *Satellite Positioning-Methods, Models and Applications. In Tech-Publisher, Rijeka, Croatia*, pp. 149–174, 2015.

[175] C. Pappas, S. M. Papalexiou, and D. Koutsoyiannis, "A quick gap filling of missing hydrometeorological data", *Journal of Geophysical Research: Atmospheres*, vol. 119, no. 15, pp. 9290–9300, 2014.

[176] S. Pasari, "Estimation of current earthquake hazard through nowcasting method", in *Advances in Computational Modeling and Simulation*, Springer, pp. 55–60, 2022.

[177] S. Pasari, "Understanding Himalayan Tectonics from Geodetic and Stochastic Modeling", *Unpublished PhD Thesis, Indian Institute of Technology Kanpur*, vol. 376, 2015.

[178] S. Pasari, A. Simanjuntak, A. Mehta, N. Neha, and Y. Sharma, "The current state of earthquake potential on Java Island, Indonesia", *Pure and Applied Geophysics*, vol. 178, no. 8, pp. 2789–2806, 2021.

[179] S. Pasari, "Nowcasting earthquakes in the Bay of Bengal region", *Pure and Applied Geophysics*, vol. 176, no. 4, pp. 1417–1432, 2019.

[180] S. Pasari and O. Dikshit, "Distribution of earthquake interevent times in northeast India and adjoining regions", *Pure and Applied Geophysics*, vol. 172, no. 10, pp. 2533–2544, 2015.

[181] S. Pasari, "Stochastic modeling of earthquake interevent counts (Natural Times) in Northwest Himalaya and adjoining regions", in *International Conference on Applied and Computational Mathematics*, Springer, pp. 495–501, 2018.

[182] S. Pasari and O. Dikshit, "Three-parameter generalized exponential distribution in earthquake recurrence interval estimation", *Natural Hazards*, vol. 73, no. 2, pp. 639–656, 2014.

[183] S. Pasari and A. Mehta, "Nowcasting earthquakes in the northwest Himalaya and surrounding regions", *The International Archives of Photogrammetry, Remote Sensing and Spatial Information Sciences*, vol. 42, pp. 855–859, 2018.

[184] S. Pasari and N. Neha, "A review of empirical orthogonal function (EOF) with an emphasis on the co-seismic crustal deformation analysis", *Natural Hazards*, vol. 110, pp. 29–56, 2022.

[185] S. Pasari and Y. Sharma, "Contemporary earthquake hazards in the west-northwest Himalaya: A statistical perspective through natural times", *Seismological Research Letters*, vol. 91, no. 6, pp. 3358–3369, 2020.

[186] S. Pasari, Y. Sharma, and N. Neha, "Quantifying the current state of earthquake hazards in Nepal", *Applied Computing and Geosciences*, vol. 10, p. 100 058, 2021.

[187] S. Pasari, A. Simanjuntak, A. Mehta, N. Neha, and Y. Sharma, "A synoptic view of the natural time distribution and contemporary earthquake hazards in Sumatra, Indonesia", *Natural Hazards*, vol. 108, no. 1, pp. 309–321, 2021.

[188] S. Pasari, A. Simanjuntak, N. Neha, and Y. Sharma, "Nowcasting earthquakes in Sulawesi Island, Indonesia", *Geoscience Letters*, vol. 8, no. 1, pp. 1–13, 2021.

[189] F. Pedregosa, G. Varoquaux, A. Gramfort, V. Michel, B. Thirion, O. Grisel, M. Blondel, P. Prettenhofer, R. Weiss, and V. Dubourg, "Scikit-learn: Machine learning in Python", *The Journal of Machine Learning Research*, vol. 12, pp. 2825–2830, 2011.

[190] J. Perez-Oregon, F. Angulo-Brown, and N. V. Sarlis, "Nowcasting avalanches as earthquakes and the predictability of strong avalanches in the Olami-Feder-Christensen Model", *Entropy*, vol. 22, no. 11, pp. 1228–1236, 2020.

[191] N. Pondard and P. M. Barnes, "Structure and paleoearthquake records of active submarine faults, Cook Strait, New Zealand: Implications for fault interactions, stress loading, and seismic hazard", *Journal of Geophysical Research: Solid Earth*, vol. 115, no. B12, 2010.

[192] M. Quigley, R. Van Dissen, N. Litchfield, P. Villamor, B. Duffy, D. Barrell, K. Furlong, T. Stahl, E. Bilderback, and D. Noble, "Surface rupture during the 2010 M_w7.1 Darfield (Canterbury) earthquake: Implications for fault rupture dynamics and seismic-hazard analysis", *Geology*, vol. 40, no. 1, pp. 55–58, 2012.

[193] M. Radiguet, H. Perfettini, N. Cotte, A. Gualandi, B. Valette, V. Kostoglodov, T. Lhomme, A. Walpersdorf, E. Cabral Cano, and M. Campillo, "Triggering of the 2014 M_w7.3 Papanoa earthquake by a slow slip event in Guerrero, Mexico", *Nature Geoscience*, vol. 9, no. 11, pp. 829–833, 2016.

[194] A. Rashidi, H. Kianimehr, F. Yamini-Fard, M. Tatar, and H. Zafarani, "Present stress map and deformation distribution in the NE Lut block, Eastern Iran: Insights from seismic and geodetic strain and moment rates", *Pure and Applied Geophysics*, pp. 1–31, 2022.

[195] H. F. Reid, "The machanism of the earthquake, in the California Earthquake of April 18, 1906", *Report of the State Earthquake Investigation Commission*, vol. 2, pp. 16–28, 1910.

[196] M. Reyners, R. Robinson, and P. McGinty, "Plate coupling in the northern South Island and southernmost North Island, New Zealand, as illuminated by earthquake focal mechanisms", *Journal of Geophysical Research: Solid Earth*, vol. 102, no. B7, pp. 15 197–15 210, 1997.

[197] R. W. Reynolds and T. M. Smith, "Improved global sea surface temperature analyses using optimum interpolation", *Journal of Climate*, vol. 7, no. 6, pp. 929–948, 1994.

[198] M. B. Richman, "Rotation of principal components", *Journal of Climatology*, vol. 6, no. 3, pp. 293–335, 1986.

[199] F. Riguzzi, M. Crespi, R. Devoti, C. Doglioni, G. Pietrantonio, and A. R. Pisani, "Geodetic strain rate and earthquake size: New clues for seismic hazard studies", *Physics of the Earth and Planetary Interiors*, vol. 206, pp. 67–75, 2012.

[200] H. Rishbeth, I. C. F. Müller-Wodarg, L. Zou, T. J. Fuller Rowell, G. H. Millward, R. J. Moffett, D. W. Idenden, and A. D. Aylward, "Annual and semiannual variations in the ionospheric F2-layer: II. Physical discussion", in *Annales Geophysicae*, Springer, vol. 18, pp. 945–956, 2000.

[201] J. Ristau, "Implementation of routine regional moment tensor analysis in New Zealand", *Seismological Research Letters*, vol. 79, no. 3, pp. 400–415, 2008.

[202] R. Robiana, I. Meilano, A. D. Nugraha, and Susilo, "Preliminary result: Earthquake rates analysis from seismic and geodetic strain at Nusa Tenggara and Banda region, Indonesia", in *AIP Conference Proceedings*, AIP Publishing LLC, vol. 1987, pp. 020 013–020019, 2018.

[203] R. Robinson, "Potential earthquake triggering in a complex fault network: the northern South Island, New Zealand", *Geophysical Journal International*, vol. 159, no. 2, pp. 734–748, 2004.

[204] T. Robinson and T. Davies, "Review Article: Potential geomorphic consequences of a future great (M_w combining double low line 8.0+) Alpine Fault earthquake, South Island, New Zealand", *Natural Hazards and Earth System Sciences*, vol. 13, no. 9, pp. 2279–2299, 2013.

[205] Y. Rong, P. Bird, and D. Jackson, "Earthquake potential and magnitude limits inferred from a geodetic strain-rate model for southern Europe", *Geophysical Supplements to the Monthly Notices of the Royal Astronomical Society*, vol. 205, no. 1, pp. 509–522, 2016.

[206] S. Rontogianni, "Comparison of geodetic and seismic strain rates in Greece by using a uniform processing approach to campaign GPS measurements over the interval 1994–2000", *Journal of Geodynamics*, vol. 50, no. 5, pp. 381–399, 2010.

[207] J. B. Rundle, K. Tiampo, W. Klein, and J. Sa Martins, "Self-organization in leaky threshold systems: The influence of near-mean field dynamics and its implications for earthquakes, neurobiology, and forecasting", *Proceedings of the National Academy of Sciences*, vol. 99, no. 1, pp. 2514–2521, 2002.

[208] J. B. Rundle and A. Donnellan, "Nowcasting earthquakes in Southern California with machine learning: bursts, swarms, and aftershocks may be related to levels of regional tectonic stress", *Earth and Space Science*, vol. 7, no. 9, e2020EA001097, 2020.

[209] J. B. Rundle, A. Donnellan, G. Fox, and J. P. Crutchfield, "Nowcasting earthquakes by visualizing the earthquake cycle with machine learning: A comparison of two methods", *Surveys in Geophysics*, vol. 43, no. 2, pp. 483–501, 2022.

[210] J. B. Rundle, A. Donnellan, G. Fox, J. P. Crutchfield, and R. Granat, "Nowcasting earthquakes: imaging the earthquake cycle in California with machine learning", *Earth and Space Science*, vol. 8, no. 12, e2021EA001757, 2021.

[211] J. B. Rundle, S. Gross, W. Klein, C. Ferguson, and D. L. Turcotte, "The statistical mechanics of earthquakes", *Tectonophysics*, vol. 277, no. 3, pp. 147–164, 1997.

[212] J. B. Rundle, J. R. Holliday, W. R. Graves, D. L. Turcotte, K. F. Tiampo, and W. Klein, "Probabilities for large events in driven threshold systems", *Physical Review E*, vol. 86, no. 2, pp. 021 106–021 112, 2012.

[213] J. B. Rundle, W. Klein, S. Gross, and C. Ferguson, "Traveling density wave models for earthquakes and driven threshold systems", *Physical Review E*, vol. 56, no. 1, pp. 293–301, 1997.

[214] J. B. Rundle, W. Klein, S. Gross, and D. L. Turcotte, "Boltzmann fluctuations in numerical simulations of nonequilibrium lattice threshold systems", *Physical Review Letters*, vol. 75, no. 8, pp. 1658–1669, 1995.

[215] J. B. Rundle, M. Luginbuhl, A. Giguere, and D. L. Turcotte, "Natural time, nowcasting and the physics of earthquakes: Estimation of seismic risk to global megacities", in *Earthquakes and Multi-hazards Around the Pacific Rim, Vol. II*, Springer, pp. 123–136, 2019.

[216] J. B. Rundle, P. B. Rundle, A. Donnellan, D. L. Turcotte, R. Shcherbakov, P. Li, B. Malamud, L. Grant, G. Fox, and D. McLeod, "A simulation-based approach to forecasting the next great San Francisco earthquake", *Proceedings of the National Academy of Sciences*, vol. 102, no. 43, pp. 15 363–15 367, 2005.

[217] J. B. Rundle, S. Stein, A. Donnellan, D. L. Turcotte, W. Klein, and C. Saylor, "The complex dynamics of earthquake fault systems: New approaches to forecasting and nowcasting of earthquakes", *Reports on Progress in Physics*, vol. 84, no. 7, pp. 076 801–076 810, 2021.

[218] J. B. Rundle, D. Turcotte, A. Donnellan, L. Grant Ludwig, M. Luginbuhl, and G. Gong, "Nowcasting earthquakes", *Earth and Space Science*, vol. 3, no. 11, pp. 480–486, 2016.

[219] J. B. Rundle, D. L. Turcotte, R. Shcherbakov, W. Klein, and C. Sammis, "Statistical physics approach to understanding the multiscale dynamics of earthquake fault systems", *Reviews of Geophysics*, vol. 41, no. 4, 2003.

[220] J. B. Rundle, J. Yazbeck, A. Donnellan, G. Fox, L. G. Ludwig, M. Heflin, and J. Crutchfield, "Optimizing earthquake nowcasting with machine learning: The role of strain hardening in the earthquake cycle", *Earth and Space Science*, e2022EA002343, 2022.

[221] L. Salditch, S. Stein, J. Neely, B. D. Spencer, E. M. Brooks, A. Agnon, and M. Liu, "Earthquake supercycles and long-term fault memory", *Tectonophysics*, vol. 774, pp. 89–96, 2020.

[222] N. Sarlis, E. Skordas, and P. Varotsos, "A remarkable change of the entropy of seismicity in natural time under time reversal before the super-giant M_w9.0 Tohoku earthquake on 11 March 2011", *Europhysics Letters*, vol. 124, no. 2, pp. 29 001–29 012, 2018.

[223] J. C. Savage and R. W. Simpson, "Surface strain accumulation and the seismic moment tensor", *Bulletin of the Seismological Society of America*, vol. 87, no. 5, pp. 1345–1353, 1997.

[224] R. Sawires, J. A. Peláez, F. Sparacino, A. M. Radwan, M. Rashwan, and M. Palano, "Seismic and geodetic crustal moment-rates comparison: New insights on the seismic hazard of Egypt", *Applied Sciences*, vol. 11, no. 17, pp. 7836–7845, 2021.

[225] C. H. Scholz, *The Mechanics of Earthquakes and Faulting*. Cambridge University Press, 2019.

[226] P. Segall and M. Matthews, "Time dependent inversion of geodetic data", *Journal of Geophysical Research: Solid Earth*, vol. 102, no. B10, pp. 22 391–22 409, 1997.

[227] Y. Sharma, S. Pasari, K. E. Ching, O. Dikshit, T. Kato, J. N. Malik, C. P. Chang, and J. Y. Yen, "Spatial distribution of earthquake potential along the Himalayan arc", *Tectonophysics*, vol. 791, pp. 228 556–228 565, 2020.

[228] R. Shcherbakov, D. L. Turcotte, and J. B. Rundle, "Aftershock statistics", *Pure and Applied Geophysics*, vol. 162, no. 6, pp. 1051–1076, 2005.

[229] Z. K. Shen, D. D. Jackson, and B. X. Ge, "Crustal deformation across and beyond the Los Angeles basin from geodetic measurements", *Journal of Geophysical Research: Solid Earth*, vol. 101, no. B12, pp. 27 957–27 980, 1996.

[230] N. V. Shestakov, H. Takahashi, M. Ohzono, A. S. Prytkov, V. G. Bykov, M. D. Gerasimenko, M. N. Luneva, G. N. Gerasimov, A. G. Kolomiets, and V. A. Bormotov, "Analysis of the far-field crustal displacements caused by the 2011 Great Tohoku earthquake inferred from continuous GPS observations", *Tectonophysics*, vol. 524, pp. 76–86, 2012.

[231] X. Shi, P. Tapponnier, T. Wang, S. Wei, Y. Wang, X. Wang, and L. Jiao, "Triple junction kinematics accounts for the 2016 M_w7.8 Kaikoura earthquake rupture complexity", *Proceedings of the National Academy of Sciences*, vol. 116, no. 52, pp. 26 367–26 375, 2019.

[232] X. Shi, Y. Wang, J. Liu-Zeng, R. Weldon, S. Wei, T. Wang, and K. Sieh, "How complex is the 2016 M_w7.8 Kaikoura earthquake, South Island, New Zealand", *Science Bulletin*, vol. 62, no. 5, pp. 309–311, 2017.

[233] M. N. Shrivastava, G. Gonzalez, M. Moreno, M. Chlieh, P. Salazar, C. D. Reddy, J. C. Baez, G. Yanez, J. Gonzalez, and J. Llera, "Coseismic slip and afterslip of the 2015 M_w8.3 Illapel (Chile) earthquake determined from continuous GPS data", *Geophysical Research Letters*, vol. 43, no. 20, pp. 10–710, 2016.

[234] W. D. Smith, "Earthquake hazaed in New Zealand; Inferences from seismology and geology", *Royal Society of New Zealand Bulletin*, vol. 24, pp. 223–243, 1986.

[235] W. Spakman and M. Nyst, "Inversion of relative motion data for estimates of the velocity gradient field and fault slip", *Earth and Planetary Science Letters*, vol. 203, no. 1, pp. 577–591, 2002.

[236] K. Sreejith, P. Sunil, R. Agrawal, A. P. Saji, D. Ramesh, and A. Rajawat, "Coseismic and early postseismic deformation due to the 25 April 2015, M_w7.8 Gorkha, Nepal, earthquake from InSAR and GPS measurements", *Geophysical Research Letters*, vol. 43, no. 7, pp. 3160–3168, 2016.

[237] M. Stirling and M. Gerstenberger, "Ground motion–based testing of seismic hazard models in New Zealand", *Bulletin of the Seismological Society of America*, vol. 100, no. 4, pp. 1407–1414, 2010.

[238] M. Stirling, J. Griffin, and E. van den Berg, "Paleoseismology of the Hyde and Northwest Cardrona faults, Otago", 2020.

[239] M. Stirling, G. McVerry, K. Berryman, P. McGinty, P. Villamor, R. Van Dissen, D. Dowrick, J. Cousins, and R. Sutherland, *Probabilistic Seismic Hazard Assessment of New Zealand: New Active Fault Data, Seismicity Data, Attenuation Relationships and Methods*. Institute of Geological and Nuclear Sciences Limited, 2000.

[240] M. Stirling, G. McVerry, M. Gerstenberger, N. Litchfield, R. Van Dissen, K. Berryman, P. Barnes, L. Wallace, P. Villamor, and R. Langridge, "National seismic hazard model for New Zealand: 2010 update", *Bulletin of the Seismological Society of America*, vol. 102, no. 4, pp. 1514–1542, 2012.

[241] M. Stirling, G. Verry, and K. Berryman, "A new seismic hazard model for New Zealand", *Bulletin of the Seismological Society of America*, vol. 92, no. 5, pp. 1878–1903, 2002.

[242] M. Stirling, S. G. Wesnousky, and K. R. Berryman, "Probabilistic seismic hazard analysis of New Zealand", *New Zealand Journal of Geology and Geophysics*, vol. 41, no. 4, pp. 355–375, 1998.

[243] X. Su, G. Meng, L. Su, W. Wu, and T. Liu, "Coseismic and early postseismic deformation of the 2016 M_w7.8 Kaikōura earthquake, New Zealand, from continuous GPS observations", *Pure and Applied Geophysics*, vol. 177, no. 1, pp. 285–303, 2020.

[244] R. Sutherland, D. Eberhart Phillips, R. Harris, T. Stern, J. Beavan, S. Ellis, S. Henrys, S. Cox, R. Norris, and K. Berryman, "Do great earthquakes occur on the Alpine fault in central South Island, New Zealand?", *Geophysical Monograph-American Geophysical Union*, vol. 175, pp. 237–240, 2007.

[245] R. Sutherland, K. Berryman, and R. Norris, "Quaternary slip rate and geomorphology of the Alpine fault: Implications for kinematics and seismic hazard in southwest New Zealand", *Geological Society of America Bulletin*, vol. 118, no. 4, pp. 464–474, 2006.

[246] M. H. Taylor, M. Losch, M. Wenzel, and J. Schröter, "On the sensitivity of field reconstruction and prediction using empirical orthogonal functions derived from gappy data", *Journal of Climate*, vol. 26, no. 22, pp. 9194–9205, 2013.

[247] R. Tenzer and A. Fadil, "Tectonic classification of vertical crustal motions–a case study for New Zealand", *Contributions to Geophysics and Geodesy*, vol. 46, no. 2, pp. 91–109, 2016.

[248] R. E. Thomson and W. J. Emery, *Data Analysis Methods in Physical Oceanography*. Newnes, 2014.

[249] K. F. Tiampo, J. B. Rundle, W. Klein, J. Holliday, J. S. Martins, and C. Ferguson, "Ergodicity in natural earthquake fault networks", *Physical Review E*, vol. 75, no. 6, pp. 066 107–066 117, 2007.

[250] K. F. Tiampo, J. B. Rundle, W Klein, J. S. Martins, and C. Ferguson, "Ergodic dynamics in a natural threshold system", *Physical Review Letters*, vol. 91, no. 23, pp. 238 501–238 512, 2003.

[251] K. F. Tiampo, J. B. Rundle, S. McGinnis, S. J. Gross, and W. Klein, "Eigenpatterns in southern California seismicity", *Journal of Geophysical Research: Solid Earth*, vol. 107, no. B12, ESE8–13, 2002.

[252] K. F. Tiampo, J. B. Rundle, W. Klein, Y. Ben-Zion, and S. McGinnis, "Using eigenpattern analysis to constrain seasonal signals in Southern California", in *Computational Earthquake Science Part I*, Springer, pp. 1991–2003, 2004.

[253] K. F. Tiampo, J. B. Rundle, S. A. McGinnis, and W. Klein, "Pattern dynamics and forecast methods in seismically active regions", in *Earthquake Processes: Physical Modelling, Numerical Simulation and Data Analysis Part II*, Springer, pp. 2429–2467, 2002.

[254] G. R. Toro and W. J. Silva, *Scenario Earthquakes for Saint Louis, MO, Memphis, TN, and Seismic Hazard Maps for the Central United States Region: Including the Effect of Site Conditions*. Risk Engineering Boulder, Colorado, 2001.

[255] J. C. Uwamahoro, J. B. Habarulema, and D. Buresova, "Highlights about the performances of storm-time TEC modelling techniques for low/equatorial and mid-latitude locations", *Advances in Space Research*, vol. 63, no. 10, pp. 3102–3118, 2019.

[256] T. Van Dam, J. Wahr, P. C. D. Milly, A. B. Shmakin, G. Blewitt, D. Lavallée, and K. M. Larson, "Crustal displacements due to continental water loading", *Geophysical Research Letters*, vol. 28, no. 4, pp. 651–654, 2001.

[257] Q. H. Van Der Meer, M. Storey, J. M. Scott, and T. E. Waight, "Abrupt spatial and geochemical changes in lamprophyre magmatism related to Gondwana fragmentation prior, during and after opening of the Tasman Sea", *Gondwana Research*, vol. 36, pp. 142–156, 2016.

[258] R. Van Dissen, J. Cousins, R. Robinson, and M. Reyners, "The Fiordland earthquake of 10 August, 1993: A reconnaissance report covering tectonic setting, peak ground acceleration, and landslide damage", *Bulletin of the New Zealand Society for Earthquake Engineering*, vol. 27, no. 2, pp. 147–154, 1994.

[259] R. Van Dissen and R. S. Yeats, "Hope fault, Jordan thrust, and uplift of the seaward Kaikoura Range, New Zealand", *Geology*, vol. 19, no. 4, pp. 393–396, 1991.

[260] C. A. Varotsos, Y. Mazei, D. Saldaev, M. Efstathiou, T. Voronova, and Y. Xue, "Nowcasting of air pollution episodes in megacities: A case study for Athens, Greece", *Atmospheric Pollution Research*, vol. 12, no. 7, pp. 101 099–101 105, 2021.

[261] P. Varotsos, N. Sarlis, and E. Skordas, "Spatio-temporal complexity aspects on the interrelation between seismic electric signals and seismicity", *Practica of Athens Academy*, vol. 76, pp. 294–321, 2001.

[262] P. Varotsos, N. Sarlis, H. Tanaka, and E. Skordas, "Some properties of the entropy in the natural time", *Physical Review E*, vol. 71, no. 3, pp. 032 102–032 109, 2005.

[263] P. Varotsos, N. V. Sarlis, and E. S. Skordas, *Natural Time Analysis: The New View of Time: Precursory Seismic Electric Signals, Earthquakes and other Complex Time Series*. Springer Science & Business Media, 2011.

[264] R. Vautard, P. Yiou, and M. Ghil, "Singular-spectrum analysis: A toolkit for short, noisy chaotic signals", *Physica D: Nonlinear Phenomena*, vol. 58, no. 1-4, pp. 95–126, 1992.

[265] J. M. Wallace and R. E. Dickinson, "Empirical orthogonal representation of time series in the frequency domain. Part I: Theoretical considerations", *Journal of Applied Meteorology and Climatology*, vol. 11, no. 6, pp. 887–892, 1972.

[266] L. M. Wallace, P. M. Barnes, J. Beavan, R. Van Dissen, N. Litchfield, J. Mountjoy, R. Langridge, G. Lamarche, and N. Pondard, "The kinematics of a transition from subduction to strike-slip: An example from the central New Zealand plate boundary", *Journal of Geophysical Research: Solid Earth*, vol. 117, no. B02405, 2012.

[267] L. M. Wallace, J. Beavan, R. McCaffrey, K. Berryman, and P. Denys, "Balancing the plate motion budget in the South Island, New Zealand using GPS, geological and seismological data", *Geophysical Journal International*, vol. 168, no. 1, pp. 332–352, 2007.

[268] L. M. Wallace, J. Beavan, R. McCaffrey, and D. Darby, "Subduction zone coupling and tectonic block rotations in the North Island, New Zealand", *Journal of Geophysical Research: Solid Earth*, vol. 109, no. B12, 2004.

[269] L. M. Wallace, S. Hreinsdóttir, S. Ellis, I. J. Hamling, E. D'Anastasio, and P. Denys, "Triggered slow slip and afterslip on the southern Hikurangi subduction zone following the Kaikōura earthquake", *Geophysical Research Letters*, vol. 45, no. 10, pp. 4710–4718, 2018.

[270] L. M. Wallace, Y. Kaneko, S. Hreinsdóttir, I. J. Hamling, Z. Peng, N. Bartlow, E. D'Anastasio, and B. Fry, "Large-scale dynamic triggering of shallow slow slip enhanced by overlying sedimentary wedge", *Nature Geoscience*, vol. 10, no. 10, pp. 765–770, 2017.

[271] L. M. Wallace, M. Reyners, U. Cochran, S. Bannister, P. M. Barnes, K. Berryman, G. Downes, D. Eberhart-Phillips, A. Fagereng, S. Ellis, and A. Nicol, "Characterizing the seismogenic zone of a major plate boundary subduction thrust: Hikurangi Margin, New Zealand", *Geochemistry, Geophysics, Geosystems*, vol. 10, no. 10, pp. 1–39, 2009.

[272] L. M. Wallace, S. C. Webb, Y. Ito, K. Mochizuki, R. Hino, S. Henrys, S. Y. Schwartz, and A. F. Sheehan, "Slow slip near the trench at the Hikurangi subduction zone, New Zealand", *Science*, vol. 352, no. 6286, pp. 701–704, 2016.

[273] W. Wan, F. Ding, Z. Ren, M. Zhang, L. Liu, and B. Ning, "Modeling the global ionospheric total electron content with empirical orthogonal function analysis", *Science China Technological Sciences*, vol. 55, no. 5, pp. 1161–1168, 2012.

[274] T. Wang, S. Wei, X. Shi, Q. Qiu, L. Li, D. Peng, R. J. Weldon, and S. Barbot, "The 2016 Kaikōura earthquake: Simultaneous rupture of the subduction interface and overlying faults", *Earth and Planetary Science Letters*, vol. 482, pp. 44–51, 2018.

[275] X. Wang and P. L. F. Liu, "An analysis of 2004 Sumatra earthquake fault plane mechanisms and Indian Ocean tsunami", *Journal of Hydraulic Research*, vol. 44, no. 2, pp. 147–154, 2006.

[276] S. N. Ward, "On the consistency of earthquake moment rates, geological fault data, and space geodetic strain: the United States", *Geophysical Journal International*, vol. 134, no. 1, pp. 172–186, 1998.

[277] S. N. Ward, "A multidisciplinary approach to seismic hazard in southern California", *Bulletin of the Seismological Society of America*, vol. 84, no. 5, pp. 1293–1309, 1994.

[278] B. C. Weare and J. S. Nasstrom, "Examples of extended empirical orthogonal function analyses", *Monthly Weather Review*, vol. 110, no. 6, pp. 481–485, 1982.

[279] W. Weibull, "A statistical distribution function of wide applicability", *Journal of Applied Mechanics*, vol. 18, pp. 290–293, 1951.

[280] S. Wiemer, "Introducing probabilistic aftershock hazard mapping", *Geophysical Research Letters*, vol. 27, no. 20, pp. 3405–3408, 2000.

[281] C. Xu, "Reconstruction of gappy GPS coordinate time series using empirical orthogonal functions", *Journal of Geophysical Research: Solid Earth*, vol. 121, no. 12, pp. 9020–9033, 2016.

[282] T. K. Yeh, C. Hwang, J. F. Huang, B. F. Chao, and C. Ming Han, "Vertical displacement due to ocean tidal loading around Taiwan based on GPS observations", *TAO: Terrestrial, Atmospheric and Oceanic Sciences*, vol. 22, no. 4, pp. 3–10, 2011.

[283] D. H. Zhang, Z Xiao, Y. Q. Hao, A. J. Ridley, and M. Moldwin, "Modeling ionospheric foF2 by using empirical orthogonal function analysis", in *Annales Geophysicae*, Copernicus GmbH, vol. 29, pp. 1501–1515, 2011.

[284] D. Zhang, A. J. Ridley, Z. Xiao, and Y. Hao, "A global model: Empirical orthogonal function analysis of total electron content 1999–2009 data", *Journal of Geophysical Research*, vol. 117, A03328, 2012.

[285] X. Zhou, W. Sun, B. Zhao, G. Fu, J. Dong, and Z. Nie, "Geodetic observations detecting coseismic displacements and gravity changes caused by the M_w9.0 Tohoku-Oki earthquake", *Journal of Geophysical Research: Solid Earth*, vol. 117, no. B5, 2012.

List of Refereed Publications and Research Awards

Research Awards

1. Appreciation award felicitated by the Department of Mathematics, BITS Pilani, Pilani for outstanding research activities.

2. International travel support, funded by Science and Engineering Research Board (SERB) (Government of India), for participating in *2022 Taiwan-Japan-New Zealand Seismic Hazard Assessment Meeting*..

Refereed Publications

1. **Neha** and S. Pasari, "A review of empirical orthogonal function (EOF) with an emphasis on the co-seismic crustal deformation analysis", *Natural Hazards*, vol. 110, pp. 29–56, 2022 (SCIE).

2. S. Pasari and **Neha**, "Nowcasting based earthquake hazard estimation at major cities in New Zealand", *Pure and Applied Geophysics*, vol. 179, pp. 1597–1612, 2022 (SCI).

3. S. Pasari, H. Verma, Y. Sharma, and **Neha**, "Spatial distribution of seismic cycle progression in northeast India and Bangladesh regions inferred from natural time analysis", *Acta Geophysica*, 2022 (SCI).

4. S. Pasari, A. Simanjuntak, **Neha**, and Y. Sharma, "Nowcasting earthquakes in Sulawesi Island, Indonesia", *Geoscience Letters*, vol. 8, pp. 1–13, 2021 (SCIE).

5. S. Pasari, A. Simanjuntak, A. Mehta, **Neha**, and Y. Sharma, "A synoptic view of the natural time distribution and contemporary earthquake hazards in Sumatra, Indonesia", *Natural Hazards*, vol. 108, pp. 309–321, 2021 (SCIE).

6. S. Pasari, A. Simanjuntak, A. Mehta, **Neha**, and Y. Sharma, "The current state of earthquake potential in Ja va Island, Indonesia", *Pure and Applied Geophysics*, vol. 178, pp. 2789–2806, 2021 (SCI).

7. S. Pasari, Y. Sharma, and **Neha**, "Quantifying the current state of earthquake hazards in Nepal", *Applied Computing and Geosciences*, vol. 10, pp. 100058, 2021 (Scopus).

8. **Neha**, R, Marwah, and S. Pasari, "Application of empirical orthogonal function on geodetic time-series data", *2021 IEEE International India Geoscience and Remote Sensing Symposium (InGARSS)*, pp. 198–201, 2021 (Scopus).

9. **Neha**, S. Mehrotra, H. Verma, and S. Pasari, "Iterative empirical orthogonal function in gap filling of GPS and InSAR data", *2021 IEEE International India Geoscience and Remote Sensing Symposium (InGARSS)*, pp. 496–499, 2021 (Scopus).

10. S. Pasari, P. Agarwal, and **Neha**, "Use of Shannon information entropy in earthquake nowcasting", *2021 IEEE International India Geoscience and Remote Sensing Symposium (InGARSS)*, pp. 222–225, 2021 (Scopus).

11. Y. Sharma, S. Pasari, and **Neha**, "Indian plate motion revealed by GPS observations: preliminary results", In: R. Kulshrestha, C. Shekhar, M. Jain, and S.R. Chakravarthy (Eds.) *Mathematical Modeling and Computation of Real-Time Problems: An Interdisciplinary Approach*, CRC Press, 2021.

12. **Neha**, S. Pasari, and S. Devi, "Determining coseismic deformation pattern associated with the 2016 Kaikoura earthquake inferred from EOF analysis" (under preparation).

13. **Neha**, S. Pasari, Y. Sharma, and S. Devi, "Spatial distribution of earthquake potential in New Zealand" (under preparation).

14. **Neha**, S. Pasari, Y. Sharma, and S. Devi, "Space-time evolution of crustal deformation after the 2016 Kaikoura earthquake in New Zealand from principal component analysis inversion method" (under preparation).

15. Atmesh, **Neha**, and S. Pasari, "EOF: An interactive graphical user interface (GUI) for spatio-temporal data" (under preparation).

16. S. Pasari, S. Devi, and **Neha**, "Distribution of earthquake interevent times in New Zealand" (under preparation).

List of Attended Conferences/Workshops/Schools

Presented work in international conferences/workshops

1. Presented paper entitled “Statistical analysis of natural times in the central-east Himalaya”, in international conference and 22^{nd} Annual Convention of Vijnana Parishad of India on Advances in Operations Research, Statistics and Mathematics (AOSM 2019), organized by the Department of Mathematics, BITS Pilani, Pilani Campus, Rajasthan, during December 28–30, 2019.

2. Presented paper entitled “Application of empirical orthogonal function on geodetic time-series data” in 2021 IEEE International India Geoscience and Remote Sensing Symposium (InGARSS), Ahmedabad (India), during December 6–10, 2021.

3. Presented paper entitled “Iterative empirical orthogonal function in gap filling of GPS and InSAR data” in 2021 IEEE International India Geoscience and Remote Sensing Symposium (InGARSS), Ahmedabad (India), during December 6–10, 2021.

4. Presented paper entitled “Contemporary geodetic strain distribution in New Zealand” in International Conference on Advances in Mechanics, Modelling, Computing and Statistics (ICAMMCS 2022), organized by the Department of Mathematics, BITS Pilani, Pilani Campus, Rajasthan, during March 19–21, 2022.

5. Presented poster entitled “Determining seismic spatio-temporal characteristics of the 2016 Kaikoura (M_w7.8) earthquake through EOF analysis” in 2022 Taiwan-Japan-New Zealand Seismic Hazard Assessment Meeting, Taitung (Taiwan), during October 31–November 4, 2022.

Attended workshops/schools

1. Attended "Summer School on Geospatial information and Disaster Management", organized by the Department of Geomatics, National Cheng Kung University (NCKU), Tainan, Taiwan, during July 1–10, 2019.

2. Attended "Autumn School on Physical Geodesy and Its Applications", organized by National Center in Geodesy (NCG) at IIT Kanpur, during October 14–24, 2019.

3. Attended "International Workshop on Advanced Seismology, Seismic Hazards and Earthquake Engineering: Theory, Simulation and Observations", organized by the Department of Civil Engineering, National Institute of Technology, Agartala, during December 12–17, 2019.

Brief Biography of the Candidate

Ms. Neha graduated with B.Sc. degree in Mathematics from Maharani College, University of Rajasthan, Jaipur in 2014, and post-graduated with M.Sc. degree in Mathematics from the Department of Mathematics, University of Rajasthan, Jaipur in 2016. Currently, she is working towards a Ph.D. degree from Birla Institute of Technology and Science, Pilani Campus, Pilani. Her research interests lie in earthquake cycle deformation with an emphasis on the spatio-temporal techniques in New Zealand using GPS geodesy, statistical seismology, and seismic hazard estimation. She has 11 research publications in peer-reviewed journals and conference proceedings to her credit. She is a recipient of the UGC NET-JRF. She has attended eight international conferences, summer schools, and international workshops during her Ph.D. tenure. During her Ph.D. time, she has received an appreciation award in the Department of Mathematics, BITS Pilani for her outstanding research capability. Recently, she has been granted an international travel support from the Science and Engineering Research Board (SERB), Government of India to participate in 2022 Taiwan-Japan-New Zealand Seismic Hazard Assessment Meeting, Taitung (Taiwan).

Brief Biography of the Supervisor

Dr. Sumanta Pasari is an associate professor in the Department of Mathematics, Birla Institute of Technology and Science, Pilani. He completed his Ph.D. in Civil Engineering (Geoinformatics specialization) from the Indian Institute of Technology Kanpur (IITK) and his Masters in Mathematics from the same Institute. His research interests include crustal deformation and active tectonics, statistical seismology, and renewable energy modeling. He has several research publications in refereed journals/proceedings. One Ph.D. student (Dr. Yogendra Sharma) has recently graduated from his research group, while six other Ph.D. scholars are working on various problems in the areas of crustal deformation analysis, machine learning in geosciences, and multidisciplinary approaches to renewable energy prediction.